8-13-2019

Seeing Stars Like Never Before: A Long-term Interferometric Imaging Survey of Red Supergiants

Ryan P. Norris
Georgia State University

SEEING STARS LIKE NEVER BEFORE: A LONG-TERM INTERFEROMETRIC IMAGING SURVEY OF RED SUPERGIANTS

by

RYAN PATRICK NORRIS

Under the Direction of Fabien Baron, PhD

ABSTRACT

Red supergiants (RSGs) are cool, luminous stars with radii that can exceed 1000 $R_{\odot}$. Indeed, such is their size that nearly every advance in stellar imaging has used the closest RSG, Betelgeuse, as a test case! These objects represent a late stage in the evolution of some massive stars, and, via their mass-loss and eventual demise in supernovae, they play an important role in the chemical evolution of the Universe. Moreover, their high luminosities have made them an object of interest for astronomers studying nearby galaxies. As a result of their increasingly broad use in astronomy, a solid understanding of RSGs and in the limitations of models of these objects is important.

One of the biggest challenges in modeling red supergiants is convection. In RSGs, granules and convection cells are quite large relative to the size of the star—with granules roughly 0.10-0.30 R_* and convection cells at least 0.50 R_*. This results in large surface features that can be studied using optical interferometry, but which can also corrupt measurements of parallax and other stellar parameters. Increasingly, there exist models of RSGs which take into account this behavior, but it is important to constrain these models with actual observations.

In this dissertation, we present a long-term study of surface features on RSGs using the Michigan InfraRed Combiner (MIRC/MIRC-X after 2016) at the Center for High Angular Resolution (CHARA) Astronomy Array on Mt. Wilson. Images resulting from these data are among the highest resolution obtained for any star (apart from the Sun). Fitting to model spectra, we derive $T_{\rm eff} = 3989 \pm 117$ K and $\log(g) = 0.29 \pm 0.26$ for the RSG AZ Cyg and $T_{\rm eff} = 3650 \pm 50$ K and $\log(g) = 0.30 \pm 0.26$ for the RSG SU Per. We also determine radii for 17 RSGs including AZ Cyg and SU Per. We reconstruct images of AZ Cyg from 2011, 2012, 2014, 2015 and 2016, and reconstruct images of SU Per from 2015 and two months in 2016. In both cases, we find evidence of long lived ($>$ 1 year) features roughly 0.50 R_* in size and short lived ($<$ 1 year) features roughly 0.10 R_* in size. We compare these observations to predictions from 2D and 3D models. We also discuss future directions for studying RSGs using optical interferometric imaging.

INDEX WORDS: stars: convection — stars: imaging — stars: individual (AZ Cyg, SU Per) — techniques: high angular resolution — techniques: interferometric

SEEING STARS LIKE NEVER BEFORE: A LONG-TERM INTERFEROMETRIC IMAGING SURVEY OF RED SUPERGIANTS

by

RYAN PATRICK NORRIS

A Dissertation Submitted in Partial Fulfillment of the Requirements for the Degree of

Doctor of Philosophy

in the College of Arts and Sciences

Georgia State University

2019

SEEING STARS LIKE NEVER BEFORE: A LONG-TERM INTERFEROMETRIC IMAGING SURVEY OF RED SUPERGIANTS

by

RYAN PATRICK NORRIS

Committee Chair:	Fabien Baron
Committee:	Douglas Gies
	Russel White
	John Monnier

Electronic Version Approved:

Office of Graduate Studies

College of Arts and Sciences

Georgia State University

August 2019

DEDICATION

For my brother Owen

ACKNOWLEDGMENTS

Poco parer potea lì del di fori;

per quel poco, vedea io le stelle

lor solere e più chiare e maggiori.

Purgatorio, XXVII 88-90[1]

Dante Alighieri

In the *Divine Comedy*, Dante writes that after walking up Purgatory on his way to Paradise, the stars "appeared brighter and clearer and larger" than they usually did. I think this is an apt thought to begin a dissertation using interferometry, which provides in some sense, a view of stars as larger and clearer than is possible with a normal telescope. And, like Dante's journey, this work has been one of purgation and transformation. And, just like Dante was helped along his journey by friends, by wise guides, by a beloved, and by Love, so too is this work the result of the support, guidance, and care of so many people in my life.

I must start by acknowledging the guidance and patience of my advisor Fabien Baron. Several years ago, I approached him about working on an imaging project in optical interferometry, and he proposed several, this among them. Since then he has taught me everything I needed to make this manuscript a reality. Along the way, he has offered encouragement and support during more difficult times, while also offering frank and challenging perspectives.

I also want to acknowledge funding through the Second Century Initiative at GSU, which

[1] Alighieri (1966)

provided me with a University Doctoral Fellowship for most of my time here. I also want to acknowledge funding through Fabien's grants, NSF Awards 1616483 and 1814777.

I must also thank the rest of my committee, especially Doug Gies, with whom I worked on OB Star research prior to my project with Fabien and who also taught me much about astronomical research. I also thank Russel White for his assistance with observing proposals and useful suggestions for this manuscript and the direction of this project. To my outside committee member, John Monnier, I offer double thanks, because without MIRC, which he designed and built, this project would not exist.

I also want to acknowledge the help of the staff at the CHARA Array. Special thanks goes to the telescope operators Norm Vargas, Chris Farrington, and Olli Majoinen, who helped make this project possible. I am also thankful to everyone who works to keep the Array running and has helped make CHARA a friendly place to visit and work: Matt Anderson, Theo ten Brummelaar, Steve Golden, Judit and Laszlo Surmann, Nils Turner, Larry Webster, and Craig Woods. A special shout out goes to Gail Schaefer for helping me to learn to use MIRC, and for numerous troubleshoots. The CHARA Array is supported by the National Science Foundation under Grant No. AST-1636624 and AST-1715788. Institutional support has been provided from the GSU College of Arts and Sciences and the GSU Office of the Vice President for Research and Economic Development.

I am also thankful for the help of the staff the NASA InfraRed Telescope Facility (IRTF). Special thanks goes to Mike Connelley for training me to use SpeX and for his help during observing runs as the support astronomer. The IRTF is operated by the University of Hawaii

under contract NNH14CK55B with the National Aeronautics and Space Administration.

My work has made use of tools from the Jean-Marie Mariotti Center; the SIMBAD database and the VizieR catalogue access tool from CDS, Strasbourg, France; and data from the European Space Agency (ESA) mission *Gaia* (`https://www.cosmos.esa.int/gaia`), processed by the *Gaia* Data Processing and Analysis Consortium (DPAC, `https://www.cosmos.esa.int/web/gaia/dpac/consortium`). Funding for the DPAC has been provided by national institutions, in particular the institutions participating in the *Gaia* Multilateral Agreement.

I am thankful to my collaborators for their support and the many good ideas they shared with me. Special thanks goes to Claudia Paladini for sharing the power spectrum code I used to measure the scale of convection in my stars. Thank you to John Young for providing me with the planned configurations of the Magdalena Ridge Optical Interferometer used in the final chapter of this manuscript. Thank you also to Miguel Montargès and Andrea Chiavassa for hosting me during a visit to the Observatoire de la Côte d'Azur and for many excellent discussions, as well as including me in their research on interferometric imaging of evolved stars. Thank you also to Anges Lèbre and Kateryna Kravchenko for including my targets in their observing programs.

I am thankful to entire GSU astronomy community, faculty, staff, and students included but I want to acknowledge several people whose friendship and support made a big difference: Michele Silverstein, Crystal Pope, Katie Gordon, Emily Manne-Nicholas, and Nicole Cabrera.

I want to thank my numerous roommates during my time at GSU, especially Sarah

Tunkle, who taught me recipes I still use regularly and offered some life-changing advice during my first year in Atlanta.

Thanks goes to my friends in Atlanta, especially the Saccaggis, the Magrees, the Gowasacks, the Pierpaolis, the Berzovinis, Timothy Jackson, Noah Lett, Pietro Avigni, Giovanni Maronati, Fr. Branson, and the rest of the Communion and Liberation community. Also want to thank Fr. Desmond Drummer and the Most Blessed Sacrament community for their support and encouragement.

I also want to thank the professors and teachers from before my time at GSU. I am especially thankful for the guidance and support of my advisors at CUA, Fred Bruhweiler and Glenn Wahlgren. Dr. Wahlgren taught me to be an astronomer, guiding me during a project studying high resolution spectra of Betelgeuse and other supergiants during the summer before my senior year of undergrad. That project led me to CUA where I also worked on symbiotic stars with Dr. Bruhweiler, who also offered much support and guidance. I also thank Steve Kraemer for the suggestion to apply to GSU when I realized that I wanted to be in a more astronomy focused environment. At MSU I want to thank Timothy Beers, who taught the first astronomy class I took and with whom I worked on a senior thesis. Also thanks to my first research advisor, in nuclear physics rather than astronomy, Krzysztof Starosta. I learned a good deal about what it means to be an independent researcher from him and got my first experiences working through new and unusual problems in the projects he assigned me.

Along the way I have been helped by numerous friends. From my time in the physics

department CUA, I want to especially thank Meriem Alaoui, Heather Stewart, Ryan Vilbig, and Sean and Maria Luck.

While in DC I met a small community of other Catholics whose friendship and support is probably what kept me in graduate school during that time. Thank you to the people in the Communion and Liberation community in DC then and now. Special thanks goes to Ellen Roderick who introduced me to her friends during what was one of the more difficult moments in my life.

I also would like to thank friends from MSU, especially my roommates Alan Legg and Richard Worhatch.

I have many reasons to be thankful for family, both here in Atlanta and at home. Thank you to my wife's family here, who made this city a second home to me and treated me with kindness and love. Countless thanks goes to my parents and siblings. My parents have always been supportive, encouraging, and patient. My dad introduced me to the night sky and to science and planted the seeds that led to this manuscript. My mom taught me to work hard, have curiosity, and to love learning. My brother Matthew and sister Megan have been patient and encouraging. I also want to offer special thanks to my youngest brother Owen, to whom I have dedicated this work. Owen was my biggest supporter and often asked how my research was going. He showed me how to live a life of service, how to help others overcome their challenges, and how to face challenges with bravery and hope. Like so many people, I miss him dearly, but the words he spoke near the end of his life: "Today is a blessed day" remain a challenge to be grateful and help others see the goodness of existence.

My deepest gratitude goes to my wife Katie. You have been a companion on this journey almost since I began it at GSU. You have offered more support and patience and love than I could have ever asked for. You make each day easier, more interesting, and the world more full of wonder. Thank you always for your good ideas, your support, and your presence.

Finally, I thank, to borrow the words of Dante: “L’amor che move il sole e l’altre stelle.”

TABLE OF CONTENTS

LIST OF TABLES

LIST OF FIGURES

CHAPTER 1
Introduction

1.1 Beginnings

In 1887, Albert Michelson, working with Edward Morley, used an interferometer to test the aether theory. Subsequently, Michelson, perhaps inspired by an idea proposed by Hippolyte Fizeau in 1868, wanted to use the technique (albeit in a different setup) to measure the size of distant objects in space. In a 1891 paper published in the *Philosophical Journal* and later revised and republished in the *Astronomical Journal* in 1920, Michelson wrote that the angular separation between binary components or the angular diameter of a uniformly brightened disk could be measured by placing two apertures at the objective of a telescope, producing a fringe pattern at the focus resulting from the interference of light passing through each aperture. By separating those apertures until the resulting fringes at the focus vanished, one could find the minimum of the visibility of the fringes, which is related to the angular size (or separation) of the observed object (Michelson 1891b, 1920).

Michelson tested the method on the Galilean moons of Jupiter at Mt. Hopkins in 1891 (Michelson 1891a). This confirmed the accuracy of the method but because stars have significantly smaller angular diameters, a different method for forming interference fringes was required. Thus, he proposed a new instrument, using mirrors rather than slits. The device, as it was applied to the 100 inch Hooker telescope, consisted of a series of four mirrors attached to a 20 foot steel plate above the casing of the telescope. By adjusting the separation of the mirrors slightly until fringes vanished, one could measure the angular diameter of a

star, provided it was sufficiently large for the limited baseline of the instrument. Using this technique on Betelgeuse, Michelson and Francis Pease determined that the angular diameter of the star was roughly 47 mas (Michelson & Pease 1921).

1.2 Interferometry

1.2.1 The wave nature of light and the diffraction limit

Why was it even necessary for Michelson to build an interferometer in order to measure the diameter of Betelgeuse? Consider a telescope: the two major tasks of the instrument are to collect light and to resolve the source of that light. Imaging, even measuring of diameters, originates from this second task. The ability of a telescope to resolve an object is given by the Rayleigh criterion:

$$\theta_R \approx 1.22\frac{\lambda}{D} \tag{1.1}$$

where θ_R is an angular diameter in radians, λ denotes the wavelength of the light collected by a telescope, and D is the diameter of the objective (light collecting) mirror or lens. Note that this relation is approximate because the numerical factor 1.22 contains π. In order to resolve Betelgeuse at 555 nm, the wavelength at which the human eye is most effective, a telescope mirror needs to be about 3 m. However, this is based on a perfect optical system and describes the size of mirror needed simply to resolve the object as more than a point source. In order to resolve smaller features on a star, even a large one like Betelgeuse, it is necessary to use a technique that can reach resolutions beyond that of a single aperture

telescope. This method is rooted in the wavelike nature of light.

In our discussion about waves, we will use certain terminology. In addition to wavelength (the spatial separation between similar sections of a wave), a wave can be described by an amplitude (the maximum displacement of the wave), frequency (the number of oscillations the wave makes in a given time), and phase (a quantity that defines the behavior of a wave by denoting a position on the wave at a given time relative to an origin point). A wavefront is a surface along which a wave has the same phase. When two waves interact, the superposition of the waves depends on the phase difference between the two waves.

The idea that light is a wave originated in the 17th century in the theoretical work of Dutch physicist Christiaan Huygens and experiments conducted by the Italian Jesuit Francesco Maria Grimaldi, the French Jesuit Ignace-Gaston Pardies, and English natural scientist Robert Hooke (Labeyrie et al. 2006). Of particular interest for our discussion is the diffraction that Grimaldi observed (and named, the etymology coming from the Latin 'dis' (apart) and 'frangere' (break into pieces; Cecchini & Pelosi 1990). In his experiment, Grimaldi noted that light passing through a small hole produced a cone of light. However, from this behavior, Grimaldi surmised that light was fluid in nature. Shortly after the death of Grimaldi and the publication of his theoretical work, Pardies explained that diffraction and other optical phenomena could be explained if light was wavelike in nature. From this work, Huygens developed his wave theory of light (Ziggelaar 1980). The Huygens-Fresnel principal encapsulates the description of light that Huygens proposed: light is a wavefront consisting of a summation of spherical wavelets. In other words, as light propagates, the

form of the wavefront at that moment is the summation of the spherical waves formed at an earlier point (Shapiro 1989). Unfortunately, Huygens' theory was eclipsed by Newton's corpuscular theory throughout most of the 18th century. It was not until 1803 that a new experiment which showed the interference of light resurrected broad interest in a undulatory description of light. For this we owe credit to English experimental physicist Thomas Young.

In Young's "double slit" experiment, sunlight was split by a thin card after first passing through a small pinhole in order to create an artificial point source. Young placed a screen in the path of the split beams and observed an interference pattern, with light and dark bands. Young noted that the fringes only appeared when both of the split beams were present; blocking one beam caused the pattern to disappear: exactly the behavior one expects from a wave.

1.2.2 The theory behind interferometry

Interference fringes such as those produced in the double slit experiment only result when the wavefronts originating from the source are coherent, that is if the phase difference between two wavefronts from the same source have a constant phase difference at a particular point in space. Although light from most astronomical objects is spatially incoherent, at the large distances involved in astronomy the light collected from a source displays partial coherence. This partial coherence is useful because of the Van Cittert-Zernike theorem, which states that the Fourier transform of the complex spatial coherence function of an incoherent source is the angular intensity distribution of that source (Labeyrie et al. 2006).

To see how the coherence function relates to an astronomical object, we can follow

Labeyrie et al. (2006) to derive the Van Cittert-Zernike theorem. Consider light from a distant astronomical source as illustrated in Figure 1.1, which is adapted from Labeyrie et al. (2006). The object has intensity $I = \langle |A(l,m)|^2 \rangle$, where A is the amplitude of the optical field originating from the source. The object covers spatial extent (l, m) where $l = \sin(\theta_x) \approx \theta_x$ and $m = sin(\theta_y) \approx \theta_y$ because the source is very distant and near the z-axis. Light from this object is a contribution from numerous light sources across the object, travelling with wavevector $-k_0$. In the z=0 plane the optical field is $A(l,m)e^{i(\omega t + k_0 l \cdot \mathbf{r})}dldm$. In this equation, the circular frequency is $\omega = 2\pi c/\lambda$ where c is the speed of light and λ the wavelength, and t is time. Integrating the equation gives (Labeyrie et al. 2006)

$$\phi(k_0 x, k_0 y) = e^{i\omega t} \iint A(l,m) e^{i(k_0(lx+my))} dldm. \tag{1.2}$$

We can write Equation 1.2 as a Fourier integral (Labeyrie et al. 2006)

$$\phi(k_0 x, k_0 y) = e^{i\omega t} a(-k_0 x, -k_0 y). \tag{1.3}$$

The coherence function of the optical field from the source is (Labeyrie et al. 2006)

$$\gamma(k_0 \mathbf{r}) = \langle \phi(k_0 \mathbf{r}) \star \phi^*(k_0 \mathbf{r}) \rangle = \langle a(-k_0 \mathbf{r}) \star a^*(-k_0 \mathbf{r}) \rangle \tag{1.4}$$

where the $= e^{i\omega t}$ has canceled because of multiplication with the complex conjugate.

Taking the Fourier transform of Equation 1.4 yields (Labeyrie et al. 2006):

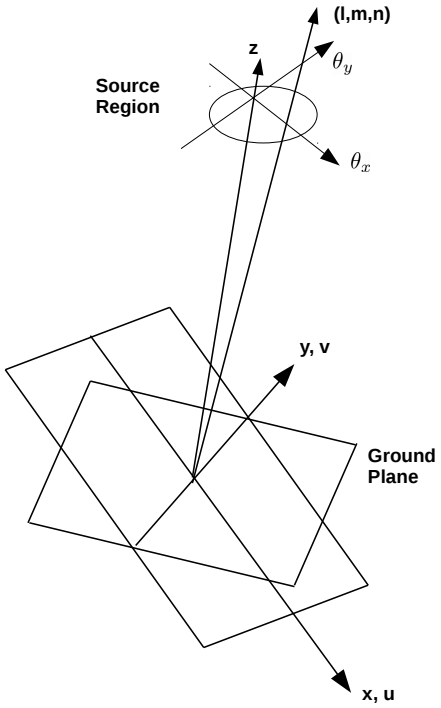

Figure 1.1: Geometry used in the proof of the Van Cittert-Zernike theorem, adapated from Labeyrie et al. (2006).

$$\Gamma(l,m) = \left\langle A(l,m) \cdot A^*(l,m) \right\rangle = \left\langle |A(l,m)|^2 \right\rangle = I(l,m) \tag{1.5}$$

and thus we find find the Van Cittert-Zernike theorem. Imaging in optical interferometry is thus a problem of finding the coherence function of the light from an astronomical source, which we can use to recover the angular intensity distribution of that object.

To understand coherence and its relation to interference fringes, let's return to Young's

double slit experiment. If the light emerging from each of the two pinholes has mean intensities A_1^2 and A_2^2, we can write the optical waves as $A_1\phi(\mathbf{r})$ and $A_2\phi(\mathbf{r})$, where ϕ_x describes the complex optical field. Using the notation of Lawson (2000) and Jackson (1998), we can write the real part of this optical wave in the familiar form $\phi \sim Ae^{i(\mathbf{k}\cdot\mathbf{x}-\omega t)}$. In this equation the wavenumber is $\mathbf{k} = k\hat{\mathbf{n}}$ with $k = 2\pi f$ where the frequency is f, the circular frequency is $\omega = 2\pi c/\lambda$, where c is the speed of light, λ is the wavelength, and t is time. The coherence function (Zernike 1938) of the (normalized) optical fields from each of the pinholes is (Labeyrie et al. 2006):

$$\gamma(\mathbf{r}_1, \mathbf{r}_2) = \frac{\left\langle A_1\phi(\mathbf{r}_1) \cdot A_2\phi^*(\mathbf{r}_2)\right\rangle}{A_1A_2} = \left\langle \phi(\mathbf{r}_1)\phi^*(\mathbf{r}_2)\right\rangle. \tag{1.6}$$

The light from each pinhole produces an interference pattern of fringes, which is the result of the superposition of the two optical fields. The time averaged instantaneous intensity of this pattern is (Labeyrie et al. 2006):

$$I(\delta) = A_1^2 + A_2^2 + 2A_1A_2|\gamma(\mathbf{r}_1, \mathbf{r}_2)|cos(\delta + \Delta) \tag{1.7}$$

with Δ describing the position of the central fringe and δ the phase difference between the two optical fields.

In his experiments on interferometry, Michelson (1891b) defined the contrast of fringes

as the visibility, described by:

$$V = \frac{I_{max} - I_{min}}{I_{max} + I_{min}} \tag{1.8}$$

which for equation 1.7 is

$$V = \frac{2E_1E_2}{E_1^2 + E_2^2} \cdot |\gamma(\mathbf{r}_1, \mathbf{r}_2)| \tag{1.9}$$

Thus, by measuring the visibility and phase of fringes, one can access the coherence function, which, via a Fourier transform, offers information about the size and appearance of an object in the sky.

1.2.3 Observational interferometry

The goal of an astronomical optical interferometer is to form fringes by combing light from multiple apertures in order to measure the coherence function and recover information about an object in the sky at a higher resolution than is possible with a single aperture instrument. In Figure 1.2, which is adapted from Lawson (2000) and Labeyrie et al. (2006), we depict a simple interferometer: Two telescopes are separated on Earth by a baseline B. Usually some delay is included in the path to the combination site in order to make up for the fact that the light travel time to each receiver is not the same, shown as delay lines in Figure 1.2. Because the measured coherence function is a Fourier transform of the spatial light distribution, the separation of the telescopes in the plane normal to the direction of the source, $\mathbf{r} = (l, m)$, is written in Fourier space in the form of a vector normalized by the wavelength of the light $\mathbf{u} = (u, v) = \mathbf{r}/\lambda$. A measurement of an interferometer is a sample of this (u, v) plane. In

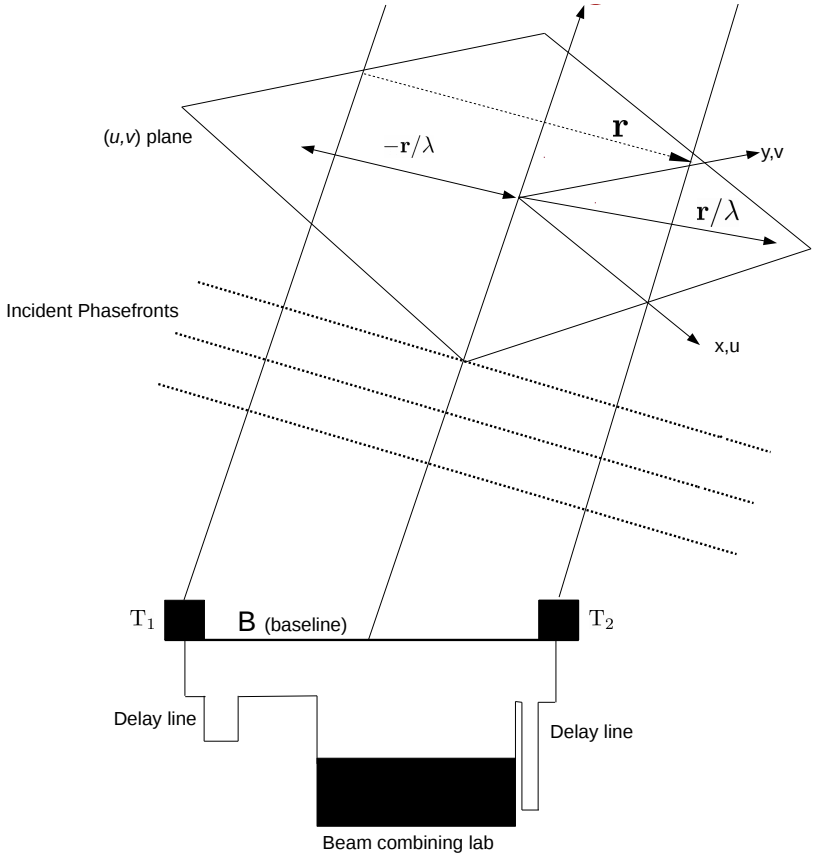

Figure 1.2: Model of a simple interferometer adapted from Lawson (2000) and Labeyrie et al. (2006).

order to perform imaging with interferometry, astronomers observe as many points in the (u, v) plane as possible. This can be done by observing at many wavelengths, by varying the separation between the receiving elements (or by having many different receiving elements, each combining with each other), and/or by using the Earth's rotation to result in a slightly different sample of the (u, v) plane. The resolution of an interferometer comes from the maximum baseline, B, as described by the equation $\theta_r \approx 206265\frac{\lambda}{2B}$, where θ_r is in arseconds and λ is the wavelength.

Recovering the pure amplitude and phase of the light from the fringes is limited by the fact that the light is impacted by atmospheric turbulence and instrumental effects along the way to the detector. Although visibility amplitudes can be used to measure diameters and effects like limb darkening, phases are vital for imaging. In order to recover part of the phase, the so-called closure phase approach was first developed in radio astronomy (Jennison 1958). In this technique, light from a closed triangle of three telescopes is combined. Fringes are formed for each pair (for example, 1-2) in this triangle, with a phase error ϕ_i introduced by the atmosphere above telescope i:

$$\widetilde{V}_{12}^{obs} = |V_{12}^{\rm obs}| e^{i(\Phi_{12}^{\rm true}\phi_1 - \phi_2)} \tag{1.10}$$

where we have $\widetilde{V}_{12}^{obs}$ as the complex visibility at the detector and $\Phi_{12}^{\rm true}$ the actual complex visibility phase of the object measured at the frequency. Note that the visibility amplitude $|V_{12}^{obs}|$ is also impacted by gain from instrumental and atmospheric effects. This gain can mostly be corrected using calibration techniques, although when four or more telescopes are available, there is a closure technique called closure amplitude that can also correct for gain.

Multiplying the measured complex visibility from three baselines on a closed triangle, one forms the so-called triple product or bispectrum (Monnier 2007):

$$\begin{aligned}
\widetilde{V}_{12}^{obs}\widetilde{V}_{23}^{obs}\widetilde{V}_{31}^{obs} &= |V_{12}^{obs}||V_{23}^{obs}||V_{31}^{obs}| e^{i(\Phi_{12}^{\rm obs}+\Phi_{23}^{\rm obs}+\Phi_{31}^{\rm obs})} \\
&= |V_{12}^{obs}||V_{23}^{obs}||V_{31}^{obs}| e^{i(\Phi_{12}^{\rm true}+\phi_1-\phi_2)} e^{i(\Phi_{23}^{\rm true}+\phi_2-\phi_3)} e^{i(\Phi_{31}^{\rm true}+\phi_3-\phi_1)} \\
&= |V_{12}^{obs}||V_{23}^{obs}||V_{31}^{obs}| e^{i(\Phi_{12}^{\rm true}+\Phi_{23}^{\rm true}+\Phi_{31}^{\rm true})}.
\end{aligned} \tag{1.11}$$

Since the atmospheric contributions cancel out, the measured closure phase ($\Phi_{12}^{\rm obs} + \Phi_{23}^{\rm obs} + \Phi_{31}^{\rm obs}$) is equal to the true closure phase ($\Phi_{12}^{\rm true} + \Phi_{23}^{\rm true} + \Phi_{31}^{\rm true}$) on the original object brigthness distribution. The closure phase is consequently impervious to atmospheric perturbations. In particular, the closure phase provides information on departures from centrosymmetry. For a symmetric object, closure phases are always 0 or $\pm$180 degrees (Monnier 2007). Thus any deviation from this in the closure phase provides information about the structure of the brightness distribution.

This technique requires at least three telescopes, and so imaging in optical interferometry did not come about until facilities with more than three telescopes were built, although aperture masking at facilities such as the William Herschel Telescope (WHT) did apply closure phases prior to the construction of multi-telescope interferometers. While closure phase does provide phase information, it does not permit the complete recovery of the complex coherence function. Instead, only some percentage of the total missing phase information is recovered and the closure phase becomes an ingredient in the image reconstruction process, with an imaging algorithm or tool aiming to replicate the closure phase observed. The number of independent closure phases recovered for N telescopes is $\frac{(N-1)(N-2)}{2}$ and the fraction of phase information recovered is $\frac{N-2}{N}$ (Monnier 2007).

To measure closure phases, the bispectrum vector (amplitude and phase) is averaged over time. The modulus of the bispectrum, called the triple amplitude, is therefore measured simultaneously with its phase (closure phase). In addition to the triple amplitude and closure phase, the other common observable from interferometry is the *squared visibility*, sometimes

called the V^2. This is a measurement of the squared amplitude of the complex coherence function $|\gamma|^2$. The plot of V^2 against spatial frequencies gives what is called a squared visibility curve. This curve provides information about the size of the object and at high spatial frequencies may provide some information about the structure of an object, albeit without positional information. For a star, the first lobe provides information about the size of an object, the second lobe provides information about limb darkening, and the third and onward lobes provides evidence of features smaller than the stellar disk that might also be causing departures from perfect circular symmetry.

1.3 Image Reconstruction

Unfortunately, recovering an image from the data an interferometric array collects is not so simple as performing an inverse Fourier transform on these data. The primary obstacles to this approach are: 1) a small number of telescopes, which limits the Fourier frequencies from which to recover an image; and 2) the corruption of data due to instrumental and atmospheric effects. In order to find a unique solution under these constraints, we apply prior information to constrain the image. We can then describe the problem of finding an image $\boldsymbol{x}$ in terms of maximum *a posteriori*, which contains two penalty terms, a likelihood, given by the χ^2 of the data to the image and which constrains the image to the data, and a prior or regularization term $\mu f_p(\boldsymbol{x})$, which constrains the image to some known or assumed

information (Baron 2016):

$$\boldsymbol{x}_{\text{opt}} = \text{argmin}\left\{\chi^2(\boldsymbol{x}) + \mu f_p(\boldsymbol{x})\right\} \tag{1.12}$$

In Equation 1.12, argmin means we are seeking the value of $\boldsymbol{x}$ which minimizes the relation and μ is called the *hyperparameter* a weight which determines the "influence" of the prior versus the likelihood in finding an image. Using too high a hyperparameter results in an over-regularized image that looks like the prior and using too low a hyperparameter results in an image riddled with artifacts. Finding the proper hyperparameter is an important step in imaging reconstruction and will be discussed more in chapter 4.

Equation 1.12 is the equation which most image reconstruction techniques seek to solve. Clearly, the selection of priors plays an important role in constraining the possible images that solve these equations. Two of the most important priors, which usually used in optical interferometry, are that the image is normalized and the image is positive. The latter is an attribute of a physical brightness distribution and the former is necessary because the data used in optical interferometry comes from the complex visibility, which is normalized per Equation 1.9.

Solving the image problem is an optimization problem which searches for a minima in the regularized maximum likelihood Equation 1.12. One approach is to do some sort of gradient descent based searching for this minima. This is the approach taken by image reconstruction codes such as the one found in OITOOLS.jl[1] and in MiRA (Thiébaut 2008),

[1] `https://github.com/fabienbaron/OITOOLS.jl`

one of the most commonly used image reconstruction codes in optical interferometry. In the case of MiRA, an image is modeled as complex visibilities, with minimization using a version of the semi-Newton limited memory BFGS. Because MiRA and OITOOL.jl do not perform global optimization, a starting image is required for the reconstruction. Often this is done via an iterative process, starting with some very simple image and judicious selection of regularizers and hyperparameters, and inputting the result of that attempt as the starting image of the following reconstruction attempt, and so on until the algorithm converges. A benefit of an approach like gradient descent is that it can be very fast, but it is sensitive to local minima and cannot employ non-convex or non-differentiable regularizers.

An alternative approach to gradient descent is to try a stochastic approach. A pioneer of this technique was the MArkov Chain IMager (MACIM) (Ireland et al. 2006). For the work reported in this manuscript, we used SQUEEZE (Baron et al. 2010, 2012), a Markov Chain Monte Carlo (MCMC) reconstruction tool that was based upon MACIM. In SQUEEZE, MCMC is used to search for the best solution to the optimization problem. SQUEEZE uses parallel tempering and parallel simulated annealing.

The problem of searching probability space can be imagined as as being lost in the mountains whilst looking for a village at the lowest elevation in the region (remember that we have set up our problem such we are seeking to minimize the negative log of the probability, which results in maximizing the probability). There are many different regions of lower elevation, which appear as if they are going to be the location of the village but are not. In a gradient descent search, one uses the direction one is travelling to decide whether to move

forward or backwards, with the aim being to move lower until one finds a spot where the gradient no longer changes. Unfortunately, it is easy to get stuck in an intermediary valley using this method. In particular, this method makes the selection of a starting image very important! With MCMC methods, one is able to jump randomly to different locations in the probability space. This is akin to having a drone that you can call to pick you up while lost in the mountains and which drops you randomly somewhere else.

The two methods SQUEEZE uses are slightly different in their operation. Keeping the language of metallurgy from which these methods are inspired, they use the notion of "temperature", which is a factor which determines the ability of a chain to move to a very different solution and is essentially a proxy for the strength of the regularizer versus the likelihood. As the chains progress, the temperature is lowered and so the chance of moving to a radically different solution is decreased. In parallel simulated annealing, multiple chains are run, each with a different starting point. Each chain follows the process of simulated annealing, that is, a random nearby solution is found and then compared to the previous solution. When the new solution improves the solution it is accepted without reservations, otherwise, there is a probability that this "worse" solution is accepted. The probability of this acceptance is based the distance of this new solution from the optimal solution, as well as the temperature: $P \sim 1 - e^{\frac{-\Delta E}{kT}}$ where ΔE is the energy, essentially the location in probability space, with a lower E being the goal, k a constant, and T the temperature. At the end of SQUEEZE's multichain parallel simulated annealing approach, the result of each chain's search is co-aligned and averaged so that the result is independent of minimization path. Returning to

our village search analogy, this method is akin to having a team of searchers, each looking for the village on their own paths. They have access to the aforementioned randomly moving drones. Each time an individual is dropped off a random location they choose to stay put or to move on to a random nearby stop. As time progresses, they move less and less until they settle wherever they are and then tell everyone else, their location. At this point, the best guess for the location of the village is the average of all their locations and hopefully it is quite close.

In parallel tempering, multiple, randomly initialized, chains are run, each starting at a different temperature. Throughout the reconstruction, the temperature for a given change remains the same but it can exchange images with chains of similar temperatures. Thus, the algorithm is able to explore more of the probability space. Returning to the hiking analogy, this is like having a team again, except that now nearby hikers can see each other and go to a nearby location while making their search.

Looking to the future, there is the possibility of using quantum annealing (Finnila et al. 1994; Kadowaki & Nishimori 1998; Venegas-Andraca et al. 2018), a relatively new technology, for searching image probability space. In the hiker analogy, it is akin to being able to tunnel through mountains in search for a better solution, and thus is not impacted by very high peaks in the mountain ranges (that is not impacted by strong local maxima and minima).

SQUEEZE has been very successful in the semi-annual Interferometry Imaging Contests. In addition to a robust search method, it is able to use non-convex and non-differentiable regularizers, can do multi-wavelength imaging, and can do Bayesian model selection. SQUEEZE

is the primary image reconstruction tool used in this dissertation, with gradient descent tools used as tests of the solutions, following best practices for image reconstruction, which require that multiple methods be used in imaging.

1.4 Red Supergiants

Betelgeuse was an apt first target for Michelson's interferometer because it is a red supergiant (RSG), a class that is among the largest stars in spatial size, with radii ∼100 to 1500 $R_\odot$ (Levesque 2017). RSGs are defined physically as helium burning descendants of stars with mass 8 to 40 $M_\odot$ (Levesque 2017), although one should keep in mind that stars in this stage will burn heavier elements as they continue to evolve. Observationally, RSGs are defined as late K to M-type supergiants. This translates to stars with effective temperatures ($T_{\rm eff}$) of $\sim$ 3400 to 4500 K (Levesque 2017) and luminosities $\geq 10^{4.5-5.8}\ L_\odot$ (Humphreys & Davidson 1979). This high luminosity allows RSGs to be studied in galaxies tens of mega-parsecs away, and because they are a stage in the life of short-lived massive stars, RSGs serve as a means of measuring the metallicity of such a galaxy—offering a test of stellar evolutionary models (Drout et al. 2012; Patrick et al. 2015; Davies et al. 2015; Gazak et al. 2015). Locally, these stars have a significant impact on the chemical evolution of their host galaxies, as they experience significant mass-loss and many, if not all, will end their lives in supernovae (either as RSGs or after evolving blueward Meynet et al. 2015). Thus, a solid understanding of RSGs is vital to astronomical questions related to phenomena both near and far.

Stars at the beginning of the RSG stage fuse helium through the triple-α process, resulting

in carbon and oxygen. Unlike in less massive stars, fusion is able to progress beyond helium within the cores of RSGs as the star evolves. Increases in the mean particle mass due to the fusion of helium to heavier elements results in contraction of the core (Levesque 2017). Eventually, the temperature and density increases to a point which permits carbon fusion. This process also increases temperatures around the core, which in turn permits the beginning of helium fusion around the core and a shell of hydrogen fusion around that inner shell. This process, fusion of heavier and heavier elements, surrounded by shells of fusion of lighter elements continues as the star evolves. When the core is comprised primarily of iron, fusion no longer produces more energy than it takes in, resulting in the end of the balancing act of hydrostatic equilibrium and the beginnings of processes that may lead to a supernova.

In addition to this interior activity, the RSG stage is also a phase of dramatic changes in surface abundances. During this stage, the size of the outer convection zone increases dramatically. This results in a dredge up of material from the core, showing up as an enrichment of nitrogen and oxygen in the spectra of RSG. In addition to this mixing, chemical enrichment results from the weak *s*-process, whereby neutrons from fusion processes are able to build heavier nuclei at a rater slower than the decay rate of the resulting isotopes (Pignatari et al. 2010). This results in an enrichment in isotopes close to the "island of stability", which can be identified in high resolution spectra of red supergiants (e.g., Lundqvist & Wahlgren 2005; Wahlgren et al. 2009; Norris et al. 2010). Although RSGs are not nearly as strong contributors as asymptotic giant branch (AGB) stars to *s*-process abundances, the weak *s*-process is an important source of isotopes of intermediate mass elements including some

of the rare earth elements used in semiconductors and found in computers such as the one being used to produce this manuscript.

The end life stage of RSGs depends heavily on several factors, including the mass of the star, the rate of mass-loss, rotation, and metallicity. Thanks to the advent of transient detection techniques and tools for for detecting the progenitors of supernovae, there is now a strong consensus that Type II-P supernovae are caused by RSGs, so called because these supernovae manifest a large hydrogen fraction and long decay plateau. Despite this success, for awhile, there seemed to be a discrepancy between theory, which predicted that stars as massive as 25 $M_{\odot}$ should produce II-P supernovae, and observations, as the highest mass progenitor was found to be 17 $M_{\odot}$. Recent work by Davies & Beasor (2018) offers an answer to this so called "red supergiant problem". Because progenitor detections generally happen in only one or two passbands and mass determinations are made based on the brightness of the star, the mass measurement is sensitive to assumptions about the star and its environment. Davies & Beasor (2018) showed that using an improved bolometric correction and better accounting for extinction leads to higher mass estimates of the progenitors. Moreover, they showed that the current sample size of observed supernovae progenitors, which is rather small, is also a contributing factor to the problem.

There are alternate explanations for the lack of higher mass supernovae progenitors among RSGs. One is that RSGs above about 18 $M_{\odot}$ experience significantly higher mass-loss rates and evolve blueward into luminous blue variables or Wolf-Rayet stars. Another explanation is that massive RSGs skip a supernovae entirely and simply implode into a black

hole. This would be the result of the core-structure at the end of core fusion processes, as it is ultimately core structure that determines whether a star's collapse upon cessation of hydrostatic equilibrium results in a "rebound" explosion of a supernova or implosion into a compact object. In a recent paper, Sukhbold & Adams (2019) used models of nuclear burning inside RSGs to suggest the key difference between a massive RSG that supernovas and one which collapses is whether core carbon fusion takes place in convective (as in those with lower mass RSGs) or radiative (as in those with higher mass) conditions. A radiative core during carbon burning results in shells which are further out in the star and thus subsequent cores (O, Si...) which are more extended—this effect is what causes the transition between explosion and implosion at the end of a star's life, because these extended cores explode with greater difficulty.

1.4.1 Mass-loss and the environment of a red supergiant

Red supergiants have a complex extended atmosphere and experience extreme mass-loss, which has an impact on their future evolution and contributes to the chemical enrichment of their host galaxy. Various explanations of this mass-loss have been put forth, such as wind driven by radiation pressure on dust grains, radial pulsations that decrease the density gradient in the extended atmosphere, convection shells that drive shocks, and dissipation of Alfvén waves (Levesque 2017). Observational mass-loss rates rely on estimates of gas velocity in the extended atmosphere, usually determined via studies of gas emission, such as H I 21 cm emission or CO at millimeter wavelengths, as well as measurements of gas-to-dust ratio. For stars without this information, researchers have developed empirical laws

that use some other measurement as a proxy for mass-loss, such as the relation of Jura & Kleinmann (1990) which uses flux at 60μm and a standard outflow velocity. van Loon et al. (2005) studied dusty RSGs and AGBs and used gas-to-dust ratios to determine mass-loss. They found the Jura & Kleinmann (1990) law works well for dust enshrouded RSGs but over-estimates mass-loss rates for optically bright RSGs. de Jager et al. (1988) used mass-loss measurements from numerous sources to develop a prescription that relates mass-loss to temperature and luminosity using Chebyshev polynomials. Mauron & Josselin (2011) found the prescription from de Jager et al. (1988) works reasonably well for Galactic RSGs, except for those with very high luminosities.

Despite these successes, there is a large scatter of mass-loss rates with respect to luminosity. Further complicating descriptions of mass-loss, interferometric observations of red supergiants have shown evidence for episodic mass-loss (Danchi et al. 1994). Recently, observations of the extended atmosphere of Betelgeuse with ALMA at submillimeter wavelengths showed asymmetries in the chromosphere and that the temperature at 1.4 R_* was cooler than the photosphere (O'Gorman et al. 2017). Images reconstructed from these data showed that the extended atmosphere was asymmetric with a bright feature in one quadrant of the star and elongation along one axis. Because the bright feature, which was 1000 K warmer than its surroundings, matched the location of a bright feature observed on the surface of the star around the same time, the authors suggested that convection related heating, perhaps influenced by convection related magnetic fields, could cause asymmetries observed in the extended atmospheres of RSGs.

Arroyo-Torres et al. (2015) studied three red supergiants in the K-band (1.92-2.47 μm) at R$\sim$1500 using AMBER on VLTI. In addition to determining the fundamental parameters of these stars, they used spectrointerferometry to collect spectra across their resolved disks and studied atmospheric extension in these stars. They found good agreement with continuum predictions from stellar atmospheres but noted that both 1D and 3D models failed to match the observed extension in CO lines. Indeed, even 3D RHD models with convection and 1D pulsation models produced atmospheres which were more compact. The authors suggested that because extension increased with decreased gravity and increased luminosity, radiative acceleration on Doppler-shifted lines could explain this extension in molecular layers, similar to what is observed in AGB stars.

Ohnaka et al. (2017) determined line-of-sight velocities across the disk and extended atmosphere of Antares, finding a clumpy velocity field ranging from -20 km s^{-1} to 10 km s^{-1}. Furthermore, a bright spot in the continuum image was blueshifted, which is suggestive of updwelling from convection. Comparing their results to model predictions, they also found that convection alone cannot explain the extended atmosphere, nor the vigorous motions found above the continuum photosphere, and thus cannot be responsible for mass-loss on its own.

1.4.2 Convection

Images of the Sun show that it is not uniform in appearance across its disk. Besides the occasional sunspot, filament, and coronal mass ejection, even when "quiet", the surface appears to boil with many thousands of small bright features that are surrounded by dark

lanes between them. These small bright areas are called granules and are the result of convection, one of the major means of energy transport in a star. In contrast to radiative energy transport, which involves the transfer of energy via photos, in convection energy is transferred via the motion of macroscopic mass elements.

Although incomplete, mixing length theory serves as a good starting point for understanding the mechanisms of convection in a star. The most widely used formulation of mixing length theory is that of Böhm-Vitense (1958), which is the one we'll use, as it has informed the much of the discussion of convection in red supergiants.

Consider a convective element which is warmer than its surroundings. This element rises due to buoyancy because it is less dense. If this rise happens adiabatically, meaning there is no change in heat in the bubble, and if this element and its surroundings remain at the same pressure during the rise, what determines the continued rise of this element is the temperature gradient. When the temperature gradient of the surrounding gas is steeper than that experienced by an element rising adiabatically, conditions are unstable against convection. The buoyancy force experienced by the rising element is $f = \frac{g\rho\Delta T}{T}$ where g is the gravity, ρ is the density, and T temperature. The equation of motion for this element is:

$$\frac{d^2r}{d^2t} = \frac{g\Delta T}{T}. \tag{1.13}$$

Using Equation 1.13 one can find that the time before an element mixes with its sur-

roundings is described by

$$t \propto \left(\frac{\alpha r T}{g \Delta T}\right)^{1/2}. \tag{1.14}$$

In Equation 1.14 αr is called the mixing length, l_m (Bowers & Deeming 1984). This is the distance an element moves before it mixes with its surroundings. In discussions of the large convection cells theorized to exist in RSGs, this is generally used as a limit to the size of a convective element.

The pressure (P) scale height is the distance in which pressure changes by e over some distance r and is defined as $\frac{1}{H_p} = -\frac{1}{P}\frac{dP}{dr}$. We can rewrite this using the equation of hydrostatic equilibrium

$$H_p = \frac{P}{\rho g} \tag{1.15}$$

with ρ the density and g the gravity of the star. Because convection depends on similar pressure between an element and its surroundings, the pressure scale height is considered a limit on the mixing length.

1.4.3 Convection in RSGs

Investigation into convection in RSGs began in the 1970s when Stothers & Leung (1971) and Schwarzschild (1975) both undertook to estimate the scale and nature of convection in these stars as a way of better understanding the origin of their mass-loss and photometric variability. RSGs are variable stars which exhibit semi-regular and/or irregular variations

(Gaposchkin & Shapley 1938; Kholopov et al. 1985). Both the irregular, abbreviated Lc, and semi-regular stars, abbreviated SRc, have amplitudes of 1 mag in the visual. SRc stars have periods of 30-1000s of days, with the larger periods sometimes called long secondary periods (Kiss et al. 2006). Stothers & Leung (1971) primarily investigated the possibly of the primary periodicity of RSGs being caused by pulsation. However, the researchers also used a modification of mixing length theory to test whether the long secondary periods of RSGs could be explained by giant convection cells of size comparable to the convection zone. They found that a turnover time predicted by mixing length for cells spanning the extent of the stellar envelope closely matched the secondary periods.

Schwarzschild (1975) also investigated the role of convection cells in generating some of the variability of RSGs. However, in the paper, Schwarzschild considered the motion of material smaller than the full extent of a convection cell but physically more akin to what are called supergranules in solar physics. Extrapolating from observations of the Sun, he set the ratio of the horizontal extent of a granule over the depth of a granule to be 1 to 3. Applying this to models of RSGs, he found that an RSG would have 90 or so granules on its surface. Then, he used the size of these convective elements and the sound velocity to determine that these granules have a turnover time on the order of 100s of days. Comparing the estimated brightness of the features and this turnover time he found that it roughly matched the short-term irregular variations found in the stars. As a final test, he proposed using linear polarization from scattered light, suggesting that visual polarization is evidence of non-spherical activity.

1.4.4 Photometric indicators of convection in RSGs

As mentioned in the previous section, the irregular variability of RSGs was the first indication that something unusual might be present on the surface of these stars. One of the most thorough investigations into a possible link between variability and surface activity was made by Kiss et al. (2006). In this paper, the authors studied light curves of 50 RSGs from the American Association of Variable Star Observers (AAVSO). To determine periods, the authors calculated Fourier power spectra from the light curves and used iterative sine fitting to find frequencies of power excess in the spectra, removing the peak identified from subsequent iterations until peaks were less than three times the noise of the Fourier spectra.

The result of this work was the identification of periods for 37 stars, and in some cases, the identification of multiple periods, both long (1500-2000s of days) and short (100s of days). The short periods were identified with pulsation processes, possibly driven by convection, and the authors noted similarities in the longer periods to long secondary periods found in AGBs. Kiss et al. (2006) also conducted Lorentzian fits of the power spectra to study the stochastic processes suggested by their data. These fits showed similarities to solar oscillations tied to convection. In addition, investigation into the shape of the noise in the calculated power spectra, in particular the $1/f^{\alpha}$ noise, showed similarities to granulation related variability in the Sun in almost every RSG in the sample. The authors concluded, like Schwarzschild (1975), that the irregular variations had convective origins.

This study was followed by other analyses of photometric variability in RSGs. Percy & Sato (2009) used the dataset of Kiss et al. (2006), applying self-correlation analysis as an

alternative approach. In their investigation, the authors found additional stars with long secondary periods, and noted that the length of the longer periods appeared to be related to the short periods (being 5-10 times the length). From this, the authors suggested that just as with the short periods, which are tied to radial pulsations, the long periods may also be related to the size of the star.

Percy & Khatu (2014) used Fourier and wavelet analysis of AAVSO light curves of 44 RSGs to further investigate variations in the amplitudes within these light curves, the idea being that such variations might hint at long term processes driving the light curve. They found that the period of amplitude variation was similar for long and short period variations and that these variations were often quite small. They suggested that amplitude variations may result from rotation of a surface with large, long lived convection features.

Stothers (2010) returned to the connection between the long secondary periods and giant convection cells. By using an improved value of the mixing length parameter α (1.3-1.5 rather than 0.5), Stothers showed that mixing length predicted observed radial velocity amplitudes and that turnover times closely matched those of the long secondary periods of RSGs. Stothers suggested that the variations of the long secondary periods result from the dominance of brighter, hotter, upward swelling material during the first half of a period and then cooling and falling material during the second. Because radial velocity amplitudes of the short periods of RSGs are similar to those of the long secondary periods, Stothers also noted that this was evidence in support of a link between the irregularity of those periods and the motion of supergranules as described in Schwarzschild (1975).

1.4.5 Spectroscopic indicators of convection in RSGs

In addition to photometric variability, RSGs show variability in their spectral lines. Understanding the role of convection within these lines has been a rather winding path. Gray (2000) looked at high resolution spectra of Betelgeuse from 5380-6320 Å. He noted that spectral lines varied in depth by $\sim 20\%$, in a quasi-periodic fashion over timescales on the order of 100 days. In this variation, lines were less deep during periods when the star was photometrically fainter, and there was a slightly delayed drop in temperature (as measured by line ratios) corresponding to the decrease in line depth. All of these effects were explained by variability in opacity in the star. Under this explanation, the bright spot observed in Betelgeuse was not a convection cell, but rather a region unimpacted by the change in opacity. Nonetheless, in the same study, Gray noted that small structural changes in line cores could be explained by motion of hot gas within a convection cell.

Gray (2008a) argued against spectroscopic evidence for large convection cells because of the long term stability of line broadening and stability in shape of line profiles. If large convection cells were present on the surface of Betelgeuse, its spectra should show significant temporal variations in shape due to the influence of such large cells. Instead, Gray proposed that the Doppler shift that was observed was indicative of many hundreds of cells, rather than the few which previous studies suggested.

However, the use of spectra shifted to an absolute wavelength scale set by telluric lines marked a major change in the arguments of Gray (Gray 2008b). Plots of spectral line bisectors, which can be used to measure the motion of material, showed shape changes at a

scale larger than pulsation would produce, offering some evidence that large mass motions were taking place in Betelgeuse. Most notably, when temperature sensitive line ratios were plotted as a function of core velocity, measured using the absolute wavelength scale, the result was a hysteresis curve suggestive of material heating up, rising, and then cooling and falling back down: exactly what would be expected from convection! These motions were found to take place on a roughly 400 day period and suggested motion over roughly $0.05R_*$. Reflecting on previous studies, the authors suggested that the 400 day motions observed in this study were indicative of very large convection cells, and that previously observed line broadening was the result of a combination of effects from supergranulation and granulation, although in this case the timescale of motion would describe the amount of time between the appearance of giant cells, rather than a turnover time. Noting that line bisectors in Betelgeuse often showed a reverse C-shape, similar to hot stars, the authors suggested that the small scale behavior may be more like that of hotter stars (small motions dominating the granulation signature). A similar investigation using observations of Antares A by Pugh & Gray (2013) tied a 100 day radial velocity variation in the star to resonant oscillations caused by large convective motions. Analyzing changes in line-depth ratio, the authors found smaller motions than in Betelgeuse (and in some years, an incomplete cycle of rising and following) and noted that because both stars have similar mass-loss rates, that convection alone was likely not the cause of mass-loss in RSGs.

Gray & Pugh (2012) investigated granulation, the smallest scale of convection, in a variety of stars, including a RSG, α Sco. Using the so-called "third-signature of granulation",

differential shifts of spectral lines (the first being macroturbulence and second line bisectors), the authors found for α Sco that weaker lines, formed deeper in the atmosphere, showed more motion than stronger lines from further out in the photosphere. The authors suggested that this could be explained by large convection cells which penetrate only the lower layers of the photosphere. Moreover, investigations into the movement of material found weaker motions than in Betelgeuse or Antares, suggesting a possible connection to luminosity (or some factor that is related to luminosity).

A new method using tomography with high resolution spectroscopy promises to offer even an deeper understanding of convection in these stars. In this method, the line of sight velocity as a function of optical depth is recovered from cross-correlation with a mask produced from 1D synthetic spectra and line depths calculated using the contribution function as determined by the 3D radiative transport code (see below) OPTIM3D (Kravchenko et al. 2018). Preliminary results using this method were presented by Kravchenko (2018). When applied to 7 years of high resolution ($R \sim 86000$) spectra of the RSG μ Cep, hysteresis loops similar to those found by Gray (2008b) resulted. Calculated radial velocities were also compared to a visual light curve, showing a strikingly similar variation, but lagged by 100 days. When applied to snapshots of 3D radiative hydrodynamics (RHD) models of a RSG, a very similar loop to that of μ Cep was found, providing further evidence of convection's impact on photometric variations. Kravchenko is currently running a project to use the technique on a range of RSGs, including some stars presented in this document, but at the moment of writing, no new results have been published.

1.4.6 3D modeling of convection

A significant boost in the understanding of convection in RSGs came from the development of 3D radiative hydrodynamics (RHD) models, particularly the COnservative COde for the COmputation of COmpressible COnvection in a BOx of L Dimensions, L=3,3, or CO^{5}BOLD (Freytag et al. 2012). In this code, the equations of radiative hydrodynamics (RHD) are calculated in a cube with an equidistant grid and open boundary conditions on each of the faces, with radiative transport taking place under local thermal equilibrium (LTE) and a fixed external gravitational field. For RSGs, a setup called *star in a box* is used which permits calculation of the entire convective envelope because the low gravities of these stars means that spherical factors play an important role in the final outcome of the calculations. In this case, the entire star is within the grid and a fixed gravitational potential is used to replicate the gravitational field of the star. An additional contribution to the field was the development of the 3D LTE radiative transfer code OPTIM3D (Chiavassa et al. 2009), which uses snapshots of 3D RHD models in the calculation of synthetic spectra and intensity maps, using extinction coefficients from the MARCS stellar atmosphere code.

Freytag et al. (2002) modeled a star with parameters similar to Betelgeuse using CO^{5}BOLD. These models predicted a surface influenced by the presence of 5-7 giant convection cells and their interaction with pulsation. In some cases, the giant cells were darker than the rest of the star and surrounded by brighter lanes and occasionally neighbored by bright features. The authors note that this matched observations which suggested that hot spots are most often imaged during times of decreased brightness. These models also showed large atmo-

spheric velocities, on the order of 20 km s^{-1}, and shock waves originating in convection cells. Modeling of granulation patterns in the Sun calculated using *box in a star* setups suggested that the key factor determining the size of surface granulation was the surface pressure scale height via the relation $x_{\rm gran} \sim 10 \times H_{po}$ (Freytag et al. 1997) in units of stellar radii, which for Betelgeuse suggested granules of 0.1 R_* and thus 100s of surface granules.

In these simulations, convective flows generate acoustic waves that are compressed in the atmosphere of RSGs, generating shocks, but models also show that convective velocities do not exceed escape velocity and thus are not involved in mass-loss. These models also show that the appearance and turn-over time of surface features is strongly wavelength dependent, suggesting that different scales of convection are visible at different levels of the stellar atmosphere. For example, at optical wavelengths, where TiO plays a significant role in appearance, bright regions have an intensity 50 times greater than dark regions. In the near-infrared, this difference is 10 times. Chiavassa et al. (2009) showed that 3D RHD models of RSGs in the H-band suggest surfaces with large convection cells that last years. In addition, models presented in Chiavassa et al. (2010a) displayed smaller surface features that last weeks to months.

In Chiavassa et al. (2009, 2010a) intensity maps based on 3D RHD models of RSGs showed giant convection cells of scale ~ 0.5 R_* that changed on a time-scale of years and smaller granules of scale $\sim 0.05-0.1$ R_* which persisted on a scale of months to one year. To better predict the giant convection cell size, the authors proposed using a modified pressure scale height calculation: $H_p = \frac{kT_{eff}}{g\mu m_H}(1 + \beta\gamma(\frac{v_{turb}}{c_s})^2)$ with γ the adiabatic exponent, c_s the

sound speed, and β a factor close to 1 that is related to the ratio of turbulent pressure and the gas density times turbulent velocity. For the parameters of a typical RSG, they suggested that this equation produced values roughly five times greater than the relation from Freytag et al. (1997), $x_{\rm gran} \sim 10 \times H_{po}$, and predicted granule sizes of $0.5R_*$. We note that there seems to be some conflation of terminology in this paper, as the "granules" being calculated in this paper are the long lived features rather than smaller granules. These are probably more akin to the "supergranules" described by other authors, being intermediate between the small granules also observed in the models and the giant convection cells.

Chiavassa et al. (2009, 2010a) showed that in synthetic visibilities and closure phases calculated from 3D model snapshots, convection cells and granulation caused significant departure from uniform and limb darkened disk visibility curves, especially in the second lobe and onward, with visibilities of higher intensity at higher frequency than predicted by disk models (suggesting that it should be easier to measure these visibilities in stars with strong surface features). They noted deviations in squared visibilities from measured uniform disks could amount to 5%, and thus should be included as source of uncertainty in measurements of the diameters of these stars. Closure phases showed, as expected, departure from the 0, $\pm 180^\circ$ phases of symmetric objects.

Chiavassa et al. (2009, 2010a,b) compared various interferometric observations of red supergiant stars with RHD models to show the connection between surface activity and the observations. Starting with a grid of snapshots of a 3D RHD model at various position angles, the authors then computed the synthetic complex visibility of the image using a

Fourier transform. Next, the closest fitting snapshot was determined by a χ^2 comparison of the synthetic visibilities and closure phases to the actual data. Then, the authors filtered the visibilities of the best fitting snapshot at different frequencies and performed an inverse Fourier transform on the filtered data. This resulted in intensity maps of the star at scales corresponding to the spatial frequencies, which can be computed in terms of solar radius using the equation:

$$\nu\left[\frac{1}{''}\right] = \nu\left[\frac{1}{R_\odot}\right] * d_{pc} * 214.9. \tag{1.16}$$

Doing this, the authors were able to confirm that signals observed in interferometric activity arise from surface activity. Note, however, that bright spots were imaged by Chiavassa et al. (2010b) using interferometric observations of continuum regions of the H-band and also using K-band observations which included extended molecular layers. They note that it is unclear where the spots emerge.

1.4.7 Imaging of Red Supergiants

Just as it was the first to be measured, Betelgeuse was also the first star other than the Sun to be imaged. Following the invention of speckle interferometry by Labeyrie (1970), Lynds et al. (1976) imaged Betelgeuse using the technique. In this and subsequent images produced by McDonnell & Bates (1976) using these same data, it appeared that Betelgeuse had an irregular surface. Application of this imaging technique in 1970s provided more evidence that the star did not have a uniform disk (Worden et al. 1976; Wilkerson & Worden 1977;

Welter & Worden 1980). Continuing into the 1980s, speckle observations of Betelgeuse in the 1980s provided such evidence (Goldberg et al. 1982; Cheng et al. 1986). In the middle of that decade, multi-year speckle observations of the star at 6563 nm showed a persistent large asymmetric feature and small scale features changing on the time-scale of months (Hebden et al. 1986).

A notable development was the application of non-redundant aperture masking to imaging. Using the WHT in the visible (633 nm, 700 nm, and 710 nm), Buscher et al. (1990) observed Betelgeuse with the technique. These data showed strong evidence of asymmetry in the closure phases and visibilities. These observables were fitted to a model of a uniform disk plus a spot that contributed 10% of the flux. In addition, the authors used a maximum entropy (MEM) algorithm to reconstruct images, which showed a large hotspot that was close to the surface, as evidenced by the fact that the spot and photosphere both displayed similar levels of obscuration at wavelengths blanked by TiO.

Betelgeuse was observed once more by WHT, at 546, 633, 700, and 710 nm a couple of years later (Wilson et al. 1992). In these data, the best fit was a model of a uniform disk plus two spots, each contributing 10% of the flux. In reconstructions using MEM, two hotspots were visible, a clear change from the previous image made by Buscher et al. (1990). Using the same technique, Tuthill et al. (1997) produced images of two RSGs, in addition to Betelgeuse, α Sco and α Her. All images showed evidence of surface features, with images of α Sco and Betelgeuse both showing changes on a time-scale under one year but greater than a few months. Continued observations of Betelgeuse by Wilson et al. (1997) showed features

changing over a time-scale of 8 weeks. However, that same year, the Cambridge Optical Aperture Synthesis Telescope (COAST) produced an image of a star using multi-telescope interferometry—once more of Betelgeuse. This image, at 830 nm, showed no evidence for asymmetry (Burns et al. 1997).

Imaging in the 1990s was not limited to interferometric methods. In 1996, the Hubble Space Telescope imaged Betelgeuse in the UV at 255 and 280 nm (Gilliland & Dupree 1996), showing a large bright feature at both wavelengths. This was hailed as the first direct image of any star other than the Sun.

New questions about the nature of RSG surfaces resulted from a multi-facility project by Young et al. (2000) using COAST and WHT images of Betelgeuse at 700, 905, and 1290 nm. These images showed three bright spots at 700 nm, one less bright spot at 905 nm, and no features at 1290nm. The interpretation of these authors was that the features which had previously been observed in the aforementioned works were regions of lower opacity resulting from convective features on the surface and that convective features allowed a glance at the surface in regions with high opacity from TiO lines. The reason for a featureless appearance at 1290 nm then, is that this wavelength does not have such line blanketing and indeed it seemed as if perhaps surface features could not be imaged, either due to size or more likely due to contrast issues at the relevant wavelengths.

The next major image of a RSG was, once more, of Betelgeuse, this time at 1.6 μm with the 3-telescope combiner IONIC on the IOTA interferometer by Haubois et al. (2009). These images showed two bright features. These authors also noted that higher lobes of the

visibility curve suggested evidence of features smaller than the 11 mas resolution of their data. Because this wavelength range probes a region with low continuum opacity, these features were interpreted as existing on the surface and a tie to convection was suggested.

The development of 4 and 6 telescope interferometers and beam combiners ushered in a new era of high resolution imaging for RSGs. Notably, two RSGs, RS Per and T Per, were observed by Baron et al. (2014) using the Michigan InfraRed Combiner (MIRC) combiner on the CHARA Array. In images reconstructed from these data, T Per showed evidence of a bright spot, but RS Per showed only a large bright region surrounded by some dark regions. Nonetheless, these data provided further evidence that previous images of a spotty Betelgeuse were not signals unique to that star but of behavior common to RSGs.

Ohnaka et al. (2017) used AMBER at the VLTI to study Antares at a spectral resolution of 12,000 for the CO lines between 2.28 μm and 2.31 μm. This resulted in eight images reconstructed at different wavelengths. These images showed a large, low contrast spot at continuum wavelengths, and two large, high intensity contrast (20%) spots and an irregular extended atmosphere at the CO lines and bandhead. Referencing previous images, the authors note that visual images with spots were produced at wavelengths with significant TiO bands, and H-band images cover a spectral region with CO and CN lines. Thus, they suggest that the continuum of RSGs appears smooth but that spots in images result from regions of lower molecular densities.

Montargès et al. (2018) studied the RSG CE Tau, resulting in two images roughly one month apart. These images showed some slight variation between observations, with a

prominent bright spot changing size and location, the emergence of a new feature on the limb in the later observation, and shifts in the contrast of other regions of the star. Thus, it does seem that interferometric imaging can offer insight into short-term changes in these stars. Comparison to 3D RHD models showed significantly less contrast in the reconstructed images, probably in part because no model matching the stellar parameters of the star was available and the closest model was of a more evolved star.

In addition to interferometric imaging, a new technique using spectropolarimetry was recently used to image convection cells on Betelgeuse (López Ariste et al. 2018). In RSGs, the continuum is polarized by Rayleigh scattering. This linearly polarized light is depolarized during the formation of absorption lines further up in the atmosphere. The idea behind this method is that the linear polarization offers insight into the location of bright features through analysis of the ratio of Stokes Q to Stokes U, which provides the polar angle, and that measurement of Doppler shifts in polarized lines, corrected for the velocity of the star, provides a distance to the disk center. That these bright features might be related to convection is suggested by the fact that these lines are mostly blue-shifted, whereas circularly polarized lines, due to the Zeeman effect, are red-shifted. In this model, as rising material moves from the center of a granule outward, it drags magnetic fields into intergranular lanes where gas is sinking. By modeling the surface of Betelgeuse using spherical harmonics and performing inverse imaging, the authors were able to image the surface of the star over 4.5 years in increments on the scale of months. Because of the limited number of spherical harmonic coefficients used, the authors were only able to image features on a scale of 0.6 R_*,

the largest of which they found persisted for four years, suggesting that such is the scale of large convection cells in these stars. Despite such long lasting features, images between short time periods showed notable change, suggesting that smaller features were changing as well. As confirmation of the relation between the surface and these reconstructions, the authors were able to use spectropolarimetric observations of CE Tau that were coincidentally contemporaneous to those of Montargès et al. (2018). The image produced using this method was strikingly similar to the one produced using interferometry. We are currently involved in an observing campaign to conduct multi-epoch near simultaneous interferometry and spectropolarimetry of AZ Cyg and SU Per, two RSGs, in order to further test this imaging method.

When images have sufficient resolution, analysis of granule size and contrast can be done without the need for model fitting. In Paladini et al. (2018), a detailed image of an AGB star was used to study granulation in such stars. The authors calculated 2D power spectra of their images with the limb-darkened disks filtered out. After correction for limb darkening they also estimated an intensity contrast via $\frac{\Delta I_{rms}}{\langle I \rangle}$. To get granule size, they determined the wavenumbers of the peaks of the power spectra. These results can be compared to a 3D RHD snapshot convolved to the same resolution and also to theoretical predictions. They found granule sizes that matched predictions based on 3D model atmospheres, despite the fact that these atmospheres were not designed specifically for AGBs.

1.5 Summary of This Work

In this work, we study a set of RSGs using optical interferometry. We use the Michigan InfraRed Combiner (MIRC) on the CHARA Array to image the surfaces of two red supergiants, AZ Cyg and SU Per, over long (3-5 years) time periods, in order to understand how changes on the surface relate to convection and predictions by models. In Chapter 2, we describe the data used in this analysis. We describe how we obtained the interferometric data, including the manner of calibration, and how we obtained the spectra we also used for stellar parameters. In Chapter 3, we present the fundamental stellar parameters of the stars we observed. In Chapter 4, we describe our method of finding the best reconstruction parameters for each observation and of verifying the images we produce. In that same chapter, we also present our images and discuss what information about red supergiants these images provide. In Chapter 5, we conclude with a review of our results, and look to the future, describing the promise of new interferometers and the possibility of an unprecedented view of the lives of these stars.

CHAPTER 2

Observations

The goal of this dissertation is to study convection in RSGs using surface imaging from optical interferometry. To do this, we must consider the limits of our interferometer as well as the need for high resolution images from which to infer the properties of convection. Moreover, although the images provide a visual depiction of the surface, interpreting these results requires knowledge of the fundamental stellar proprieties of these objects. Such information is not available from interferometry alone, and additional observational techniques are required. In this chapter we describe the process of target selection as well as the processes for obtaining and processing the interferometric and spectroscopic data used in this dissertation.

2.1 Target selection

As the goal of this project was to study convection on the surfaces of RSGs via interferometric imaging, target selection began with several key limitations. First, a star needed to meet the observational limits of the CHARA Array and the instrument we used, the Michigan InfraRed Combiner (MIRC), with adequate apparent magnitude (V$\leq$ 10.0 and H$\leq$6.9) and declination roughly $\geq -10°$. Next, we needed to know or at least suspect that the star was large enough in angular diameter for imaging surface features. Finally, we needed reason to suspect that strong surface convection was taking place on this star.

We started with searches for RSGs that would be observable by CHARA. For this we used papers such as Levesque et al. (2005) and the search tool provided by the Simbad

service[1] (Wenger et al. 2000) into which we input the magnitude and declination limits of CHARA and searched for objects described as RSGs in the Simbad database. The next step was to determine which stars would work well for an imaging project with the CHARA Array. CHARA's angular resolution limit is 0.5 mas in the H-band. Simulations suggest that the smaller granulation-like surface features on RSGs are on the order of 25% the diameter of the star. Thus, a hard limit for the minimum angular diameter of a target for imaging was 2 mas, even accounting for the super-resolution which image reconstruction permits. Another limitation in angular diameter imposed by the CHARA Array came from the shortest baselines. In order to do imaging, we need access to the high visibility portions of the first lobe of the visibility curve, and so some stars, such as Betelgeuse, were too large for our purposes. Using the ASPRO tool[2] (Duchene et al. 2004) provided by the Jean-Marie Mariotti Center, we determined that the limit for this maximum angular diameter was about 8 mas.

Prior to our work, there did exist some measurements of RSGs diameters, for example Dyck et al. (1996a) and van Belle et al. (2009). For stars in our list that did not have measured angular diameters, we used stellar parameters to estimate a size. To this end, we used the Stefan-Boltzman equation $L = 4\pi\sigma R^2 T_{\rm eff}^4$ and published values for temperature and luminosity. From this radius, we calculated the angular diameter $\theta \approx 206265\ d\ D^{-1}$ (in arcsec), where d is the stellar diameter and D is the distance to the star, using parallaxes found via the Vizier service[3] (Ochsenbein et al. 2000) and/or literature searches, when available,

[1] http://simbad.u-strasbg.fr/simbad/
[2] http://www.jmmc.fr/aspro
[3] http://vizier.u-strasbg.fr/viz-bin/VizieR

or distance moduli from the literature.

The next step was to select from this list of RSGs those stars with evidence of surface activity. For this, we used existing research on variability in RSGs, primarily that by Kiss et al. (2006). In this paper, the authors used AAVSO observations to study long term photometric variability in RSGs. The authors noted that there is a stochastic element to the variability in RSGs, similar to that observed for solar granulation. In addition to the list of RSGs from this paper, we looked at papers studying mass-loss in RSGs, because we were interested in seeing whether these stars showed evidence of increased surface activity as well. We present the list which resulted from these selection criteria in Table 2.1. Because of limitations in observing time, we narrowed this list further by selecting those targets visible during what we considered to be the optimum time for imaging at CHARA—late summer through early fall.

In addition to these methods for selecting targets, we were able to use past experience to find targets. Several RSGs had already been observed with CHARA, including T Per and RS Per by Baron et al. (2014). In addition, several years of observations of the RSG AZ Cyg had already been collected, thanks to evidence of surface activity discussed in Kiss et al. (2010). Thus, AZ Cyg was immediately put on our list, as we measured an angular diameter of slightly less than 4 mas using these past observations and noticed strong evidence of asymmetry in the closure phases. T Per and RS Per, being smaller, were included on the list but at lower priority.

During our first observing run, we used the first several nights to collect observations

of as many of the objects on our target list as possible. Each afternoon, we did fast data reductions to get estimates of the angular diameters and asymmetry of the stars we observed the previous night in order to decide which targets were worth re-observing. We also found that our estimates of maximum useful size were overestimated. We found that for targets greater than 5 mas, it was difficult to detect low visibility fringes from long baselines. Thus our list of ideal imaging targets was further shortened. In the end, we determined two targets to be worth our full efforts for long and short term imaging based on their size, clear evidence of surface activity, and ease of observing: AZ Cyg and SU Per. In addition, we collected multiple observations of several other targets, based on their right ascensions, which fell between those of the top priority targets (thus enabling continual data collection each night), evidence of interesting features, and ease of observing. A full list of targets and observing information is at the end of this chapter in Tables 2.3-2.5.

Table 2.1: Starting Target List.

Name	Spectral Type	RA (H,M,S)	Dec (°,',")	V (mag)	H (mag)	Distance (pc)	θ (mas)	T_{eff} (K)
V366 And	M2Ib	01 43 11.11	+48 31 00.37	6.76	1.86	3571[2]	2.81[2]	3530[2]
V589 Cas	M4 Iab	01 46 05.48	+60 59 36.60	8.59	3.01	1995[1]	2.84±0.57[1]	3525[1]
V774 Cas	M2 Iab	01 47 00.01	+60 22 20.37	8.59	3.28	2187[1]	2.21±0.44[1]	3625[1]
V778 Cas	M2 Iab	01 58 28.91	+59 16 08.77	8.38	2.97	1905[1]	2.04±0.40[1]	3650[1]
XX Per	M4Ib+	02 03 09.36	+55 13 56.62	8.20	2.15	877[2]	2.95[2]	3339[2]
KK Per	M2 Iab-b	02 10 15.79	+56 33 32.67	7.74	2.14	1690[3]	2.57±0.06[3,4]	4030±25[4]
BU Per	M4 Ib	02 18 53.30	+67 25 16.81	10.40	2.68	$2344^{+88:\ 5}_{-85}$	2.50±0.5[1];	4090±35[4]
T Per	M2Iab	02 19 21.88	+58 57 40.35	8.45	3.02	2345±55[7]	2.01±0.03[8]	3750±60[8]
AD Per	M2.5 Iab	02 20 29.00	+56 59 35.23	7.88	2.45	$2344^{+88:\ 5}_{-85}$	2.5±0.06[1,3,4]	3900±25[4]
FZ Per	M1Iab	02 20 59.65	+57 09 29.97	8.00	2.68	$2344^{+88:\ 5}_{-85}$	1.31[5,9]	3920[9]
PR Per	M1-Iab-Ib	02 21 42.41	+57 51 46.15	8.00	2.68	980[2]	1.61±0.04[2,4]	4010±25[4]
SU Per	M3 Iab	02 22 06.89	+56 36 14.87	9.40	1.93	$2317^{+88:\ 5}_{-85}$	2.80[3,4,5] ± 0.07	3820±25[4]
RS Per	M4 Iab	02 22 24.30	+57 06 34.36	7.82	2.12	2345±55[7]	3.05±0.05[8]	3470±90[8]
S Per	M4.5-7Iae	02 22 51.71	+58 35 11.45	7.90	1.85	1897[3]	6.13±1.23[1,3]	3500[1]
W Per	M4.5 Iab	02 50 37.89	+56 59 00.27	9.62	1.99	1904[3]	3.07±0.62[1,3]	3550[1]
HD 17958	K2 Iab	02 56 24.65	+64 19 56.79	6.22	1.78	699[2]	4.87±0.97[1,2]	4200[1]
V648 Cas	M2 Iab	02 51 03.95	+57 51 19.94	9.38	2.47	971[2]	6.91±1.38[1,2]	3650[1]
HD 33299	K1 Ib	05 10 34.87	+30 47 51.14	6.69	3.45	1449[2]	1.24[1,2] ± 0.25	4300[1]
V362 Aur	M1.5Ia0-Ia	05 27 10.22	+29 55 15.79	7.32	1.94	614[2]	7.70±1.54[1,2]	3700[1]
NO Aur	M2 Iab	05 40 42.05	+31 55 14.19	6.21	1.20	595[2]	10.17±2.93[1,2]	3700[1]
TV gem	M1 Iab	06 11 51.41	+21 52 05.65	6.56	1.19	952[2]	7.65±1.53[1,2]	3700[1]
WY Gem	M2 Iepab	06 11 56.25	+23 12 25.41	7.38	2.11	8333[2]	2.54[2]	3518[2]
6 Gem	M0 Iab	06 12 19.10	+22 54 30.64	6.39	1.26	1380[1]	4.59±0.92[1]	3800[1]
HD 44537	K5 Iab	06 24 53.90	+49 17 16.42	4.75	0.70	1220[2]	4.39[1,2]	3750[1]
HD 181475	M1 II	19 20 48.31	-04 30 09.01	6.96	2.12	676[2]	2.37[1,2]	3700[1]
NR Vul	M1Ia	19 50 11.93	+2455 24.18	9.36	2.14	2291[1]	4.04±0.81[1]	4000[1]
IRC+40406	M3Iab	20 21 14.07	+35 37 16.56	9.72	2.11	1585[1]	6.20±1.24[1]	3600
BI Cyg	M4 Iab	20 21 21.88	+36 55 55.77	8.40	1.15	1585[1]	7.40±1.48[1]	3575[1]
RW Cyg	M3-M4Ia-Iab	20 28 50.59	+39 58 54.42	8.00	2.06	1099[2]	8.43±1.67[1,2]	3600[1]
AZ Cyg	M2-M4Iab	20 57 59.44	+46 28 00.57	8.85	1.66	$90^{+295:\ 10}_{-39}$	3.82±0.01[11]	3450[12]
Ksi Cyg	K4.5Ib-II	21 04 55.86	+43 55 40.26	3.73	0.13	258[2]	5.89[1,2]	3800[1]
HR 8248	K1Ibv	21 33 17.88	+45 51 14.45	6.25	2.49	408[2]	4.63±0.93[1,2]	4000[1]
VV Cep	M2epIa+B8	21 56 39.14	+63 37 32.02	4.90	0.17	752[2]	5.80[2]	3570[2]
ζ Cep	K1.5Iab	22 10 51.28	+58 12 04.55	3.35	0.36	256[2]	5.24[1,2]	4000[1]
ST Cep	M3 Iab	22 30 10.73	+57 00 03.06	9.70	2.18	794[1]	3.45±0.69[1]	3600[1]
V424 Lac	M0 Iab	22 56 26.00	+49 44 00.75	4.94	1.20	490[2]	5.02±1.00[1,2]	3800[1]
V809 Cas	M1 Iab	23 19 23.77	+62 44 23.19	6.735	1.193	602[2]	6.44±1.29[1,2]	3750[1]
PZ Cas	M3Iab	23 44 03.28	+61 47 22.18	8.90	1.53	2399[1]	7.65±1.53[1]	3600[1]
TZ Cas	M3 Iab	23 52 56.24	+61 00 08.38	9.18	2.33	2564[2]	2.95±0.59[1,2]	3600[1]

Preliminary target list of RSGs capable of being observed by CHARA based on the cutoffs described in the manuscript. Spectral types, coordinates, and magnitudes are from Simbad. Other parameters are from the cited papers or calculated using parameters found in those papers. Errors are calculated when uncertainty in parameters was available in the literature. 1)Levesque et al. (2005), 2) McDonald et al. (2012), 3)Mauron & Josselin (2011), 4)Gazak et al. (2014), 5)Currie et al. (2010), 6)Pickles & Depagne (2010), 7)Slesnick et al. (2002), 8)Baron et al. (2014), 9)Josselin & Plez (2007), 10)ESA (1997), 11) Measurement using 2011 data, 12)Lancon & Rocca-Volmerange (1992)

2.2 Spectroscopy

In addition to the interferometric data, we obtained spectra close in time to our 2016 and 2017 observations using the SpeX spectrograph on the NASA Infrared Telescope Facility (IRTF) 3 meter telescope atop Mauna Kea (Rayner et al. 2003). SpeX is a cross-dispersed spectrograph that can observe at wavelengths 0.7-2.5 μm in short cross dispersed mode (SXD Mode) and longer wavelengths (2.5-5.3 μm) in two long dispersed modes (LXD short and LXD long) (Rayner et al. 2003), all of which are matched a 0.3x15" slit. Although SpeX had first light in 2000, it was upgraded in 2014, with improved control electronics as well as a new InSb array and an expanded wavelength coverage. The instrument also offers several other observing modes, including a low resolution prism mode optimized for occultations and faint objects and single order modes for extended objects.

In both 2016 and 2017, we used the SXD mode which provides spectra at R$\sim$ 2000. For one of the nights in 2017, we attempted to use ISHELL, a R$\sim$ 75000 spectrograph, to collect H-band spectra, but unfortunately, the instrument failed the night before our observing time. Instead, having already set a more limited target list for that night, we decided to observe using both SXD and the LXD short mode, which operates at R$\sim$ 2500. Using LXD short in addition to SXD extended the wavelength coverage of our observations beyond the limits of the SXD mode to 4.2 μm. SXD observations cover 8 overlapping orders, numbered 3-10, with order 1 being centered at 6.6 μm and LXD short covers another 8 orders, 5-12.

2.2.1 Observations, Calibration, and Data Reduction

Most of the targets we selected for observing with SpeX were stars we had already observed, or planned to observe with MIRC. Prior to observing, we determined that we needed a signal-to-noise ratio (S/N) of 100 or greater on our spectra. We also wanted at least 3 AB cycles (see below) per target to account for cosmic rays and improve S/N. Using the integration time calculation tool provided by SpeX we determined that for stars as bright as ours, this required an integration time of no more than 25 to 120 sec. Even accounting for longer integration times on telluric standards, this meant that we had available time for targets beyond that of our CHARA target list. After considering the limits imposed by the instrument, we selected targets based on their location in the sky, desiring targets that allowed for optimal use of observing time, most especially those that fell in right ascensions between the groups of RSGs in Cygnus and Perseus that were our primary targets. We also tried to focus on observing RSGs that were not already part of the SpeX library (Rayner et al. 2009).

Observations using SpeX use an "A-B method" for the purpose of calibration. First, in an "A" exposure set, the target is observed. Next there is an off target "B" exposure of the same integration time as used in "A" in order to account for contributions from dark current, the telescope, and the sky, excepting some residual from variance background emission in the time period between each exposure. To save time, in the case of observations of point sources, which our targets were at the resolution of the telescope, this is achieved by the so called "AB mode" in which, rather than nodding the telescope to nearby starless region of

the sky, the telescope moves only slightly so that the target is on a different section of the slit.

Flux calibration and correction for telluric lines was achieved by collecting observations of standard stars which were then used to calculate a telluric spectrum by adjusting a convolved model spectrum of Vega to match the H I lines of the standard star spectrum, as detailed in Vacca et al. (2003). The standard stars were A 0V or G 2V stars that lacked unusual features due to nebulosity, companions, emission lines, or variability. The telluric standards used for the observations reported here were selected using a tool provided by SpeX which searches a list of standards for those close in air mass to the target star. To minimize systematic errors around sharp telluric lines, the telluric spectrum was shifted roughly 0.1-0.2 pixels. The corrected target spectrum was calculated by dividing the observed target spectrum by the model telluric spectrum. This step provided flux calibration to 10% accuracy (Rayner et al. 2009).

Finally, in addition to the aforementioned calibration measurements, following collection of standard star data, calibration frames were taken. These consisted of a flat field and Argon arc lamp exposure. The SpeX data were reduced using Spextool, an Interactive Data Language (IDL) package (Cushing et al. 2004). This step included merging the order separated spectra into a single spectrum. The offset between neighboring orders was usually 1-3% (Rayner et al. 2009) and this was corrected using a scaling factor determined by a high S/N region where the spectra of adjacent orders overlapped. During data reduction, we also removed regions of the spectrum with strong telluric absorption.

2.3 Interferometry with the CHARA Array

The Center for High Angular Resolution Astronomy (CHARA) Array is an optical interferometer comprised of six one-meter telescopes arranged in a Y configuration and is located on Mt. Wilson, CA—the very same Mt. Wilson that hosted the pioneering work of Michelson and Pease mentioned in the previous chapter. Baselines between each of the six telescopes range between 34 and 331 meters, allowing a maximum resolution in H-band of roughly 0.5 mas.

Light from each of the six telescopes is directed to the light combining facility through vacuum tubes. In order maintain coherence, correction to zero optical path length is required prior to combining. This happens first via placement of movable mirrors while still in vacuum in the "Pipes of Pan" (PoPs) with fixed delay, and then via the use of continuous delay lines in the Optical Path Length Equalizers (OPLEs), which are along 46 m cart lines exposed to air. Selecting the mirrors used for PoPs is a key step of observational preparation. Likewise, control of the OPLEs is an important part of conducting an observation.

After the beams are at zero optical path length difference, they go through a series of additional corrections, including separation of visible from infrared light, before being sent to one of the beam combining instruments. At the moment, CHARA has five beam combiners. CLASSIC was the first instrument for the facility, a two beam, single channel combiner operating in H or K-bands. CLIMB is the three beam version of CLASSIC. PAVO is a 2-3 beam combiner that uses an integral-field unit to measure spatially modulated fringes in the pupil plane with a spectral dispersion across 680-950 nm of R $\sim$ 30. The

Visible spEctroGraph and polArimeter (VEGA), operates at wavelengths of 480-850 nm at resolutions R $\sim 6,000$ to $30,000$ and combines up to 4 beams. It was constructed by the Observatoire de la Côte d'Azur.

MIRC, the instrument used to obtain the data described in this manuscript was a six beam image plane combiner operating in the H-band (1.5-1.8 μm) at low spectral resolution (R=35,150, or 450) (Monnier et al. 2004). As described by Monnier et al. (2006), after being directed to the MIRC optical bench by a beam splitter, infrared light from each of the six telescopes was injected into single-mode fibers using off-axis parabolas, with the fibers arranged in non-redundant spacing such that each fringe formed at a unique spatial frequency. After collimation by a microlens array, the resulting synthetic pupil was imaged with a focusing mirror and compressed into a line of pixels by a cylindrical lens and then directed through a slit into the spectrograph. Following this, for the R$\sim$35 mode used to obtain the data described in this manuscript, a non-deviating prism pair was used to disperse the light in eight spectral channels, after which the beam entered the MIRC camera, where it passed through a bandpass filter and was imaged by a 256x256 pixel detector. To help with calibration, photometric channels that measured the flux of each beam were added in 2010 (Che et al. 2010). Additional technical details on MIRC are available in Monnier et al. (2004, 2006, 2012) and Che et al. (2010).

MIRC is now MIRC-X, after being upgraded with a C-RED ONE camera with a low noise SAPHIRA detector, with additional improvements in process (Anugu et al. 2018). The additional 'X' in the name signifies the contributions of Prof. Stefan Kraus at the

University of Exeter, who provided the funding for the upgrade. Although we also have observations collected with MIRC-X, because the pipeline is still in development, we will not discuss those observations in this manuscript.

2.4 Observation, Data Reduction and Calibration

2.4.1 Observational method

For this project we used MIRC to collect interferometric data on nearly two dozen RSGs. Prior to an observing night, we selected the PoPs configuration that would maximize the temporal coverage of the target—that is the PoPs that let us observe and re-observe a target for as much of the night as possible. As mentioned in the previous section, forming fringes requires a delay correction accounted for by the PoPs and also by the OPLEs. The OPLEs are manually controlled and the process of moving the carts by small amounts is called searching for fringes. Usually we started each night by first searching for the OPLE cart offsets using a bright, unresolved star.

Once we had an idea where the cart offsets would be at an hour angle approximately similar to that of our target, we moved to a calibrator star. After locking the fringe tracker on fringes on all 15 baselines (or as many as were available given the number of telescopes available that night), we recorded data. For calibrators, we recorded for 100 data files which came out to roughly 10 minutes of observing time with MIRC under the default settings. For both calibrator and target stars we followed data collection with a shutter calibration sequence (not to be confused with calibration star observations) consisting of 10 background

data files in which no light was directed to the camera, 10 “shutter” files per telescope consisting of light from only one single telescopes at a time (for a total of 60 files), and 30 foreground files, consisting of light from all 6 telescopes but at large cart offsets so that no fringes were formed. Thus, the shutter calibration always consisted of 100 files, or roughly 10 minutes of sample collection time.

Following the calibrator star, we moved to a target. Because our targets were quite bright, searching for and locking on fringes required using flat fields to mitigate the effects of cross fringes from bright fringes. Unlike in spectroscopy, these flat fields were not data products that were part of calibration. For our targets we used 3-6 flat fields usually, recording them after moving carts to large offsets so as to not accidentally flat field on a fringe we wanted to detect. Following this, we searched for fringes. On a “good” night, the offsets from the calibrator would make it easy to find fringes on a target and begin recording. However, most nights were not good and thus, we had to come up with a strategy for finding fringes. This consisted of first getting the easy offsets—that is those for the high visibility, short baselines (S1S2, E1E2, W1W2 although W1W2 was in the first null for some targets and thus somewhat difficult to find at times). After noting the offsets at these fringes, we would then move carts again, moving carts for telescopes of each directional arm in opposite directions (e.g., S1 and S2 in different directions), excepting the cart for W2, which was the reference cart and never moved during data recording. The goal was to find fringes for another baseline, ideally that with the reference cart, W2, so that we could determine the proper position for all carts. On really “bad” nights, of which there were many, with poor

seeing (making strongly variable fringes) or thin clouds (making faint fringes) the strategy was to at least get some closed triangles so as to collect data containing closure phases. As we gained experience with observing, we also tended to use knowledge of the size of the target to estimate which fringes would be easiest to find, based on the predicted visibility at a certain frequency, and used those to predict the positions needed for the other carts. On targets we recorded for at least 100 files (10 minutes) followed by the 10 minute shutter sequence. On very good nights we would record for longer, up to 20 minutes. Sometimes, rather than recording longer, we would record two blocks of data and shutters. Regardless, observation of a target would either be followed by a calibrator, or observation of a different target, if the time spent on the first target had not been too long.

The first observational run, in 2015 August, was hampered by poor weather, which caused strongly variable fringes and necessitated closing early on some nights. The second run, in 2015 October, resulted in no useful data, so poor were conditions, often requiring early closure or not opening at all. Although we did record fringes on two of these nights, after reduction and calibration, it became obvious that we did not collect as much data as we suspected. The third and forth runs in late August of 2016 through early September 2016, and 2016 October, respectively, were somewhat more successful. We lost only two days to poor weather in the first and two in the third.

2.4.2 Calibrator Stars

Observation of calibrator stars is necessary in optical interferometery in order to account for sources of incoherence such as changes in the atmosphere and instrumental effects. Ideally

calibrator stars are unresolved, but if they are resolved they should be of known angular diameter and much smaller than the target star. Likewise, they should not be binaries and should be of a class and type of star expected to be free of an extended atmosphere and other sources of asymmetry. Calibrator stars should be close in brightness to the target, but as our targets were so bright there were no calibrators very close in magnitude, so we tended to be careful not too use calibrators that were very dim as compared to a target.

We used several methods to select our calibrator stars. Initially we used the SearchCal tool (Chelli et al. 2016) provided by JMMC[4]. However, we preferred to use well known calibrators, especially those with measured, rather than modeled diameters, so we compared these angular diameters to published angular diameters and the angular diameters listed in the internal MIRC calibrator lists. Often calibrators in publications had diameters that were from JMMC, but in some cases, calibrators had measured diameters. These were our top choices, followed by those that seemed to be the most reliable and trusted by other teams. Finally, if no other option was available, we selected the calibrator from SearchCal which was the smallest, closest in the sky, closest in magnitude, and known to be free of other issues. We present the H-band uniform disk angular diameters, which were used for calibration, and the references for these diameters, in Table 2.2

[4]`http://www.jmmc.fr/searchcal_page.htm`

Table 2.2: Interferometric calibrators used for this study.

Star Identifier	θ_{UD} (H-Band) (mas)	Source
7 And	0.65±0.30	Mourard et al. (2015)
41 Cyg	1.01±0.11	Bourgés et al. (2014)
σ Cyg	0.54±0.02	Zhao et al. (2008)
ι Cyg	0.65±0.06	Bourgés et al. (2014)
HD 9022	1.21±0.12	Bourgés et al. (2014)
θ Cas	0.50±0.07	Bourgés et al. (2014)
HD 22427	1.09±0.09	Bourgés et al. (2014)
λ Per	0.48±0.03	Bourgés et al. (2014)
η Aur	0.45±0.01	MIRC internal list (analyzed by B. Kloppenborg)
HD 39699	1.06±0.08	Bourgés et al. (2014)
θ Gem	0.78±0.08	Bourgés et al. (2014)
71 Ori	0.59±0.02	Allende Prieto & Lambert (1999)

Calibrators used to reduce the MIRC observations presented in this manuscript. Calibrators from SearchCal are cited as Bourgés et al. (2014).

.

2.4.3 Data Processing

For reduction and calibration of the MIRC data, we used the latest version of the MIRC reduction pipeline (as of 2017 June) (Monnier et al. 2007), with modifications we and Gail Schaefer made for ease of use during the later steps which require user interaction. Following the initial processing stages which accounted for flux calibration and other instrumental effects, the pipeline uses Fourier transforms to compute squared visibilities, averaging these values and correcting them for biases. The bispectrum (triple amplitude ("T3") and closure

phase (CP)) is calculated using the phases and amplitudes of three baselines in a closed triangle. During the averaging process, the user is prompted to select low flux portions of the observation for removal. We added a clipping option to make this easier. The user inputs the threshold for clipping, based on some sigma distance from the average flux for each observational block (that is each recording on a target or calibrator). Then all data points below this threshold are removed, with the user given the option to continue or make other modifications, including resetting. A later portion of the averaging script allows users to manually remove V^2, T3, and CP points. Schaefer added a sigma clipping as an option here, allowing users to select a sigma from the average to clip and then giving the user the option to select automatic removal of points for each baseline in each observational block. Both of these features proved to save time and produce more robust final products. During reduction we used a 17 millisecond coherence time and applied a cross-talk correction for visibilities less than 0.1.

We calibrated amplitudes using a beam splitter following spatial filtering (Che et al. 2010). In order to correct for atmospheric coherence time and various optical changes in the beam path, we used reference calibrator stars, described in Table 2.2. The calibration stage also included user input and during this stage we removed V^2 points below zero, as well as those which seemed to differ vastly from trends, although we were careful not to be too zealous. Note that removing points below zero does import some bias to the data, but angular diameters obtained using data calibrated with a more conservative point removal strategy (only removing points more than a standard deviation below zero) were within one

standard deviation of the angular diameters obtained using the aggressive point removal stragety we used. Nonetheless, we recommend that other researchers not remove all points below zero. We did not remove any points from the T3 or CP measurements at this stage.

The calibration model we used included multiplicative errors (associated with the transfer function) and additive errors (associated with bias at low amplitude) for square visibility and triple amplitudes as described in Monnier et al. (2012) and followed the methods described in Zhao et al. (2011) and Monnier et al. (2012) to account for closure phase errors. In short, our multiplicative factor for V^2 was 6.6%, the additive minimum threshold was 0.0002, and the relative error factor was 0.05. For triple amplitude, the multiplicative factor was 10%, the additive minimum threshold was 0.00001, and the relative error 0.1. For closure phase we used a minimum additive error of 1°, a slope correction of 0.1, and amplitude S/N of 1.0. Because we do not expect significant brightness variation over short time periods for our targets, we combined observations that fell within two weeks of each other into single files.

We display our observational logs in Tables 2.3-2.5. Note that because of observing conditions or ongoing work on different telescopes, it was not always possible to record data with all six telescopes. We note with asterisks (*), those targets for which we recorded but which after reduction and calibration did not result in any useful data. The figures corresponding to the (u, v) coverage, squared visibilities, and closure phases, are presented in Appendix A

Table 2.3: Observing Log for AZ Cyg.

Date (UT)	$N_{telescopes}$	N_{block}	Calibrators
2011 Jul 21	6	1	7 And
2012 Jun 06	5	1	7 And
2012 Jun 11	6	1	σ Cyg
2014 Jun 16	5	1	σ Cyg, 7 And
2014 Jun 17	5	1	σ Cyg, 7 And
2015 Aug 22	5	2	σ Cyg
2015 Aug 23	6	2	σ Cyg
2015 Oct 27*	6	1	σ Cyg
2016 Aug 29	6	1	σ Cyg
2016 Aug 30	6	1	σ Cyg
2016 Sep 03	6	1	σ Cyg
2016 Sep 06	5	1	σ Cyg
2016 Sep 08	5	1	σ Cyg, 7 And
2016 Sep 09	6	1	σ Cyg, 7 And
2016 Sep 10	6,4	4	σ Cyg, 7 And
2016 Sep 11	6	1	σ Cyg, 7 And
2016 Oct 12*	6	1	σ Cyg, 7 And
2016 Oct 13*	6	1	σ Cyg, 7 And
2016 Oct 14*	6	2	ι Cyg,σ Cyg, 7 And

Observing log for AZ Cyg. Observations marked with an * did not result in useful data by the end of data reduction. Note that $N_{telescopes}$ denotes the number of telescopes available but does not imply we got fringes on all baselines associated with those telescopes.

Table 2.4: Observing Log for SU Per.

Date (UT)	$N_{telescopes}$	N_{block}	Calibrators
2015 Aug 18	6	1	HD 9022
2015 Aug 20	6	1	HD 9022
2015 Aug 21	6	1	HD 9022, HD 22427
2015 Aug 22	6	1	HD 9022
2015 Aug 23	6	4	HD 9022, HD 22427
2015 Aug 24	6	4	HD 9022, HD 22427
2015 Oct 27*	6	2	θ Cas, HD 22427
2016 Aug 28	6	2	θ Cas, HD 22427
2016 Aug 29	6	1	θ Cas, HD 22427
2016 Sep 01	6	1	θ Cas, HD 22427
2016 Sep 02	6	1	θ Cas, HD 22427
2016 Sep 07	6	2	θ Cas, HD 22427
2016 Sep 08	6	2	θ Cas, HD 22427
2016 Sep 09	6	3	θ Cas
2016 Sep 11	6	3	θ Cas,HD 22427
2016 Oct 8	6	1	θ Cas, HD 22427
2016 Oct 11	6	1	HD 6961, λ Per
2016 Oct 12	6	3	HD 6961, λ Per
2016 Oct 14	6	2	HD 6961,HD 22427, λ Per

Observing log for SU Per. Observations marked with an * did not result in useful data by the end of data reduction. Note that $N_{telescopes}$ denotes the number of telescopes available but does not imply we got fringes on all baselines associated with those telescopes.

Table 2.5: Observing Log for Other Stars.

Date (UT)	Star	$N_{telescopes}$	N_{block}	Calibrators
2015 Aug 18	RW Cyg	6	1	σ Cyg
2015 Aug 18	BI Cyg	6	1	σ Cyg
2015 Aug 18	FZ Per	6	1	HD 9022
2015 Aug 18	S Per	6	1	HD 9022
2015 Aug 18	AD Per	6	1	HD 9022
2015 Aug 18	XX Per	6	1	HD 9022
2015 Aug 19	AW Cyg*	6	1	17 Cyg, σ Cyg
2015 Aug 19	BU Per	6	1	HD 9022
2015 Aug 19	W Per	6	1	HD 9022
2015 Aug 20	ξ Cyg	6	1	41 Cyg, σ Cyg
2015 Aug 20	KK Per	6	1	HD 9022
2015 Aug 21	PP Per	6	1	HD 9022
2015 Aug 22	AD Per	6	2	HD 22427
2015 Aug 23	PP Per	6	1	HD 9022
2015 Aug 23	LW Cyg*	5	1	σ Cyg
2015 Oct 26	WY Gem*	6	1	θ Gem
2015 Oct 27	WY Gem*	6	1	HD 39699, θ Gem
2016 Aug 28	NR Vul	6	1	17 Cyg, σ Cyg
2016 Aug 28	W Per	6	1	HD 22427
2016 Aug 29	IRC+40406	6	1	17 Cyg, σ Cyg
2016 Aug 29	KK Per	6	1	θ Cas
2016 Aug 29	RS Per	6	1	θ Cas, HD 22427
2016 Aug 30	V424 Lac	6	1	7 And
2016 Aug 30	BU Per	6	1	θ Cas, HD 22427
2016 Aug 30	AD Per	6	1	θ Cas, HD 22427
2016 Sep 01	IRC+40406	6	1	17 Cyg, σ Cyg
2016 Sep 01	V366 And	6	1	θ Cas

2016 Sep 01	PR Per	6	1	θ Cas, HD 22427
2016 Sep 02	NR Vul	6	1	17 Cyg, σ Cyg
2016 Sep 02	T Per	6	1	θ Cas
2016 Sep 03	IRC+40406	6	1	σ Cyg
2016 Sep 03	BU Per	6	1	θ Cas, HD 22427
2016 Sep 05	IRC+40406	6	1	σ Cyg
2016 Sep 05	V366 And	6	1	θ Cas
2016 Sep 05	T Per	6	1	θ Cas, η Aur
2016 Sep 06	IRC+40406	6	1	σ Cyg
2016 Sep 06	V424 Lac	6	1	σ Cyg,7 And
2016 Sep 06	T Per	6	1	θ Cas, HD 22427
2016 Sep 06	RS Per	6	1	θ Cas, HD 22427, η Aur
2016 Sep 07	BI Cyg	6	1	σ Cyg
2016 Sep 07	W Per	6	1	HD 22427
2016 Sep 08	W Per	5	1	HD 22427, η Aur
2016 Sep 10	S Per	6	1	θ Cas, η Aur
2016 Sep 10	RS Per	6	1	θ Cas, η Aur
2016 Sep 11	W Per	6	1	HD 22427, η Aur
2016 Oct 8	6 Gem	6	1	θ Gem
2016 Oct 8	6 Gem	6	1	θ Gem
2016 Oct 9	XX Per	6	1	θ Cas, η Aur
2016 Oct 9	WY Gem	6	1	θ Gem
2016 Oct 10	W Per	6	1	λ Per, η Aur
2016 Oct 10	WY Gem	6	1	θ Gem
2016 Oct 11	WY Gem	6	1	θ Gem
2016 Oct 12	WY Gem	6	1	71 Ori, θ Gem
2016 Oct 12	TV Gem	6	1	71 Ori, θ Gem
2016 Oct 13	AD Per	6	1	HD 6961, HD 22427
2016 Oct 14	6 Gem	6	1	71 Ori, θ Gem
2016 Oct 14	WY Gem	6	1	71 Ori, θ Gem

Observing log for the other of the stars observed for this project. Observations marked with an * did not result in useful data by the end of data reduction. $N_{telescopes}$ does not imply we got fringes on all baselines associated with those telescopes.

CHAPTER 3

Fundamental Parameters of Red Supergiants

Determining the stellar parameters (effective temperature: $T_{\rm eff}$; luminosity: L; mass: M; and radius: R) of RSGs is notoriously tricky because of their complex extended atmospheres. The landmark work of Levesque et al. (2005) resolved a long standing controversy about the temperatures of RSGs by using revised MARCS stellar atmospheres (Gustafsson et al. 2008) with spherical symmetry and improved opacities for oxygen rich molecules, including TiO. Using these updated models, they determined a warmer temperature scale for RSGs than previously reported, which brought the position of RSGs on evolutionary tracks into agreement with predictions by Geneva models. However, later work in the near-IR by van Belle et al. (2009), Davies et al. (2013), and Gazak et al. (2014) found still warmer temperatures than in Levesque et al. (2005), which also poorly predicted the near-IR flux of RSGs. In a detailed study of the issues involved with measuring $T_{\rm eff}$, Davies et al. (2013) showed that 3D RHD simulations of RSGs predict lower temperatures in the upper atmosphere where TiO forms, and thus fits to spectral regions with TiO lines do not measure the temperature at the photosphere but rather the temperature of a cooler region of the atmosphere. Even in the near-infrared, molecular lines formed in the extended atmosphere are present. Thus, one must be very careful when determining effective temperatures to use spectral regions which probe the continuum. Davies et al. (2013) suggest fitting to line free regions of the spectral energy distribution (SED) around the near-IR ($IJHK$) continuum region and the H^- opacity minimum. Indeed, barring a complete SED collected in proximity to an interferometric

angular diameter measurement at a wavelength in which we know we are measuring the photospheric diameter, we are restricted to using model atmospheres to assist with temperature determinations, which means we are limited by the ability of these models to predict the temperature structure of RSGs, as well as the influence of convection on the temperature profile. Even in the case of 3D models, it is known that stellar atmospheres fair poorly at both these tasks. Thus, determining stellar parameters remains a difficult task.

3.1 Angular Diameters

One of the great benefits of interferometry is that it allows the direct measurement of one of the stellar parameters needed to determine the temperature: the angular diameter. The defining equation for the effective temperature is $L = 4\pi\sigma R^2 T_{\rm eff}^4$. Taking into account the definition of angular diameter (in mas), we can rewrite this equation $T_{\rm eff} \approx 1.316 \times 10^7 \left(\frac{F_{bol}}{\theta_R^2}\right)^{1/4} K$ for bolometric flux F_{bol} in $W\ cm^{-2}$ (Dyck et al. 1996b) and angular diameter θ_R in mas. Thus, given an angular diameter and a flux, one can determine the temperature, keeping in mind that the diameter one measures will be heavily wavelength dependent and thus one needs to measure the angular diameter at a wavelength that covers the continuum and is free of cool molecular lines. In fact, θ_R is the Rosseland angular diameter, which is not what an interferometer measures and thus some conversion is required (Dyck et al. 1996b; Wittkowski et al. 2004). Another caveat to this method is that F_{bol} is determined by using a spectral energy distribution and observed photometry. However, RSGs are variable, both due to pulsations and to surface variations. Thus, this method

requires photometry to be obtained in close proximity to the interferometric observations also being used. For this reason, we opted to fit model spectra to observed spectra spanning continuum regions to infer temperature and other stellar parameters.

In interferometry, an angular diameter is measured by a fit of the squared visibility curve to a model. Ordinarily, the first lobe of this curve fits the uniform disk diameter, the second lobe fits the limb darkened disk diameter, and later lobes carry information about smaller features on the surface of the star. However, because large inhomogeneities on the surface of a star can appear even in the first lobe of the squared visibility curve, the measurement of RSG angular diameters is further complicated by the effects of convection. Moreover, the extended atmospheres and convection dominated surfaces of RSGs also contribute to the difficulty of modeling limb darkening (Chiavassa et al. 2009).

To find the uniform disk (UD) angular diameters we minimized the χ^2 between the observed complex visibility on all baselines and the complex visibility of a uniform disk, given by $V_{UD}(x) = \frac{2J_1(x)}{x}$, with J_1 a Bessel function of the first kind and $x = \pi\nu\theta_{UD}$, with ν the spatial frequency at which the visibility function is sampled and θ_{UD} the angular diameter being fit. To measure the limb darkened disk (LDD) diameter, we did the same, using the Hestroffer law (Hestroffer 1997),

$$I_\lambda(\mu)/I(1) = \mu^\alpha \, ; \, \alpha \in \mathbf{R}^+ \tag{3.1}$$

where I is intensity, $\mu = \sqrt{1-(2r/\theta_{LD})^2}$ with r the angular distance from the center of the star, θ_{LD} the angular diameter of the photosphere, and α the limb darkening parameter.

$\alpha \in \mathbf{R}^+$ means that α is within the set of real, positive numbers. The complex visibility function corresponding to this law is:

$$V(x) = \sum_{k \geq 0} \frac{\Gamma(\alpha/2 + 2)}{\Gamma(\alpha/2 + k + 2)\Gamma(k + 1)} \left(-\frac{x}{2}\right)^{2k} \tag{3.2}$$

with $x = \pi\nu\theta_{LD}$ and Γ the Euler function (Lacour et al. 2008). Unlike some limb darkening laws, particularly those based on solar data, this law drops to zero at the limb of the star. In fact, this is the purpose of the law. Hestroffer (1997) also presented a two parameter law which can be used when the disk is not fully darkened, which fits the Sun well. But Hestroffer notes that for M giants, models predict a fully darkened limb. He found that the one parameter power law in Equation 3.1 performed just as well as a quadratic law for M giant models and that for Mira stars the power law fit better. With regard to RSGs, Young et al. (2000) found that the Hestroffer power law fit observations of Betelgeuse at 1290 nm just as well as a linear law and that the power law performed better at the limb of the star. This is similar to what Baron et al. (2014) found in their study on T Per and RS Per.

We initially fit the model visiblities to the complete visibility curve to derive angular diameters. However, as the visibility curve at higher frequencies is heavily influenced by the presence of surface features we also ran fits using data limited to the spatial frequencies corresponding to the first two lobes of the squared visibility curve, which contribute the majority of information about disk size and limb-darkening. We did not find any major difference between angular diameters derived using the complete data set verses those determined using only lower spatial frequencies. Thus, we report angular diameters using the entirety of the data. To get errors we bootstrapped, randomly sampling the observed squared visibilities

used in the fits. Because our observations are in the H-band, which covers a minimum in the opacity of the continuum, there is no contribution of dust and we consider our limb darkened diameters to be a measurement of the Rosseland angular diameter. We present the derived angular diameters for our observations in Table 3.4.

3.2 Model Spectra

Modeling the atmospheres and spectra of red supergiants is a difficult task. Their atmospheres are extended and the plane parallel approximations used by many modeling programs are inaccurate. Their atmosphere experiences turbulence from convection. Their spectra are rich in molecules and atomic lines with poorly known atomic data. And, they experience internal mixing, with dredge up of material from within the interior resulting in surface enrichment. As noted above for the results of Levesque et al. (2005), improvements via spherical modeling and attention to molecular opacities have been vital to better approximating the appearance of RSG spectra.

For spectral inference, we utilized spherical model atmospheres from three of the most commonly used libraries for RSGs: PHOENIX (Lançon et al. 2007), MARCS (Gustafsson et al. 2008), and SATLAS (Lester & Neilson 2008). Table 3.1 contains the parameter space of our spectral libraries.

Table 3.1: Parameter Space of Model Spectra.

Grid	$T_{\rm eff}$ (K)	$\log(g)$	[Fe/H] (dex)	$v_{\rm turb}$ (km s^{-1})	Mass $(M_\odot)$
PHOENIX	3000-4500	-1.0-+1.0	0.00*	2	15
MARCS	3300-4500	-0.5-+1.0	0.00-0.50	5	15
SATLAS	3000-4500	-1.0-+1.0	0.00	2	8-30

Parameter space of the model spectra we used. Asterisk * means abundances modified for RSGs.

3.2.1 PHOENIX

We utilized the spectral library of Lançon et al. (2007), which we downloaded using the Vizier service. This library was produced specifically with modelling RSGs in mind. The spherical model atmospheres underlying the spectra were produced using PHOENIX 13.11.00B. These models apply a mixing length of 2.0 and do not incorporate dust opacities. The spectra were calculated with a wavelength step of 0.1 Å. All spectra in this library were calculated with $v_{\rm turb}$ = 2 km s^{-1}, which is on the low side of that which has been found to best fit RSGs. We used only the portion of the library encompassing the possible range of RSGs: $T_{\rm eff} = 3000 - 4500$ K; $\log(g)$=[-1,-0.5,0,1]; $M = 15$ $M_\odot$. We used the spectra modeled with "RSG abundances"—that is those with non-solar ^{4}He, ^{12}C,^{14}N, and ^{16}O but otherwise solar values ([Fe/H]=0.00). In case of the RSG abundances, Lançon et al. (2007) selected values which would represent an RSG of $M = 20$ $M_\odot$ near the end of its life.

Lançon et al. (2007) tested these spectra against a grid of observed spectra that included RSG and warmer supergiants. They found that the warmer supergiants fit the solar metal-

lacity models best and that other supergiants had "reasonable" or poor fits. In particular, 6 of the 7 poorly fitting spectra belonged to RSGs (M0Ia and M3.5 and I,Ia, and Ib). These poor fits were attributed to contributions from CN and CO, which favor different temperatures, and also to variability. The authors noted that including optical wavelengths led to lower derived temperatures, while using CN dominant regions resulted in derived temperatures nearly 800 K higher. Using RSG abundances for RSGs did result in some improvement. Ultimately, the authors note that it is possible to achieve good fits for luminous cool stars when fitting to one specific near-IR band (such as H or K but not both). The authors also note that higher micro-turbulent velocities and lower gravities would improve fits for some stars.

3.2.2 MARCS

We produced a new atlas of synthetic spectra based on spherical MARCS models designed specifically for RSGs. We note that this atlas is probably not the only one of its kind in existence, but as we could not find public access to any of the atlases used in other publications, we elected to generate our own, which will be made publicly available.

The source grid is based on the spherical MARCS models of Gustafsson et al. (2008). Like the PHOENIX models, these are 1D, but spherically symmetric, assume local thermodynamic equilibrium (LTE), and model the effects of convection using the approximations of mixing length theory. Levesque et al. (2005) found that this grid showed significant improvement in the modeling of RSG because of the addition of improved physical data, most notably, the molecular opacities.

The RSG grid utilized for our spectra generation consists of 280 models. The parameter space covers $T_{\rm eff} = 3300$ to 4500 K, $\log(g) = -0.5$ to 1, and included metallicities [Fe/H]=0.0, 0.25, and 0.50. All models were calculated for $M = 15\ M_{\odot}$.

To generate the model spectra, we used TURBOSPECTRUM v19.1, a 1D LTE spectral synthesis code that incorporates numerous atomic and molecular features (Alvarez & Plez 1998; Plez 2012). We downloaded molecular and atomic features from the VALD database via FTP, using the extract all, long format, air wavelengths, isotropic scaling, and extended van der Vaals options. Following this, VALD files were reformatted for use in TURBOSPECTRUM using a Python implementation of Vald2Bsyn[1]. We calculated spectra with $v_{\rm turb} = 5$ km s^{-1} with 0.1 Å steps from 650-5500 nm, in order to cover the complete range of our SpeX observations. An additional grid with $v_{\rm turb} = 2$ km s^{-1} will be calculated after this dissertation for comparison to the 5 km s^{-1} grid in a paper detailing stellar parameters.

3.2.3 SATLAS

We also produced a new atlas of both model atmospheres and synthetic spectra using SATLAS (Lester & Neilson 2008) and the associated SYNTHE (Kurucz 1993) suite. Again, this is probably not the only of its kind, but as we could not find any one publicly available we elected to generate our own. This too will be made publicly available in a forthcoming paper on stellar parameters of RSGs.

Our grid of SATLAS models used the SATLAS ODF approach which uses pre-compiled opacity distribution functions. This is in contrast to an opacity sampling (OS) approach

[1] `https://github.com/EricDepagne/Vald2Bsyn`

which is also available. We selected the former simply to save time, as the OS models would require the additional step of an input ODF model anyway. In developing SATLAS, Lester and Neilson first updated the ATLAS 9 (ODF) and ATLAS 12 (OS) originally developed by Kurucz, and their updated code, described in Lester & Neilson (2008), is referred to as ATLAS_ODF and ATLAS_OS. The plane parallel models generated by these codes serve as the starting point for the spherically symmetric models produced by SATLAS_ODF and SATLAS_OS, respectively.

In either case, the SATLAS models work in the parameter space of luminosity, radius, and mass. This is because of the degeneracy of $\log(g)$ with regard to mass and radius, which are important inputs in spherical models. The code defines radius as the location where the Rosseland mean optical depth $\tau_R = 2/3$. This is in contrast to that used by spherical MARCS, which uses $\tau_R = 1$ and spherical PHOENIX which uses $\tau_{500} = 1$. Lester & Neilson (2008) note that the differences between these approaches are minor. To generate spherically symmetric models, Lester & Neilson (2008) made modifications to the plane parallel ATLAS code that are extensively described in their paper.

To generate our grid of model atmospheres, we needed to begin with a grid of plane parallel model atmospheres. Following the guidance of Lester as described in the README for SATLAS, we downloaded the necessary ingredients for producing model atmospheres. We downloaded an initial grid of model atmospheres from Fiorella Castelli's website[2] which covered the parameter space $T_{\rm eff}$=[3500, 3750, 4000, 4250, 4500], $\log(g)$=[0,0.5,1.0], [Fe/H] from -5.5 to 0.5 in 0.5 steps, and $v_{\rm turb} = 2$ km s^{-1}. We also downloaded $\kappa_{Rosseland}$ coefficents,

[2] `http://wwwuser.oats.inaf.it/castelli/`

the "new" opacity distribution functions (which were recomputed with an updated H_2O line list), and Kurucz's molecular and atomic line lists from Castelli's website. Because this initial grid did not cover much of the parameter space of RSGs, we used the starting Castelli grid to make an expanded grid covering $T_{\rm eff} = 3000$ to 4500 in 100 K steps and $\log(g) = -1.0$ to +1.0 in 0.25 steps. We did this only for [Fe/H]=0.0 and $v_{\rm turb} = 2$ km s^{-1}, although future efforts will be made to expand this atlas to other abundance ratios and micro-turbulent velocities. In generating the grid, we used as a starting point the closest existing model, used 15 iterations, and checked for convergence. If convergence was not achieved, we reran with 20 or more iterations.

Our initial plane parallel atlas served as the starting point for generating a new grid of spherical models from radius $R = 100 - 900$ $R_\odot$ (we attempted to go above $R = 1000$ $R_\odot$ but the code failed to produce such models for unknown reasons), mass M=8, 10, 15, 20, 30 $M_\odot$, and luminosity (L) determined by using the corresponding radius and temperature from 3000-4300 K in 100 K steps. Prior to calculating the atmospheres, we checked whether the L, R, and M fell into RSG parameter space, which we defined as 10000 $L_\odot < L <$ 500000 $L_\odot$ and $\log(g) = -1.0$ to 1. We started by finding the closet existing spherical or plane parallel model and used that as an input model for the code. We started with 15 iterations and following a suggestion from John Lester via email, defined convergence as a luminosity error <1% at $\log(\tau_r)$=<2.00. If a model did not converge, we reran it with more iterations. We produced models only at [Fe/H]=0.0 and v_{turb} of 2 km s^{-1} but plan on expanding that parameter space. This resulted in a grid of 542 model atmospheres. We then used the

SYNTHE (Kurucz 1993) suite to generate model spectra at a resolution of R = 500,000 from 680-2700 nm using the Kurucz linelists as inputs.

3.3 Spectral Inference

To determine stellar parameters, we minimized the χ^2 between a given interpolated model spectrum and a given observed spectrum using the Amoeba function within IDL, which uses the downhill simplex method for multi-dimensional minimization. We used an order merged spectrum of AZ Cyg collected on 2016 September 06 using SpeX on IRTF and an order merged spectrum of SU Per from the IRFT Spectral Library (Rayner et al. 2009). Because the spectrum of AZ Cyg was not shifted to zero-velocity, prior to fitting we corrected the model spectrum to match the radial velocity of AZ Cyg using the value from Gaia Data Release 2 (Gaia Collaboration et al. 2018), which was -3.88±1.19 km s^{-1}. The spectrum of SU Per we used was already shifted to zero velocity by Rayner et al. (2009), who found a radial velocity of -7.55 km s^{-1}. Because both interstellar reddening and circumstellar reddening are important in RSGs, we used a modification of the selective extinction used in the Cardelli reddening law (Cardelli et al. 1989) as proposed by Massey et al. (2005), setting $R_V = 4.2$ rather than the normal 3.1. We included the color excess, $E(B-V)$, as a parameter in fits to AZ Cyg. For SU Per, we used $E(B-V)$=0.505, which was determined by Rayner et al. (2009) and which is within the range of the color excess (0.50-0.56) found by Currie et al. (2010) for the Perseus OB-1 double cluster, where SU Per is located. Prior to correction for reddening, we used Gaussian smoothing to convolve the model spectrum to

Figure 3.1: Plots and residuals of the best fitting PHOENIX spectra.

(a) Best fit AZ Cyg

(b) Best fit SU Per

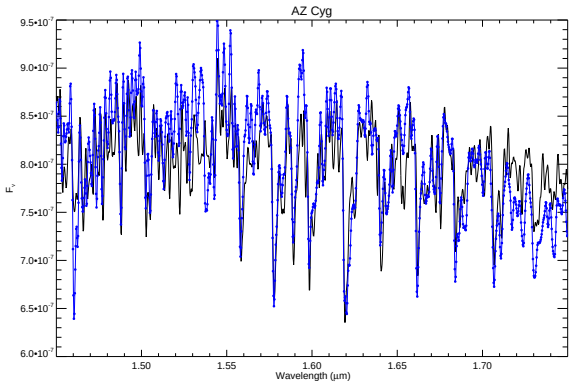

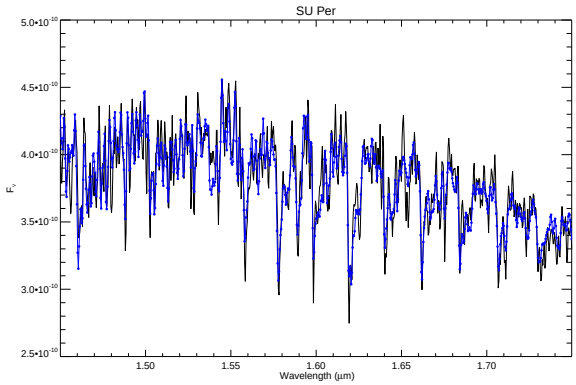

(c) Residuals AZ Cyg

(d) Residuals SU Per

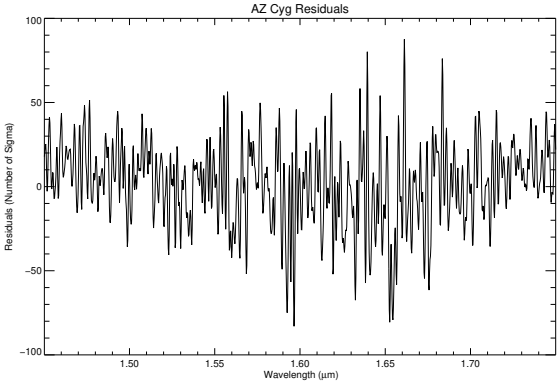

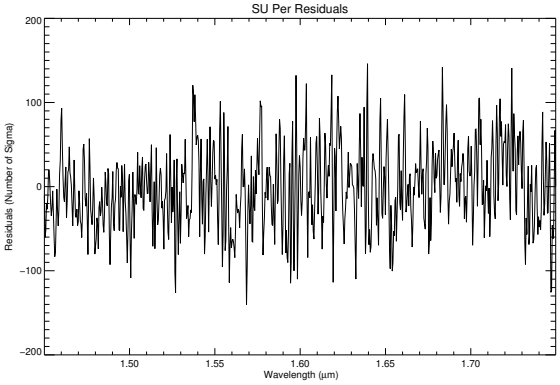

Best fitting PHOENIX model spectra (blue) compared to observed spectra. Residuals are in sigmas.

Figure 3.2: Plots and residuals of the best fitting MARCS/TURBOSPECTRUM spectra.

(a) Best fit AZ Cyg

(b) Best fit SU Per

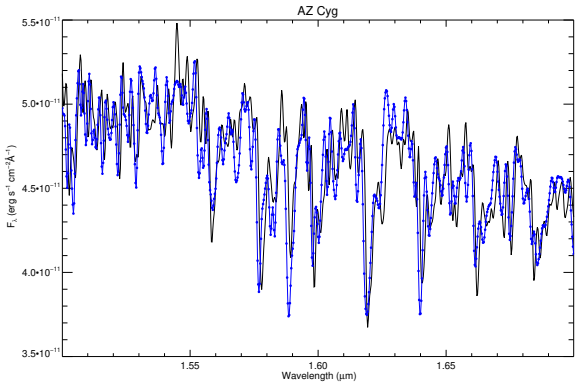

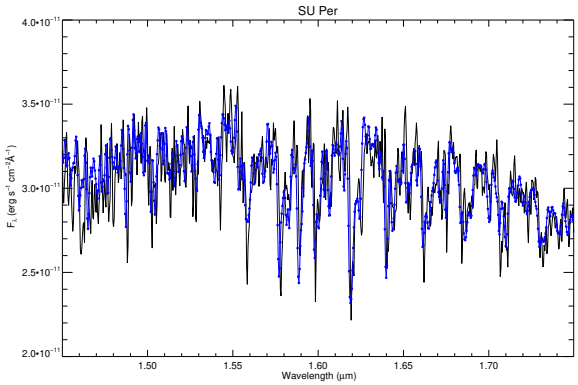

(c) Residuals AZ Cyg

(d) Residuals SU Per

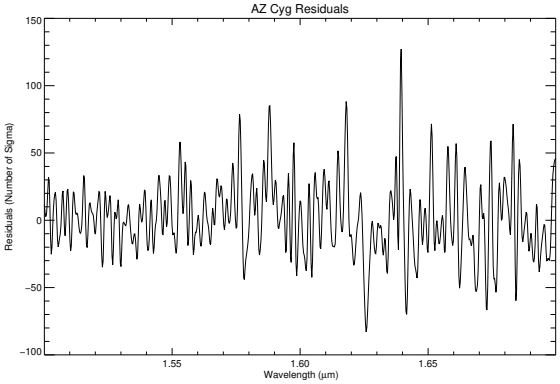

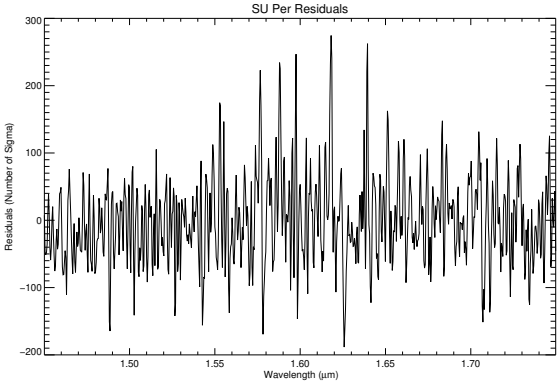

Best fitting MARCS/TURBOSPECTRUM model spectra (blue) compared to observed spectra. Residuals are in sigmas.

Figure 3.3: Plots and residuals of the best fitting SATLAS/SYNTHE spectra.

(a) Best fit AZ Cyg

(b) Best fit SU Per

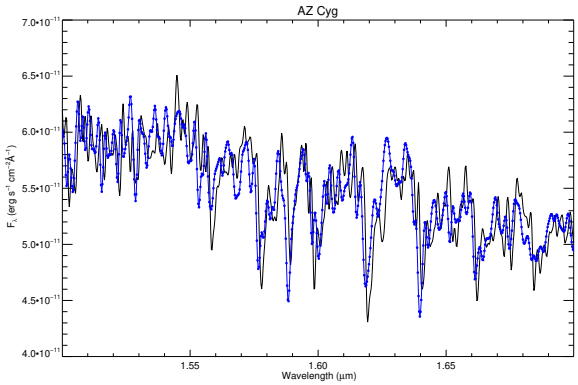

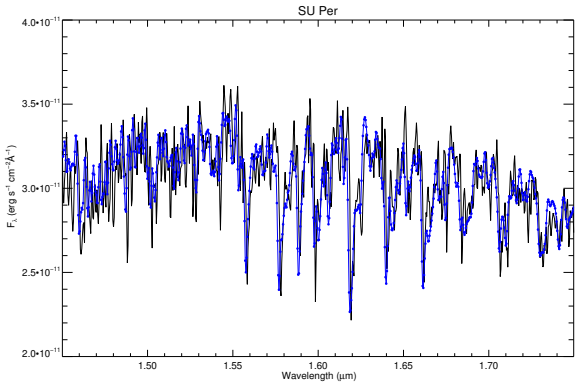

(c) Residuals AZ Cyg

(d) Residuals SU Per

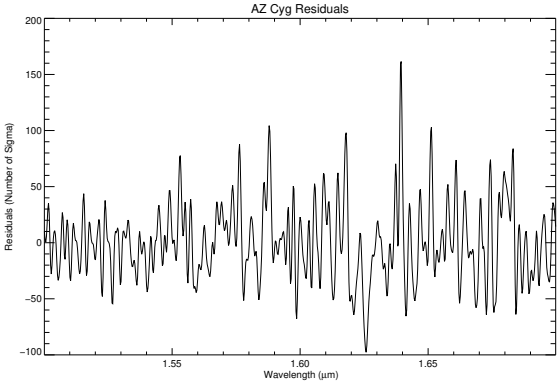

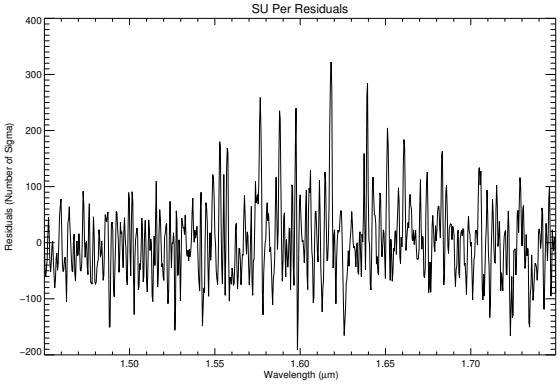

Best fitting SATLAS/SYNTHE model spectra (blue) compared to observed spectra. Residuals are in sigmas.

roughly the resolution of the observed spectrum. We restricted our fits to $1.450 - 1.750$ μm in order to avoid strong molecular features and cover the wavelength channels of MIRC. We present the derived stellar parameters of AZ Cyg and SU Per in Tables 3.2-3.3 and present plots of the best fitting spectra as well as residuals in Figures 3.1-3.3.

Table 3.2: Stellar parameters of AZ Cyg derived from model spectra.

Model	$T_{\rm eff}$ (K)	$\log(g)$	Radius $(R_\odot)$	Luminosity $(L_\odot)$	Mass $(M_\odot)$	[Fe/H] (dex)	$E(B-V)$
MARCS	4000	0.50	481	53206	15	0.00	0.76
PHOENIX	4100	0.00	642	94614	15	0.00	0.59
SATLAS	3867	0.36	600	110495	30	0.00	0.89
Average	3989± 117	0.29±0.26	574± 84	82772±35173	20±9	0.00±0.00	0.75±0.15

Stellar Parameters of AZ Cyg derived from fits to model spectra. For the MARCS and PHOENIX models, radius, luminosity and mass are calculated from $T_{\rm eff}$ and $\log(g)$. For the SATLAS model, $T_{\rm eff}$ and $\log(g)$ are calculated from radius, luminosity, and mass.

Table 3.3: Stellar parameters of SU Per derived from model spectra

Model	$T_{\rm eff}$ (K)	$\log(g)$	Radius $(R_\odot)$	Luminosity $(L_\odot)$	Mass $(M_\odot)$	[Fe/H] (dex)	$E(B-V)$
MARCS	3700	0.50	361	21904	15	0.00	0.505
PHOENIX	3600	0.00	642	62077	15	0.00	0.505
SATLAS	3650	0.39	300	14134	8	0.00	0.505
Average	3650±50	0.30±0.26	426±188	32705±25731	13±4	0.0±0.00	0.505

Stellar Parameters of SU Per derived from fits to model spectra. For the MARCS and PHOENIX models, radius, luminosity and mass are calculated from $T_{\rm eff}$ and $\log(g)$. For the SATLAS model, $T_{\rm eff}$ and $\log(g)$ are calculated from radius, luminosity, and mass.

3.4 Stellar Parameters

3.4.1 Effective Temperature and log(g)

From fits to the three atlases of model spectra we derived $T_{\rm eff} = 3989 \pm 117$ and $\log(g) = 0.29 \pm 0.26$ for AZ Cyg. These both fall within the parameter space of RSGs. There are few measurements of this star in the literature. Lancon & Rocca-Volmerange (1992) found $T_{\rm eff} = 3300\ K$ for AZ Cyg which was based on blackbody fitting to the H-K continuum. We derived a color excess of $E(B-V) = 0.75 \pm 0.15$. Using the typical B-V for a M2-3Iab star as described by Elias et al. (1985) and the B and V photometry for AZ Cyg from Ducati (2002), one finds a color excess of 0.87, which is within the error range of our fits. The best fitting SATLAS model corresponded to a mass of 30 $M_{\odot}$, which we suspect is too high. Likewise, we find differences in the radii derived from spectral fitting compared to those found via interferometry as presented in Table 3.4.

From fits of model spectra to SU Per, we derived $T_{\rm eff} = 3650 \pm 50$ and $\log(g) = 0.30 \pm 0.26$. These also fall within the parameter space of RSGs. Gazak et al. (2014) fit a J-band spectrum of SU Per to MARCS spherical models and measured $T_{\rm eff} = 3730 \pm 25$ and $\log(g) = -0.01 \pm 0.3$. It is heartening to see that the parameters we derive using spectra calculated from MARCS models is similar to this, although we find a higher $\log(g)$. Levesque et al. (2005) measured $T_{\rm eff} = 3575$, but as mentioned at the beginning of this chapter, those temperatures were determined using a method which is now known to underestimate temperatures. The radii derived from spectral fitting for SU Per are suspiciously low, with only the PHOENIX measurement approaching the inteferometric observations presented in the next section. In

a forthcoming work, we will investigate the wavelength dependence of our angular diameter measurements by deriving the angular diameter using separate wavelength channels rather than the full range.

3.4.2 Distances

In addition to the fitted parameters discussed above, we can determine distances to our targets using astrometric sources such as Gaia data release 2.0 (Gaia Collaboration et al. 2016, 2018; Gaia Collaboration 2018) and derive physical sizes for the observed stars. Prior to using these, we need to keep in mind that parallaxes, even those from Gaia, can be biased. Luri et al. (2018) warns that one should not simply use the inverse distance approach and that using Gaia parallaxes should be treated as a Bayesian inference problem. Bailer-Jones et al. (2018) took such an approach for nearly all of the stars in Gaia Data Release 2.0 using a weak distance prior that accounts for a decreasing density of stars with distance. In making their determination, they used a global zero-point of -0.029 mas as suggested by Lindegren et al. (2018), noting that in fact this value varies based on color, magnitude, and position on the sky. Chatys et al. (2019) used Gaia Data Release 2 parallaxes to derive a more accurate period-luminosity relation for RSGs, including many of those in our target list. They found that when using the inverse parallax method, their results closely matched Bailer-Jones et al. (2018), when corrected for the zero-point. In our analysis, we will use the results of Bailer-Jones et al. (2018) due to the Bayesian inference approach they take.

3.4.3 Radii of other targets

We have measured the angular diameters of 17 RSGs using data obtained with MIRC on CHARA. We followed the method described in Section 3.1 to determine the Hestroffer power law limb darkened angular diameters and used distances derived from Gaia parallaxes in Bailer-Jones et al. (2018) to derive the radii, excepting for S Per, for which we used a trigonometric parallax from Asaki et al. (2010) which was determined using H_2O masers. We present these results, including the χ^2 of the angular diameter fits in Table 3.4. Radii are calculated using the nominal solar radius of $\mathcal{R}_{\odot}^{\mathrm{N}}$=6.957 $\times$ 10^8 m, following the guidelines given by the International Astronomical Union (IAU) in IAU 2015 Resolution B3 (Prša et al. 2016). In the future we will also use spectral fitting to determine temperatures and other fundamental parameters, which will enable us to place these stars on the HR diagram.

Table 3.4: Radii of RSGs observed in this project.

Star	θ_{LD} (mas)	α	χ^2	D (pc)	R ($\mathcal{R}^{\rm N}_{\odot}$)
AZ Cyg 2011	3.93±0.01	0.42±0.1	5.24	2025^{+435}_{-309}	856^{20}_{14}
AZ CYG 2012	4.26±0.02	1.19±0.09	17.41	2025^{+435}_{-309}	927^{21}_{15}
AZ CYG 2014	4.09±0.01	0.59±0.02	8.07	2025^{+435}_{-309}	890^{21}_{15}
AZ CYG 2015	4.11±0.01	0.62±0.01	3.40	2025^{+435}_{-309}	895^{21}_{15}
AZ CYG 2016	4.09±0.01	0.72±0.02	3.44	2025^{+435}_{-309}	890^{21}_{15}
SU Per 2015	3.83±0.01	1.20±0.02	4.60	2767^{+765}_{-513}	1139^{34}_{23}
SU Per 2016 Aug	3.51±0.01	0.76± 0.01	2.82	2767^{+765}_{-513}	1044^{31}_{21}
SU Per 2016 Oct	3.68±0.02	0.96± 0.04	3.24	2767^{+765}_{-513}	1095^{33}_{22}
BD+354077	4.01±0.07	1.61±0.16	2.30	1586^{+196}_{-158}	684^{9}_{7}
BI Cyg 2015	5.94±0.12	0.54±0.15	0.77	1334^{+168}_{-135}	852^{12}_{9}
BI Cyg 2016	6.33±0.03	1.18±0.04	3.21	1334^{+168}_{-135}	908^{12}_{10}
V424 Lac	4.02±0.03	0.75± 0.09	3.98	634^{+90}_{-71}	274^{4}_{3}
V366 And	2.55±0.01	0.28± 0.02	1.99	2143^{+813}_{-510}	588^{24}_{15}
AD Per 2015	2.87±0.01	1.26±0.03	0.97	2056^{+274}_{-218}	634^{9}_{7}
AD Per 2016 Aug	3.00±0.03	1.57±0.11	3.65	2056^{+274}_{-218}	663^{10}_{8}
AD Per 2016 Oct	2.84±0.04	0.95±0.15	3.26	2056^{+274}_{-218}	628^{9}_{7}
BU Per	2.98±0.06	1.75± 0.19	7.06	1453^{+223}_{-172}	466^{8}_{6}
FZ Per	2.70±0.03	2.93±0.12	1.12	2134^{+206}_{-173}	619^{6}_{5}
KK Per	2.40±0.01	0.32±0.02	1.99	1613^{+727}_{-128}	416^{20}_{4}
RS Per	3.40±0.03	0.89± 0.07	2.21	1497^{+221}_{-172}	547^{9}_{7}
S Per	5.20±0.17	0.87±0.20	12.20	2439±60	1364±6
W Per	3.26±0.02	0.71±0.06	3.33	1222^{+141}_{-115}	428^{5}_{4}
XX Per	3.12±0.04	0.73±0.09	3.48	2029^{+325}_{-249}	681^{12}_{9}
6 Gem	5.20±0.06	2.33±0.16	4.79	$1469\ ^{+992}_{-449}$	821^{60}_{27}
TV Gem	5.30±0.02	3.0±0.0	7.23	2707^{+1289}_{-726}	1543^{79}_{44}
WY Gem	2.80±0.01	0.35±0.03	2.97	1539^{+288}_{-211}	463^{9}_{7}

Several of the stars appear to show some year-to-year variation in radius. In particular, the variation in AZ Cyg is notable, although we caution on including the 2012 data in any analysis due to its high χ^2. The variations in angular diameter roughly track AAVSO photometry presented in Chatys et al. (2019), which show an increase in visual magnitude in the star between 2009 and 2015. Note that the AAVSO measurements are not in the same bandpass as the interferometric measurements presented here, so one should be cautious about interpreting a correlation in increased magnitude with an increase in radius. In a forthcoming work we will more closely investigate the possibility that the angular diameter variations observed are connected to the variability noted in Chatys et al. (2019) and thus tied to pulsations in these stars.

CHAPTER 4

Interferometric Imaging of Red Supergiants

4.1 Method for producing optimized and verified images from SQUEEZE

As noted in the introduction, SQUEEZE is a MCMC based image reconstruction tool that enables stochastic exploration of the image probability space. Throughout this manuscript, the results we present were obtained using SQUEEZE's simulated annealing mode. In SQUEEZE, the image $\boldsymbol{x}$ is modeled as a superposition of a large number of flux elements (E), which are free to randomly move within the image. After a pre-determined number of iterations (500 throughout this manuscript), the mean, median, and mode of the last several iterations are calculated. A number of regularizers are available in SQUEEZE, but for efficiency, we limited our work to using those which experience showed were the most useful for reconstructing stellar surfaces: total variation (TV), a Laplacian regularizer (LA), the "uniform disk" regularizer (UD) from Baron et al. (2014), a ℓ_0 regularizer (L0), and a regularizer designed to promote dark narrow lanes which was a combination of the LA and UD regularizer (EDGE).

Total variation (Renard et al. 2011), acts on the image $\boldsymbol{x}$ by imposing greater sparsity on its spatial gradient $\nabla\boldsymbol{x}$. The total variation functional $R_{\rm TV}$ is the ℓ_1 norm of the spatial gradient, and can be approximated by:

$$R_{\rm TV}(\boldsymbol{x}) = \|\nabla\boldsymbol{x}\|_1^2 \simeq \sum_{i,j}\sqrt{(x_{i,j}-x_{i-1,j})^2+(x_{i,j}-x_{i,j-1})^2+\epsilon} \tag{4.1}$$

where ϵ is chosen to be a small number close to numerical precision. Total variation favors

zones of uniform flux separated by sharp boundaries.

The Laplacian regularizer used by SQUEEZE has similarities to total variation but is the ℓ_1 norm of the Laplacian, and thus is especially good with contours, which makes it particularly useful in imaging stellar surfaces with surfaces of varied flux.

The uniform disk regularizer from Baron et al. (2014) is the $\ell_{0.5}$ norm of the local gradient, approximated by:

$$R_{\mathrm{UD}}(\boldsymbol{x}) \simeq \left(\sum_{i,j} \sqrt{(x_{i,j} - x_{i-1,j})^2 + (x_{i,j} - x_{i,j-1})^2 + \epsilon} \right)^2 \tag{4.2}$$

where ϵ is chosen to be a small number close to numerical precision. The benefit of this regularizer is that it does not favor more spot-like features than the data suggests and allows the data to be the determining factor on spot size (hence the name "uniform disk" regularizer).

The ℓ_0 regularizer is a pseudo-norm, which is not a norm since it is non-convex:

$$\ell_0(\boldsymbol{x}) = \sum_{i}^{N} \mathbb{1}_{\mathbb{R}^+}(x_i) \tag{4.3}$$

where $\mathbb{1}_{\mathbb{R}^+}$ is the indicator function of $\mathbb{R}^+$, the set of real, positive numbers. The ℓ_0 pseudo-norm essentially counts the number of non-zero elements in the vector it is applied to. This regularizer can be useful in constraining pixels to a uniform region, such as the disk of a star.

In our testing of different regularizations we found that although we were able to repro-

duce large bright features decently, we struggled to replicate the smaller features suggested by 3D RHD models, such as the dark intergranular lanes surrounding bright features. In order to see if it was possible to reconstruct these features, we designed a new regularizer, the "edge" regularizer, for imaging small dark features.

Based on analysis of snapshots of 3D RHD models, we concluded that the best regularizer would be one that enforced different behavior for different types of features on a star. We used as a cutoff between the "bright" and "dark" regions the ratio of the median to mean values of non-zero pixels. For pixels above this threshold, we used the Laplacian regularizer described above and for pixels below it, the "uniform disk" $\ell_{0.5}$ norm regularizer. Unfortunately, this regularizer never performed better than other regularizers or combinations of regularizers in the optimization procedure described below.

4.1.1 Optimizing reconstructions with SQUEEZE

Because of the sparse nature of the data used for image reconstruction, there is no single solution for producing the best image. Moreover, interpreting the image in a scientific way requires some manner of analyzing both the uncertainty of the result and testing for artifacts. Unfortunately, this does not seem to be very common in most images published using optical interferometric data.

Several studies have analyzed the problem of image reconstruction in optical interferometry. Renard et al. (2011) tested regularization parameters for reconstructing images using simulations of interferometric observations of models of various astronomical sources (stars, galaxies, disks, etc.). For determining the closeness of fit, they used the mean-squared-error

between the source image and the result, although they also included a preliminary discussion on whether the L-Curve could also offer insight into optimal regularization. They found that the strongest constraints on reconstruction came from (u, v) coverage and that smoothness regularizations, such as total variation, were the best options for most astronomical sources. Perhaps the most serious limitation of this study was that the authors looked only at single regularizers at a time, rather than combinations of regularizers. Sometime later, Gomes et al. (2017) analyzed metrics for comparing reconstructed images to source images. They concluded that the best metric for comparing reconstructions to source images was the ℓ_1 norm (Gomes et al. 2017):

$$\ell_1(\boldsymbol{x}, \boldsymbol{y}) = ||\boldsymbol{x} - \boldsymbol{y}||_1 = \sum_i |x_i - y_i| \tag{4.4}$$

where $\boldsymbol{x}$ is the reconstructed image vector and $\boldsymbol{y}$ the source image vector.

Because this work seeks to study RSGs at the smallest possible scales, we became concerned with distinguishing small features from artifacts. We also noticed that preserving finer details in images, such as the intergranular lanes shown in 3D RHD models of RSGs, was very dependent on the combination of regularizers and their strengths. Thus, we decided to apply a procedure for optimizing reconstruction on a given set of data and for a given target type. We first used this method in Montargès et al. (2018) and described it in Norris et al. (2019). In this procedure, we start with a source image, such as a snapshot of a 3D RHD model of the photosphere of a RSG, like that found in Chiavassa et al. (2010a) and which is displayed in the upper left panel of Figure 4.1. The next step is to input this image into the

observation simulation code we co-developed as part of the OITOOLS.jl package. This code has two simulation options, one which copies the (u, v) coverage and noise statistics from an OIFITS file of a real observation, another which takes input hour angles, array parameters, and error statistics. When determining the best regularization technique for a particular data set, we used the former. We then use SQUEEZE to reconstruct an image from this simulated data using multiple chains, and a variety of regularizers and combinations of regularizers, various hyperparameters, different element numbers, and so forth. For each run, we take the result from each chain and get an average image and standard deviation image. Because SQUEEZE has random starting points, it is important to center each image before the stacking procedure, so we implement a subpixel-shift as described in Guizar-Sicairos et al. (2008) and implemented in Julia by Romain Franconville [1]. Doing this results in a large stack of final images. We compare this stack to our source image, convolved to the resolution of the data, and use the ℓ_1 norm to find the closeness of fit. The reconstruction with the lowest ℓ_1 norm corresponds to the reconstruction parameters which best replicate the surface structure a RSG as predicted by snapshots of 3D RHD models. These are the parameters we elect to use for reconstructing a particular data set.

In Figure 4.1 we show some results from one of the experiments we ran—this one copying observations of AZ Cyg from 2011. The original source image is a snapshot of an H-band 3D RHD simulation of Betelgeuse from Chiavassa et al. (2010a). We convolved that image to 0.25 mas pixel^{-1} and rebinned it to match a 4 mas star. The closest matching reconstruction to the convolved source image had a ℓ_1 norm of 0.014 relative to the convolved source and

[1] https://github.com/romainFr/subpixelRegistration.jl

used 3000 elements with a Laplacian regularizer as well as the "uniform disk" regularizer. On the other hand, the most distant reconstruction had a ℓ_1 norm of 0.016 relative to the convolved source and used 2500 elements with a total variation regularizer as well as the specially designed "edge" regularizer designed to reconstruct small, narrow, dark regions in images. Although the numerical difference between the lowest ℓ_1 norms seems small, clearly the reconstruction with the lowest ℓ_1 norm appears more like the convolved source image!

4.1.2 Verifying images

We identified two major sources of error and bias in our images: bias from the limited (u, v) coverage and error from the image reconstruction technique. Because our study focuses on studying surface features on stars, it is important to distinguish actual features in an image from artifacts resulting from this error and bias. Thus, in addition to the image reconstruction technique, we implemented an image verification method as well.

One of the major benefits of SQUEEZE is that its MCMC approach is ideal for showing the spread in imaging results—which is what we mean when we refer to error resulting from the image reconstruction technique. At the end of a reconstruction run, SQUEEZE outputs the mean, median, and mode images resulting from the last several hundred iterations. It also outputs a χ^2 comparing these images to the squared visibilities, triple amplitudes, and closure phases of the data and notes which iteration along the MCMC path had the lowest χ^2. It is possible to run SQUEEZE on multiple chains simultaneously, each one starting from a different location. Although each chain will use the same imaging parameters, the different starting locations will result in somewhat different final images. One can then

Figure 4.1: Example reconstructions of a model RSG, along with the source image.

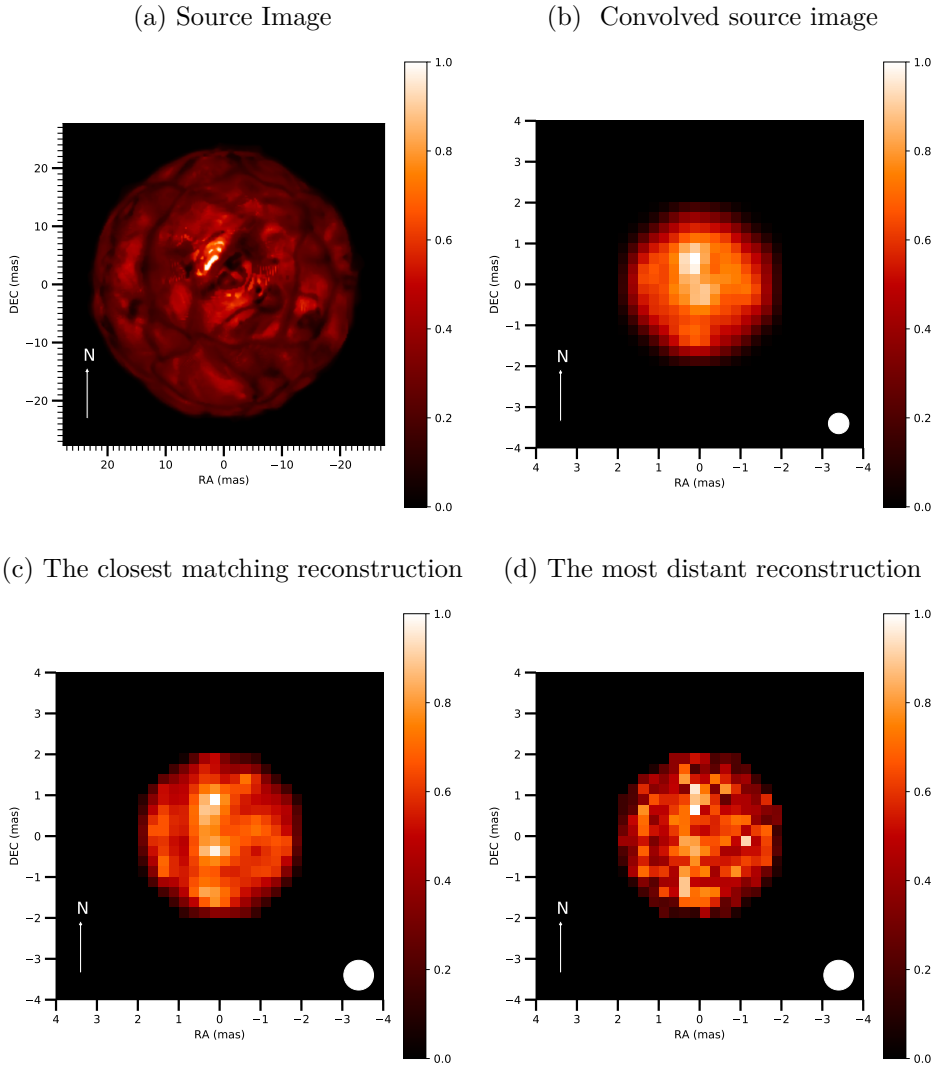

Results of the experiment to find the best reconstruction for the 2011 AZ Cyg data. The source image is a snapshot of a 3D RHD simulation of Betelgeuse from Chiavassa et al. (2010a). The convolved image is scaled to 0.25 mas pixel^{-1} and rebinned to match a 4 mas star. The closest matching reconstruction, has an ℓ_1 norm = 0.014. The most distant reconstruction has an ℓ_1 norm = 0.016. All images are scaled to their maximum pixel intensity. The beamsize is depicted in the lower right. For the convolved image it is based on the resolution we convolved to. For the reconstructions the beamsize is based on the maximum projected baseline of each dataset.

use this stack of results to produce a mean and standard deviation image resulting from the full set of reconstruction chains. This information provides an idea of the spread in reconstruction results and can offer guidance on interpreting the results within the limits of the reconstruction technique.

To find errors from the reconstruction process, we run SQUEEZE on many chains (at least 5) with the same parameters as those used to make the image with lowest ℓ_1 norm in the simulation experiment described above. After this, we align the stack of mean images from each chain using subpixel registration and calculate a mean image and a standard deviation image from the stack.

In order to account for artifacts from $(u,\ v)$ coverage, we also test our reconstructions using a simulation of a uniform disk. First, we generate an image of a uniform disk of the same diameter as whatever star we want to reconstruct. Then, we use our simulation tool to make a simulated observation of this image with the same $(u,\ v)$ coverage and noise statistics as our real data. We then input this simulated observation into SQUEEZE using exactly the same parameters as we used to reconstruct the star and follow the procedure for determining a mean and standard deviation image from the resulting stack of images. Hopefully the result comes out mostly like a uniform disk! If there is a notable feature in the image resulting from this reconstruction that matches something also found in the reconstruction of the real star, we should not trust the feature and note this in any analysis.

4.2 Images of Red Supergiant Stars

The procedure we used for imaging the RSGs in this study was the same as described in Section 4.1.1. First we found the optimal reconstruction parameters using an H-band snapshot of a 3D RHD simulation of Betelgeuse as presented in Chiavassa et al. (2010a). The parameters of this simulation are presented in Table 4.1 and the snapshot, as well as a convolved and rebinned version of the snapshot are presented in Figure 4.1.

Table 4.1: Parameters of source image simulations

M ($M_\odot$)	L ($L_\odot$)	R ($R_\odot$)	$T_{\rm eff}$ (K)	$\log(g)$	Grid (N points)	Grid res. [$R_\odot$]
12	93000±1300	832.0±0.7	3490± 13	-0.337±0.001	235^3	8.6

Parameters for the 3D model (Chiavassa et al. 2010a) from which we took a snapshot to generate simulated observations.

In every case, we reconstructed the simulated data at 0.25 mas pixel^{-1} and 32x32 pixels. We selected 0.25 mas pixel^{-1} because this is roughly $\lambda/4B$ for the maximum projected baseline of most of the data, which is the standard "super-resolution" used for reconstructing interferometric images. Renard et al. (2011) suggested that one could achieve super-resolution of $\lambda/6B$, but this was for extensive (u, v) coverage, which our data lack.

To optimize our regularizations, we produced a grid of reconstructions using simulated observations for each data set. We ran SQUEEZE using 1500, 2500, 3000, and 3500 elements. We tested the uniform disk (UD) regularizer, a ℓ_0 regularizer, a Laplacian (LA) regularizer, a total variation (TV) regularizer, and our specially designed "edge" regularizer using 7

different hyperparameter strengths of 0.1, 0.3, 0.5, 1, 1.5, 2,and 2.5 times the "optimal scale" of each regularizer, which was 1 for the UD and ℓ_0 regularizers and 1000 for the others. Our grid ran for 250 iterations on 5 chains. To help constrain the images, we used masks to keep pixels within a space slightly larger (usually 2 pixels) than the measured uniform disk size for the simulated data. We also initialized the reconstruction using an initial image derived from a χ^2 fit of the simulated data to a limb darkened disk described by the Hestroffer power law in Equation 3.1. Moreover, because we were using a mask, we turned off the image center regularizer, which varies the central starting point, in all our reconstructions.

We then followed the procedure described in Section 4.1.2 to find the best reconstructions. The reconstruction with the lowest ℓ_0 norm to the convolved snapshot gave us the regularizers, number of elements, and hyperparameters to use in our reconstructions using real data.

4.2.1 AZ Cyg

AZ Cyg was first observed using MIRC by Kiss et al. (2010). These and other data taken by John Monnier with MIRC when it was a four telescope combiner are what spurred further observations when MIRC was able to use all six telescopes. In this study, we used archival MIRC data taken by Fabien Baron in 2011, 2012, and 2014. We also obtained observations of our own in 2015 August, 2015 October, 2016 August, and 2016 October. None of the observations from October yielded enough data to reconstruct images.

We present the reconstruction parameters used for reconstructing images of AZ Cyg from 2011 to 2016 in Table 4.2. In every reconstruction, we used 4500 elements and ran for 500

iterations with 10 chains on a 64x64 grid at a resolution of 0.125 mas/pixel. For producing the reconstructed images, we used the best fitting Hestroffer power law limb darkened disk as a prior image and a Gaussian blurred disk of 3.75-4.25 mas as an initial image. Thus, we differed slightly from the optimization experiment described in Section 4.1. We did this because we found that a 32x32 grid at 0.25 mas/pixel was of insufficient resolution for the contrast and granulation scale measurements we will detail later in this chapter. When we compared these images to those produced at lower resolution and with less elements but otherwise the same reconstruction parameters, we did not find major differences in the appearance of the final images.

Table 4.2: Parameters used in the SQUEEZE reconstructions of AZ Cyg.

Year	Regularizers	Hyperparameters	χ^2
2011	TV, L0	1000, 0.3	2.06
2012	LA, L0	2500, 0.3	4.89
2014	LA, TV	2500, 500	2.36
2015	LA, TV	2500, 1500	4.09
2016	LA, TV	300, 2000	4.80

Parameters and reconstruction details for SQUEEZE reconstructions of AZ Cyg.

After running the reconstructions, we calculated mean and standard deviation images from the mean result of each chain. We present the resulting mean and standard deviation images, along with the (u, v) coverage of the data in Figure 4.2. The standard deviation

images do not show most of the major features found in the mean images and are at an intensity significantly below that of the mean images. Thus, we do not think the features in the mean images are artifacts from the reconstruction process. In Table 4.2 we present the χ^2 of each image as compared to the squared visibility, triple amplitude, and closure phase of the observations. We also present comparisons between the squared visibility and closure phases of the data and those derived from the reconstructed images in Appendix B.

In order to test for artifacts from the reconstruction process, we also simulated observations of a uniform disk, copying the (u, v) coverage and noise statistics of each dataset to make the simulated observation. We then reconstructed images using those simulated data, using exactly the same parameters (regularizers, hyperparameters, number of elements, etc.) as we used with the corresponding real data. These images do not look like the images produced using the real AZ Cyg data, which suggests that features in the images of AZ Cyg are not the result of a bias in the (u, v) coverage. We present these reconstructed images in Figure 4.3.

In addition, we used OITOOLS.jl to reconstruct images using our data in order to confirm that our results could be replicated using a different image reconstruction technique. To make these images, we reconstructed on a 32x32 grid at 0.25 mas resolution and used an initial image corresponding to best fitting Hestroffer power law limb darkened disk and masks of 4-4.25 mas in order constrain pixels. For these reconstructions we used a total variation regularizer and a centering regularizer. We present those images in Figure 4.4.

In general, the images produced with OITOOLS.jl look similar to those produced with

Figure 4.2: Results of image reconstruction with SQUEEZE for AZ Cyg

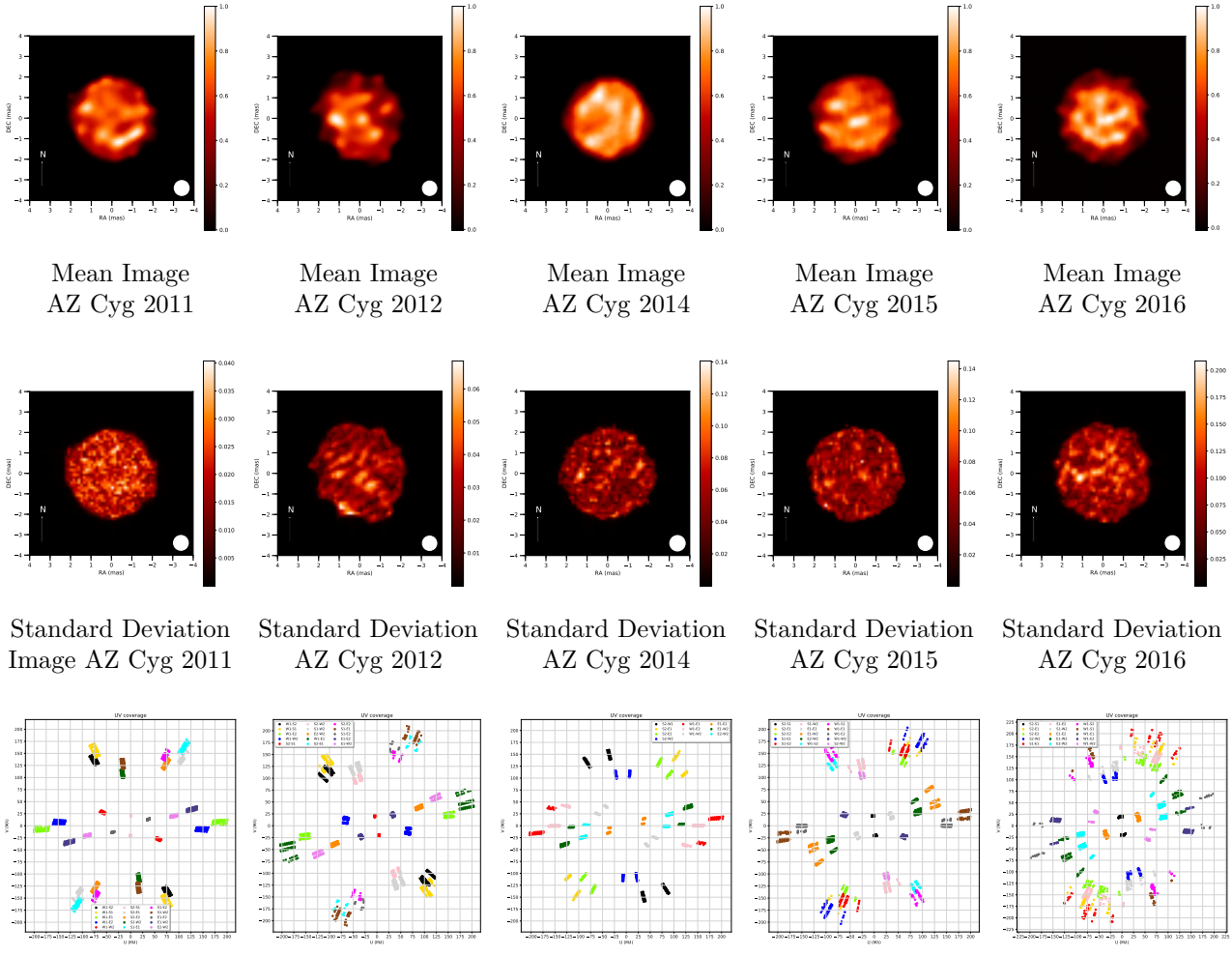

Mean images of AZ Cyg from 2011-2016 produced with 10 chains on SQUEEZE, along with the standard deviation of the 10 chains, and the (u,v) coverage of each epoch. The mean image intensity is scaled to the maximum pixel in each image and the standard deviation images are scaled to the maximum intensity in the corresponding mean image. The beamsize is depicted in the lower right and is based on the maximum projected baseline of each dataset.

SQUEEZE. The most prominent features and patterns in the 2011 and 2014 features appear in both the OITOOLS.jl and SQUEEZE reconstructions, with differences likely attributable

Figure 4.3: Image reconstruction with SQUEEZE of a uniform disk copied from AZ Cyg observations.

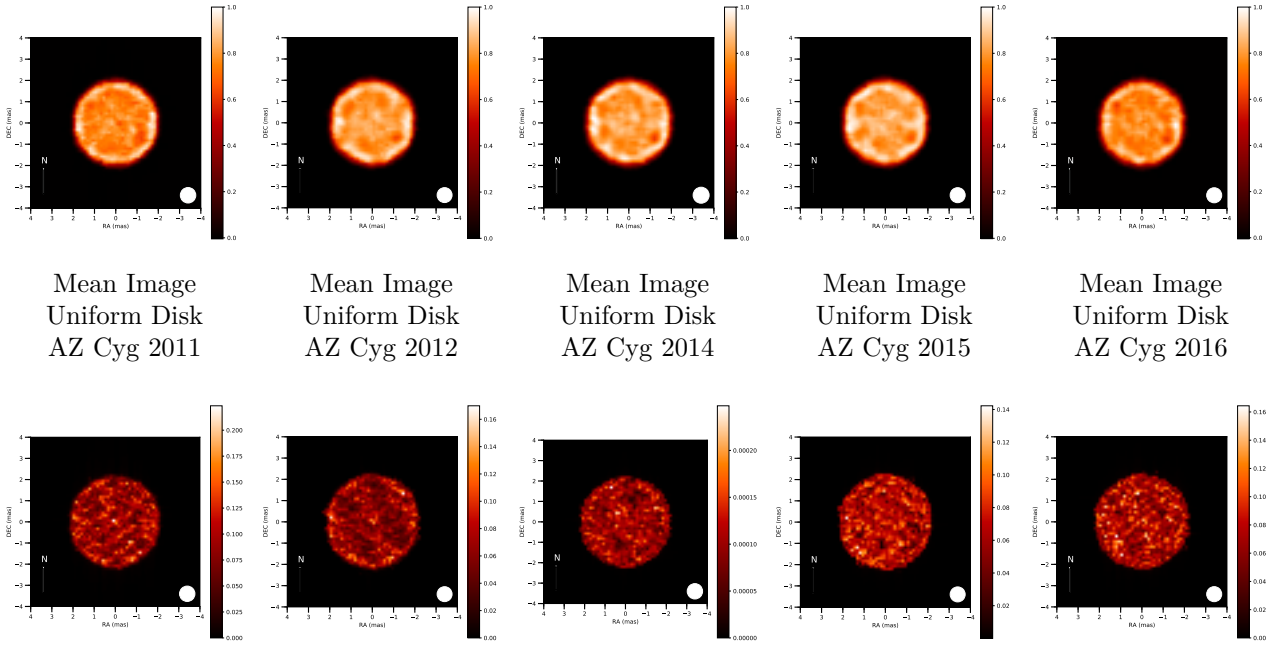

Mean Image Uniform Disk AZ Cyg 2011 | Mean Image Uniform Disk AZ Cyg 2012 | Mean Image Uniform Disk AZ Cyg 2014 | Mean Image Uniform Disk AZ Cyg 2015 | Mean Image Uniform Disk AZ Cyg 2016

Standard Deviation Image Uniform Disk AZ Cyg 2011 | Standard Deviation Image Uniform Disk AZ Cyg 2012 | Standard Deviation Image Uniform Disk AZ Cyg 2014 | Standard Deviation Image Uniform Disk AZ Cyg 2015 | Standard Deviation Image Uniform Disk AZ Cyg 2016

Mean and standard deviations images of a simulated uniform disk reconstructed using SQUEEZE on 10 chains and with data copied from each epoch of AZ Cyg observations. The mean images are scaled to their maximum intensity and the standard deviation images are scaled to the corresponding mean image. The beamsize is depicted in the lower right and is based on the maximum projected baseline of each dataset.

to differences in regularizers. The 2015 OITOOLS.jl image appears to be over-regularized but testing different hyperparameters did not yield strong differences. Nonetheless, we can see that the dark region in the west is present in both the SQUEEZE and OITOOLS.jl reconstructions, as are the central bright region and the bright region in the northwest. The 2016 OITOOLS.jl image appears significantly cleaner than the SQUEEZE reconstruction and we will defer to it for interpretation of the star during this epoch.

Figure 4.4: Images of AZ Cyg produced with OITOOLS.jl,

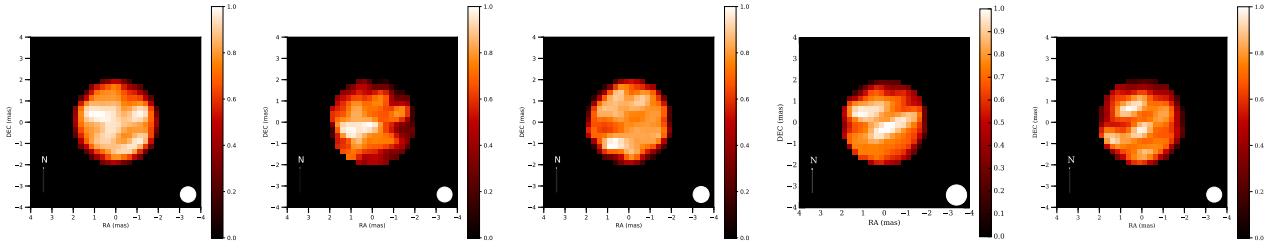

OITOOLS.jl Image AZ Cyg 2011 | OITOOLS.jl Image AZ Cyg 2012 | OITOOLS.jl Image AZ Cyg 2014 | OITOOLS.jl Image AZ Cyg 2015 | OITOOLS.jl Image AZ Cyg 2016

Reconstructions of AZ Cyg produced with OITOOLS.jl. Each image is scaled to its maximum intensity pixel. The beamsize is depicted in the lower right and is based on the maximum projected baseline of each dataset.

As depicted in Figures 4.2 and 4.4 the surface of AZ Cyg is non-uniform and consists of features of varying size and intensity. The 2012 data appears to have a calibration issue and interpretation of the image is likely not possible. However, by considering the other images, we see that surface varies from year to year. The images we present use all wavelength channels, but in a forthcoming paper we will also investigate the possibility of a wavelength dependence on surface appearance by reconstructing images using data from individual channels. In the reconstructions of the simulated observation of a 3D RHD model in Figure 4.1, the brightest regions correspond to rising granules in the simulations, while the dark regions correspond to inter-granular lanes of in-falling gas. The medium intensity, orange regions correspond to portions of convection cells without the presence of bright granules.

Relating this to the reconstruction of the 2011 observations, it would seem that there was a granule in the southeast of AZ Cyg, which like 3D RHD simulations of RSGs was boarded by a dark region of in-falling gas. In addition, there appeared to be one or two bright granules

in the west limb of the star. There also appeared to be several larger features on the star, possibly convection cells, depicted by medium intensity regions.

In 2014, the surface of AZ Cyg appears very different. As granules are expected to have lifetimes on the order of 100s of days, the disappearance of the smaller features is unsurprising. This time, there appears to be a bright feature in the northwest, as well as features in the southwest and east. We note that rotation periods of RSGs are on the order of 20 years (Gray 2000), so the similarity of the northwest feature in 2014 to the southeast feature in 2011 is likely a coincidence, unless they are both artifacts of the image reconstruction technique we have applied. The most notable difference between the 2011 and 2014 images is that there appears to be fewer dark regions. Instead we see a large medium intensity region in the south, one in the east, and one in the north.

It appears that the surface of AZ Cyg in 2015 maintains some of the pattern from 2014. There is still a dark region in the west and a large bright region in the south. The eastern and north bright features are no longer present. Likewise, there are new bright regions, this time in the center and northwest.

The 2016 observation had the most extensive (u, v) coverage and thus we expect it to have achieved the highest level of detail. Focusing only on the OITOOLS.jl reconstruction in Figure 4.4 because of the poor quality of the SQUEEZE reconstruction, we see several bright regions. The central bright region and the northwest bright region have persisted from 2015 and a new bright region in the southwest has appeared. The overall intensity pattern shows that the dark region in the west has persisted and the medium intensity regions remain in

roughly the same location. In this reconstruction, we can more clearly see the boundaries between regions and it appears that the star has four or five regions that seem analogous to the convection cells in the reconstructions in Figure 4.1.

This superficial visual interpretation suggests that in AZ Cyg there are up to five convection cells visible on the surface at any given time, which is in line with the suggestion from Chiavassa et al. (2010a) that convection cells are roughly 0.5 R_* in size. If these are cells, their lifetime would be more than one or two years, given that features persisted from 2014-2016. On the other hand, there are also small granule-like features that are on the order of 0.1 R_* and these last less than two years. This too is in line with predictions for small features in RSGs given by photometry (Chatys et al. 2019) and spectroscopy (Gray & Pugh 2012). Most of the MIRC wavelength coverage is in a continuum region of the H-band, However, we stress that because we are looking at an image produced with data from all wavelength channels combined, it is possible that we are simultaneously looking at the surface and at cooler regions of the atmosphere if one or more of the wavelength channels includes a region of the spectrum with molecular lines. If this is the case, than the brighter regions could correspond to portions of the upper atmosphere where hot surface regions are visible. In this case, the bright regions could correspond to regions of more active convection. In Section 4.3 we will attempt to analyze these images in a more rigorous manner and offer measurements of the scale of the bright features and the contrast variation across the surface.

4.2.2 SU Per

We first observed SU Per in 2015 August. During our first nights of observing, we found that the star had an angular diameter between 3.0 and 4.0 mas and that it showed evidence of asymmetries in its closure phases. It was easy to find and record fringes on the target, so we decided to use this star as a long and short-term imaging target.

We present the reconstruction parameters used for reconstructing images of SU Per in 2015 and 2016 in Table 4.3. In every reconstruction, we used 4500 elements and ran for 500 iterations with 10 chains on a 64x64 grid at a resolution of 0.125 mas/pixel. For producing the reconstructed images, we used the best fitting Hestroffer power law limb darkened disk as a prior image and a Gaussian blurred disk of 3.25 mas as an initial image. Thus, we differed slightly from the optimization experiment described in Section 4.1. We did this because we found that a 32x32 grid at 0.25 mas/pixel was of insufficient resolution for the contrast and granulation scale measurements we will detail later in this chapter. When we compared these images to those produced at lower resolution and with less elements but otherwise the same reconstruction parameters, we did not find major differences in the appearance of the final images.

Table 4.3: Parameters used in the SQUEEZE. reconstructions of SU Per.

Year	Regularizers	Hyperparameters	χ^2
2015 Aug	LA, UD	2500, 1.2	3.36
2016 Aug	LA, TV	1000, 500	4.28
2016 OCT	LA, TV	1000, 500	2.50

Parameters and reconstruction details for SQUEEZE reconstructions of SU Per.

After running the reconstructions, we calculated mean and standard deviation images from the mean result of each chain. We present the resulting mean and standard deviation images, along with the (u,v) coverage of the data in Figure 4.5. We also present comparisons between the squared visibility and closure phases of the data and those derived from the reconstructed images in Appendix B.

In order to test for artifacts from the reconstruction process, we also simulated observations of a 3.5 mas uniform disk using each dataset and reconstructed images using those simulated data under exactly the same conditions as used with the corresponding real data. We present these reconstructed images in Figure 4.6.

We also used OITOOLS.jl to reconstruct images using our data in order to confirm that our results could be replicated using a different image reconstruction technique. To make these images, we reconstructed on a 32x32 grid at 0.25 mas and used an initial image corresponding to best fitting Hestroffer power law limb darkened disk and masks of 3-3.5 mas in order constrain pixels. For these reconstructions, we used a total variation regularizer

Figure 4.5: Results of image reconstruction with SQUEEZE for SU Per.

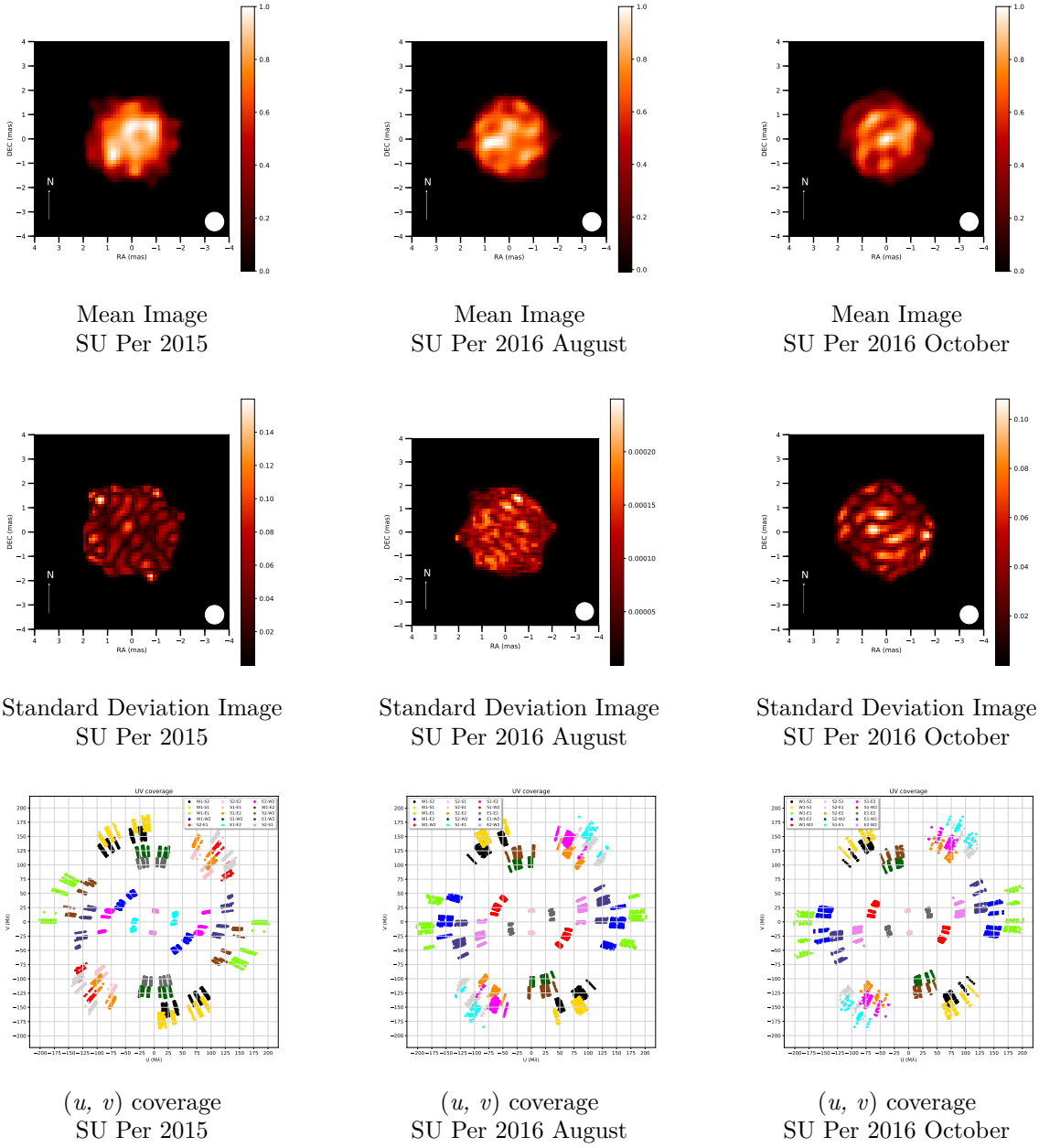

Mean Image
SU Per 2015

Mean Image
SU Per 2016 August

Mean Image
SU Per 2016 October

Standard Deviation Image
SU Per 2015

Standard Deviation Image
SU Per 2016 August

Standard Deviation Image
SU Per 2016 October

$(u,\ v)$ coverage
SU Per 2015

$(u,\ v)$ coverage
SU Per 2016 August

$(u,\ v)$ coverage
SU Per 2016 October

Mean images of SU Per from 2015 and 2016 produced with 10 chains on SQUEEZE, along with the standard deviation of the 10 chains, and the (u,v) coverage of each epoch. The mean image intensity is scaled to the maximum pixel in each image and the standard deviation images are scaled to the maximum intensity in the corresponding mean image. The beamsize is depicted in the lower right and is based on the maximum projected baseline of each dataset.

Figure 4.6: Image reconstruction with SQUEEZE of a uniform disk copied from SU Per observations.

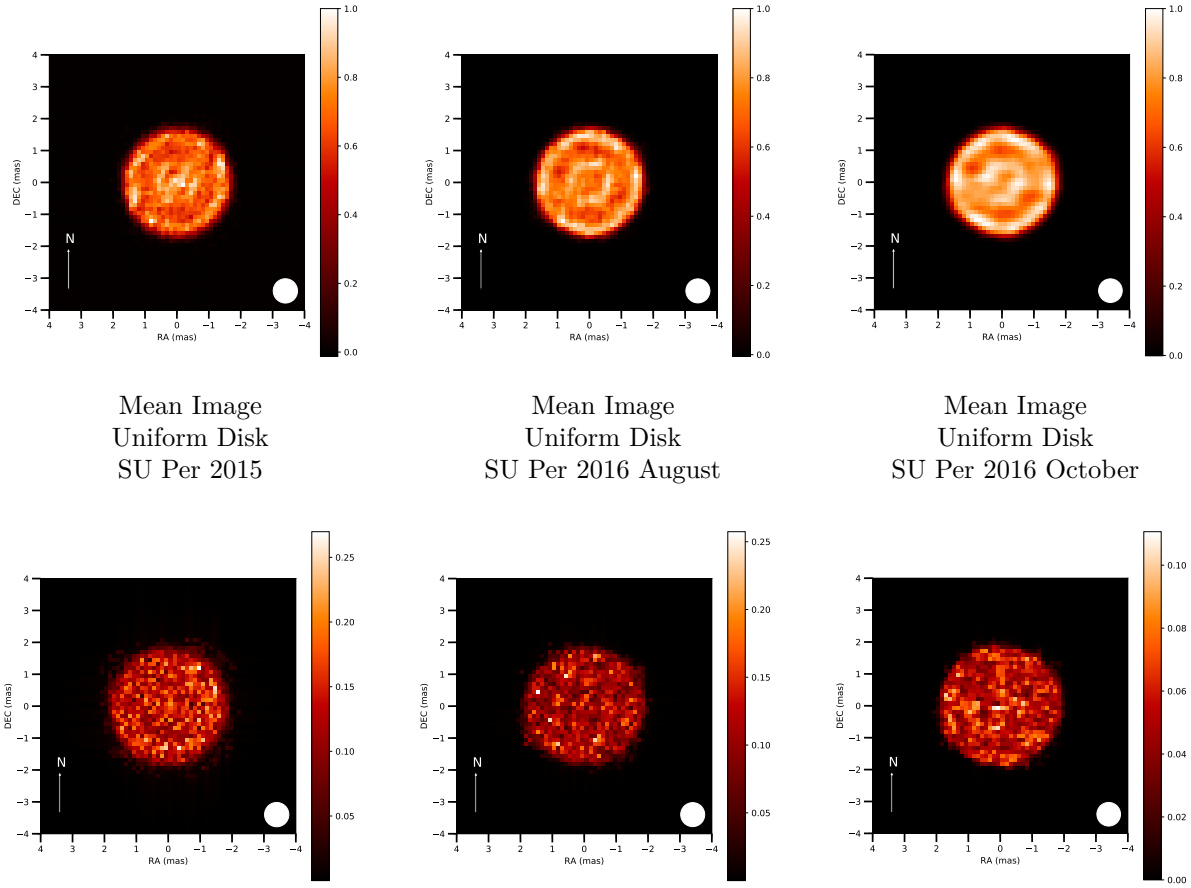

Mean Image
Uniform Disk
SU Per 2015

Mean Image
Uniform Disk
SU Per 2016 August

Mean Image
Uniform Disk
SU Per 2016 October

Standard Deviation Image
Uniform Disk
SU Per 2015

Standard Deviation Image
Uniform Disk
SU Per 2016 August

Standard Deviation Image
Uniform Disk
SU Per 2016 October

Mean and standard deviation images of a simulated uniform disk reconstructed using SQUEEZE on 10 chains and with data copied from each epoch of SU Per observations. The mean images are scaled to their maximum intensity and the standard deviation images are scaled to the corresponding mean image. The beamsize is depicted in the lower right and is based on the maximum projected baseline of each dataset.

and a centering regularizer. We present those images in Figure 4.7.

Figure 4.7: Images of SU Per produced with OITOOLS.jl,

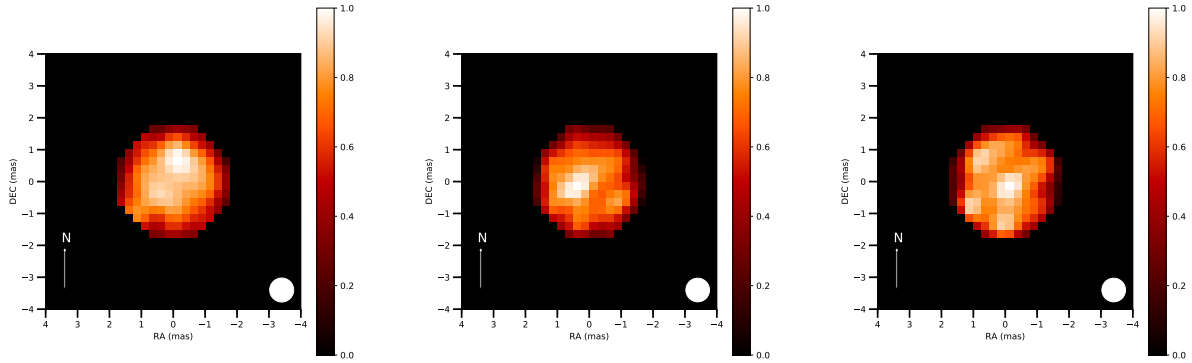

OITOOLS.jl Image
SU Per 2015

OITOOLS.jl Image
SU Per 2016 August

OITOOLS.jl Image
SU Per 2016 October

Reconstructions of SU Per produced with OITOOLS.jl. Each image is scaled to its maximum intensity pixel. The beamsize is depicted in the lower right and is based on the maximum projected baseline of each dataset.

Unfortunately, the images of SU Per are significantly noisier than those of AZ Cyg, despite the excellent (u, v) coverage of these observations. Nonetheless, we can make some comments on the appearance of the stars and the possibility of changes in surface appearance related to convective activity in the star. First, note that the standard deviation images do not show features that are present in the mean images, although they do show more variation and pixels of higher relative intensity than those in the AZ Cyg images. The reconstructions of simulated uniform disks appear to show a signature indicative of the (u, v) coverage, but as these patterns are not present in the mean images of the real data, we can feel confident in interpreting features as surface features and not artifacts. However, the comparisons of data to models in Appendix B show that the reconstructions do not fit the data very well

at higher frequencies where surface features are most likely to manifest. Thus, we should be cautious in interpreting these images.

The 2015 image of SU Per shows a bright pattern in the northeast portion of the star and a bright feature in the southwest. The irregular surface edge is likely not real but rather an artifact of the image reconstruction process. Although it is a lower resolution image, the OITOOLS.jl reconstruction of these data shows two bright features in similar locations. Based on the interpretation used in Section 4.2.1, we can surmise that the star had one or two large cells, with prominent granules manifesting as the bright features noted above.

The 2016 August reconstruction of SU Per is significantly better in appearance than the 2015 image. To produce the SQUEEZE image in Figure 4.5, we did not use the entirety of the 2016 August data but limited it to August 28 and 29 and September 7,9, and 11. Using data collected on the other days prevented the reconstruction with SQUEEZE from converging. We did use the entire dataset to produce the OITOOLS.jl reconstruction, which converged more easily than the SQUEEZE reconstruction. In both images, there appears to be a bright central granule and less intense feature in the southeast. The higher resolution SQUEEZE reconstruction shows a pattern similar to what was found in AZ Cyg with dark features, such as the one in the northeast, boarding larger regions of medium intensity within which are smaller high intensity regions. The surface appears more varied than found in AZ Cyg, with numerous small features and diversity in intensity within what we surmise are convection cells. There appears to be a central feature which persisted from 2015, although the bright features in the 2015 image are no longer present. In addition to this major feature which is

roughly 0.5 R_* in size, there are other features in the northeast, northwest, and southwest.

The SQUEEZE reconstruction 2016 October data is of poor quality, although we can see evidence of some of the same pattern as was found in the 2016 August data. Focusing on the OITOOLS.jl reconstruction, we see a similar, albeit lower resolution, appearance to the 2016 August image. There is a central bright region, and features in the northwest, southwest, and south. There do not appear to be major changes in the surface appearance between the two epochs. This suggests that any study of short-term evolution in RSGs needs to be longer than one or two months in length.

4.3 Analysis of Images

Because 3D RHD models are so computationally expensive, there are still very few 3D models of RSGs available to help us interpret our images. Nonetheless, there are several studies using 2D and 3D models which have proven useful in interpreting images of evolved stars, including RSGs. Freytag et al. (1997) used 2D radiative hydrodynamics (RHD) models, Trampedach et al. (2013) used the Stein & Nordlund (1998) code, Tremblay et al. (2013) used CO^{5}BOLD and CFIRST RHD models, and Chiavassa et al. (2009) used CO^{5}BOLD in star-in-a-box mode, a setup more apt to RSGs than the box-in-a-star setup used by the other models in this list.

Tremblay et al. (2013) offers the root-mean-square (rms) relative intensity contrast ratio (referred to as constrast throughout the rest of this manuscript) as a way of measuring deviation from a plane-parallel approximation. This can be a proxy for the strength of

convection in a star, as Trampedach et al. (2013) noted that 3D models with the highest contrast were those with the least efficient convection.

$$\frac{\delta\ I_{\rm rms}}{< I >} = \left\langle \frac{\sqrt{< I(x,y,t)^2 >_{x,y} - < I(x,y,t) >^2_{x,y}}}{< I(x,y,t) >_{x,y}} \right\rangle_t \tag{4.5}$$

Tremblay et al. (2013) shows that stars with high contrast have larger Mach numbers, which is the ratio of the flow and sound speeds. The intensity contrast ratio is also correlated with density, with lower densities corresponding to higher contrasts. Because there is also correlation between temperature and density in a star, such that lower temperature stars have lower densities, we expect a correlation between temperature and intensity contrast, with lower temperatures corresponding to larger intensity contrast ratios.

We present the intensity contrasts we derived for AZ Cyg and SU Per in Tables 4.4 and 4.5. We find that our contrast ranges from 8.00% to 12.00% in AZ Cyg and 9.00% to 15.5% in SU Per. Paladini et al. (2018) found contrasts of 11.9 ± 0.4 to 13.1±0.2% for an AGB of $T_{\rm eff} = 3200\ K$ and $\log(g) = -0.4$. Montargès et al. (2018) found contrasts of 5 to 6% for the RSG CE Tau with $T_{\rm eff} = 3820 \pm 135\ K$ and $\log(g) = 0.05^{+0.11}_{-0.17}$. Wittkowski et al. (2017) found a contrast of 10±4% for the RSG V776 Cen with $T_{\rm eff} = 4290 \pm 760\ K$. Thus, our contrasts fall within the range of those found around similar stars.

Table 4.4: Derived Surface Properties of AZ Cyg.

Year	Contrast	$x_{\rm gran}$(mas)
2011	12.0%	1.17
2014	8.0%	1.08
2015	10.5%	1.02
2016	10.2%	1.08

Table 4.5: Derived Surface Properties of SU Per

Year	Contrast	$x_{\rm gran}$ (mas)
2015	9.0%	0.91
2016 August	12.0%	1.01
2016 October	15.5%	1.25

Tremblay et al. (2013) and Trampedach et al. (2013) suggest measuring the characteristic size of surface convection, $x_{\rm gran}$, in 3D models using 2D power spectra of intensity maps generated from these models. A similar method was used by Paladini et al. (2018) to measure $x_{\rm gran}$ on the AGB π^1 Gruis using images reconstructed from Very Large Telescope Interferometer (VLTI) data. In order to measure $x_{\rm gran}$ on AZ Cyg and SU Per, we apply this technique to analyzing the mean SQUEEZE reconstructions we presented in Figures 4.2 and 4.5. Using code provided by Claudia Paladini, we derived the 2D spatial power spectra of each final mean SQUEEZE image and filtered the disk edge out of the images. We filtered the images by setting the pixel values of the portion of each image outside of the stellar disk

equal to the median flux of the pixels within the star. This smoothed the sharp boundary at the edge of the star and allowed us to detect the smaller features within the disk of the star. To make the analysis easier, we also padded this filtered image by 200 pixels. The characteristic size of granulation ($x_{\rm gran}$) was identified as the remaining peak in the power spectrum. $x_{\rm gran}$ is listed in Tables 4.4 and 4.5. We present the power spectra in Figures 4.8 and 4.9. We find that AZ Cyg has $x_{\rm gran}$ of 1.02 to 1.17 mas and SU Per 0.91 to 1.25 mas. We did not perform this measurement on the AZ Cyg 2012 image due to its poor quality.

Although there are few 3D models to compare our images to, we can compare our results to theoretical predictions. Freytag et al. (1997), Trampedach et al. (2013), and Tremblay et al. (2013) found that $x_{\rm gran}$ is proportional to scale pressure height, H_p. This relation arises because the mixing length is proportional to H_p in current theories of convection. Scaling from observations of the Sun, Freytag et al. (1997) derived the relation $H_p = RT_{\rm eff}/g$ with R the universal gas constant, which they rewrote as

$$\frac{x_{\rm gran}}{R_*} \approx\ 0.0025\ \frac{R_*}{R_\odot}\frac{T_{\rm eff,*}}{T_{\rm eff,\odot}}\frac{M_\odot}{M_*}. \tag{4.6}$$

On the other hand, Tremblay et al. (2013) derived a different relation using least squares fits of stellar parameters to $x_{\rm gran}$ as determined using power spectra of 3D models:

$$\frac{\text{Char.size}}{[\text{km}]} = 13.5 g^{-1}[T_{\rm eff} - 300\log(g)]^{1.75} 10^{0.05[Fe/H]}. \tag{4.7}$$

Applying a similar method, Trampedach et al. (2013) found (likewise in cgs units):

Figure 4.8: Power Spectra of AZ Cyg SQUEEZE images

(a) AZ Cyg 2011

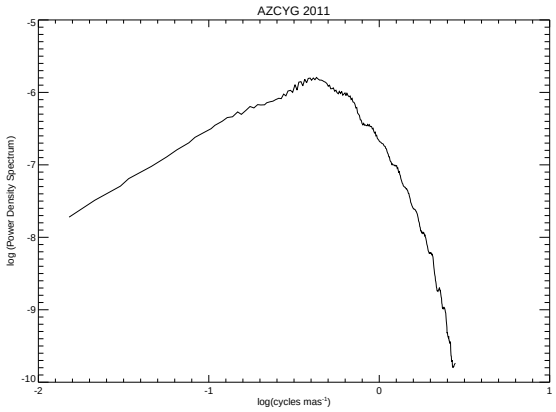

(b) AZ Cyg 2014

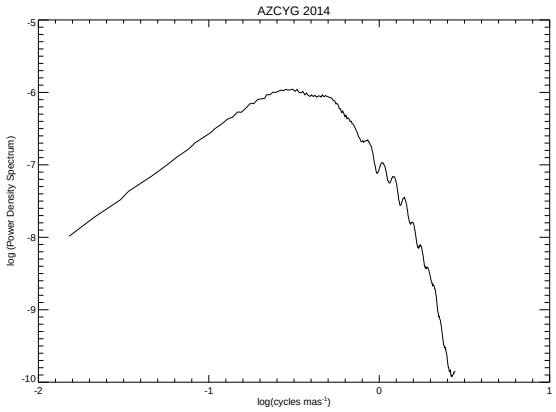

(c) AZ Cyg 2015

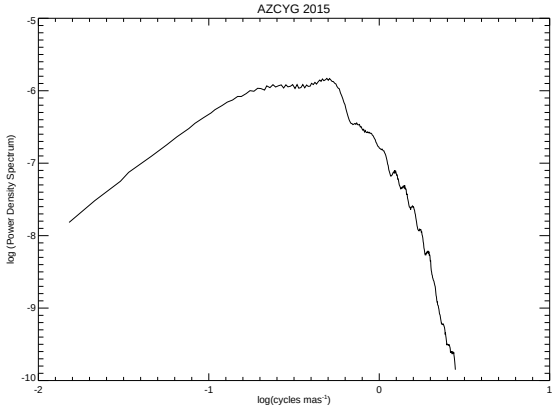

(d) AZ Cyg 2016

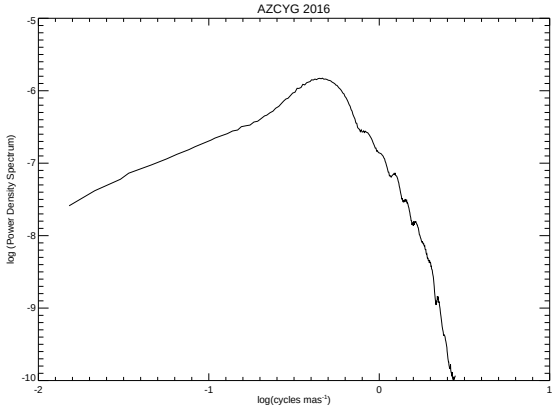

Power spectra of the reconstructed images of AZ Cyg with limb darkened disk edge filtered out.

Figure 4.9: Power Spectra of SU Per SQUEEZE images

(a) SU Per 2015 (b) SU Per 2016 August (c) SU Per 2016 October

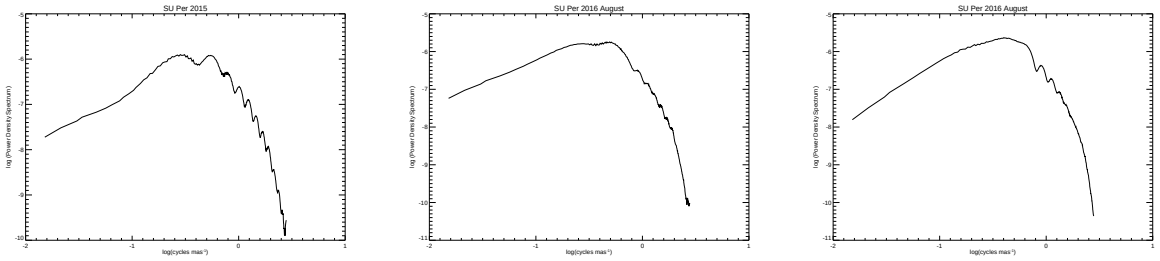

Power spectra of the reconstructed images of SU Per with limb darkened disk edge filtered out.

$$\log\frac{A_{\rm gran}}{[Mm]} \simeq (1.310 \pm 0.0038) \times \log(T_{\rm eff}) \tag{4.8}$$
$$-(1.0970 \pm 0.003) \times \log(g) + 0.0306 \pm 0.359$$

where the uncertainties come from the error on the fits to their power spectra.

On the other hand, using 3D RHD models of red supergiants, Chiavassa et al. (2009) found that the equation of Freytag et al. (1997) needed modification to account for turbulent pressure. Instead they proposed:

$$H_p = \frac{kT_{\rm eff}}{g\mu m_H}(1 + \beta\gamma(\frac{v_{turb}}{c_s})^2) \tag{4.9}$$

with β a parameter close to one, γ the adiabatic exponent, c_s the sound speed, and v_{turb} the turbulent velocity. Based on models of RSGs, they suggested that with $P_{turb}/P_{gas} \sim 2$, as is

roughly the case in RSGs, H_p would be five times larger and thus a better proportionality would would be to multiply the predictions of Equation 4.6 by five. This matched the size of large convection features predicted by the 3D RHD models in Chiavassa et al. (2009).

We present the characteristic sizes determined using each equation for x_{gran} in Tables 4.6 and 4.7.

Table 4.6: Derived Surface Properties of AZ Cyg.

Year	$x_{\text{gran, obsv}}$ (R_*)	$x_{\text{gran, Freytag}}$ (R_*)	$x_{\text{gran, Tremblay}}$ (R_*)	$x_{\text{gran, Trampedach}}$ (R_*)	$x_{\text{gran, Chiavassa}}$ (R_*)
2011	0.60	0.07	0.02	0.09	0.35
2014	0.53	0.08	0.02	0.09	0.40
2015	0.50	0.08	0.02	0.09	0.40
2016	0.53	0.08	0.02	0.09	0.40

Table 4.7: Derived Surface Properties of SU Per.

Year	$x_{\text{gran, obsv}}$ (R_*)	$x_{\text{gran, Freytag}}$ (R_*)	$x_{\text{gran, Tremblay}}$ (R_*)	$x_{\text{gran, Trampedach}}$ (R_*)	$x_{\text{gran, Chiavassa}}$ (R_*)
2015	0.48	0.14	0.01	0.06	0.70
2016 August	0.58	0.13	0.01	0.07	0.65
2016 October	0.68	0.13	0.01	0.06	0.65

Comparing the derived values of x_{gran}, we find that the equation which is closest to the values we derived with the power spectra is Equation 4.9. This suggests that the characteristic size of convection we are measuring corresponds to the larger features that Chiavassa et al. (2009) found in the 3D RHD models of RSGs. Paladini et al. (2018) found that the

other equations matched measurements of $x_{\rm gran}$ in an AGB quite well. The fact that we find different values compared to the $x_{\rm gran}$ measured using the power spectra might mean that the other models do not predict the behavior of RSGs well, even if they do manage to reproduce the characteristic size of granules in AGBs, which are even less dense than RSGs. On the other hand, in the images of AZ Cyg and SU Per, we do observe small granules of roughly the size predicted by these other equations. Instead, it may be that these granules are not the feature of convection in RSGs measured by the power spectrum method.

From these results it is clear that images can provide a test of models. However, what is needed are high quality images resulting from data collected over appropriate timescales. Our hope is that this work shows the need for further study of RSGs at high resolution, over short and long timescales. In the coming chapter we summarize our results and offer a suggestion of a future that may offer an unprecedented view of these stars.

CHAPTER 5

Future Directions and Conclusion

5.1 Summary of Results

We have obtained long term observations of two RSGs, AZ Cyg and SU Per. Fitting to model spectra, we derive $T_{\rm eff} = 3989 \pm 117\ K$ and $\log(g) = 0.29 \pm 0.26$ for AZ Cyg and $T_{\rm eff} = 3650 \pm 50\ K$ and $\log(g) = 0.30 \pm 0.26$ for SU Per. The radius of AZ Cyg derived from the Hestroffer power law limb darkened angular diameter and Gaia parallaxes ranges between $856^{+20}_{-14}\ \mathcal{R}^{\rm N}_{\odot}$ and $927^{+21}_{-15}\ \mathcal{R}^{\rm N}_{\odot}$ while for SU Per the radius falls between $1140^{+34}_{-23}\ \mathcal{R}^{\rm N}_{\odot}$ and $1094^{+31}_{-21}\ \mathcal{R}^{\rm N}_{\odot}$. We have reconstructed images from 2011-2016 (excepting 2013) for AZ Cyg and 2015-2016 for SU Per. We find that the imaging is hampered a bit by data quality and most especially by the need for more temporal coverage, a situation that we hope will be alleviated in the future with MIRC-X observations. Analyzing the AZ Cyg and SU Per images, we find evidence of features roughly 50% the radius of the star that may have lifetimes exceeding one or two years, just as predicted by 3D RHD models. We also find short lived granules that are roughly 10% the radius of the star. All of this work would be greatly helped by additional 3D RHD models with which to compare.

5.2 The Near Future of Optical Interferometry

We are on the cusp of a revolution in our ability to study the surfaces of not only RSGs, but many stars with large angular diameters. In the coming decade, improvements to existing interferometers such as the CHARA Array and the Navy Precision Optical Interferometer,

will expand the imaging capabilities of these facilities. In addition, the construction of the Magdalena Ridge Optical Interferometer (MROI), with 8 movable telescopes, will permit imaging of objects at a variety of different scales. The application of additional observables, such as quadrature quantities, made possible by this increase in telescopes will result better calibrations. The combination of other high resolution techniques will offer a multifaceted view of stars. Finally, the development of new imaging technologies including those based on neural networks and perhaps techniques using quantum annealing, will permit reconstructions of even higher resolution and greater fidelity.

As a glimpse to the future, we include a simulation of Betelgeuse observed with MROI. To make this, we received several of the planned telescope configurations for MROI from John Young and selected the one best suited to image a 42 mas star, shown in Figure 5.1. We then simulated an observation of the star covering several hours on several days using a snapshot of the Betelgeuse simulation presented in Chiavassa et al. (2010a) as source image. We reconstructed an image with the simulated data using total variation and Laplacian regularizers on five chains using SQUEEZE. We show the results in Figure 5.2.

Figure 5.1: One of the planned short configurations for MROI

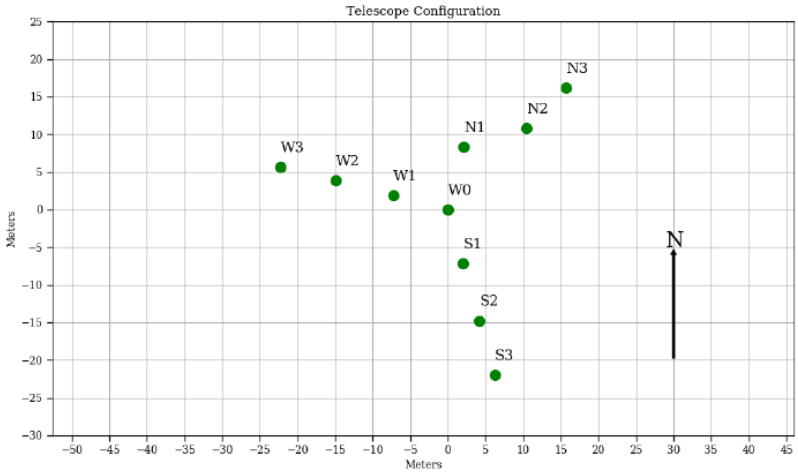

Figure 5.2: Simulation of Betelgeuse as imaged by MROI

(a) Source Image (b) Reconstructed Image

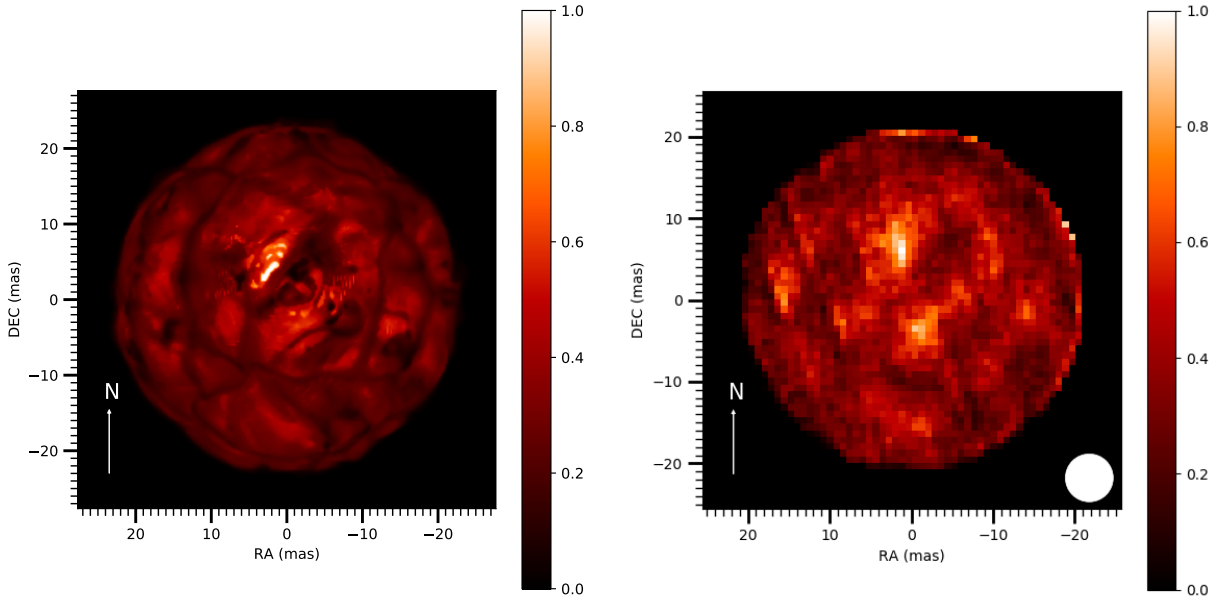

Reconstruction of a simulated observation of Betelgeuse using MROI. Pixels are scaled to the maximum intensity in each image and the beamsize in the lower right hand corner comes from the maximum projected baseline.

Although optical interferometry has many bold goals for the coming decade, it is clear that there is still room for improving our understanding of RSGs. Perhaps in the coming decade, 100 years after Michelson and Pease first observed Betelgeuse we will have the chance to once more change the way we see these and other other stars.

Appendices

A (u, v) coverage, V^2, and Closure Phases for observed stars

A 6 GEM

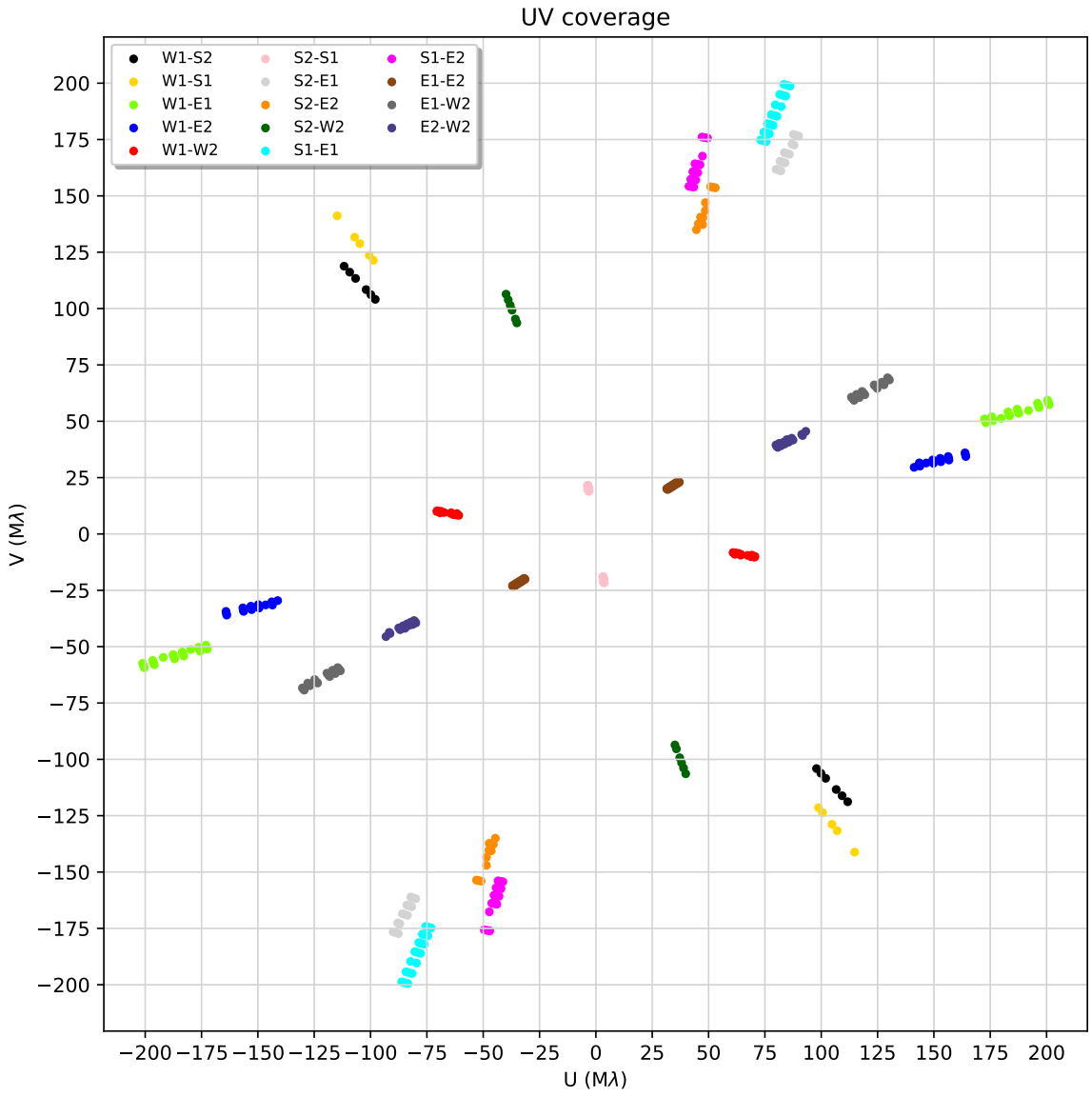

Figure A1: (u, v) coverage for 6 GEM in 2016

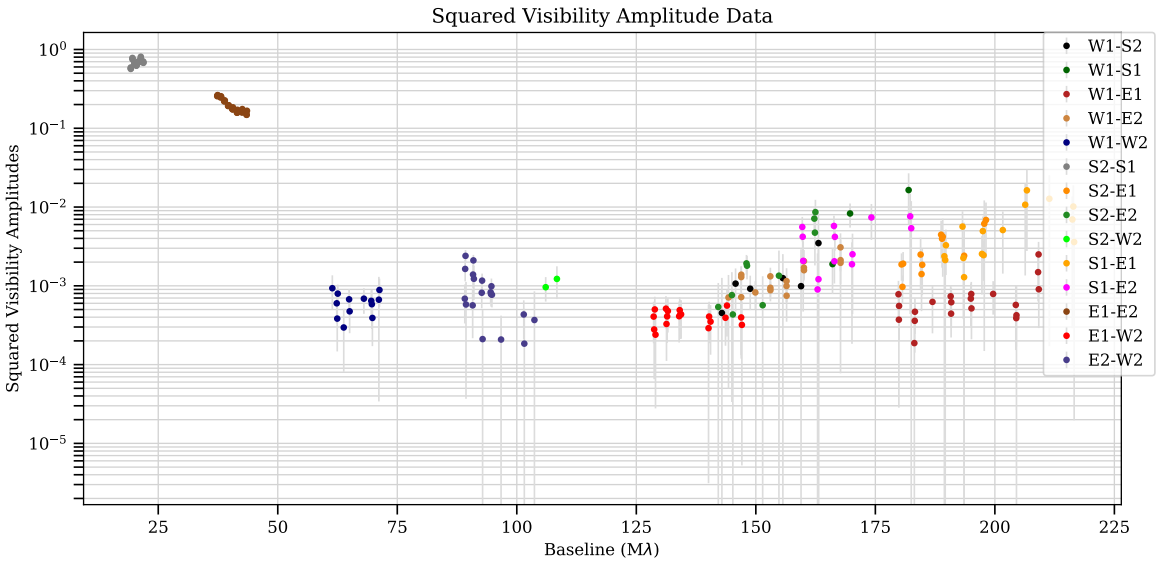

Figure A2: V^2 of 6 Gem in 2016

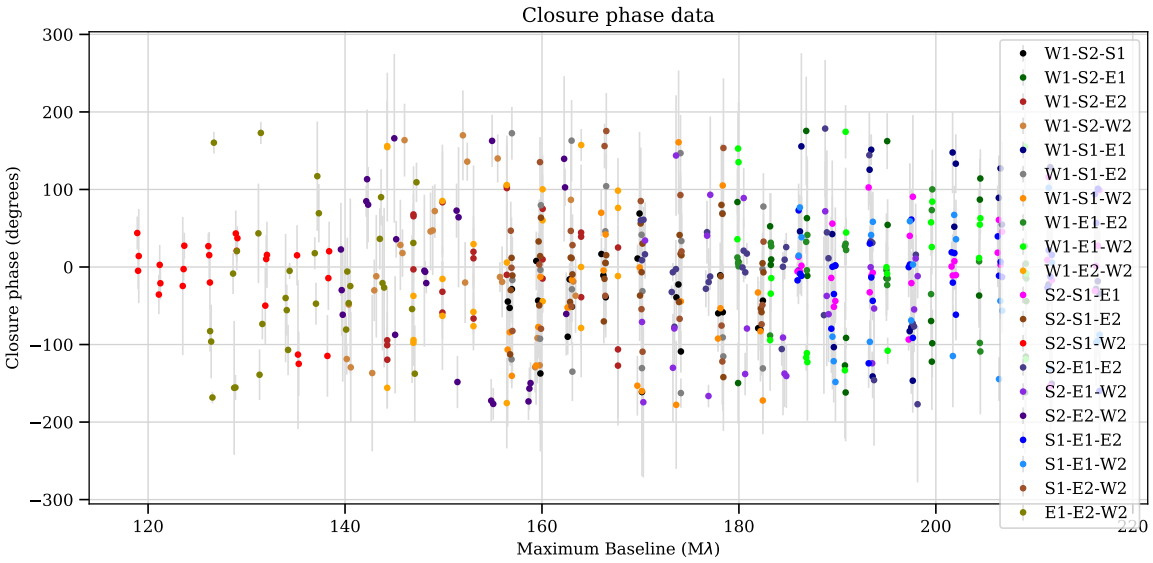

Figure A3: Closure phases of 6 Gem in 2016

B AD Per

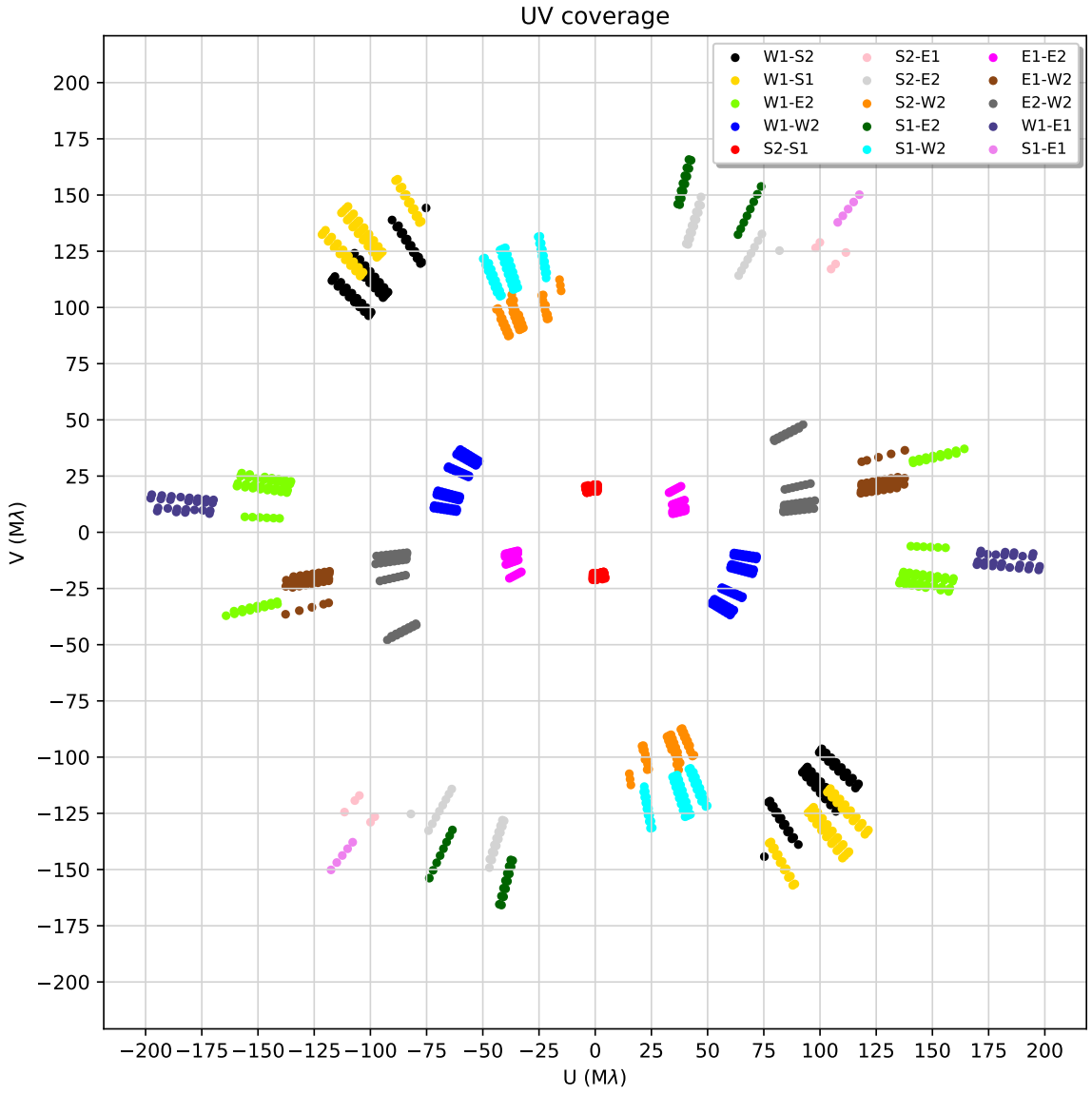

Figure A4: (u, v) coverage for AD Per in 2015

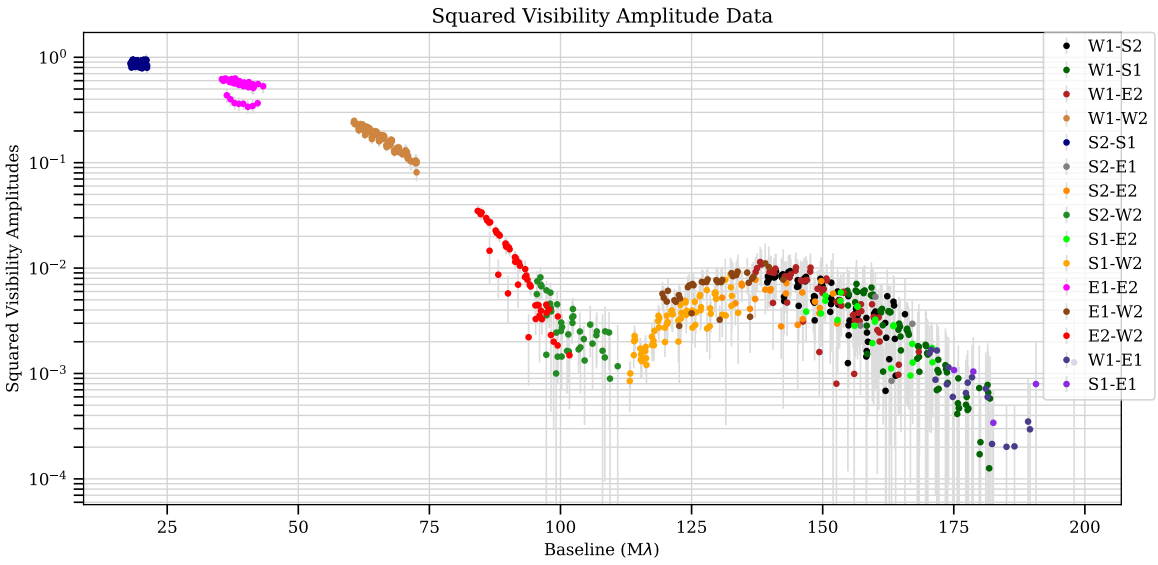

Figure A5: V^2 of AD Per in 2015

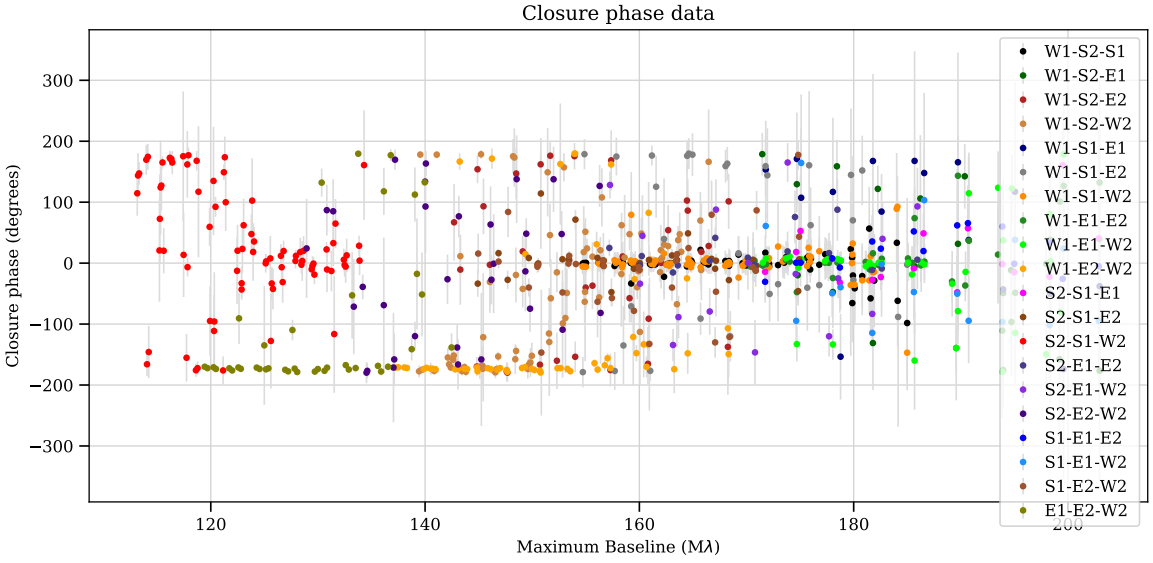

Figure A6: Closure phases of AD Per in 2015

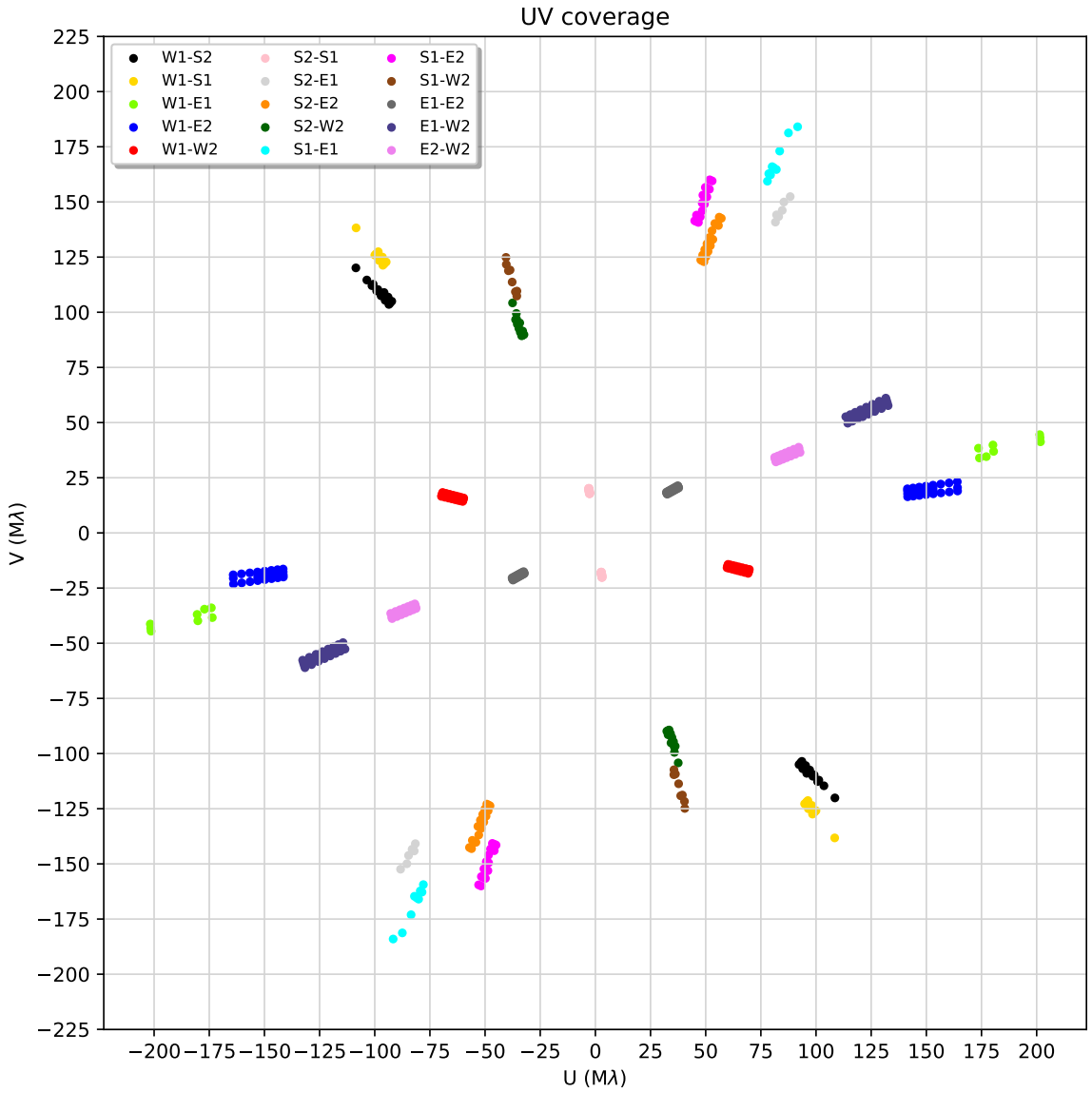

Figure A7: (u, v) coverage for AD Per in 2016 August

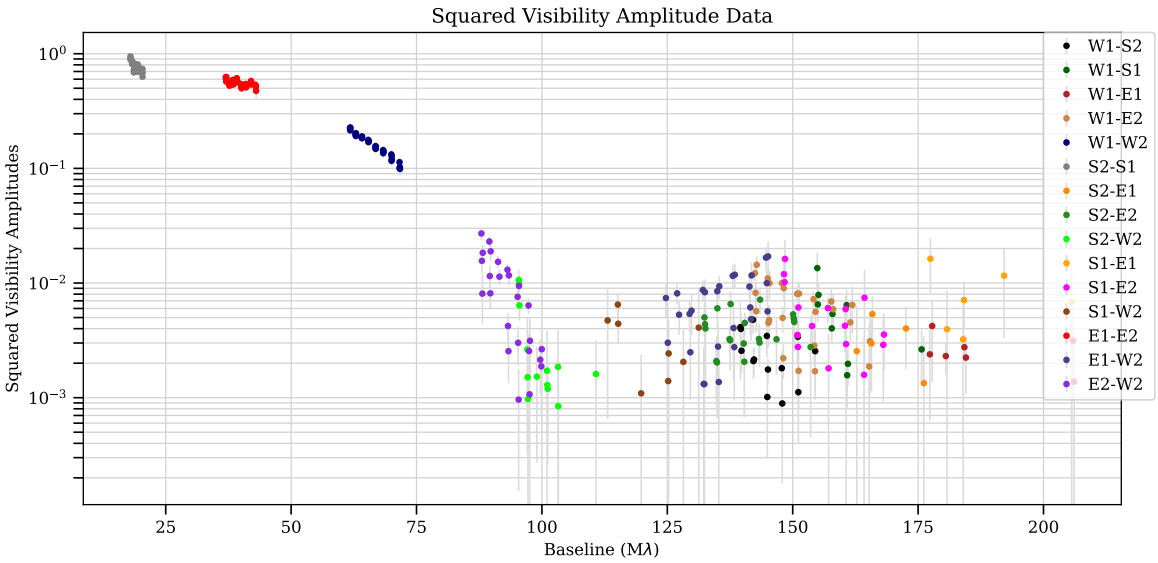

Figure A8: V^2 of AD Per in 2016 August

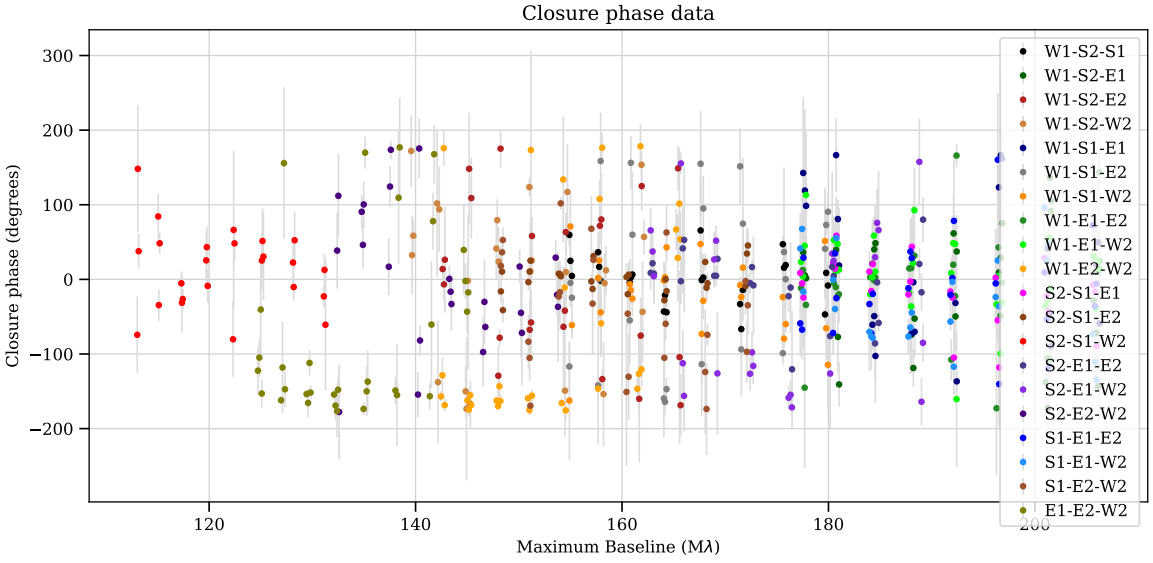

Figure A9: Closure phases of AD Per in 2016 August

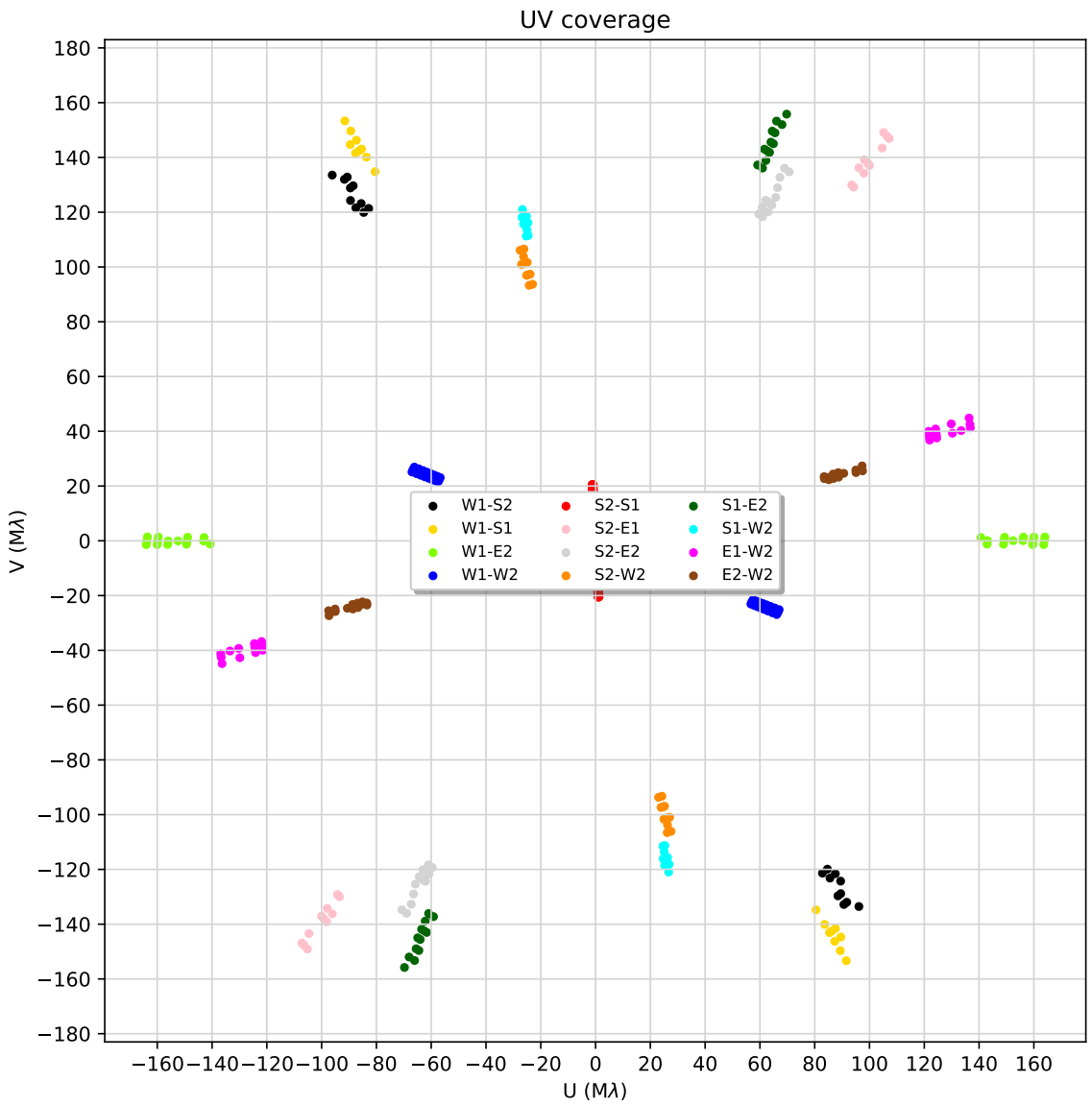

Figure A10: (u, v) coverage for AD Per in 2016 October

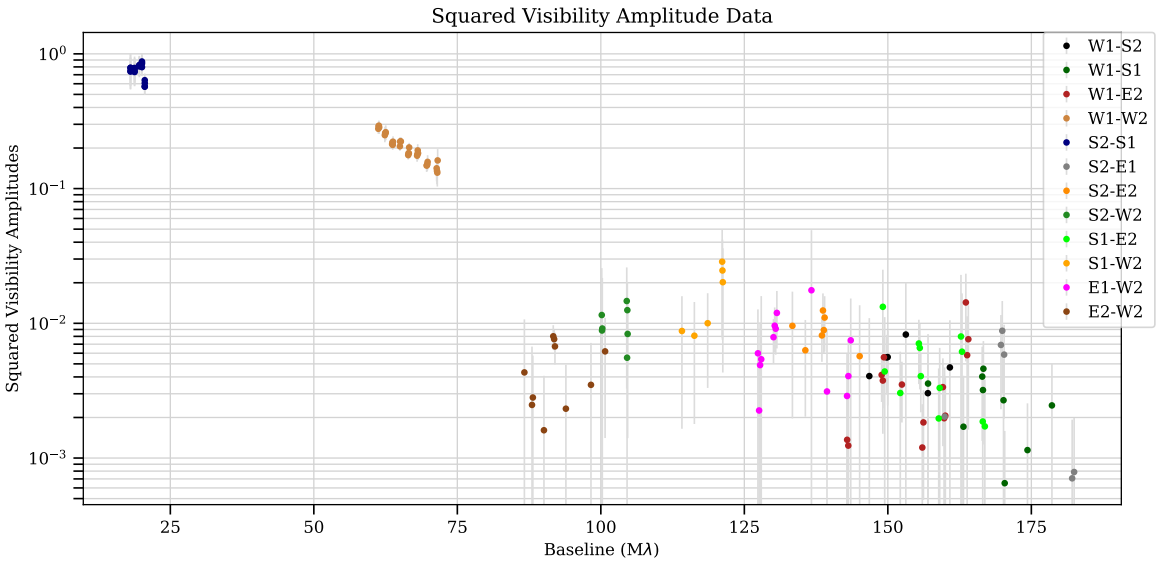

Figure A11: V^2 of AD Per in 2016 October

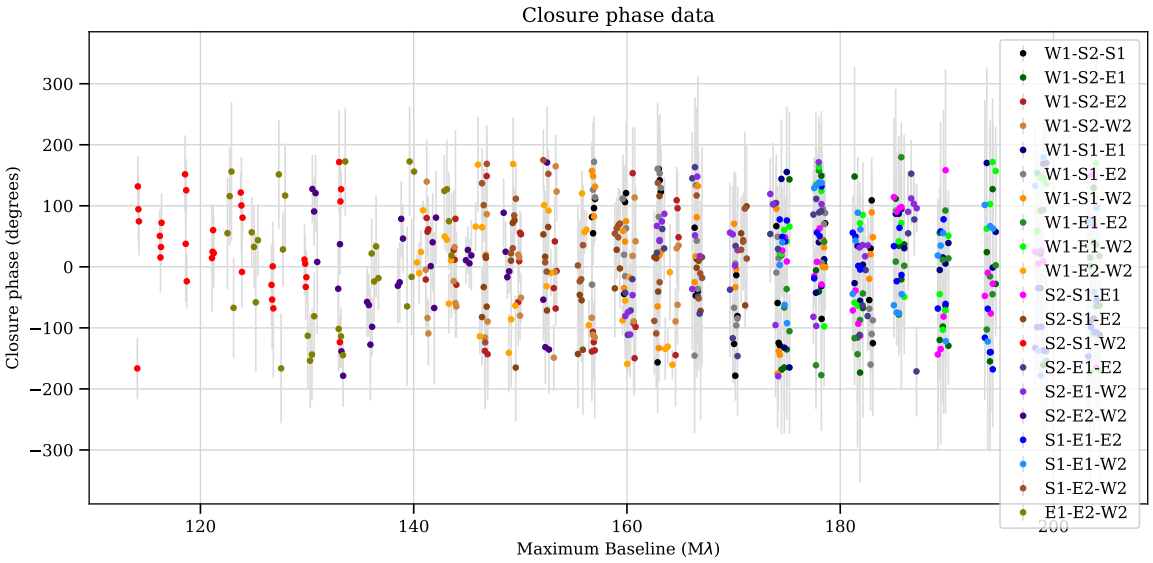

Figure A12: Closure phases of AD Per in 2016 October

C AZ Cyg

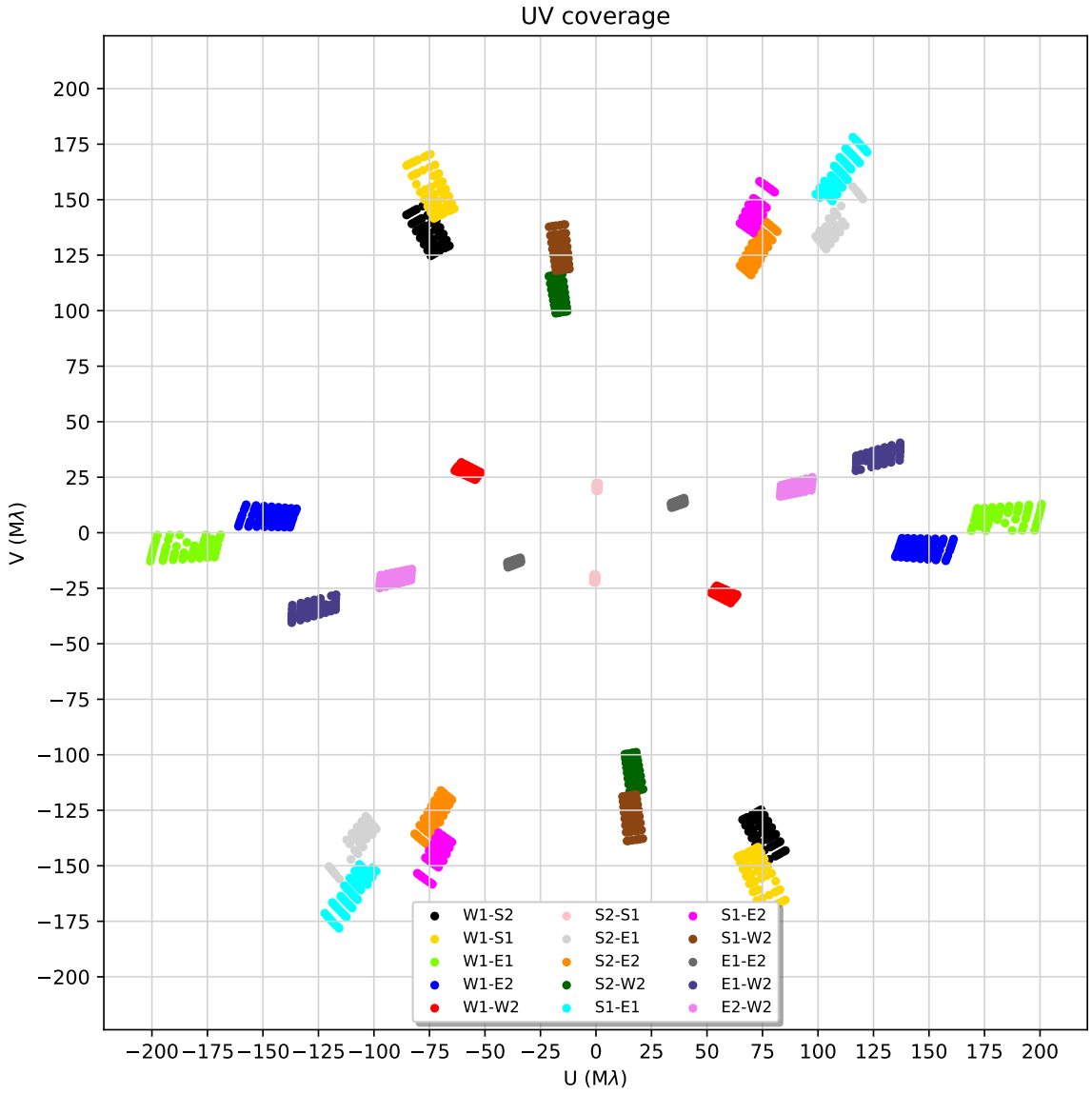

Figure A13: (u, v) coverage for AZ Cyg in 2011

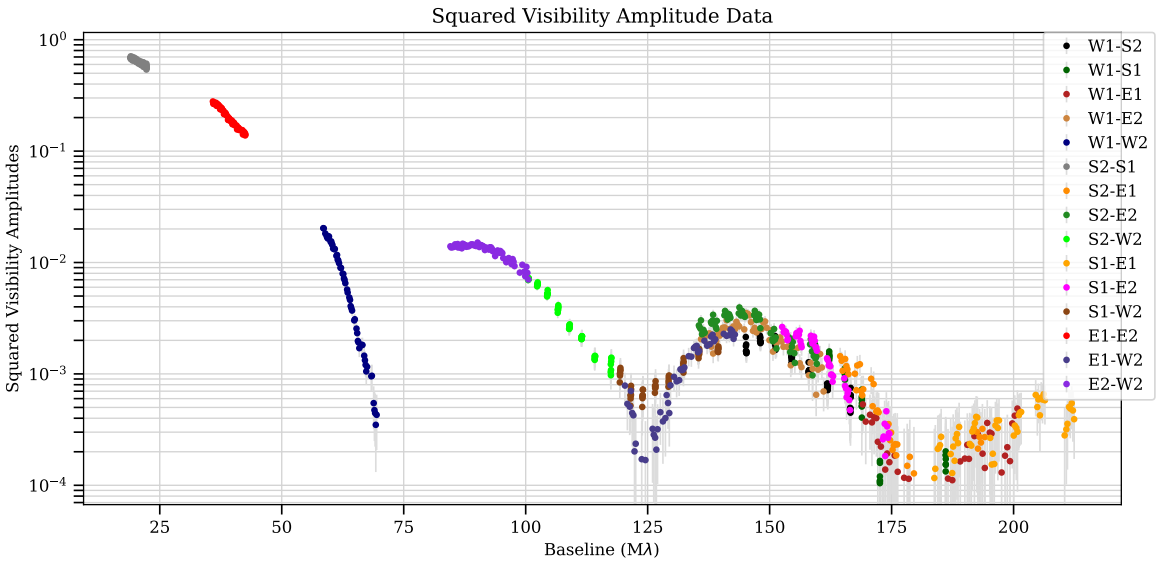

Figure A14: V^2 of AZ Cyg in 2011

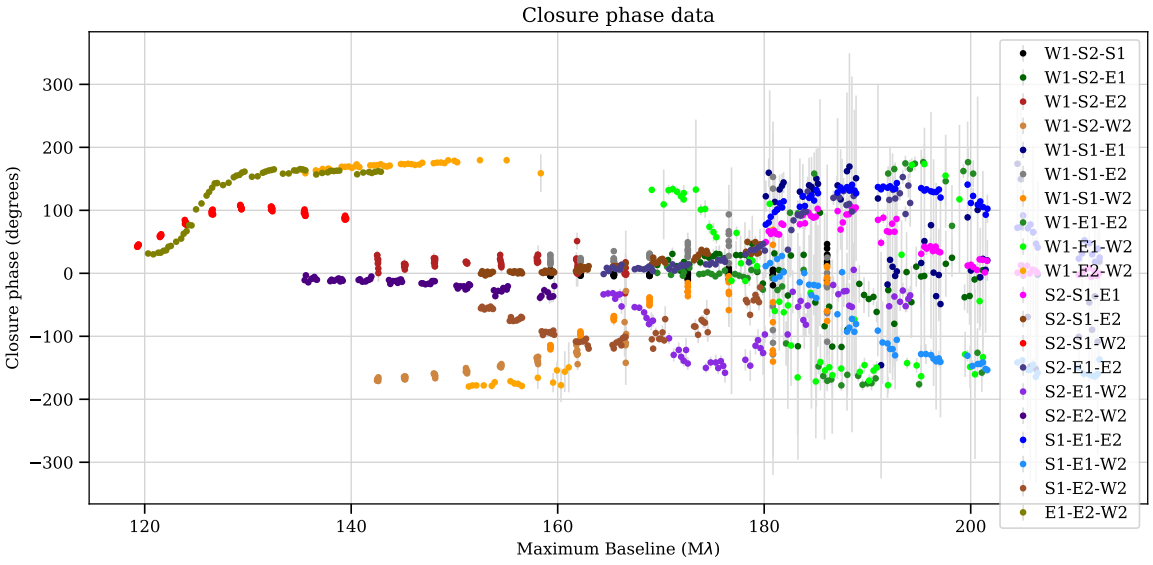

Figure A15: Closure phases of AZ Cyg in 2011

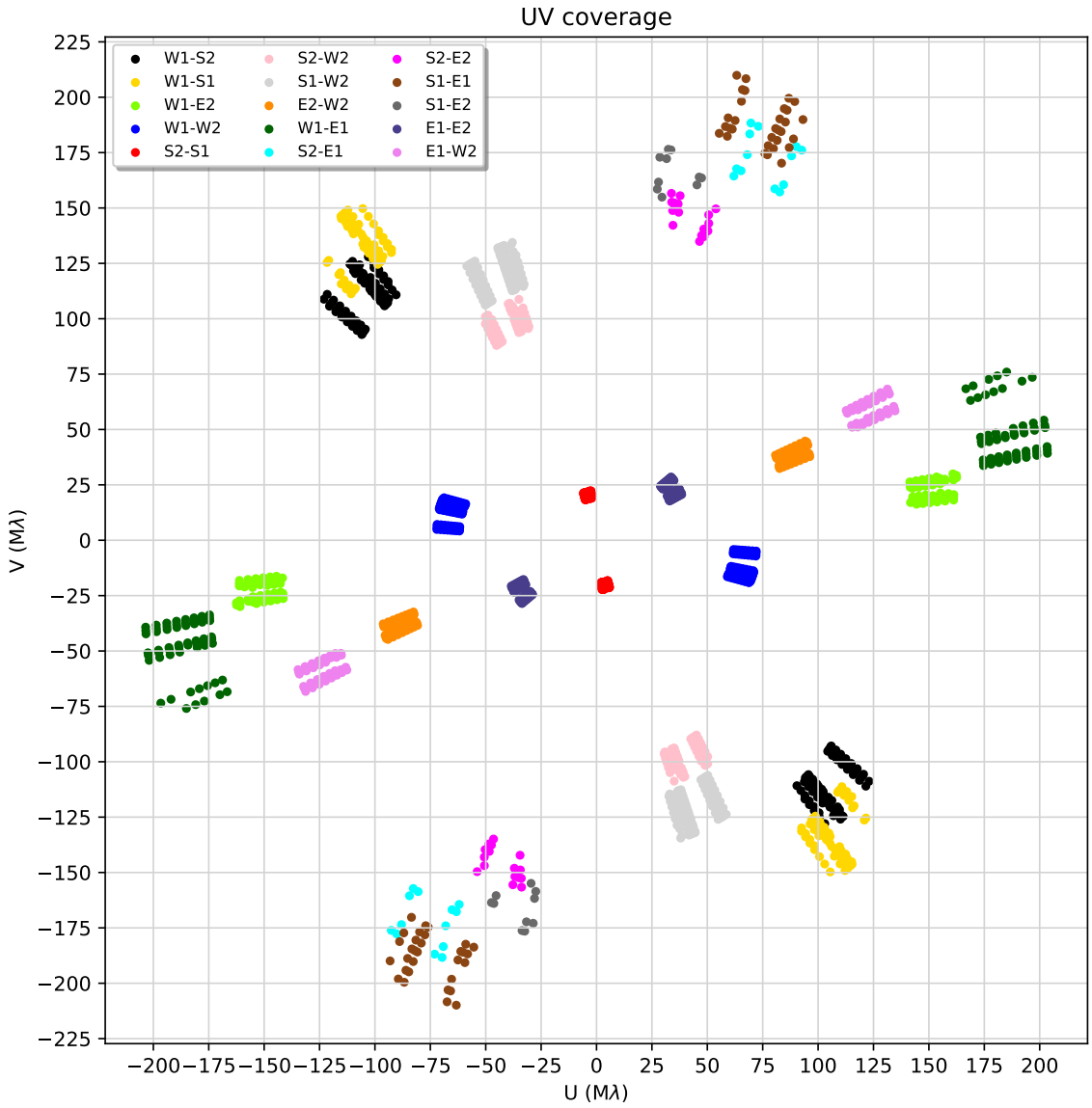

Figure A16: (u, v) coverage for AZ Cyg in 2012

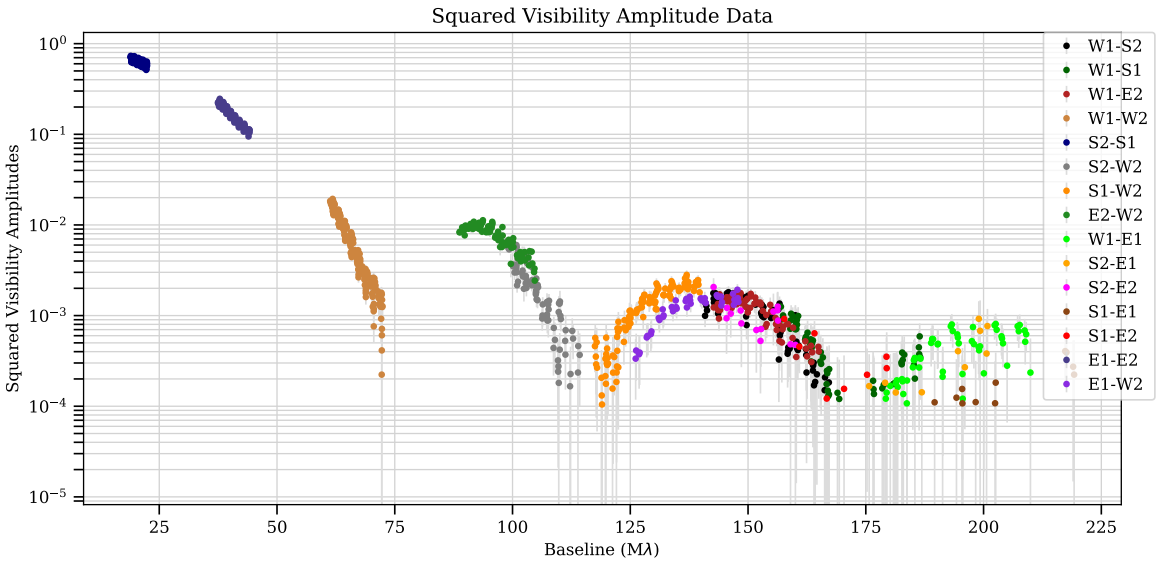

Figure A17: V^2 of AZ Cyg in 2012

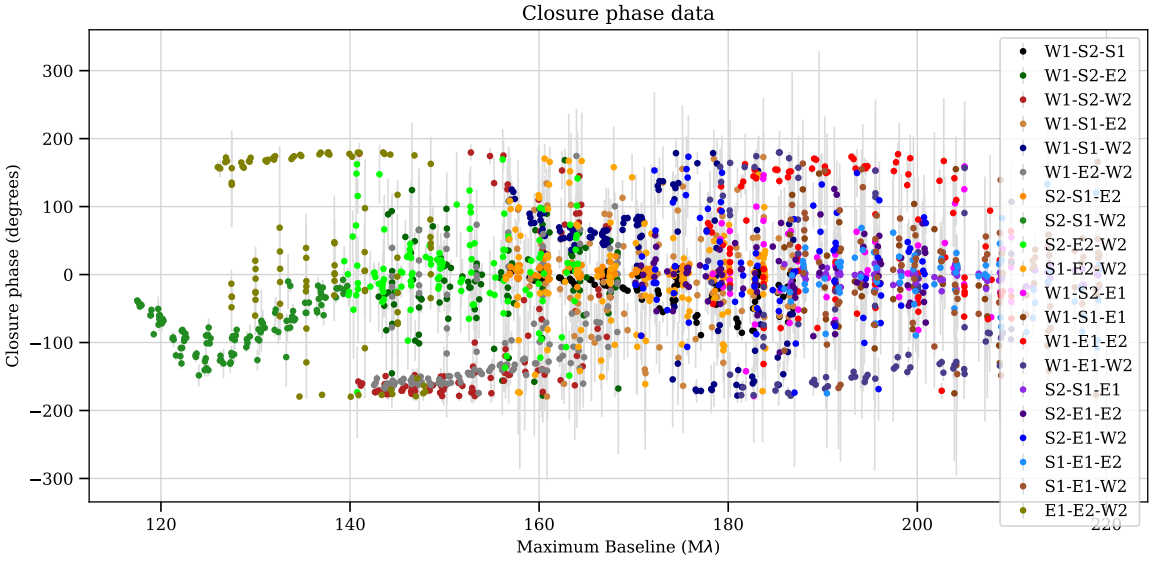

Figure A18: Closure phases of AZ Cyg in 2012

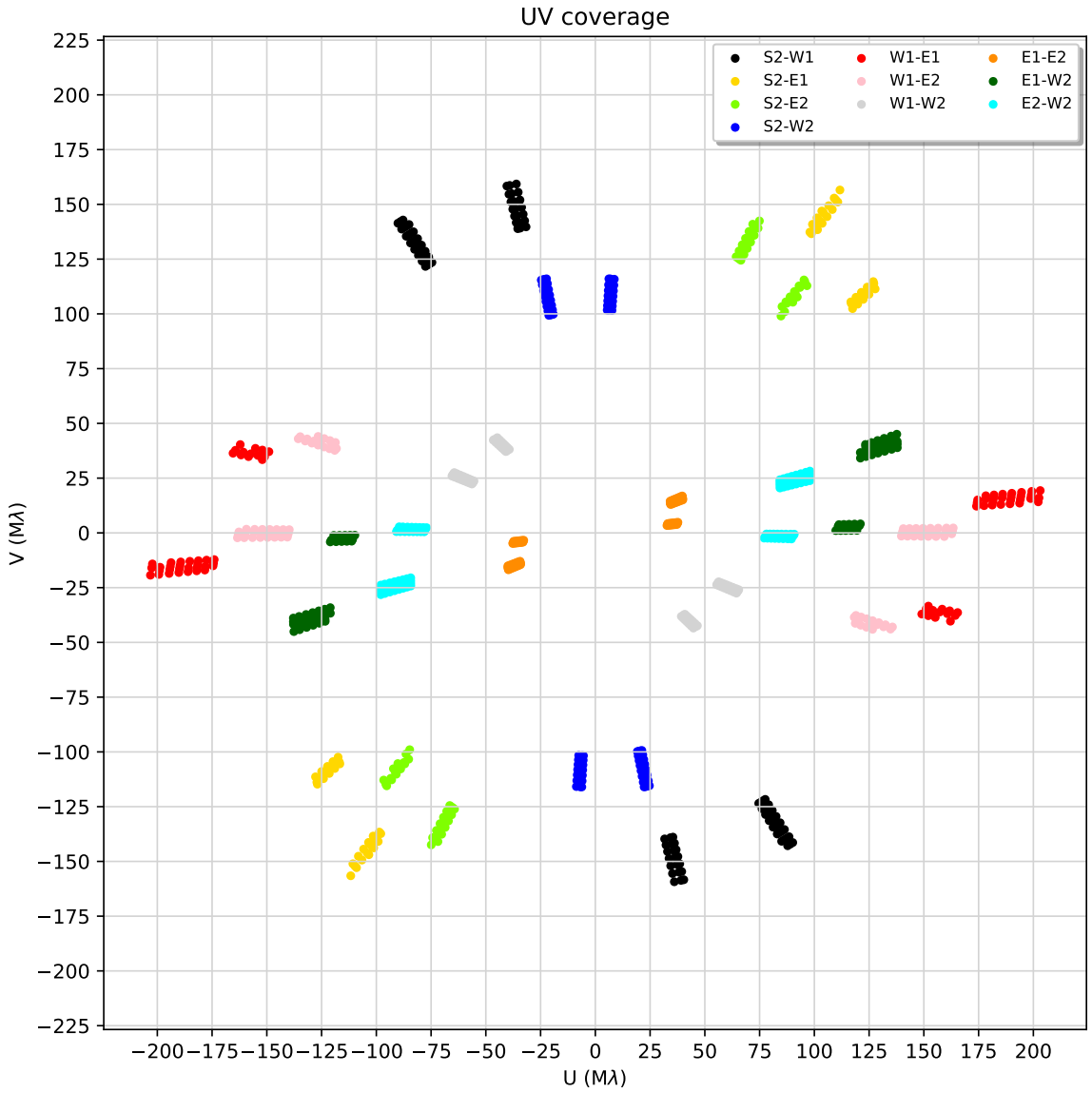

Figure A19: (u, v) coverage for AZ Cyg in 2014

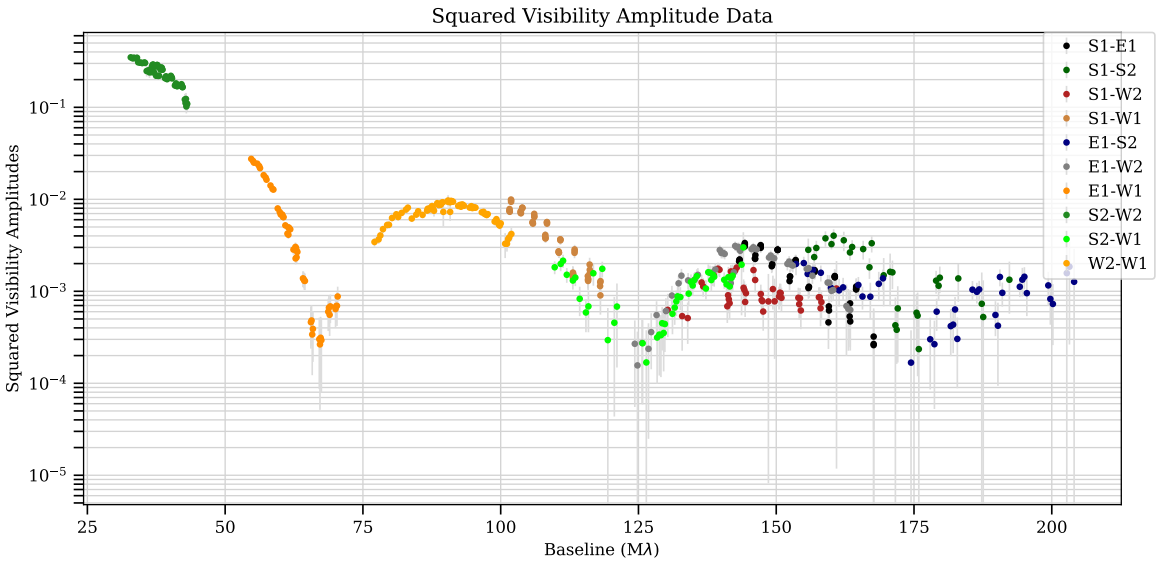

Figure A20: V^2 of AZ Cyg in 2014

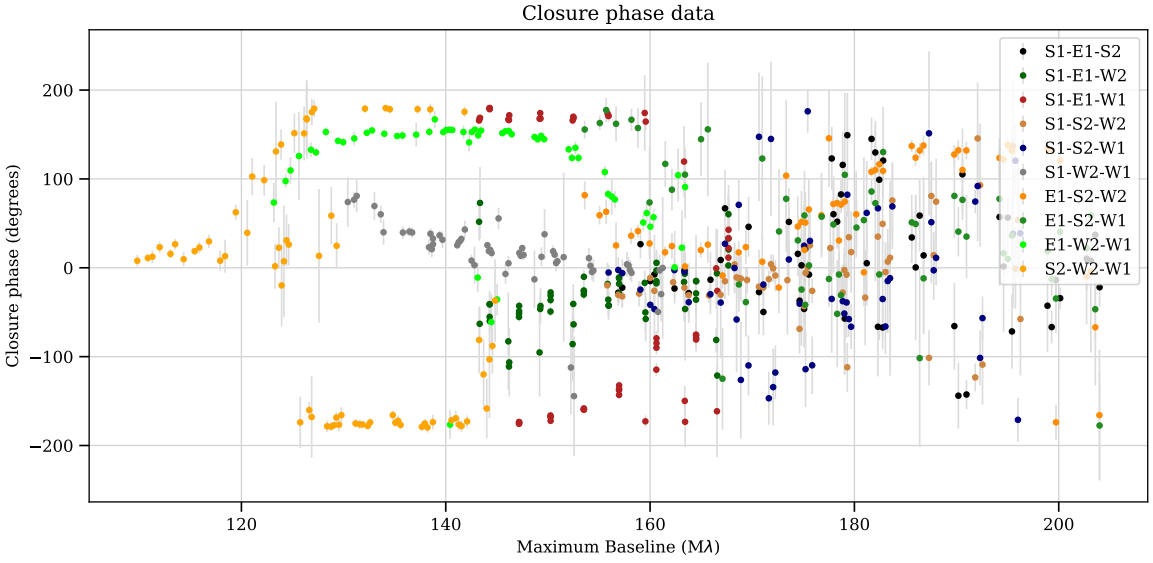

Figure A21: Closure phases of AZ Cyg in 2014

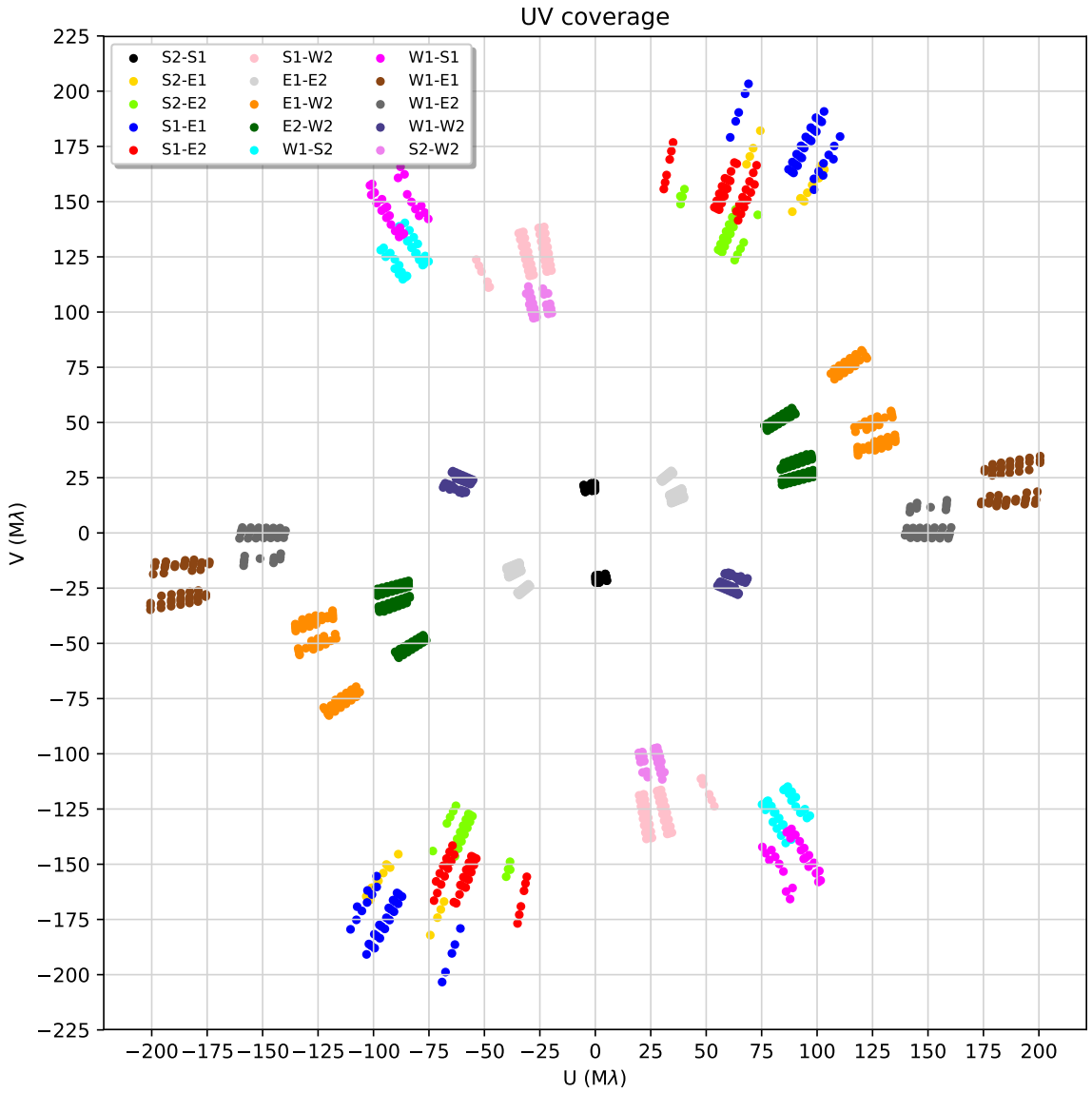

Figure A22: (u, v) coverage for AZ Cyg in 2015 August

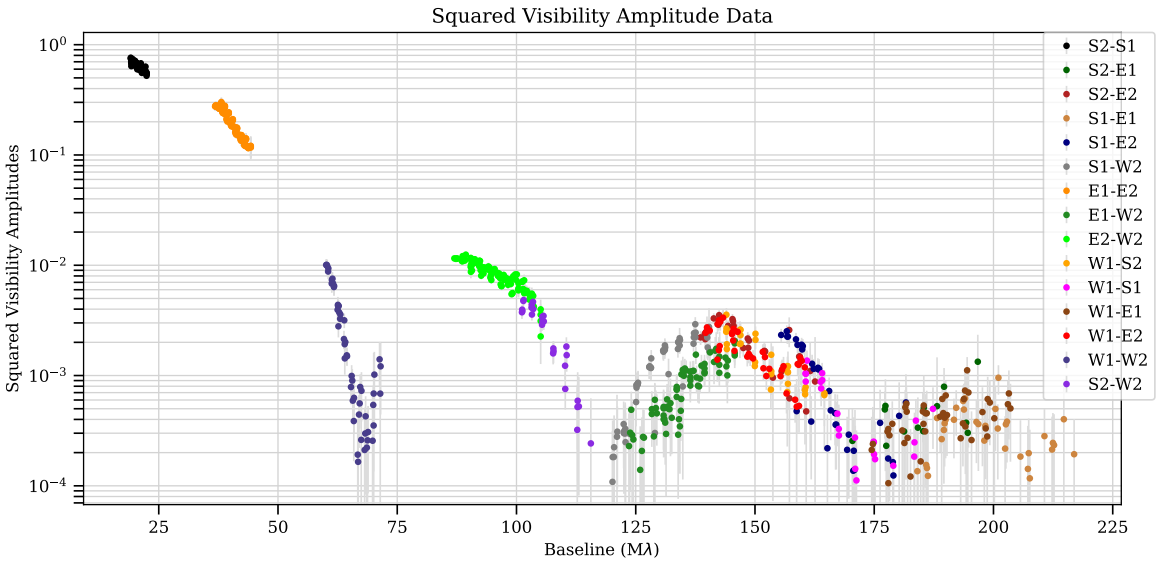

Figure A23: V^2 of AZ Cyg in 2015 August

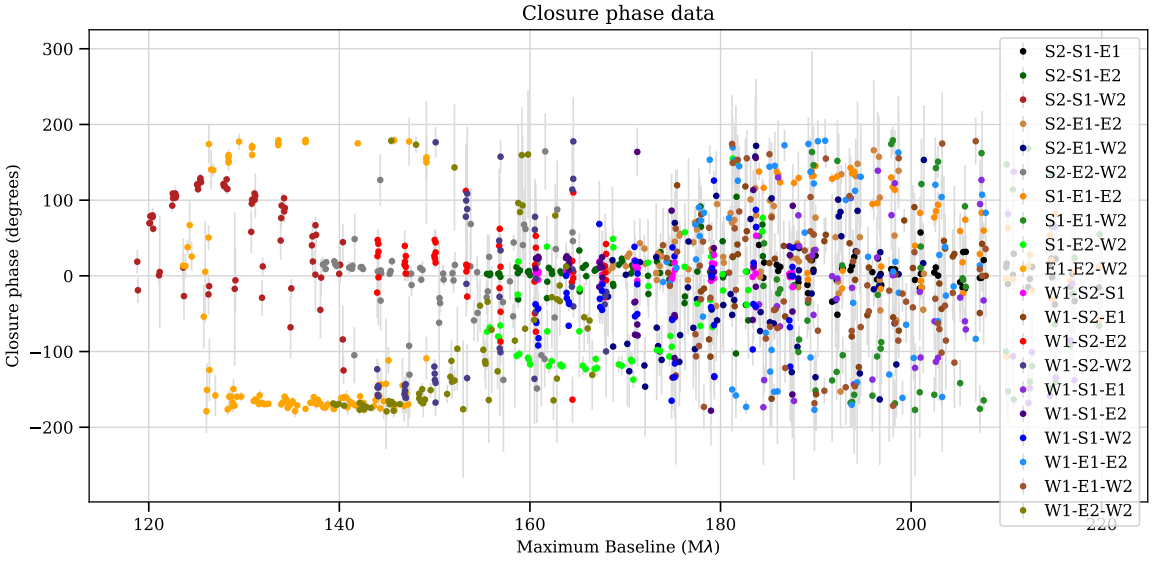

Figure A24: Closure phases of AZ Cyg in 2015 August

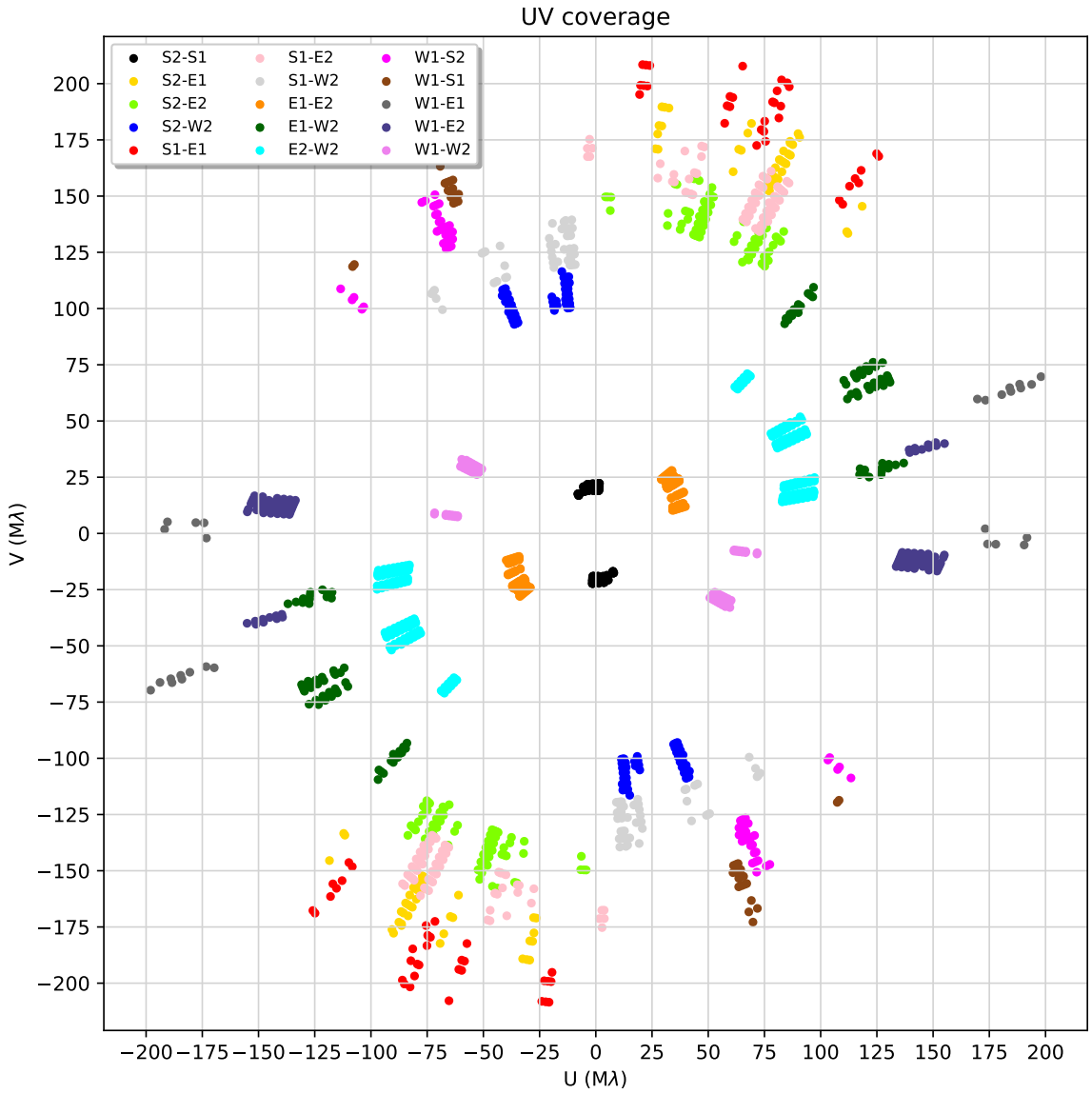

Figure A25: (u, v) coverage for AZ Cyg in 2016 August

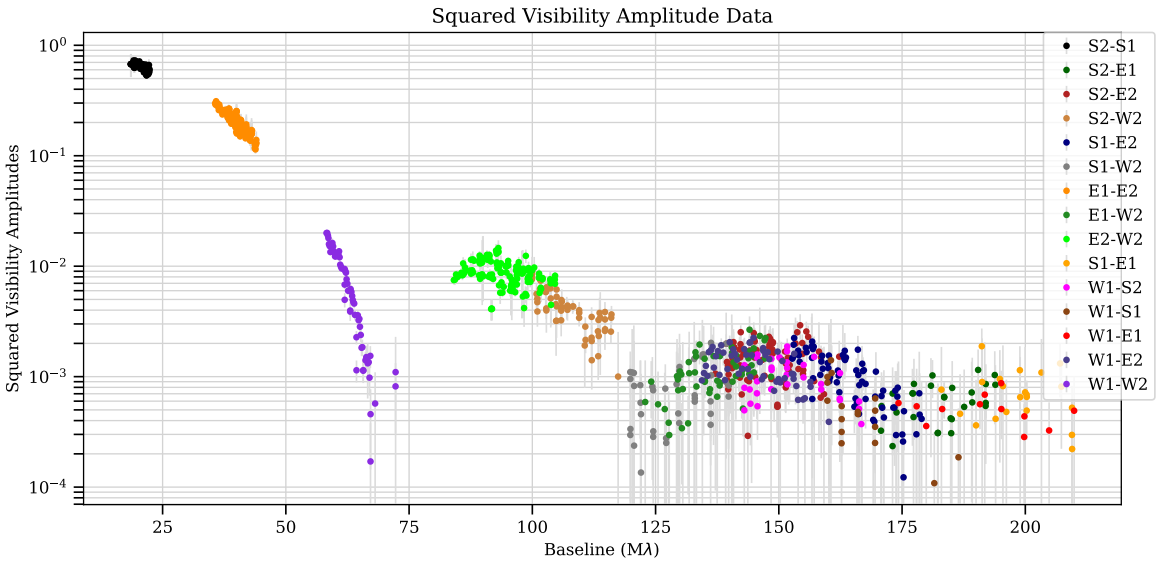

Figure A26: V^2 of AZ Cyg in 2016 August

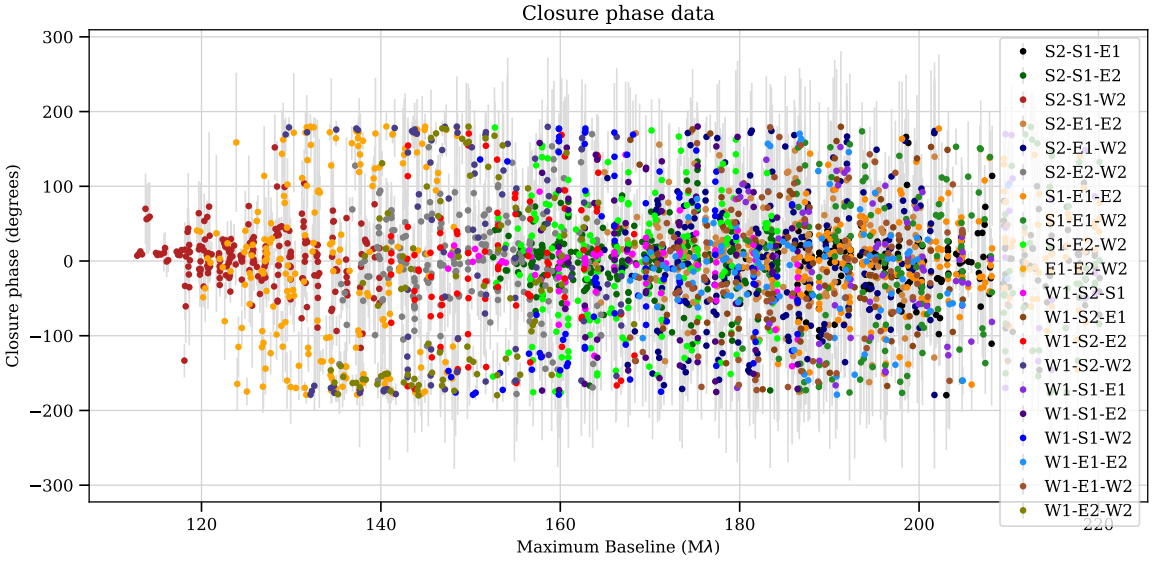

Figure A27: Closure phases of AZ Cyg in 2016 August

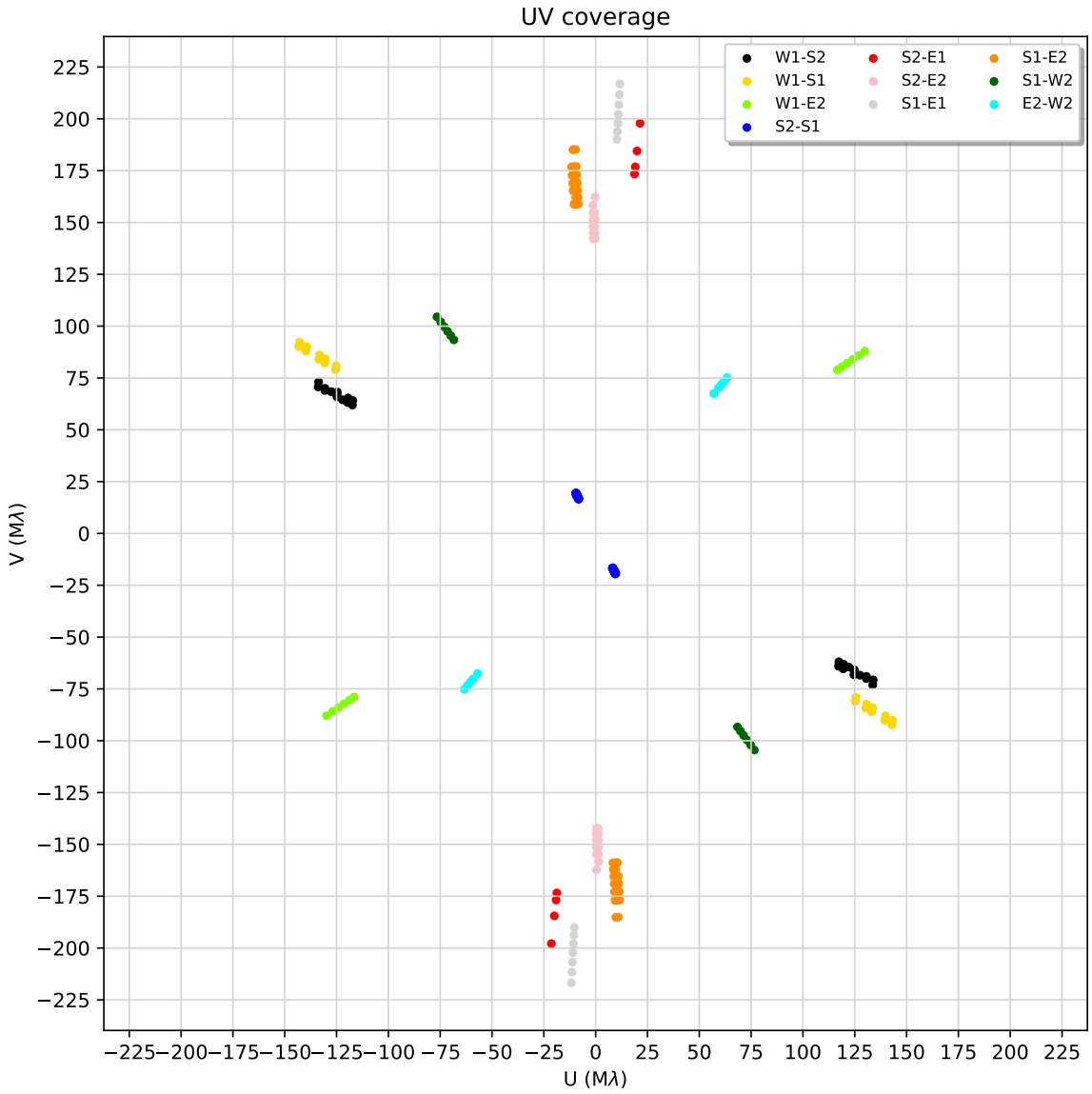

Figure A28: (u, v) coverage for AZ Cyg in 2015 October

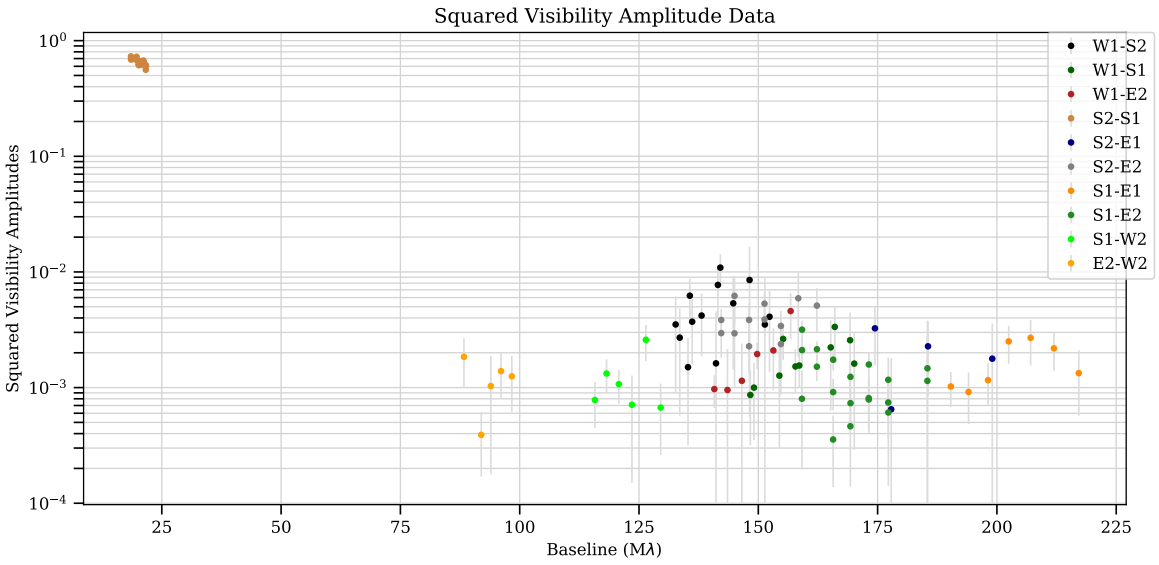

Figure A29: V^2 of AZ Cyg in 2015 October

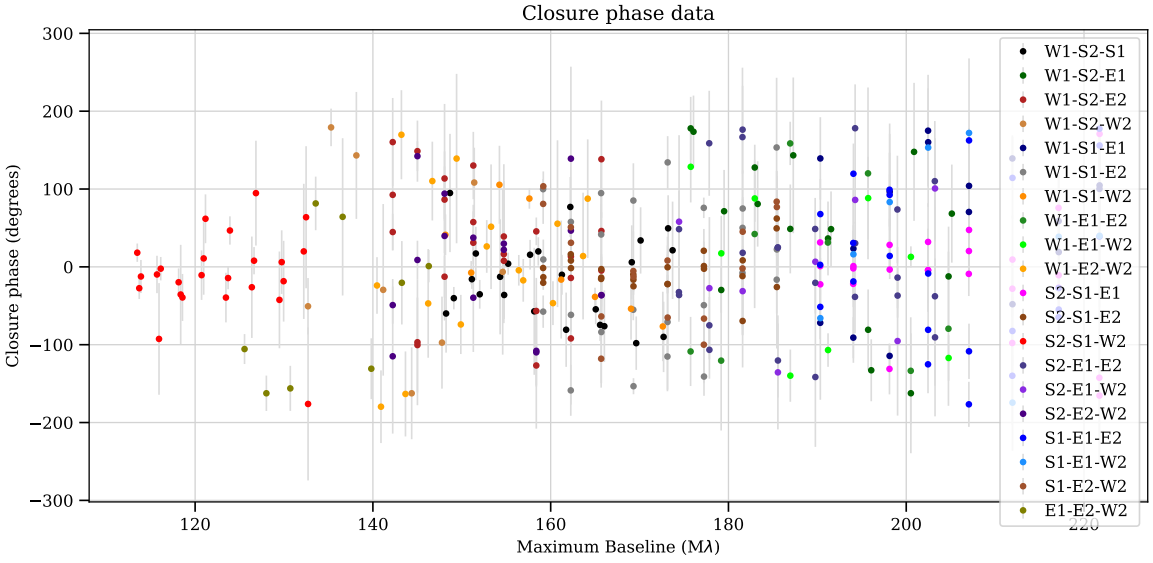

Figure A30: Closure phases of AZ Cyg in 2015 October

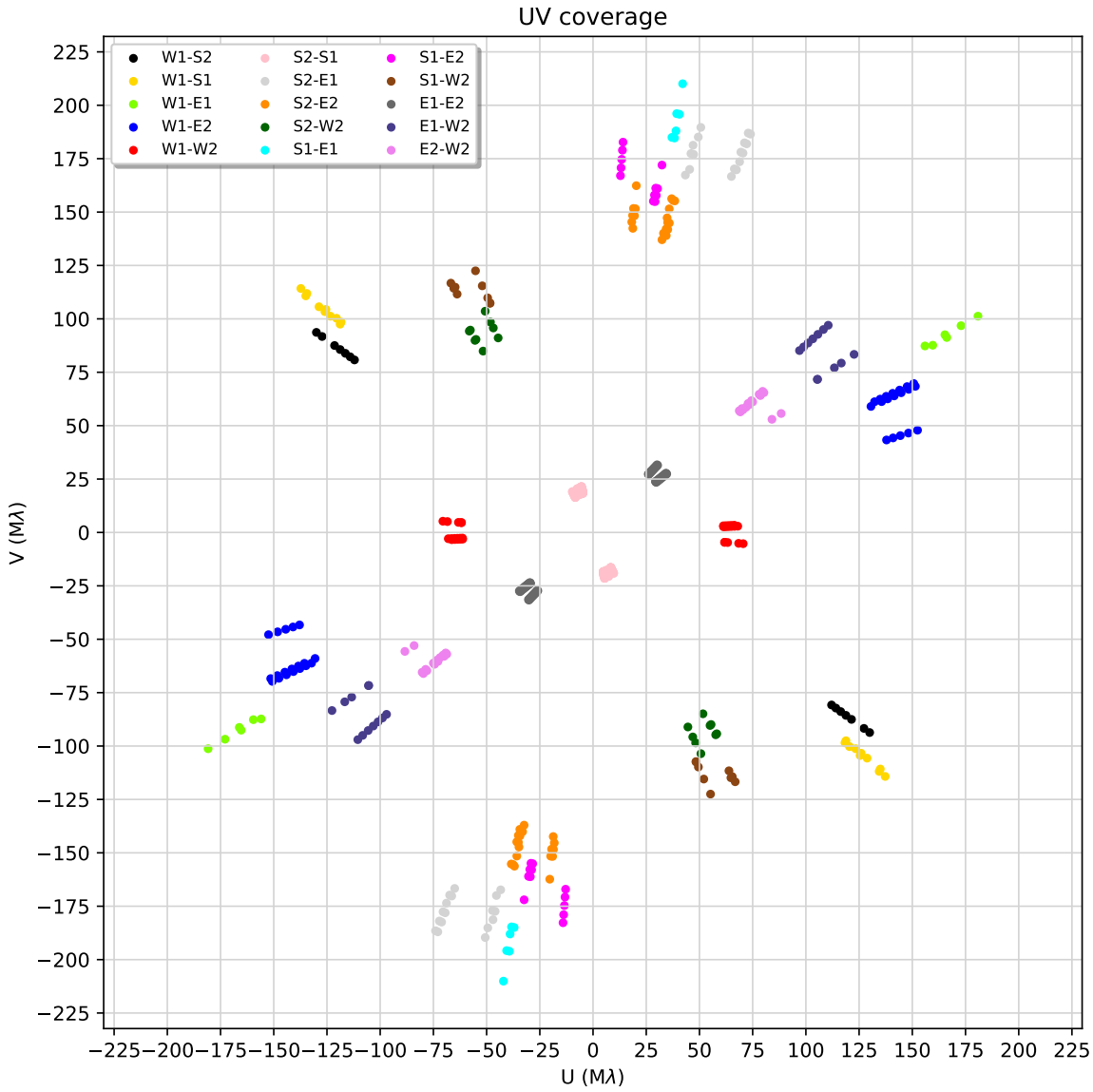

Figure A31: (u, v) coverage for AZ Cyg in 2016 October

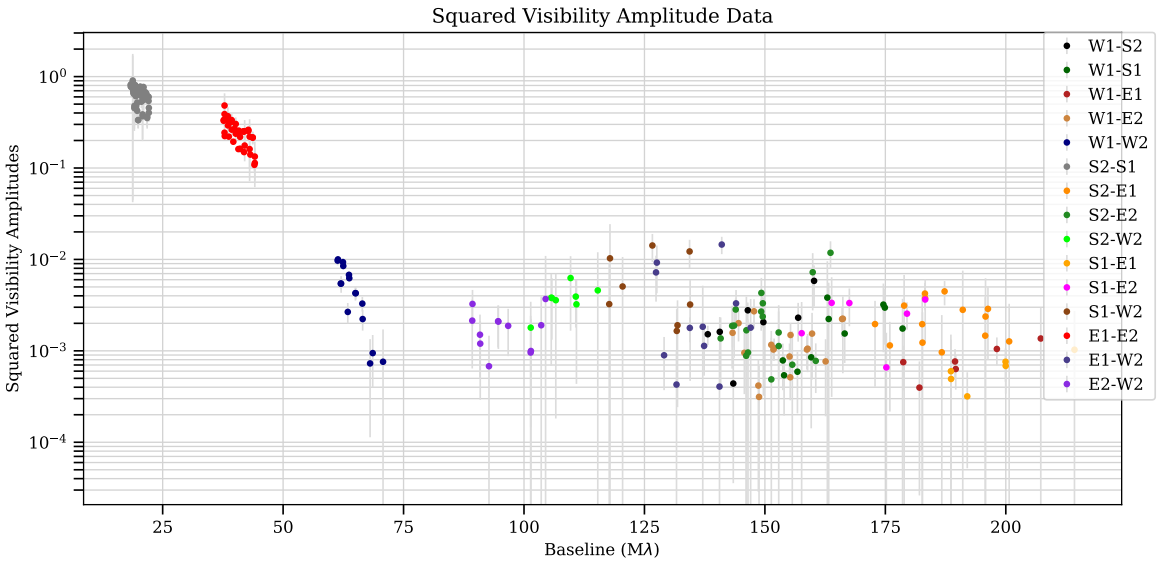

Figure A32: V^2 of AZ Cyg in 2016 October

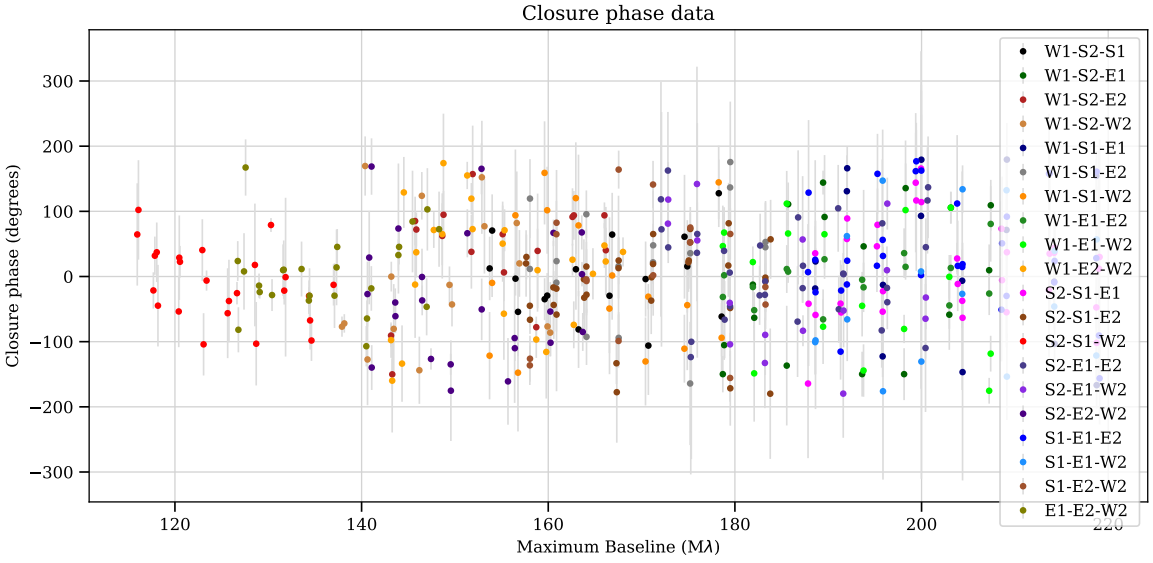

Figure A33: Closure phases of AZ Cyg in 2016 October

D BD+354077

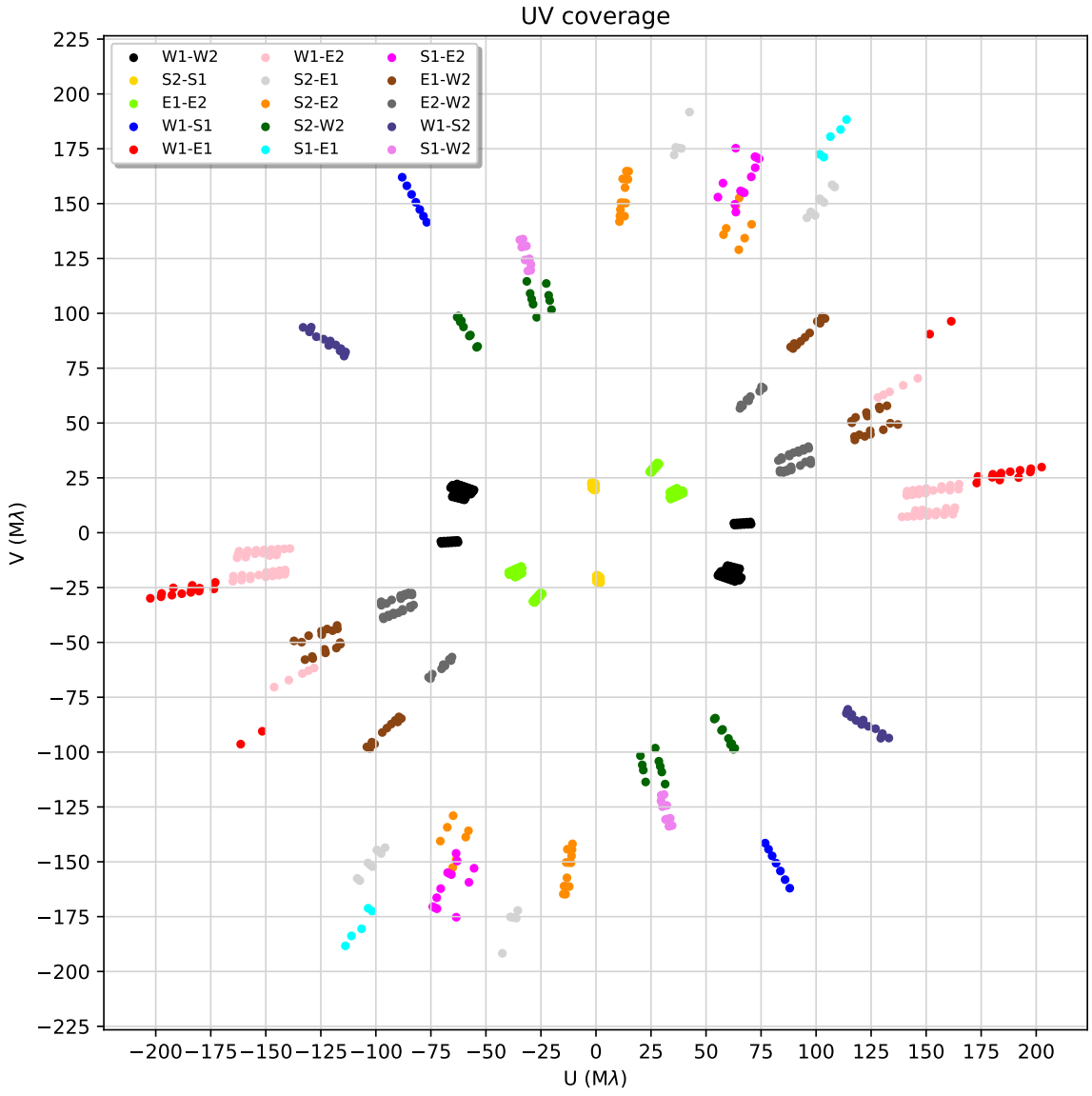

Figure A34: (u, v) coverage for BD+354077 in 2016

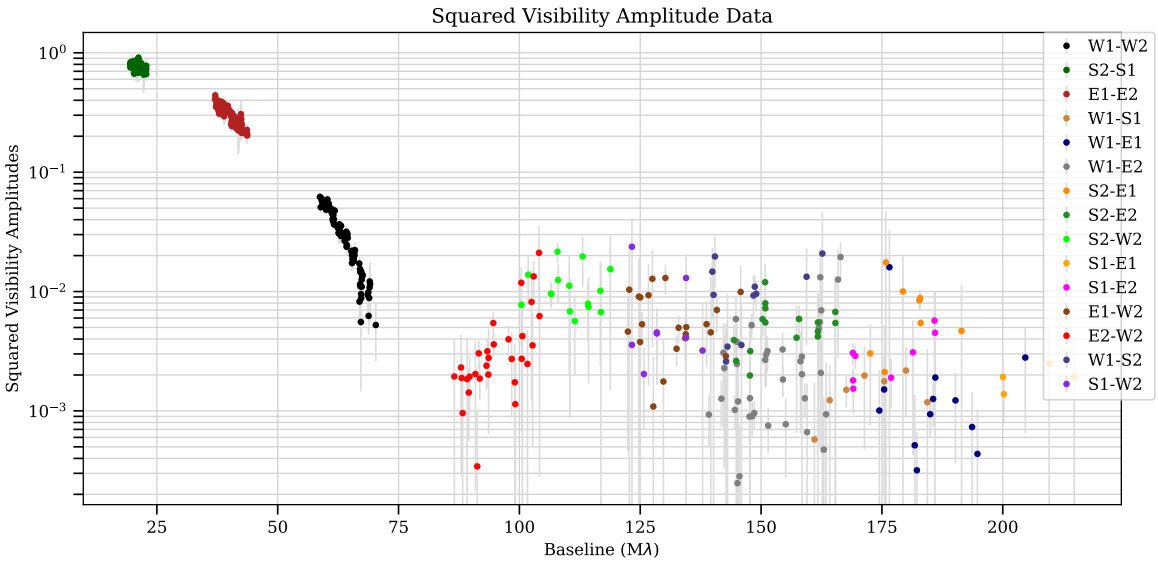

Figure A35: V^2 of BD+354077 in 2016

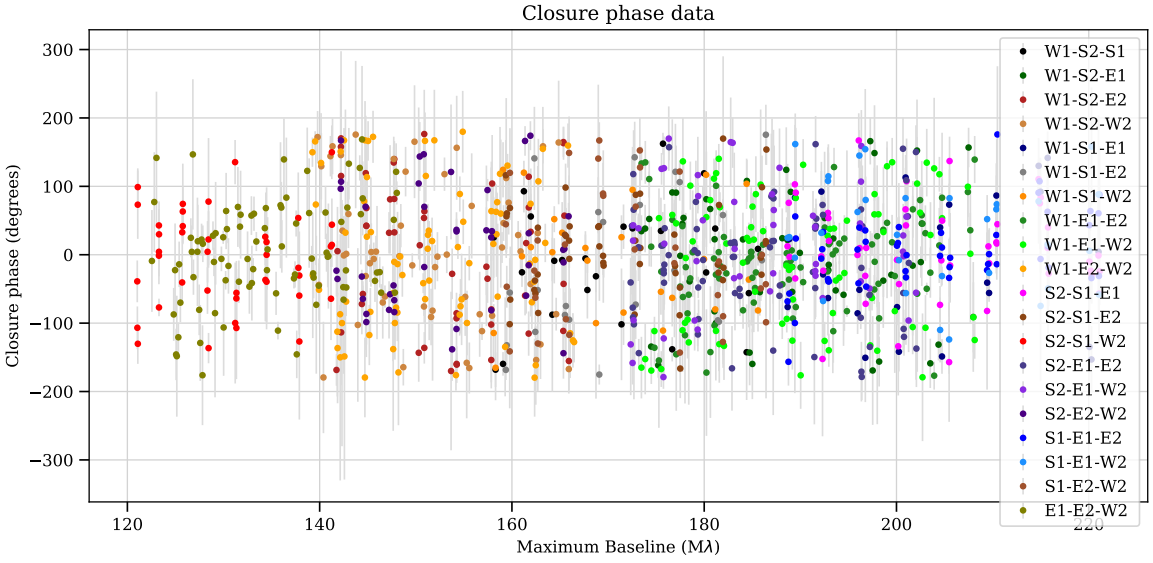

Figure A36: Closure phases of BD+354077 in 2016

E BI Cyg

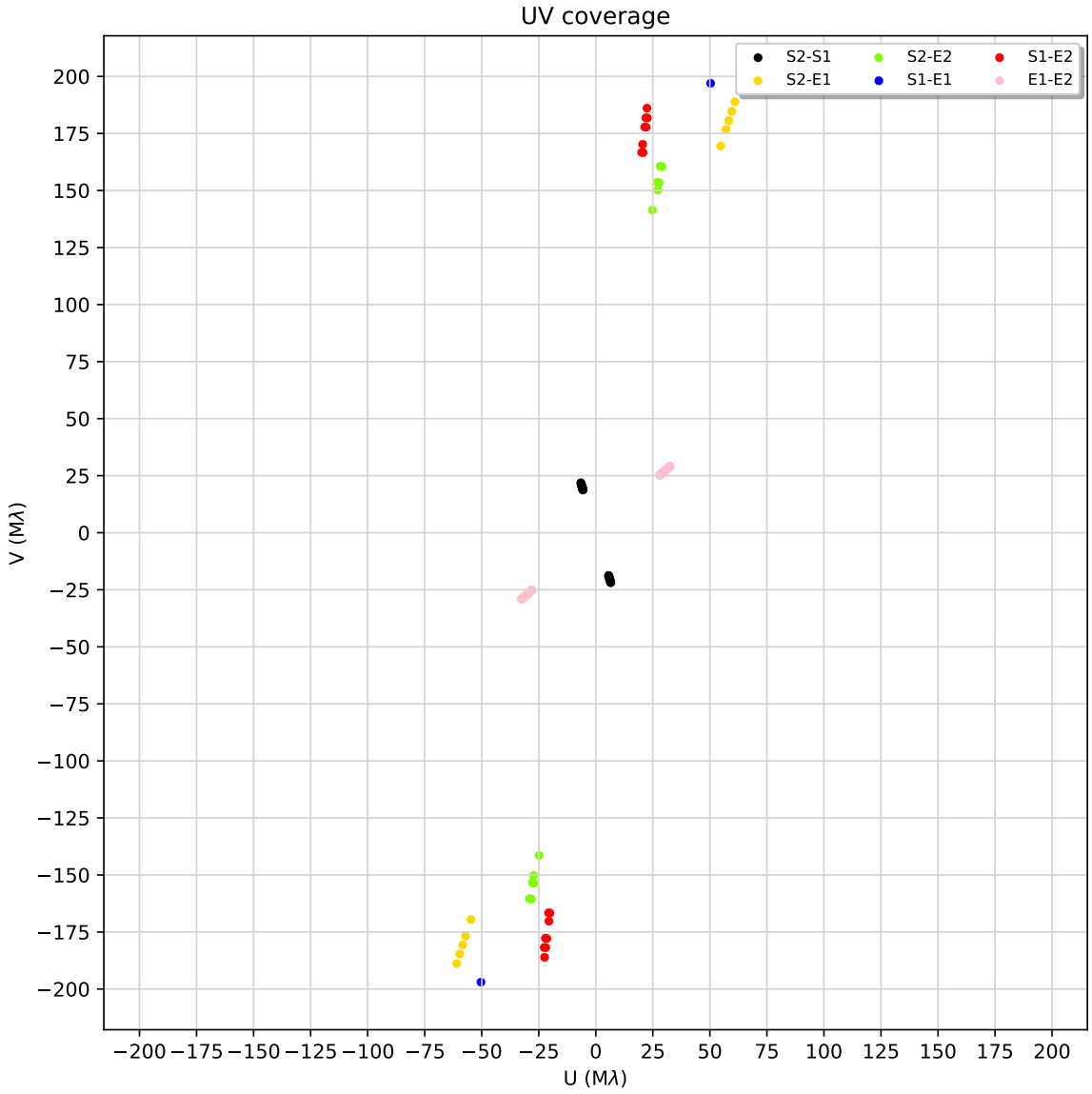

Figure A37: (u, v) coverage for BI Cyg in 2015

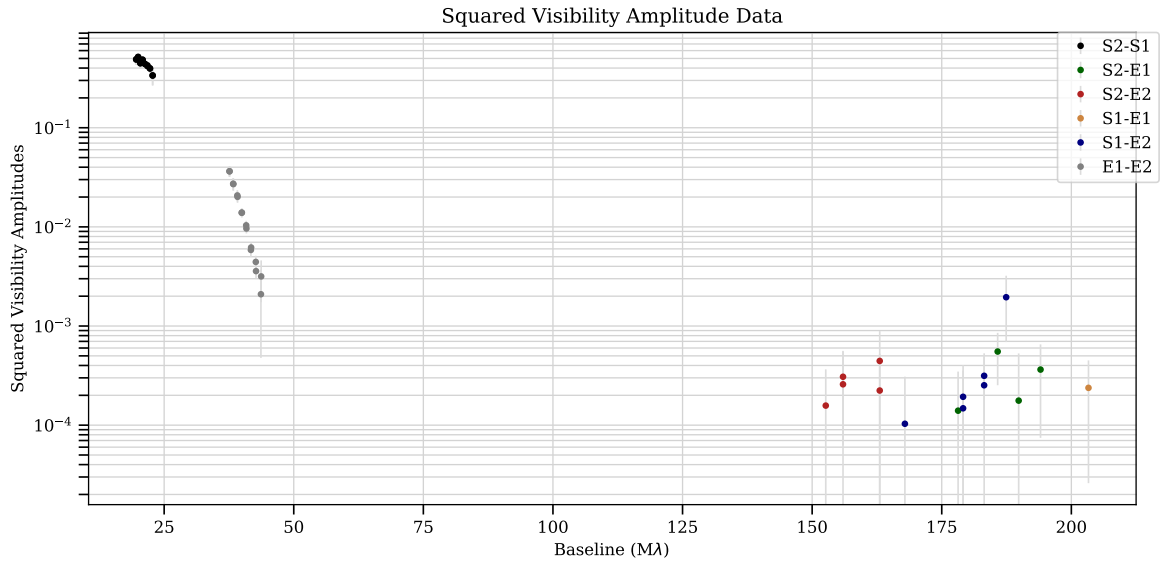

Figure A38: V^2 of BI Cyg in 2015

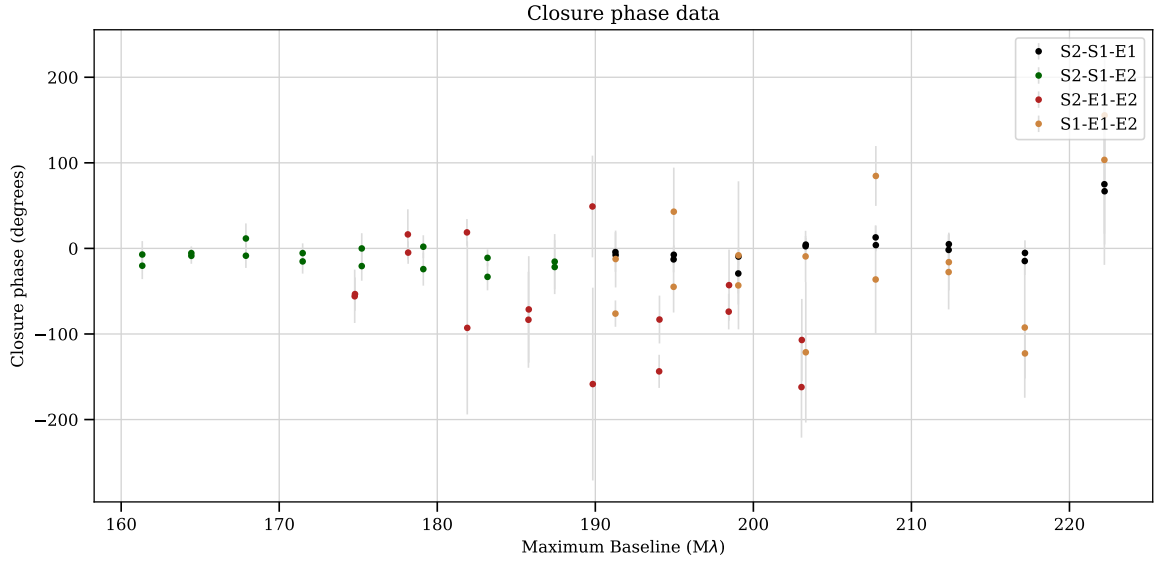

Figure A39: Closure phases of BI Cyg in 2015

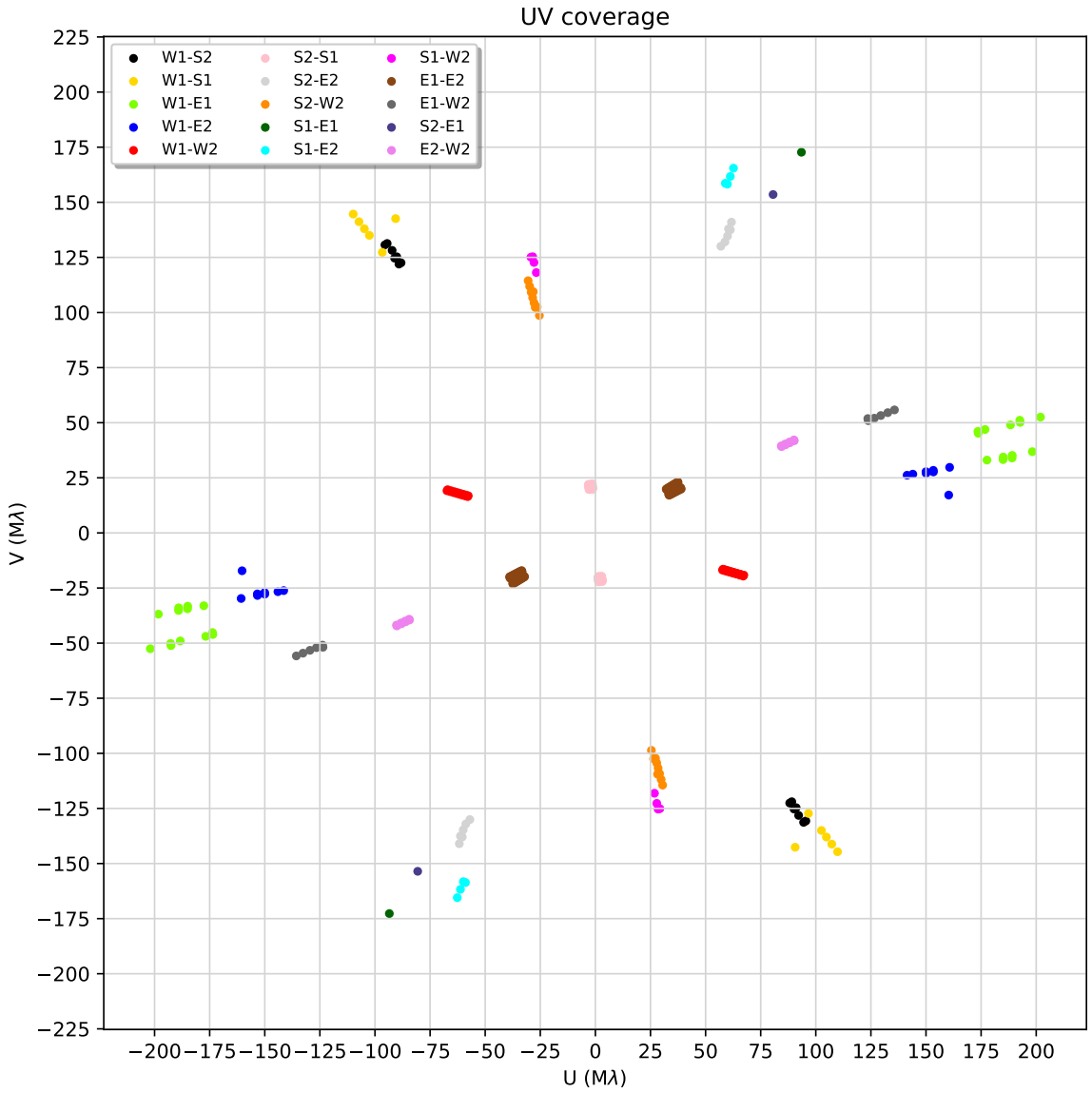

Figure A40: (u, v) coverage for BI Cyg in 2016

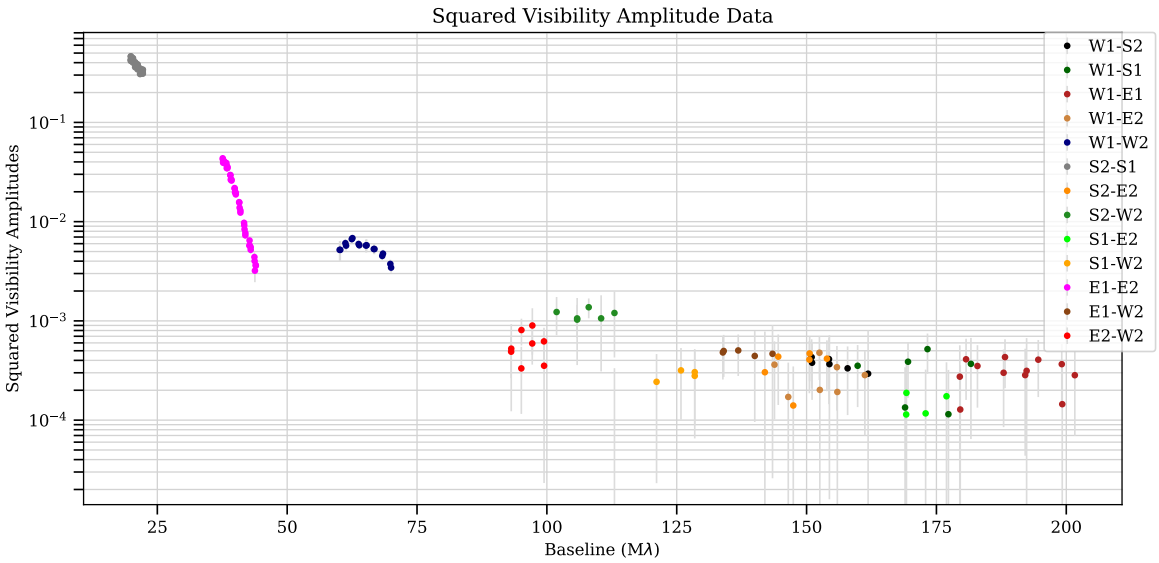

Figure A41: V^2 of BI Cyg in 2016

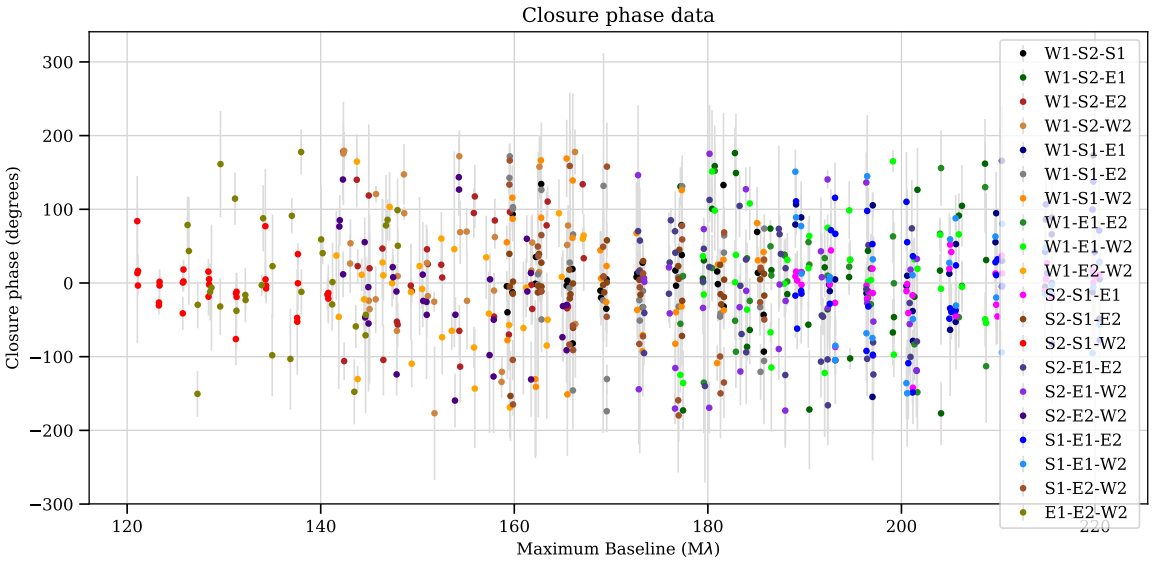

Figure A42: Closure phases of BI Cyg in 2016

F BU Per

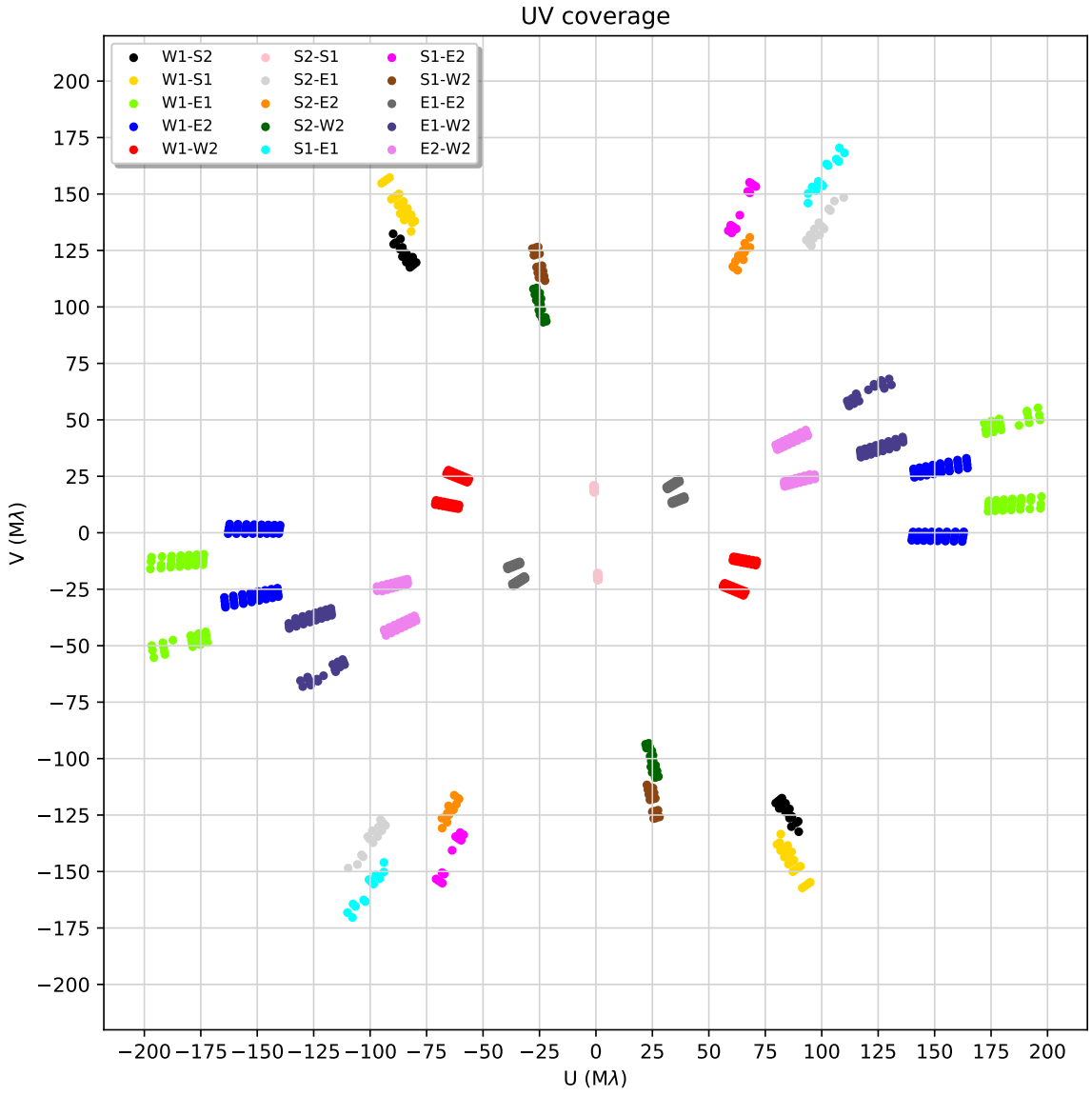

Figure A43: (u, v) coverage for BU Per in 2016

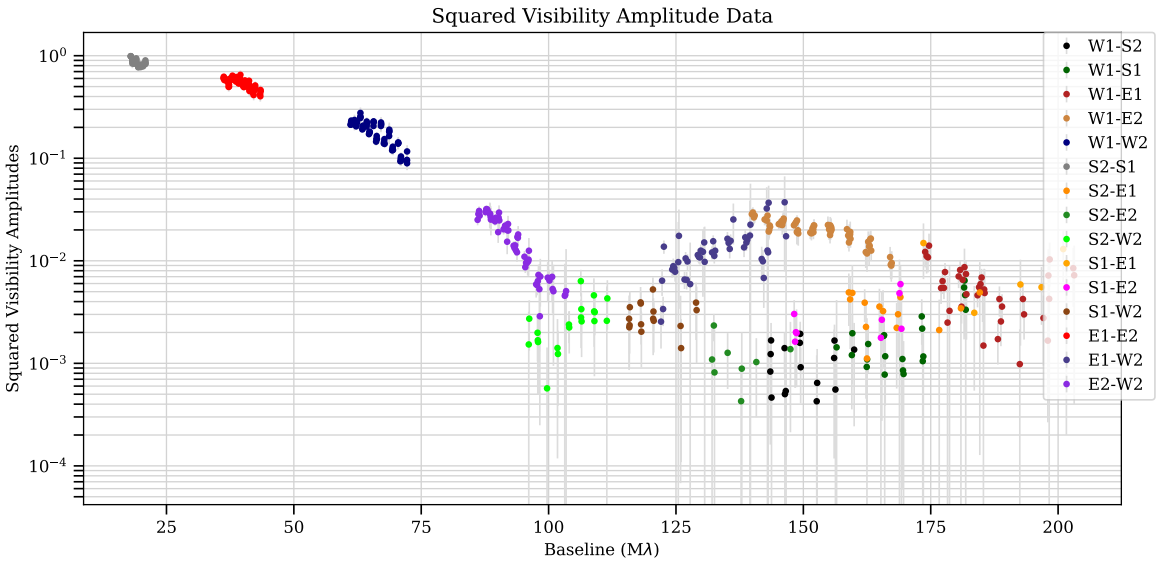

Figure A44: V^2 of BU Per in 2016

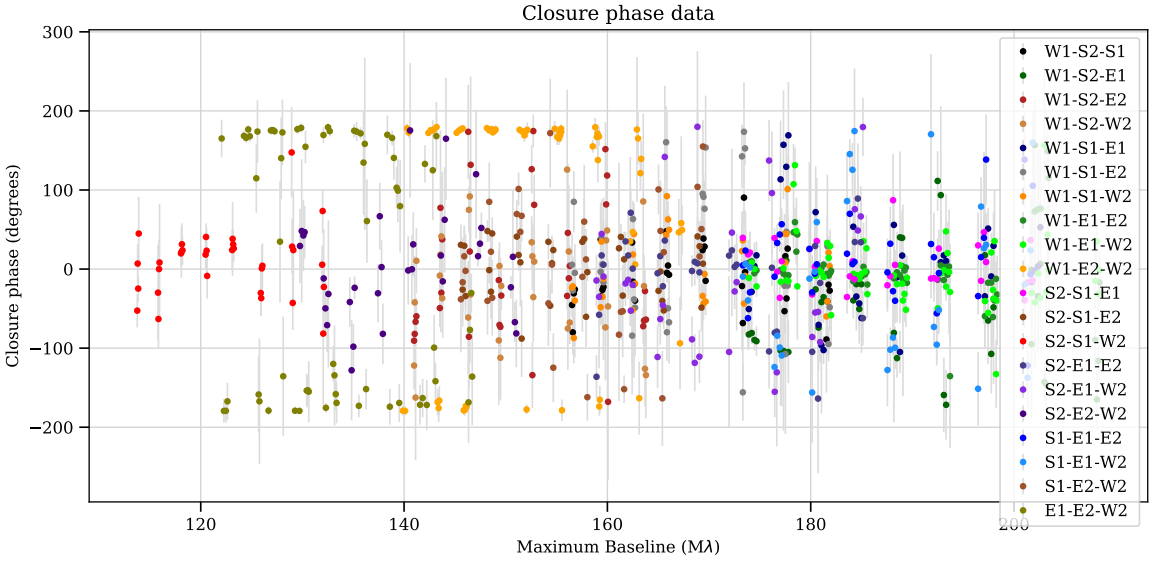

Figure A45: Closure phases of BU Per in 2016

G FZ Per

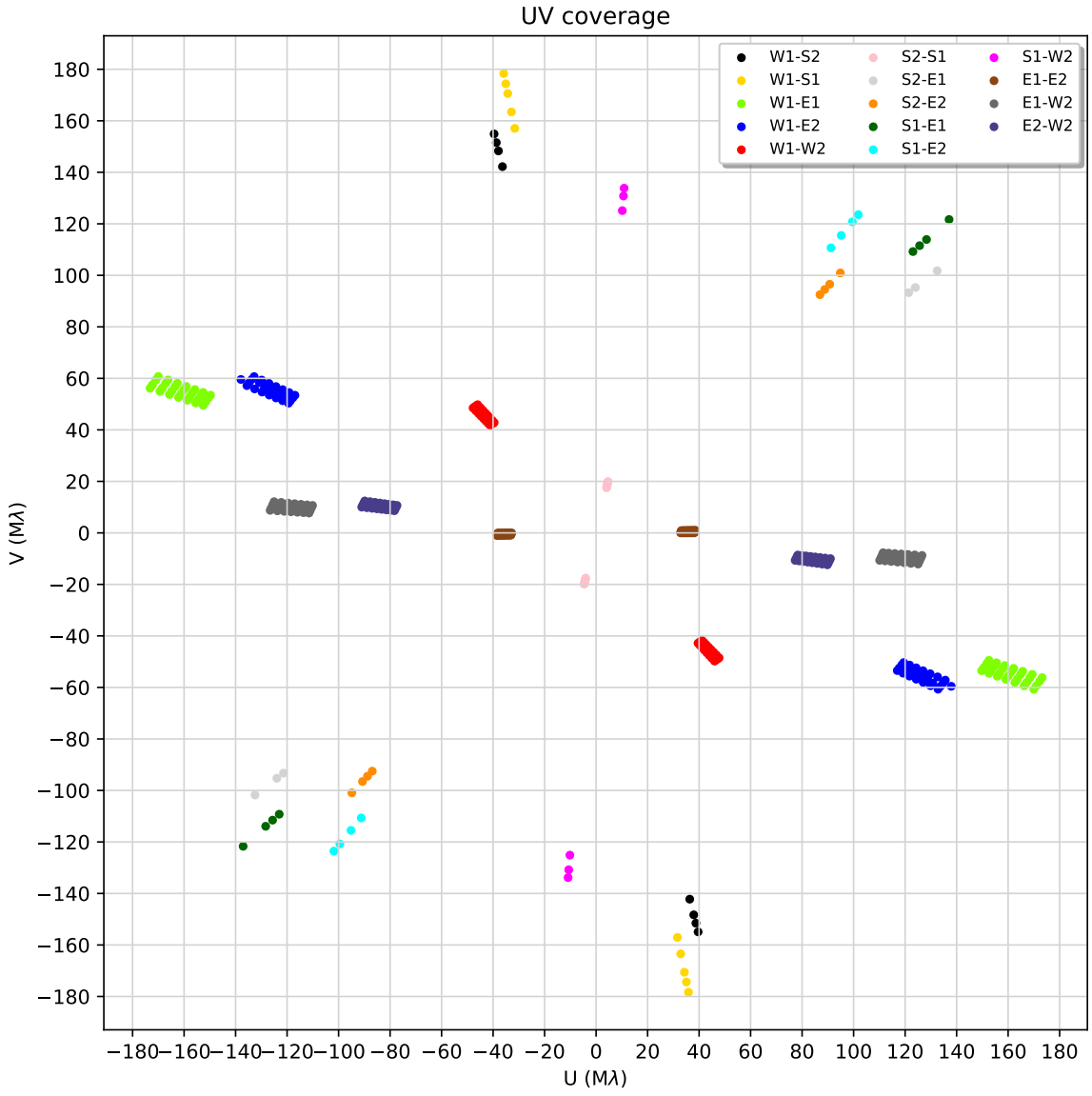

Figure A46: (u, v) coverage for FZ Per in 2015

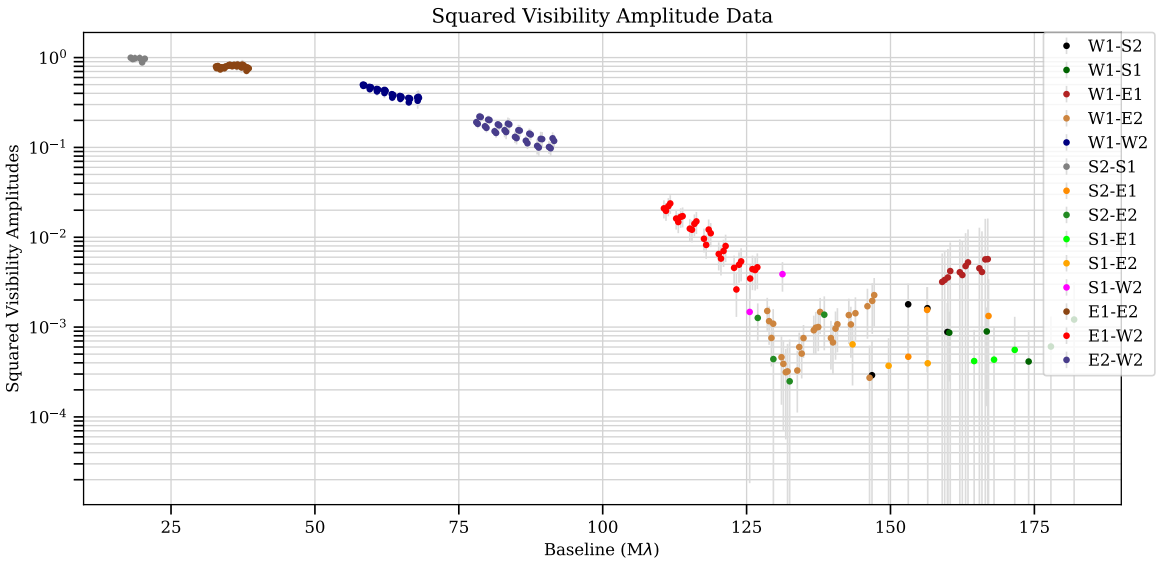

Figure A47: V^2 of FZ Per in 2015

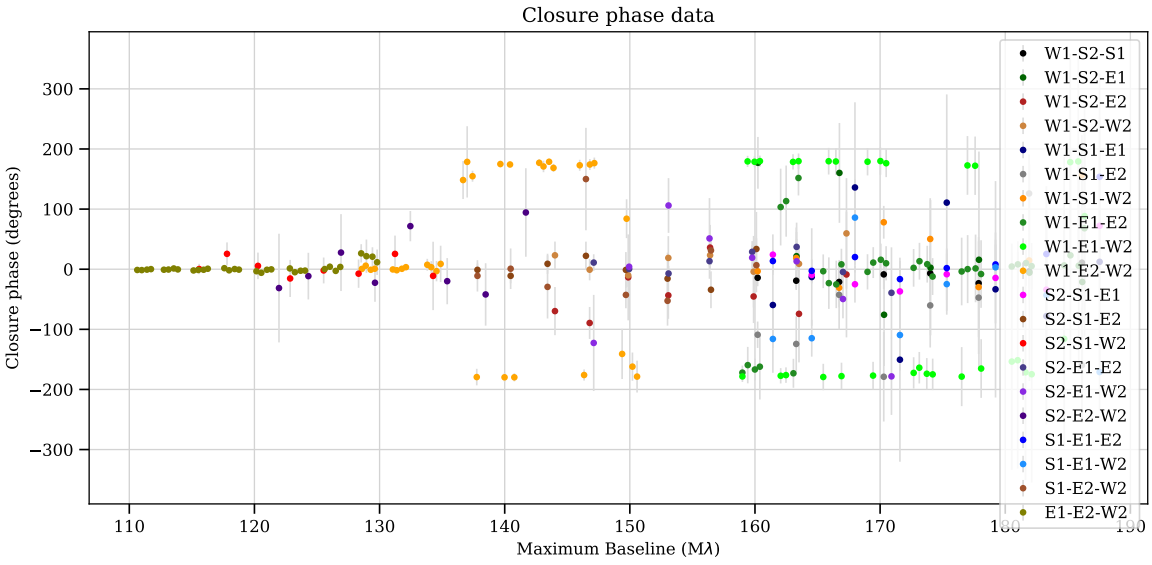

Figure A48: Closure phases of FZ Per in 2015

H KK Per

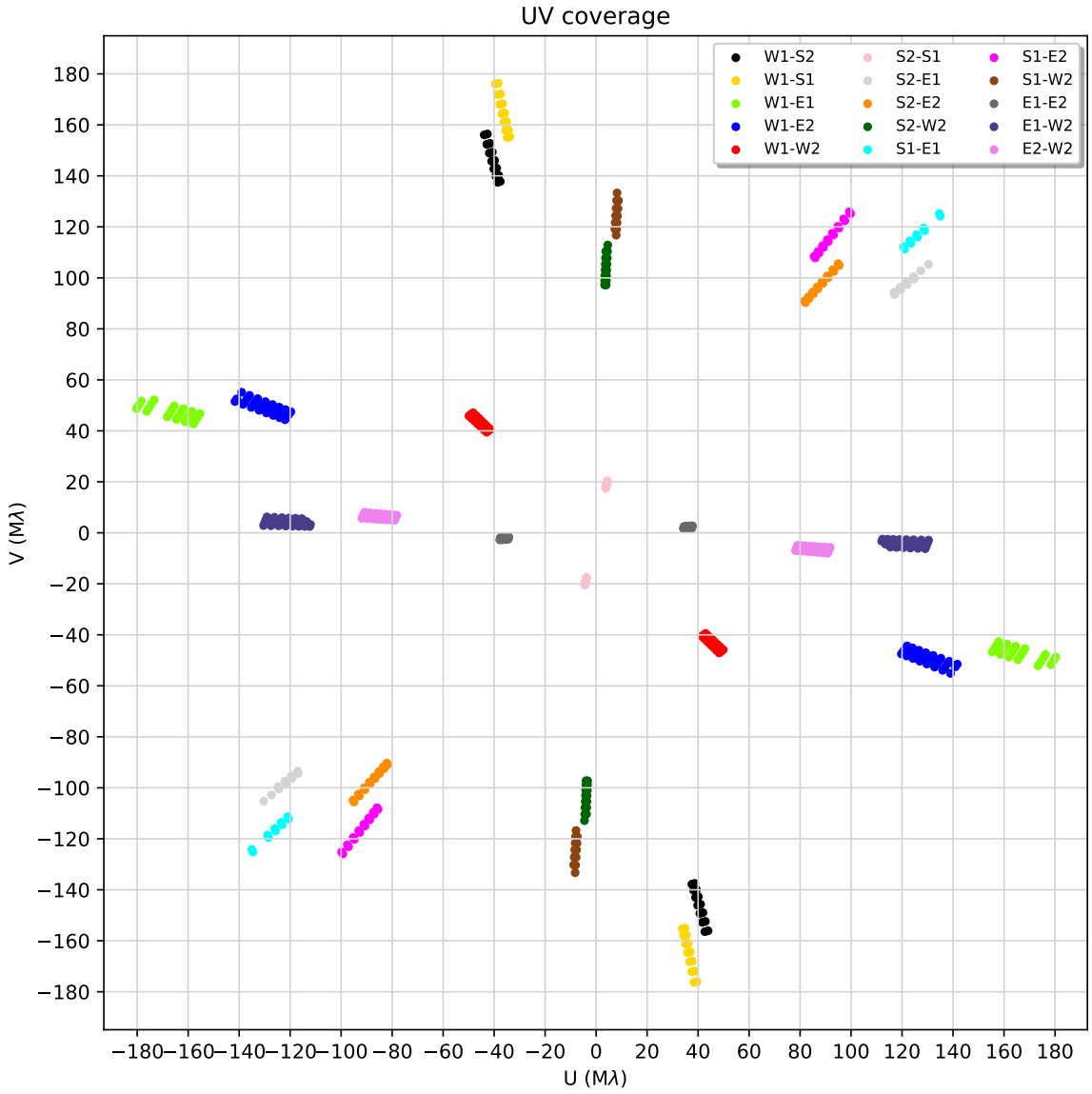

Figure A49: (u, v) coverage for KK Per in 2016

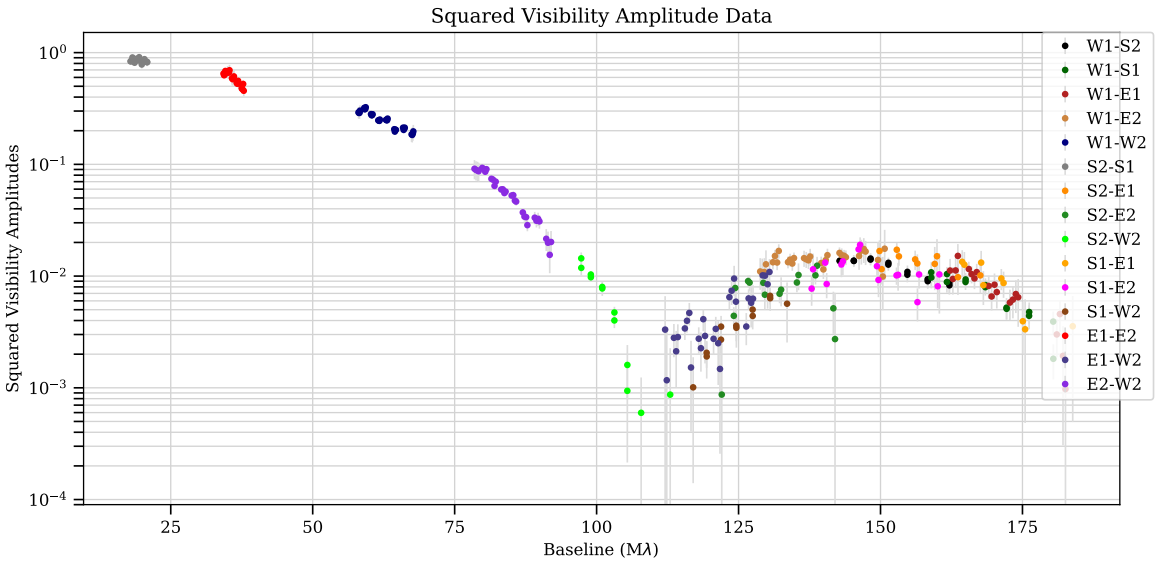

Figure A50: V^2 of KK Per in 2016

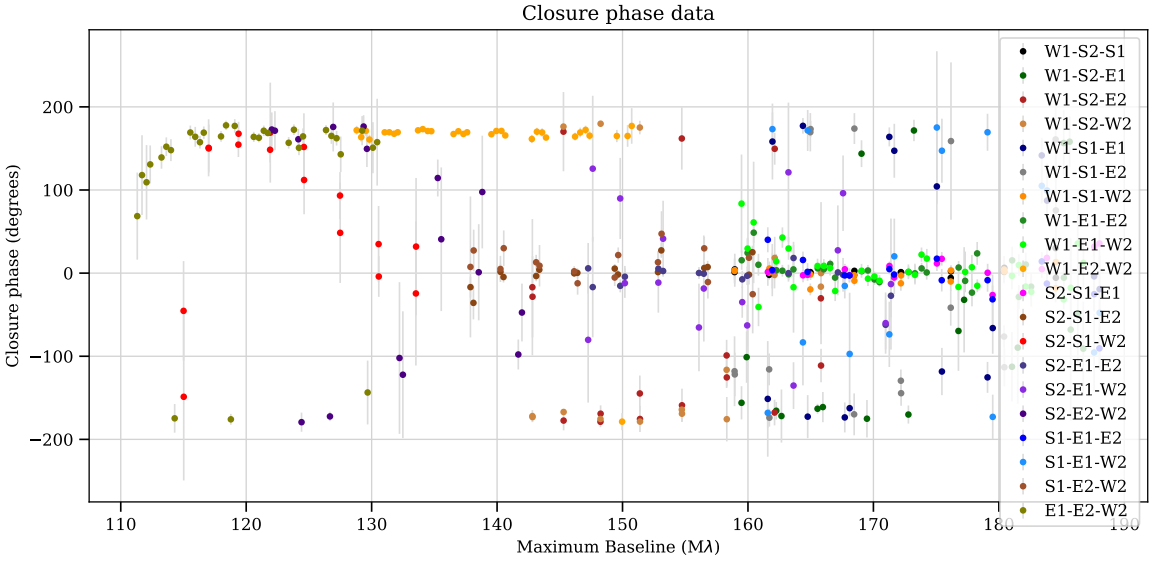

Figure A51: Closure phases of KK Per in 2016

I PP Per

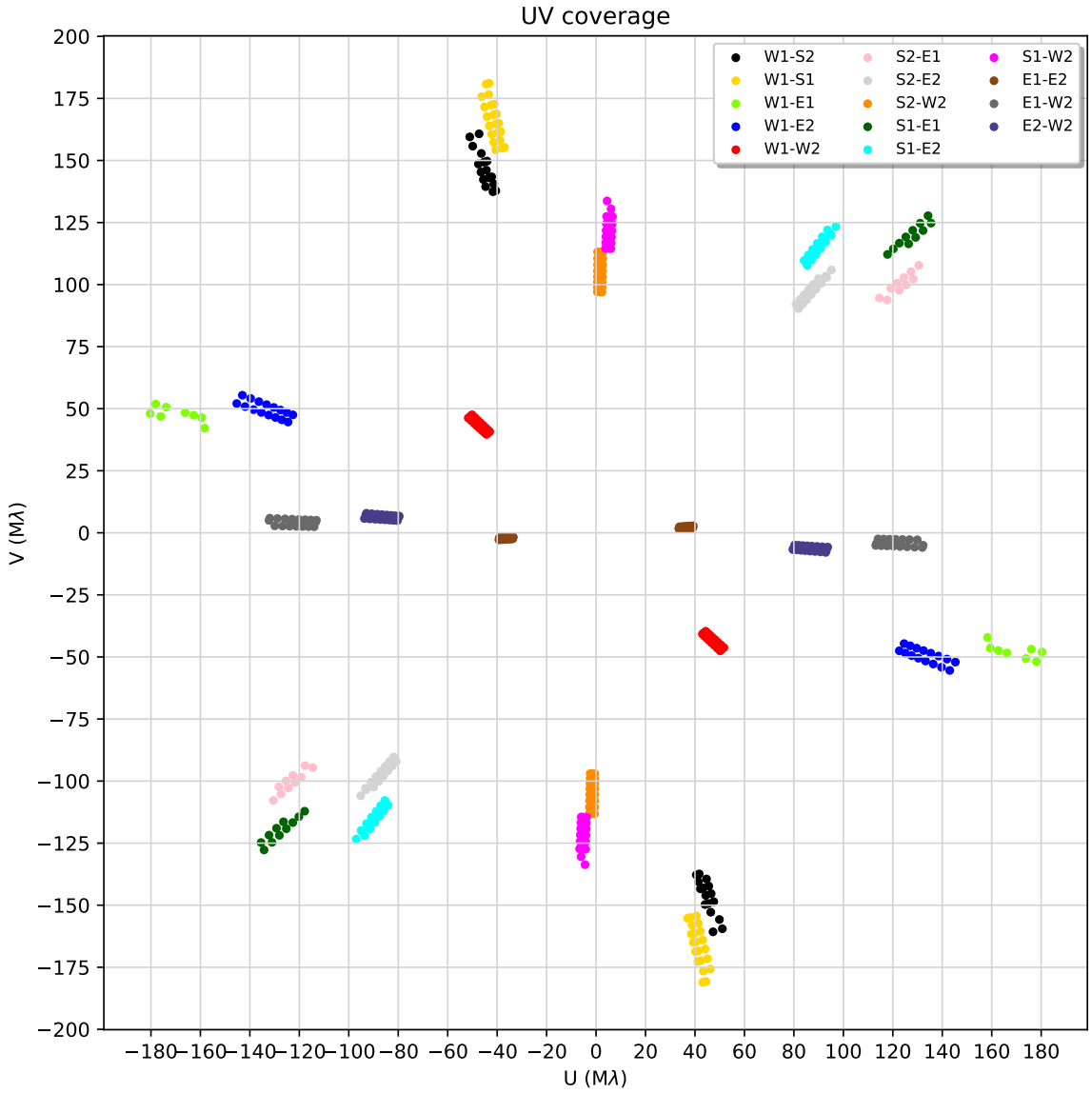

Figure A52: (u, v) coverage for PP Per in 2015

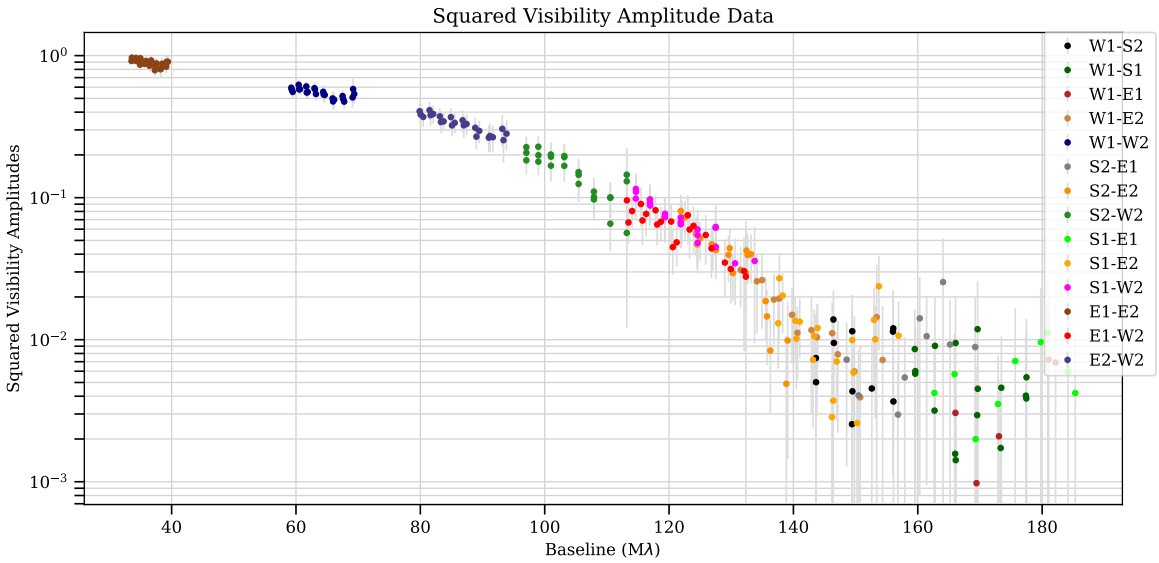

Figure A53: V^2 of PP Per in 2015

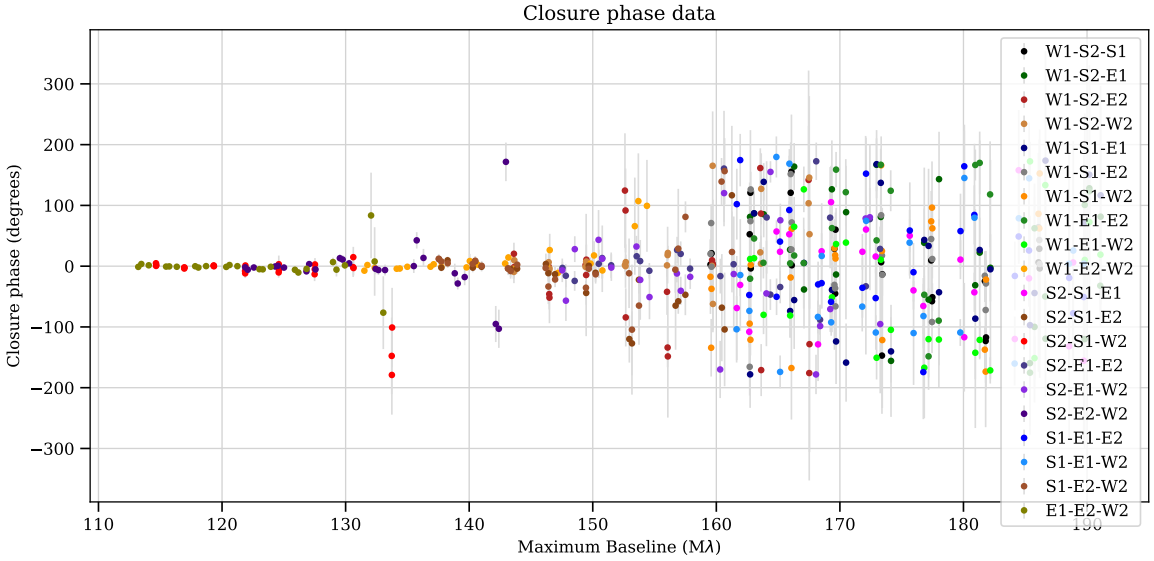

Figure A54: Closure phases of PP Per in 2015

J PR Per

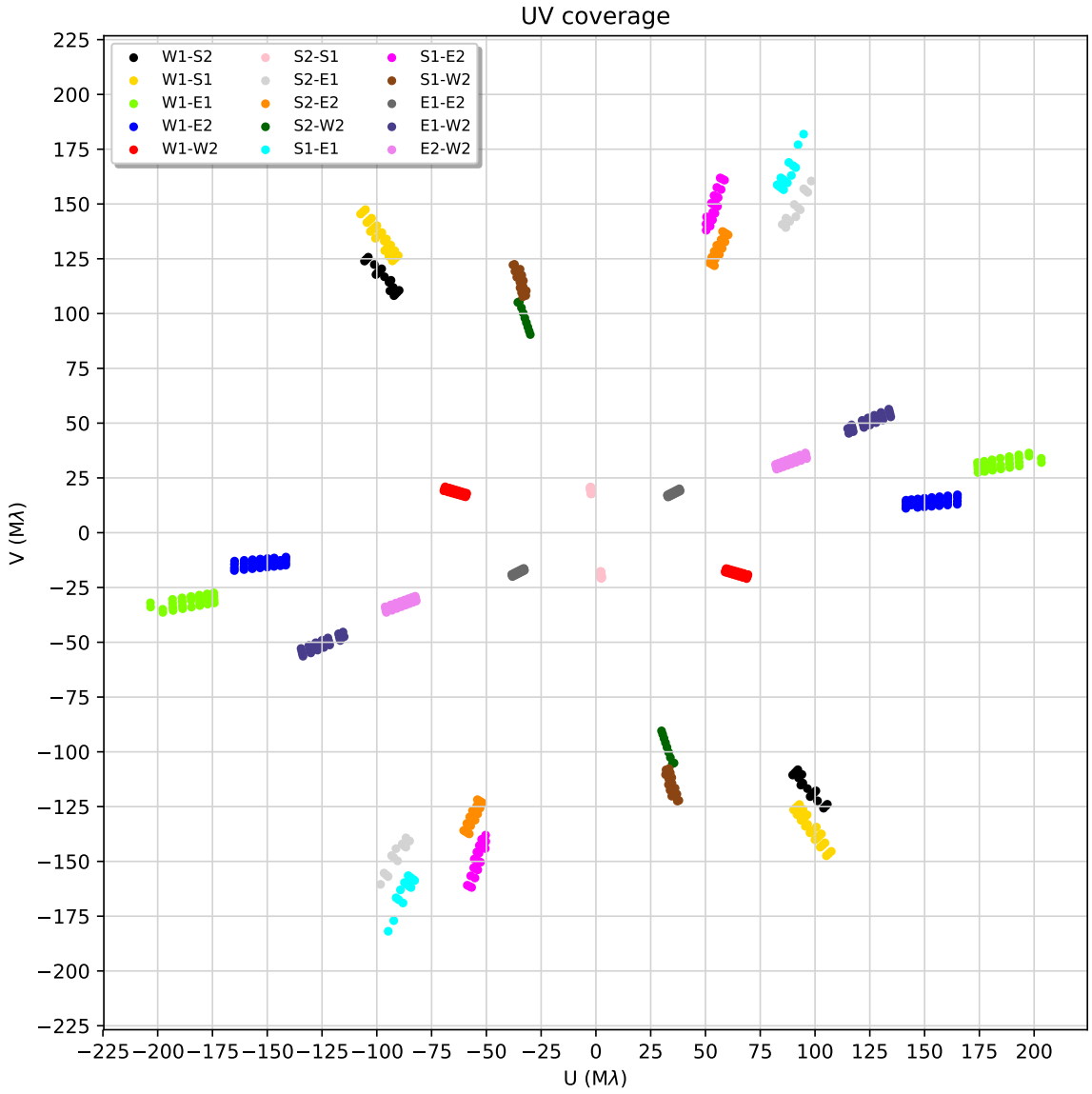

Figure A55: (u, v) coverage for PR Per in 2016

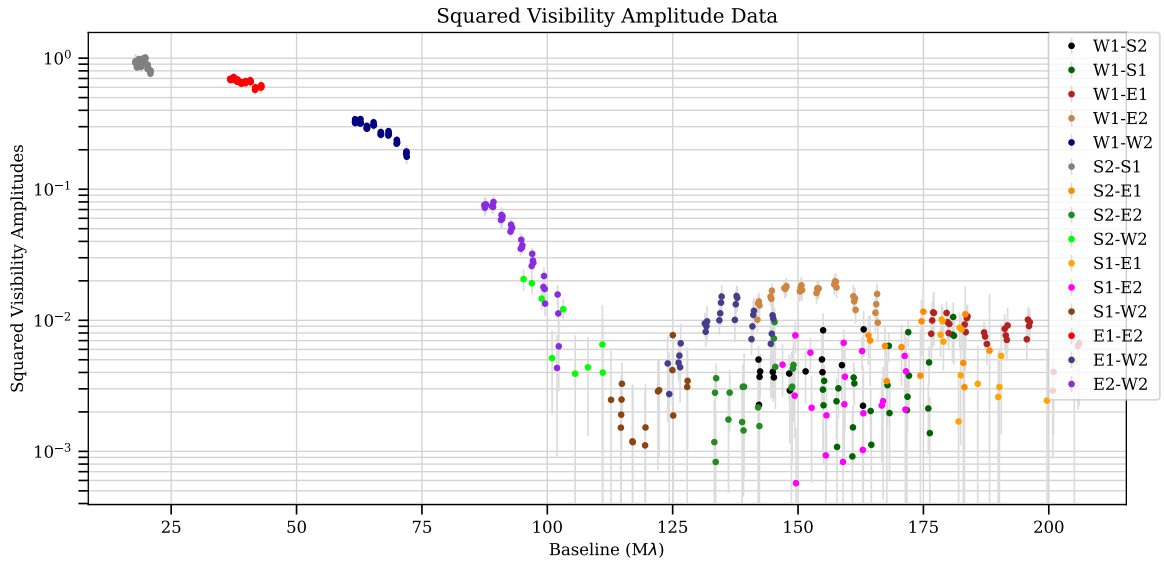

Figure A56: V^2 of PR Per in 2016

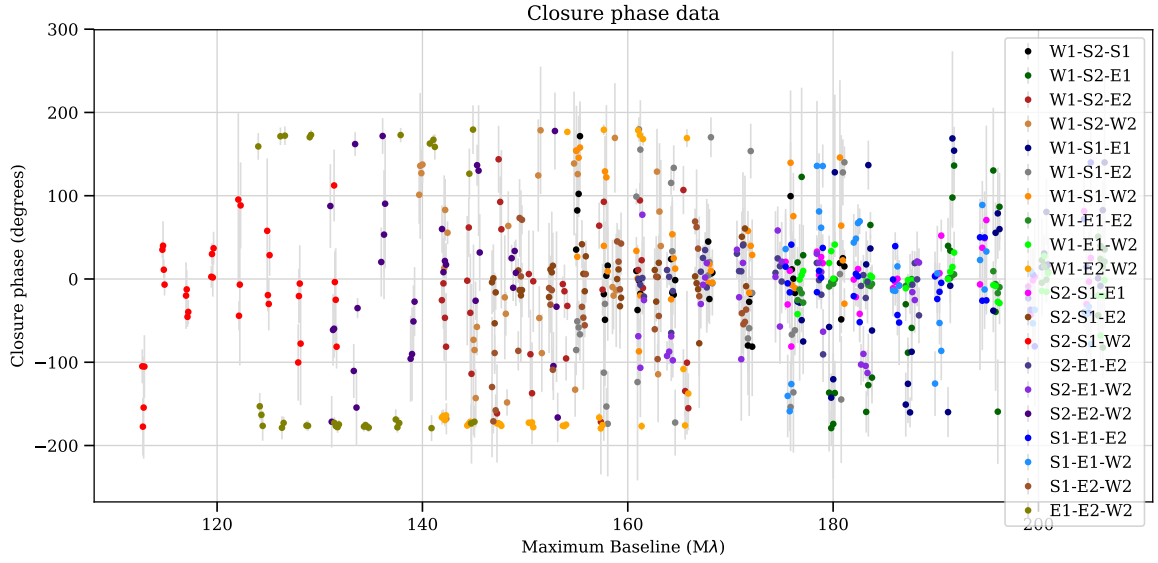

Figure A57: Closure phases of PR Per in 2016

K RS Per

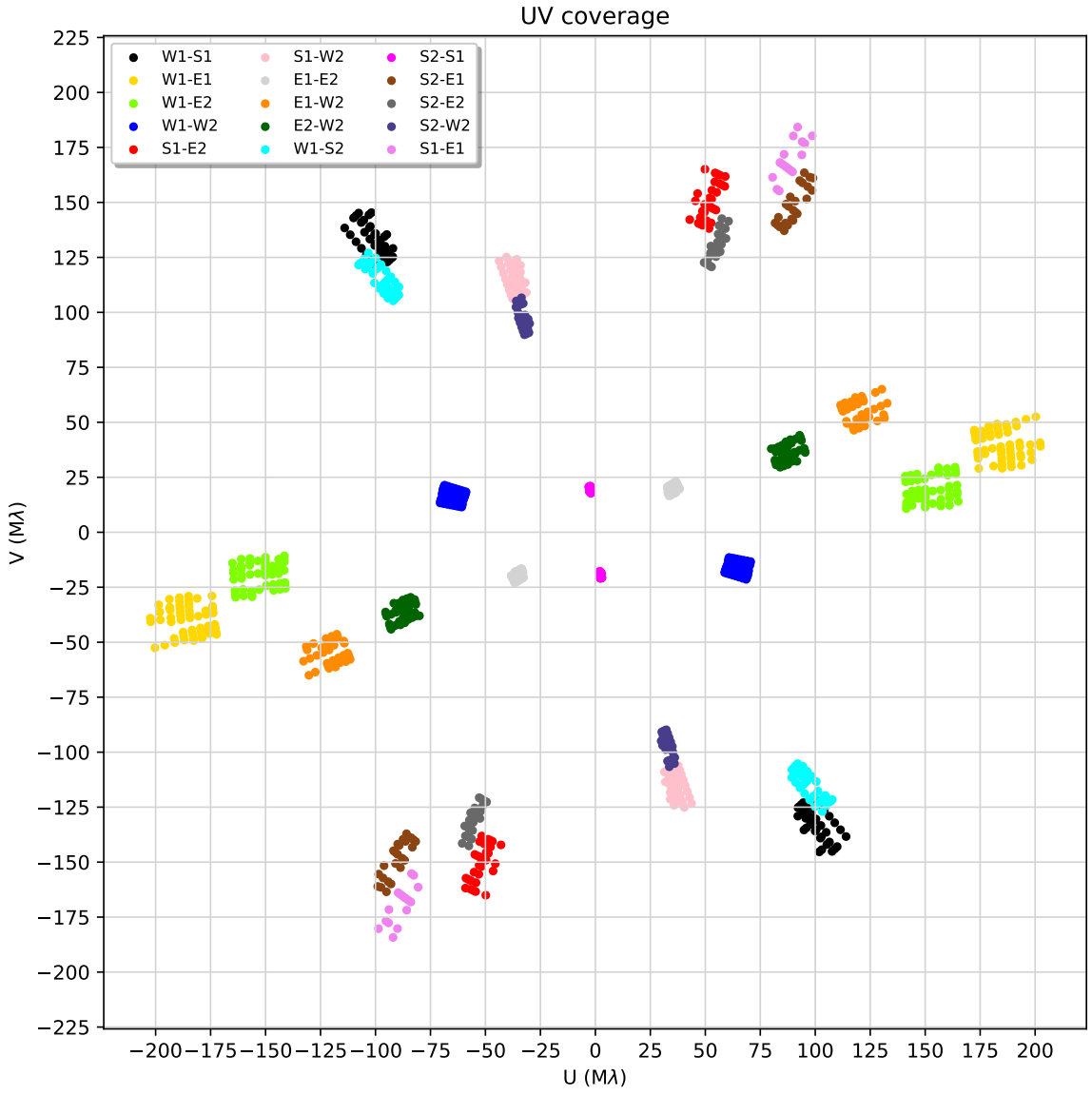

Figure A58: (u, v) coverage for RS Per in 2016

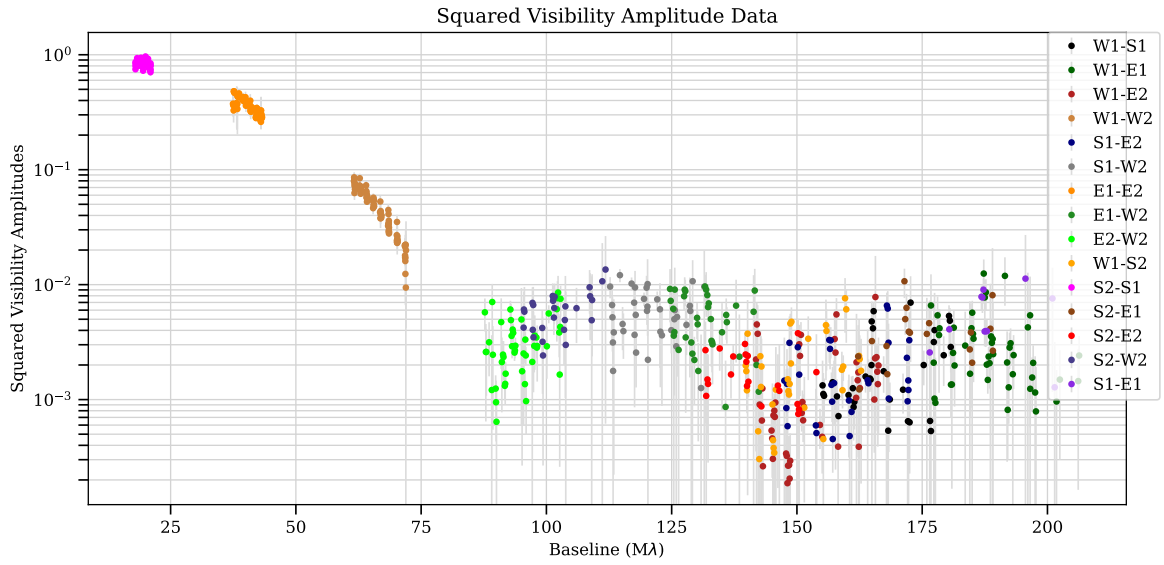

Figure A59: V^2 of RS Per in 2016

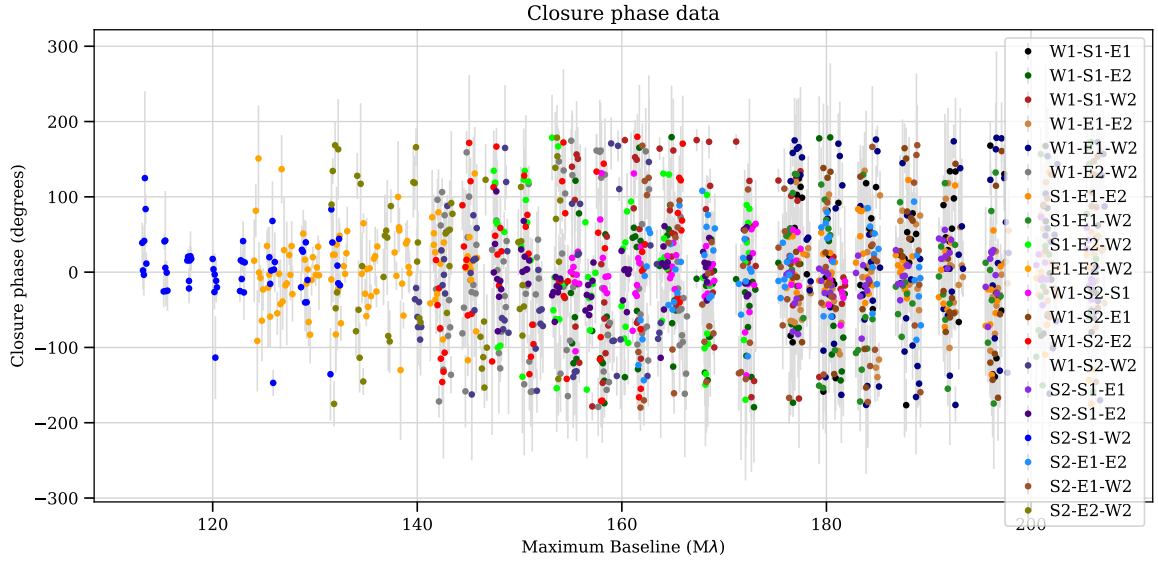

Figure A60: Closure phases of RS Per in 2016

L RW Cyg

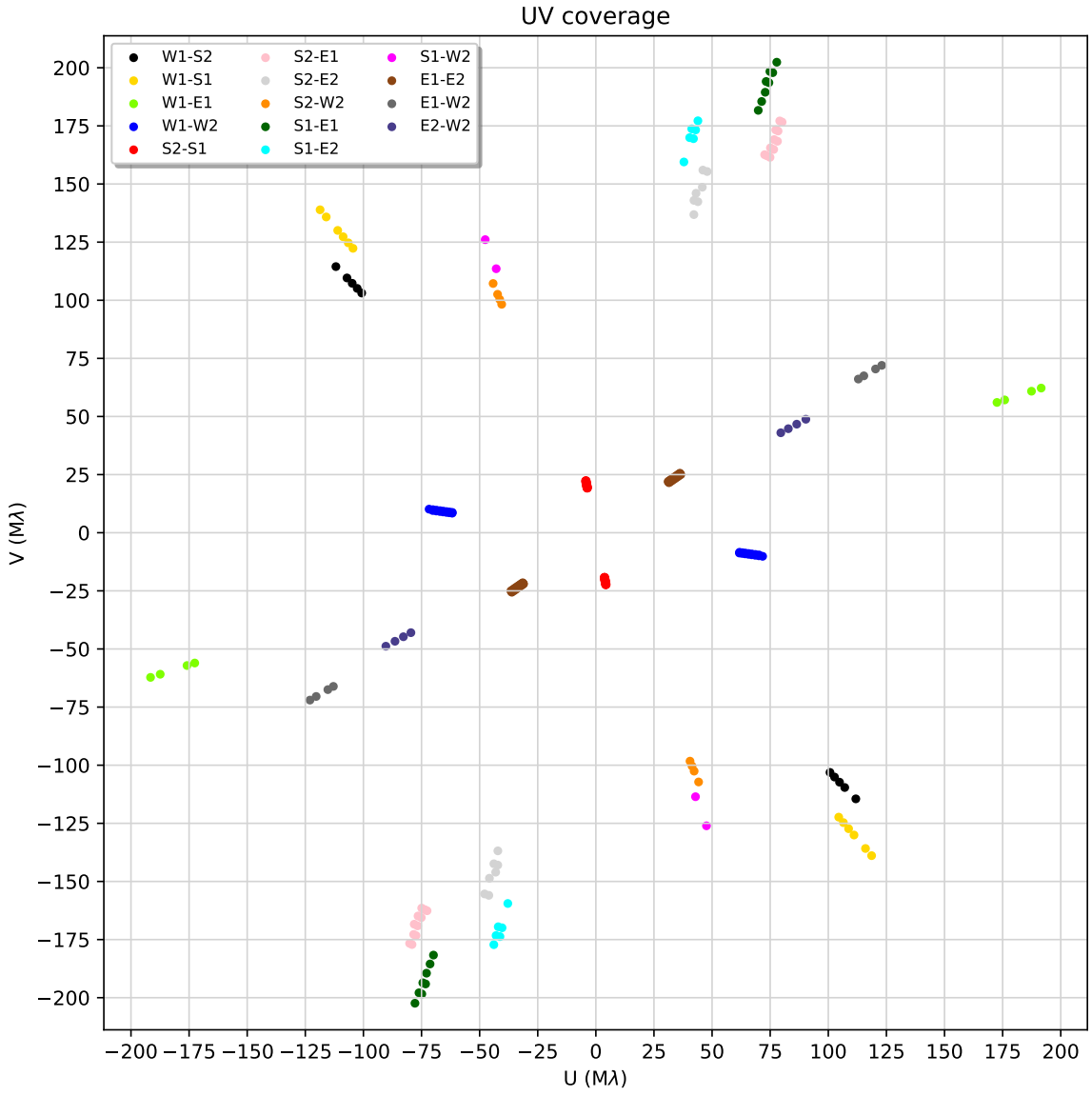

Figure A61: $(u,\ v)$ coverage for RW Cyg in 2015

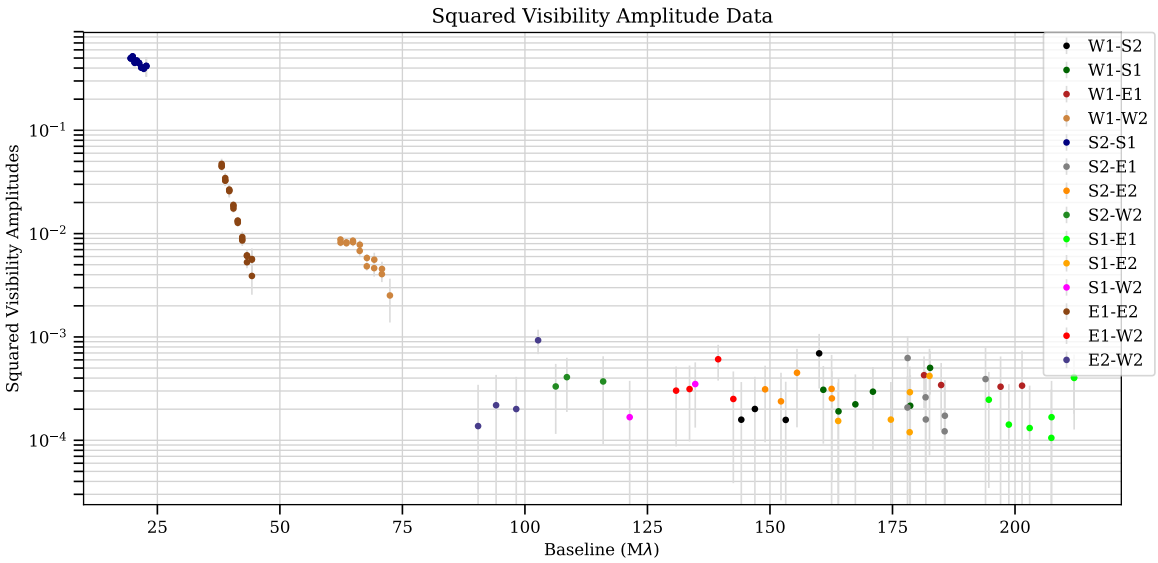

Figure A62: V^2 of RW Cyg in 2015

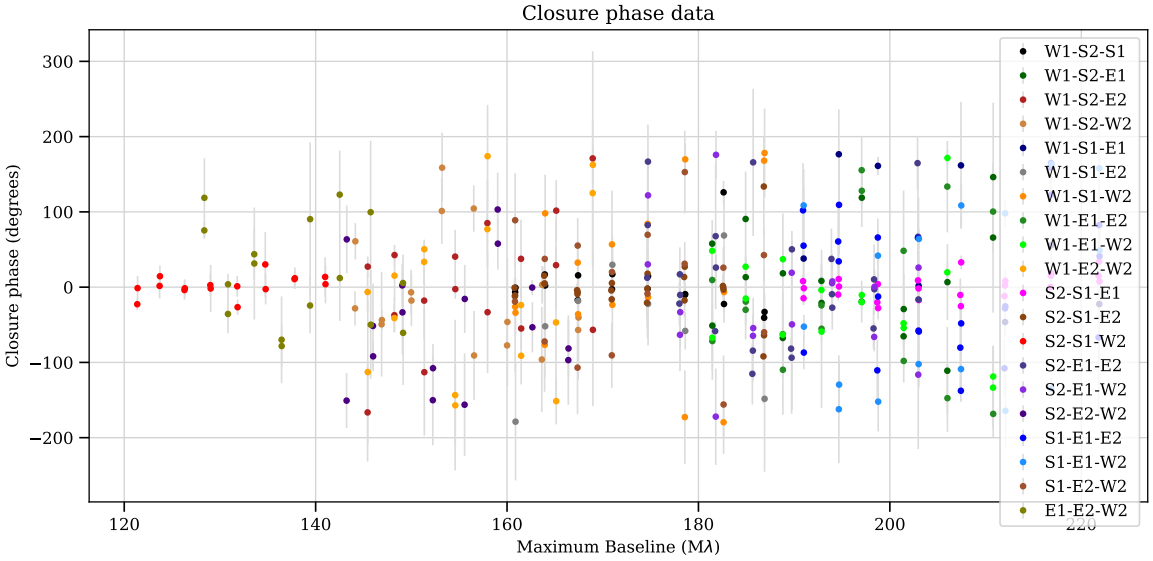

Figure A63: Closure phases of RW Cyg in 2015

M S Per

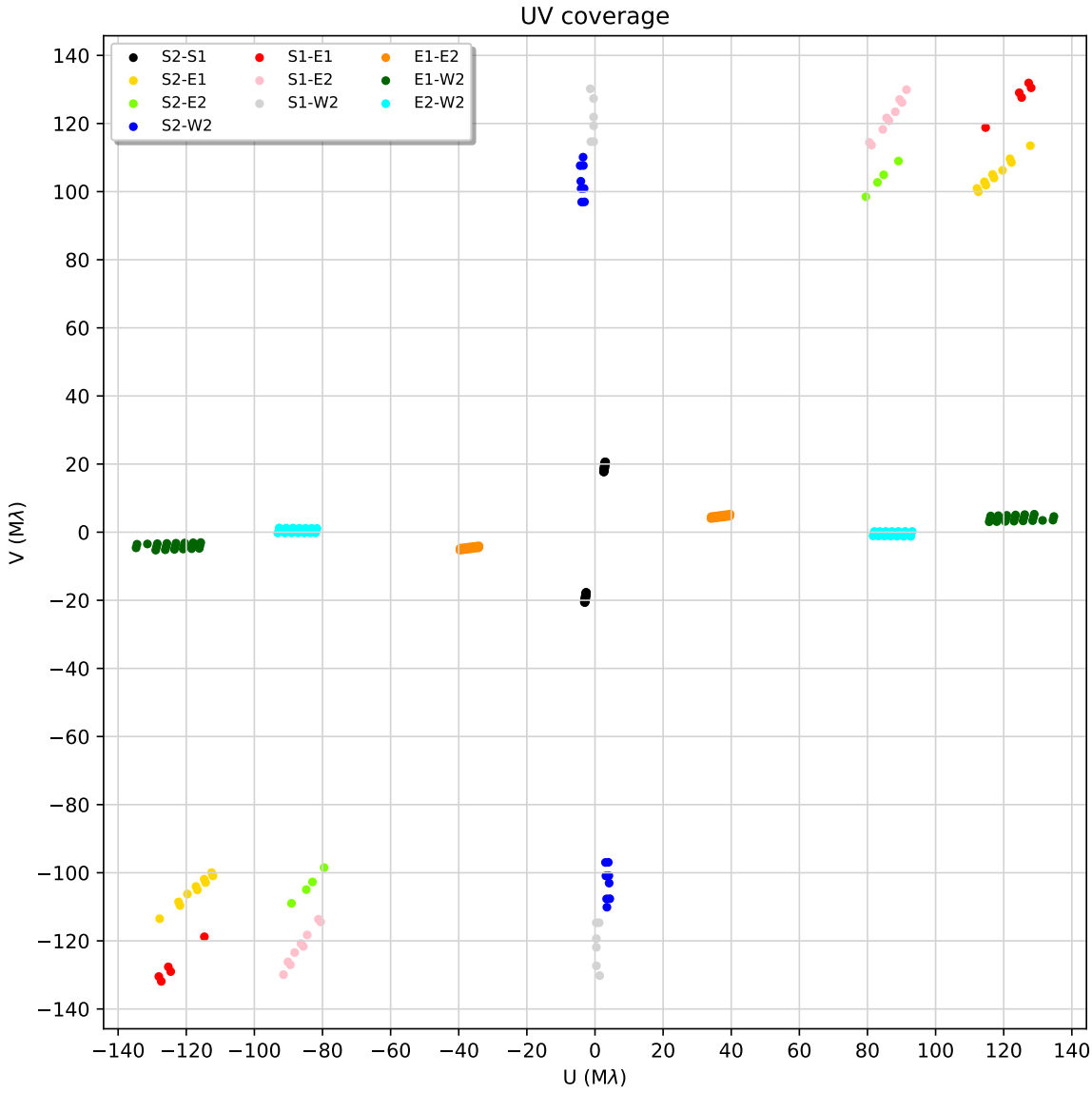

Figure A64: (u, v) coverage for S Per in 2015

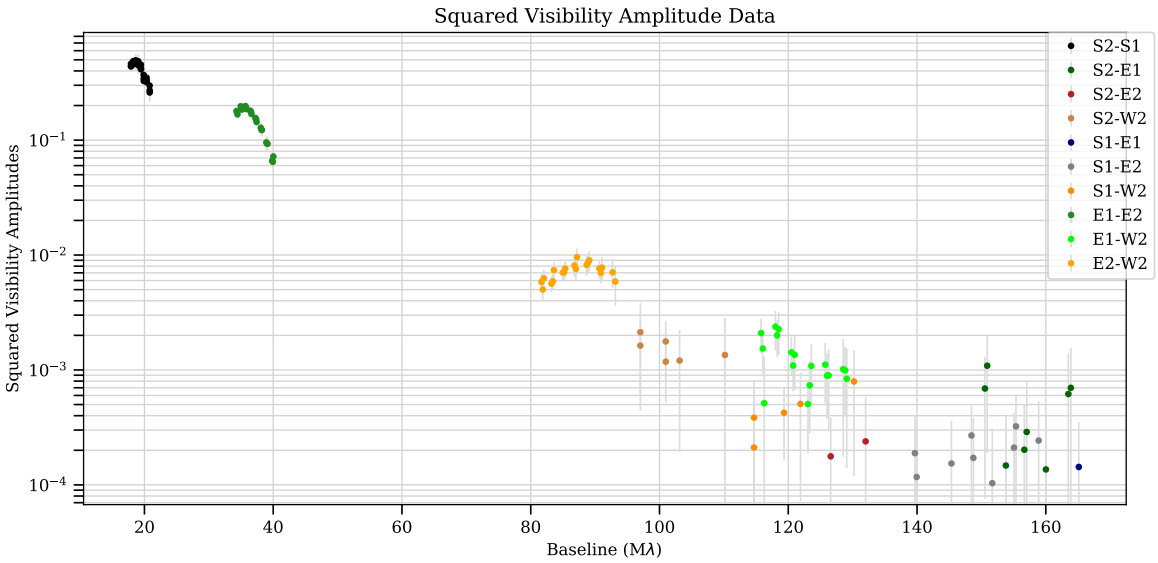

Figure A65: V^2 of S Per in 2015

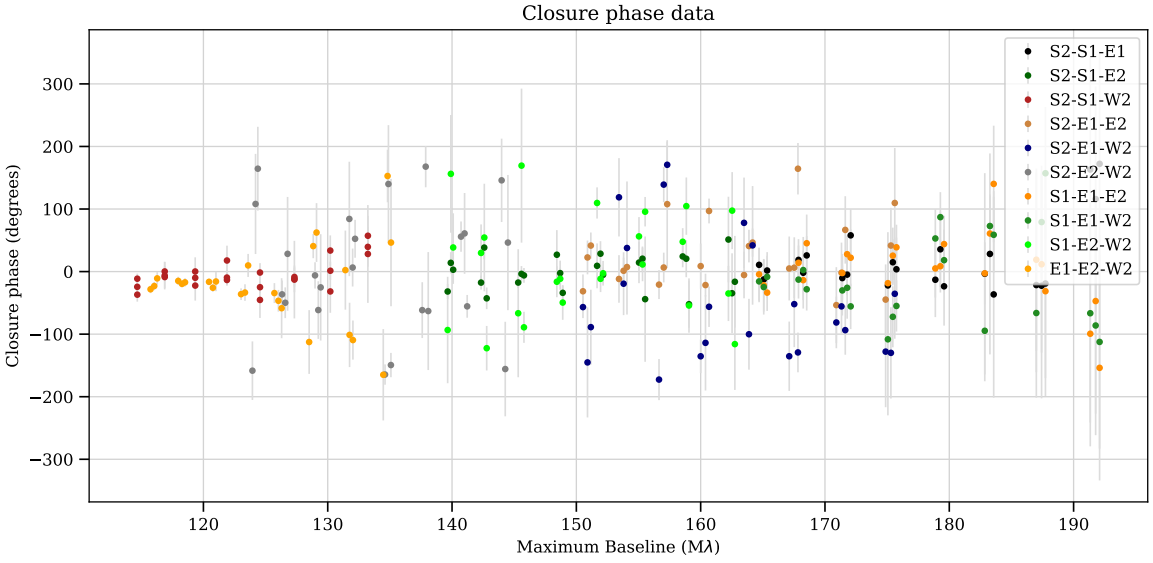

Figure A66: Closure phases of S Per in 2015

N SU Per

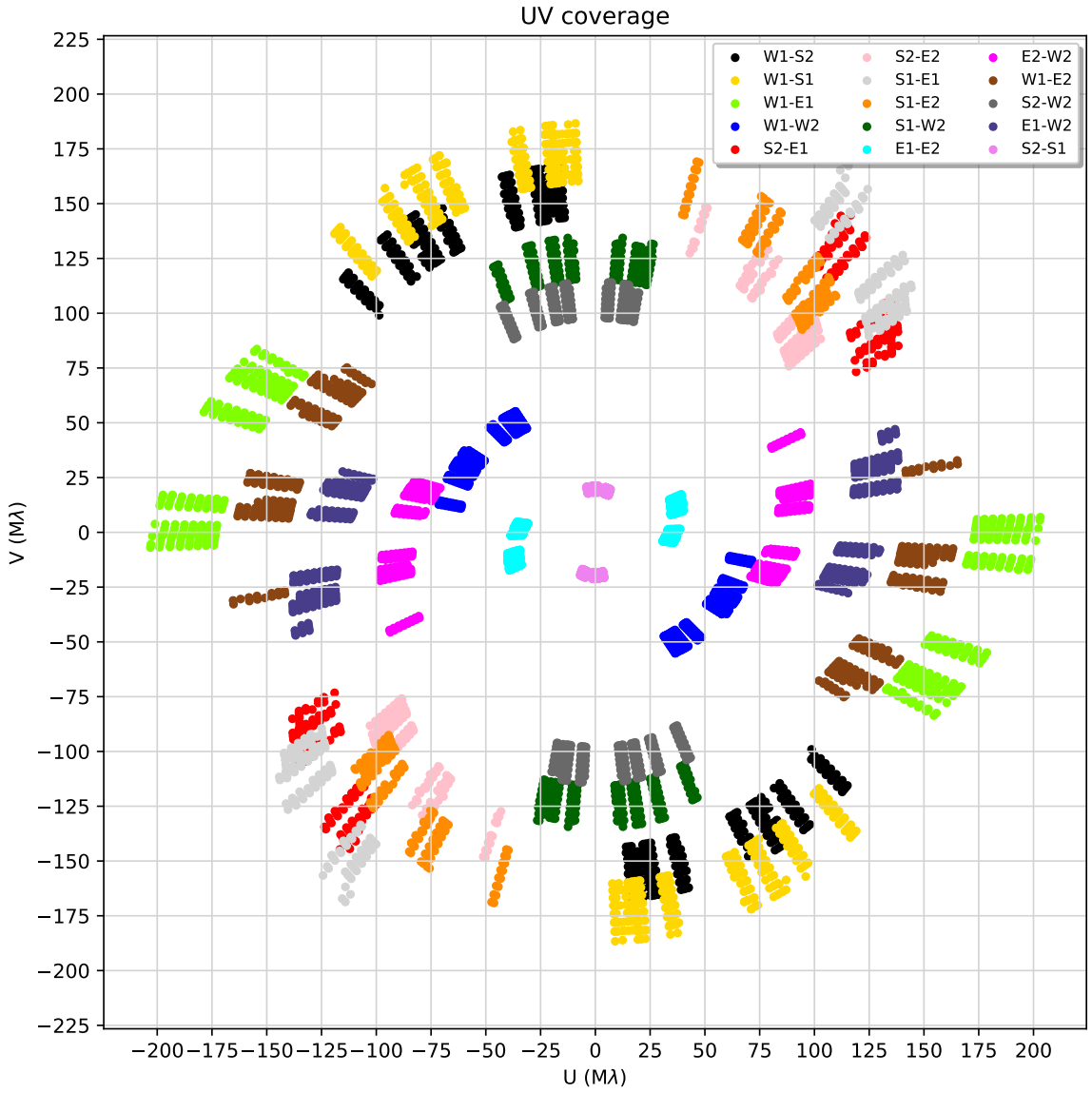

Figure A67: (u, v) coverage for SU Per in 2016 August

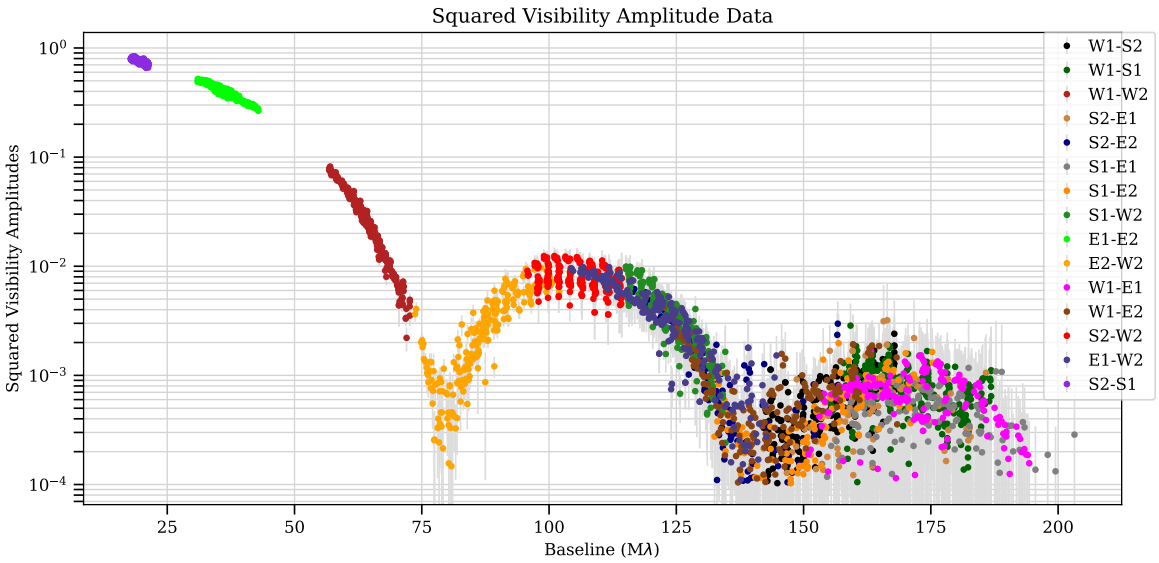

Figure A68: V^2 of SU Per in 2016 August

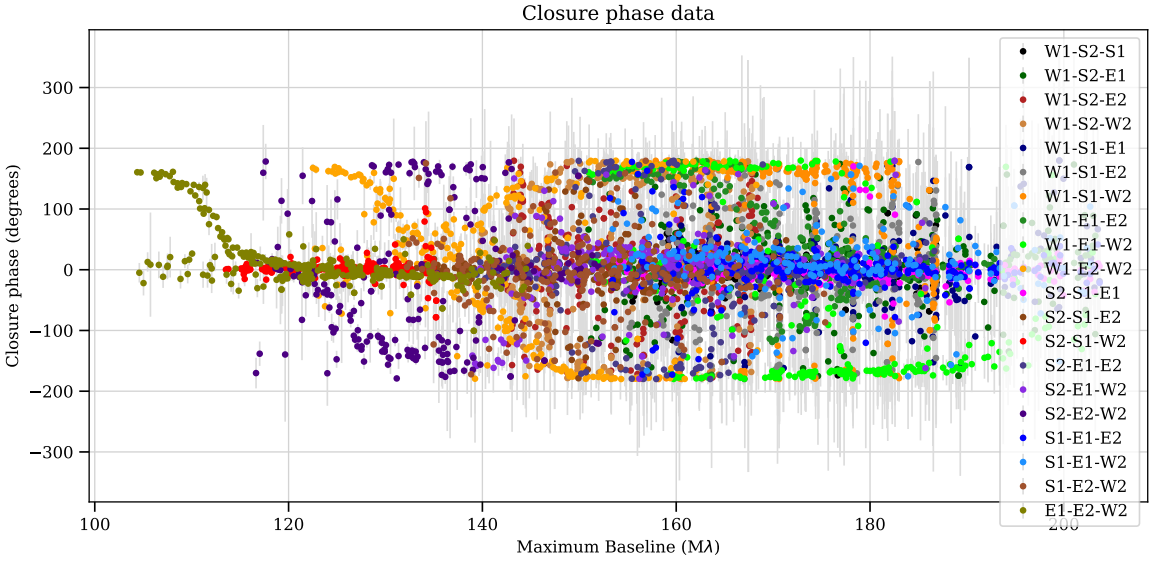

Figure A69: Closure phases of SU Per in 2015 August

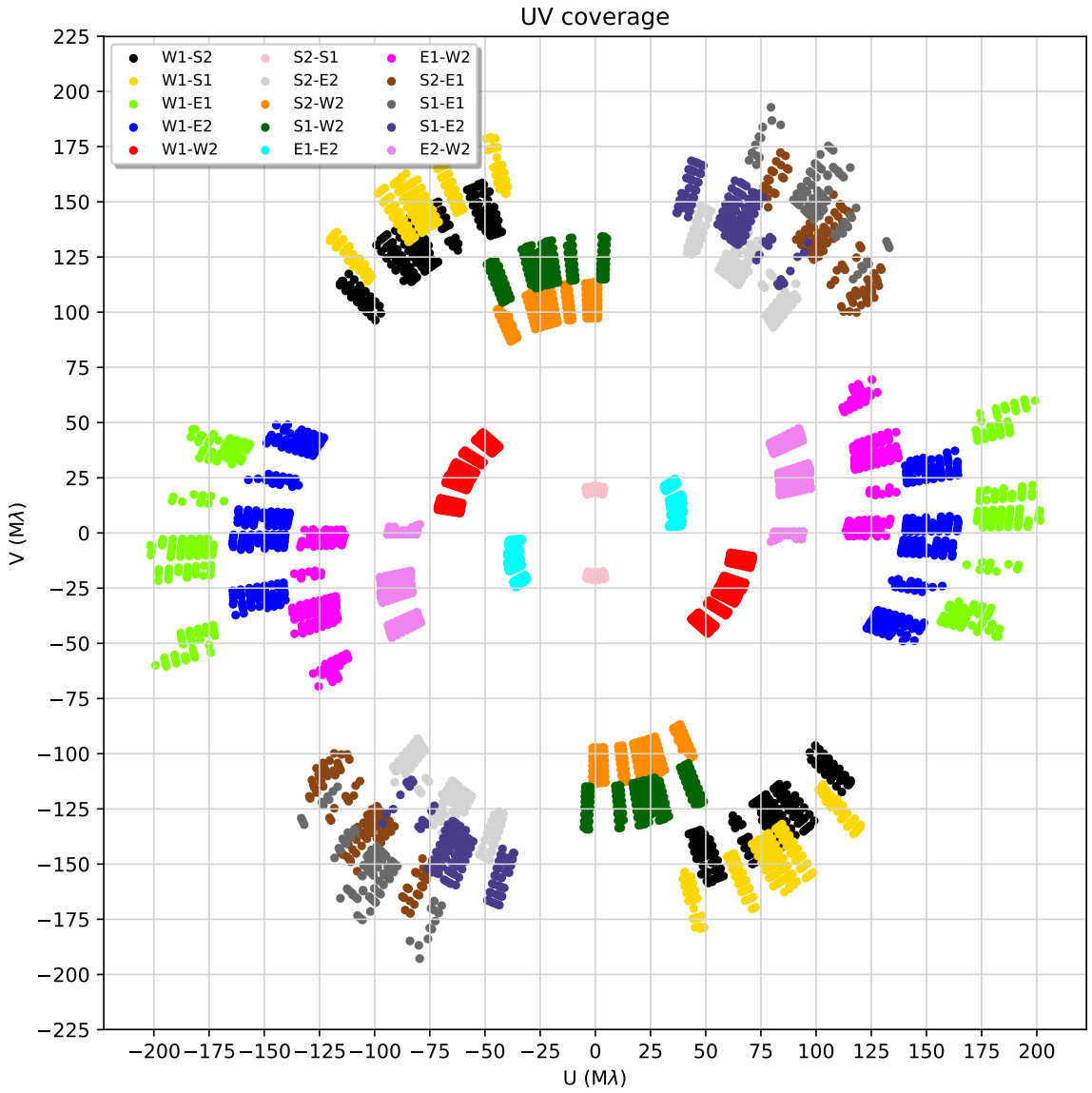

Figure A70: (u, v) coverage for SU Per in 2016 August

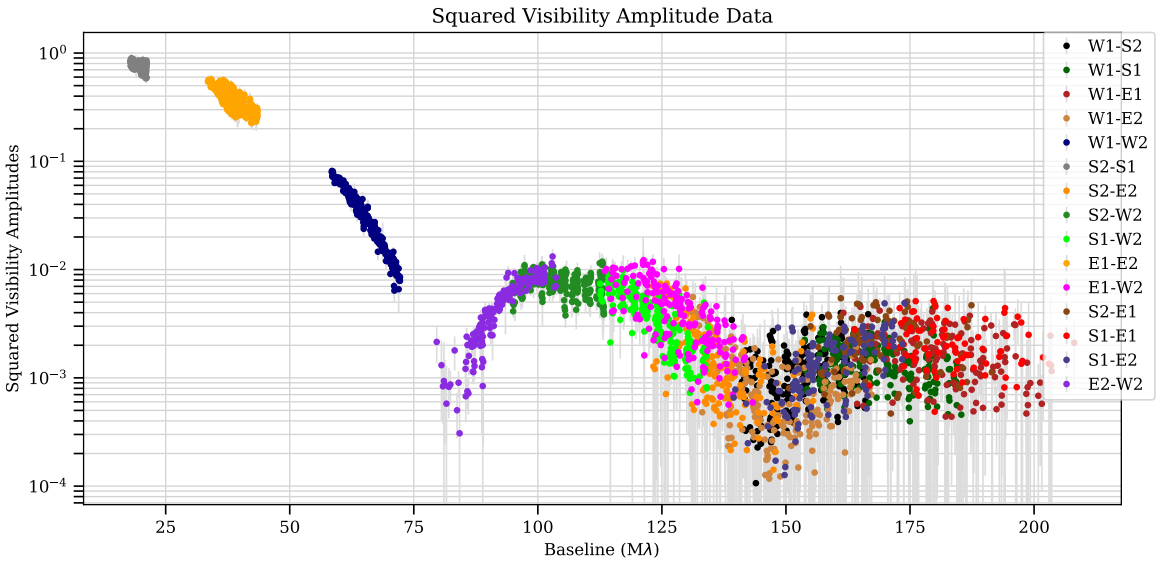

Figure A71: V^2 of SU Per in 2016 August

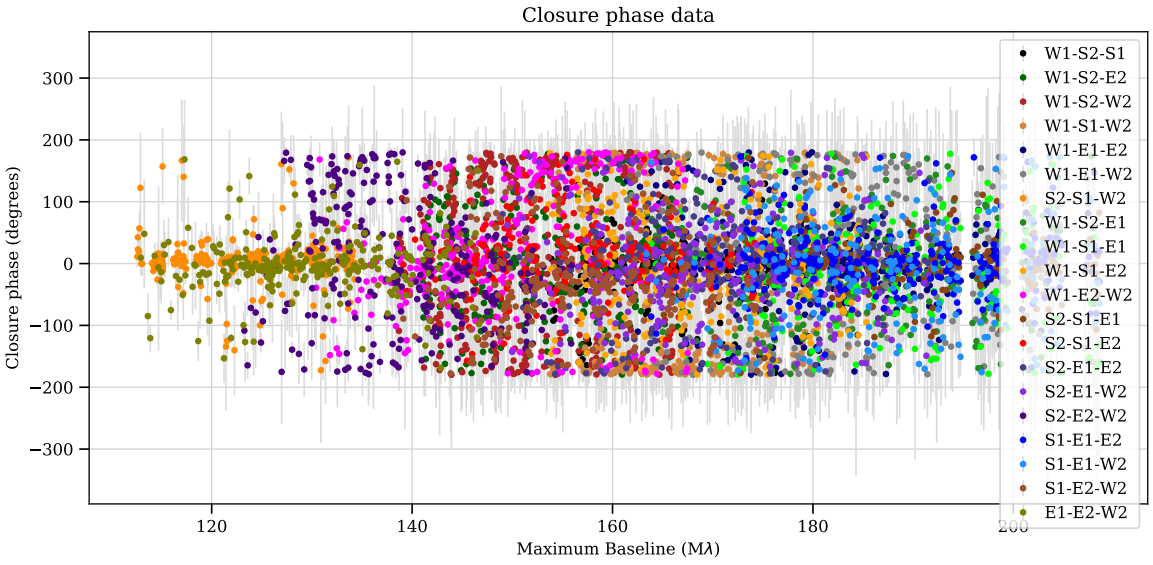

Figure A72: Closure phases of SU Per in 2016 August

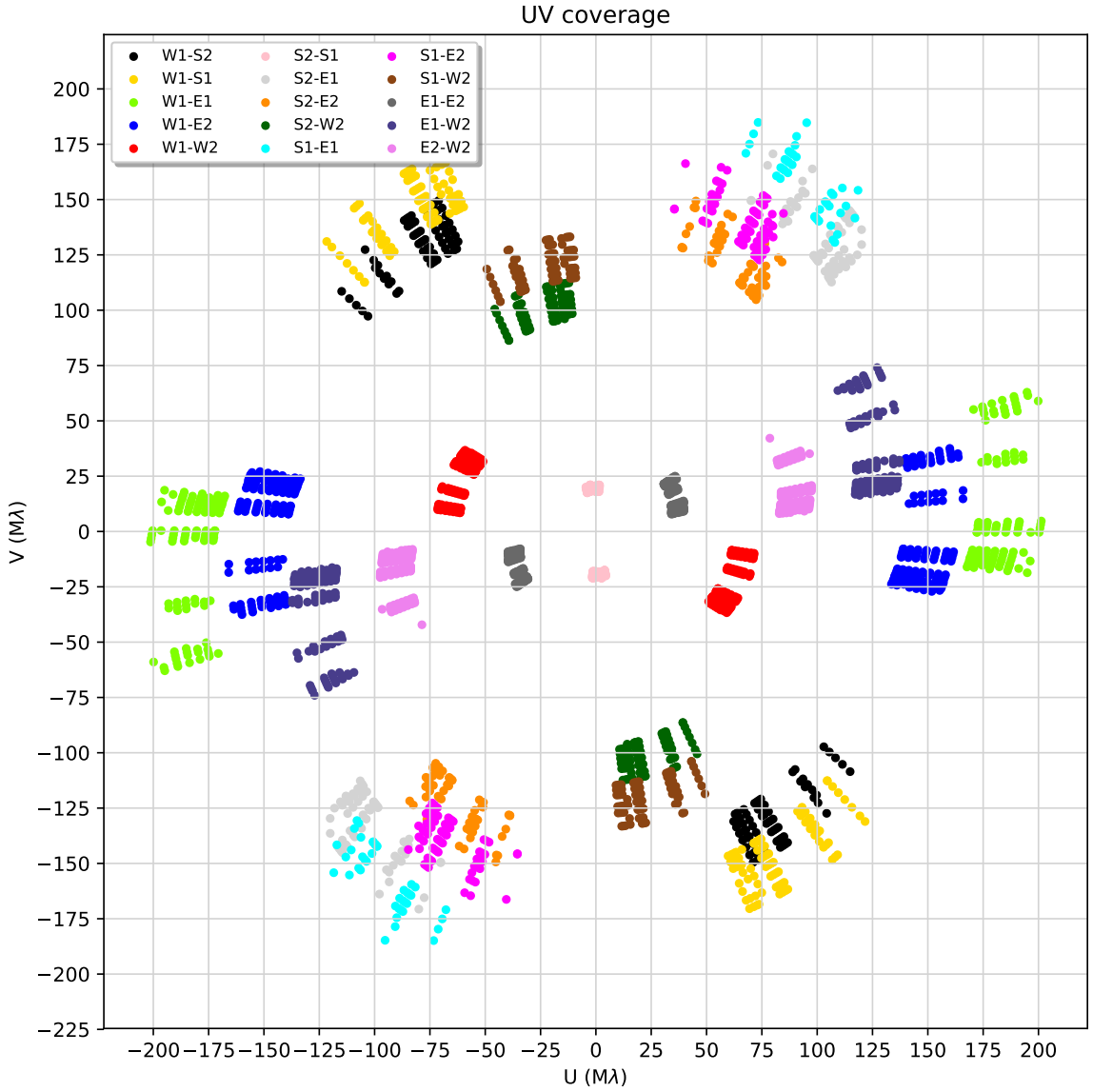

Figure A73: (u, v) coverage for SU Per in 2016 October

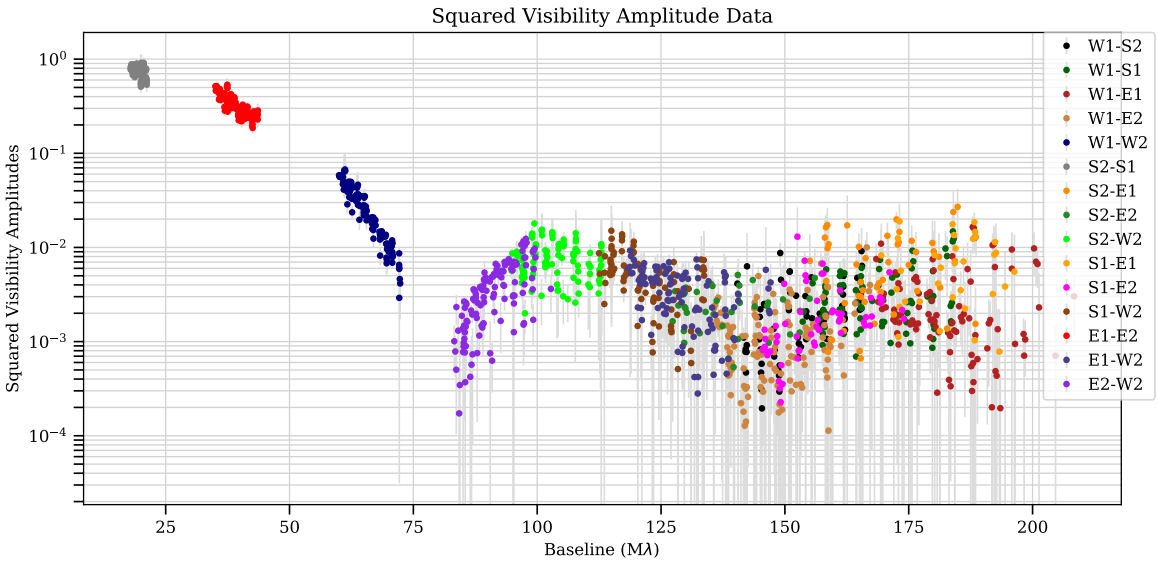

Figure A74: V^2 of SU Per in 2016 October

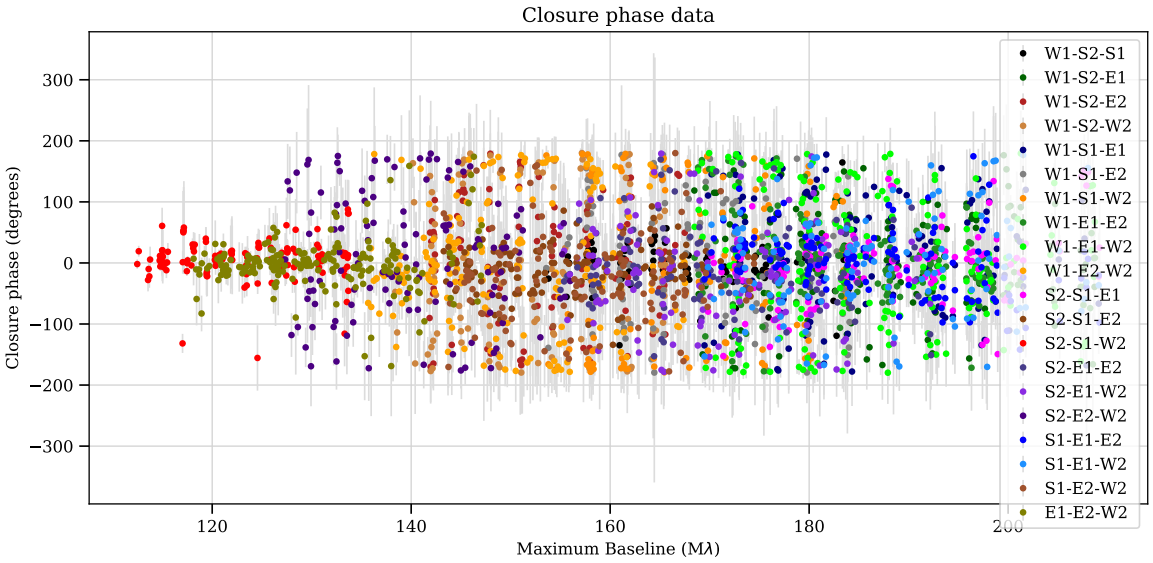

Figure A75: Closure phases of SU Per in 2016 October

O TV Gem

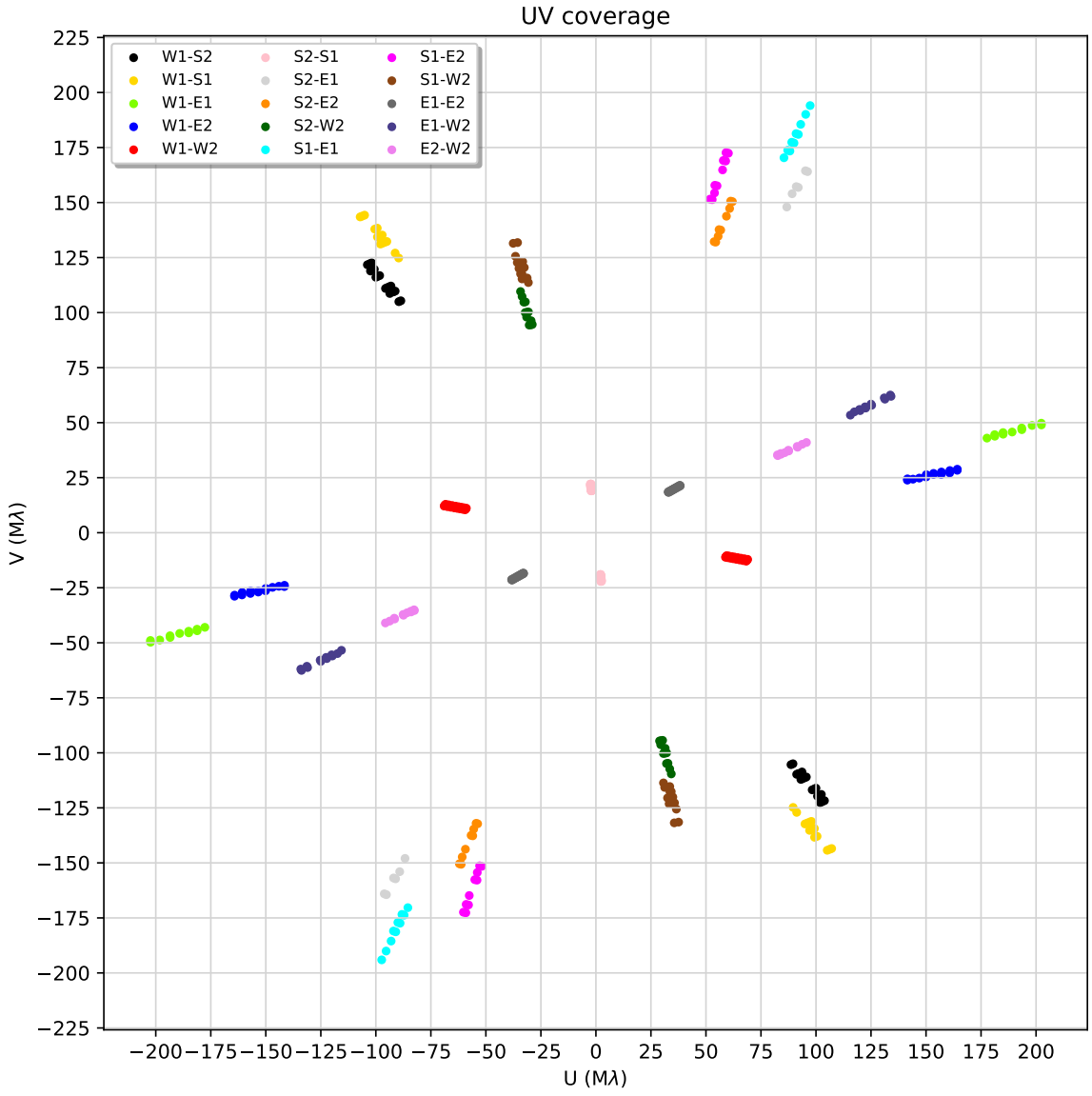

Figure A76: (u, v) coverage for TV Gem

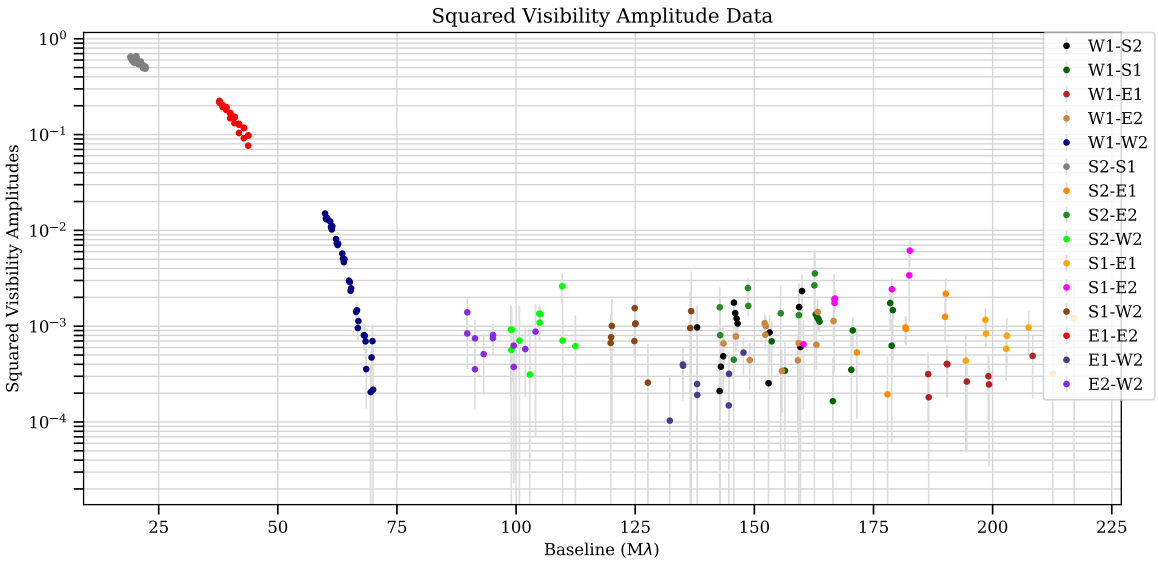

Figure A77: V^2 of TV Gem

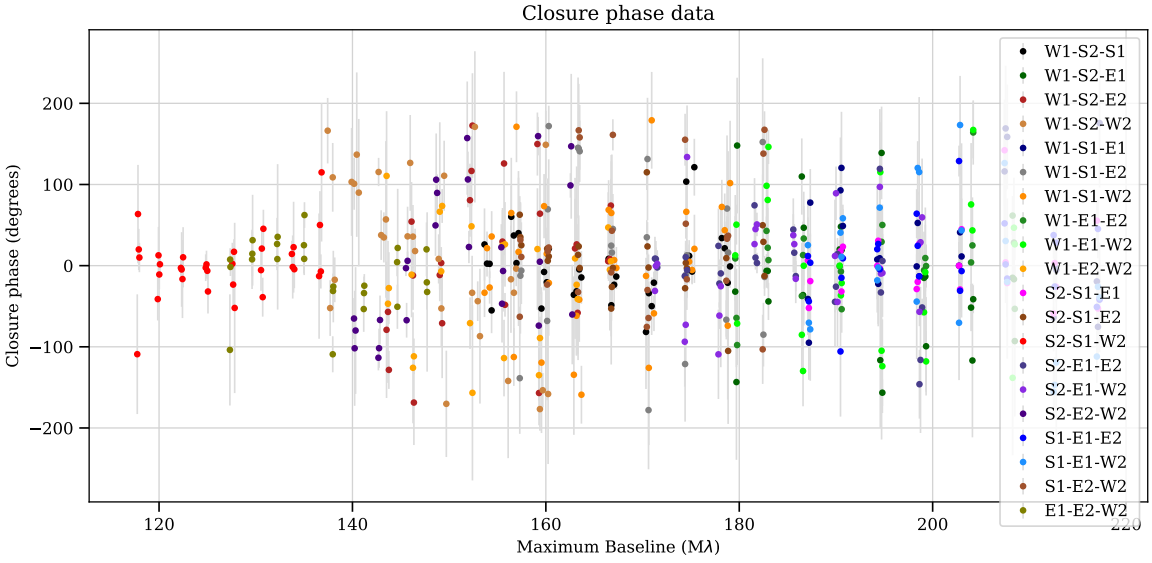

Figure A78: Closure phases of TV Gem

P V366 Amd

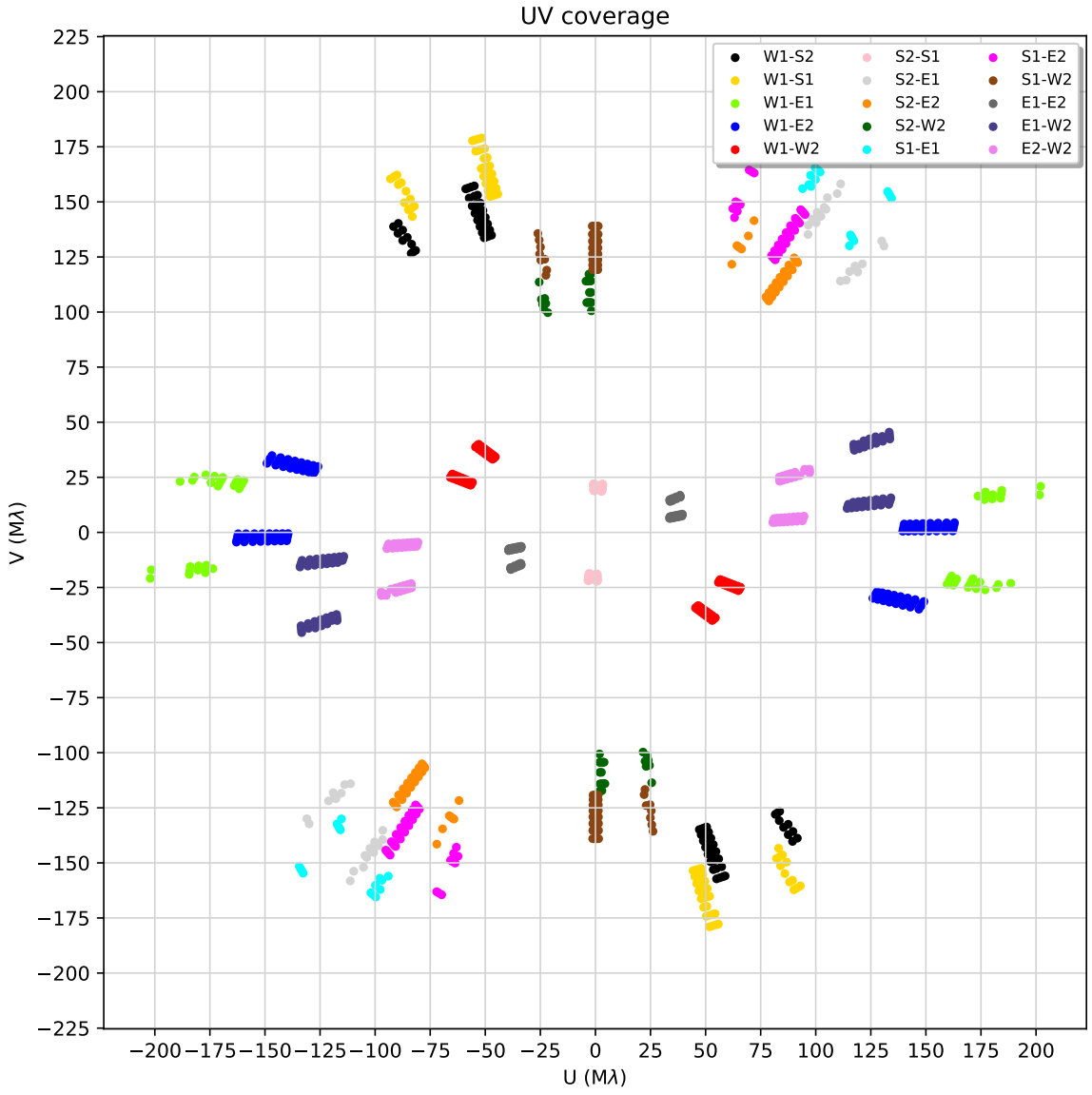

Figure A79: (u, v) coverage for V366 And in 2016

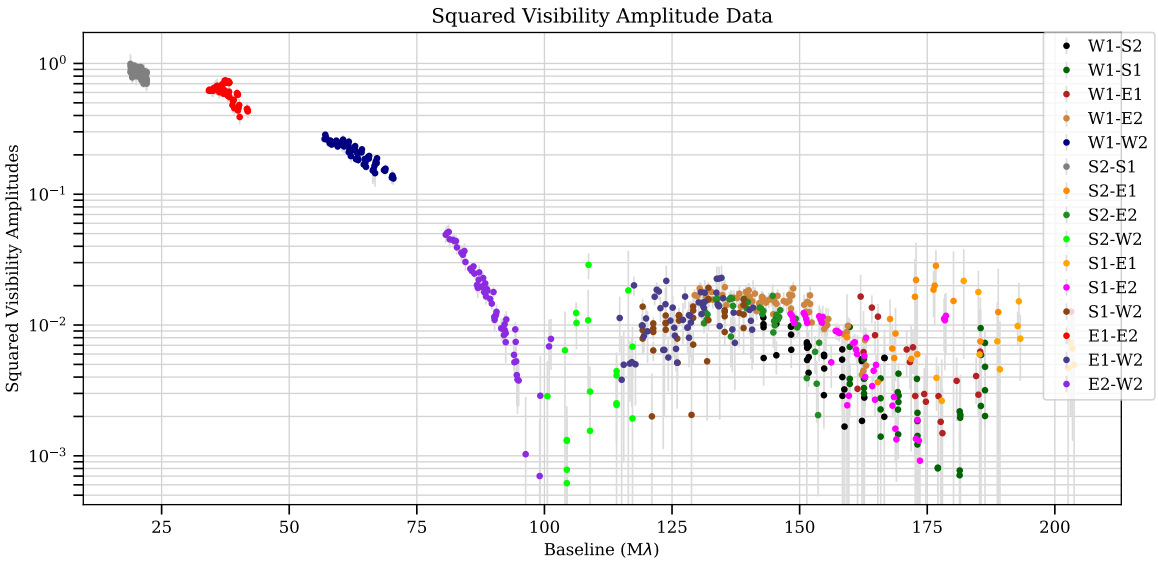

Figure A80: V^2 of V366 And in 2016

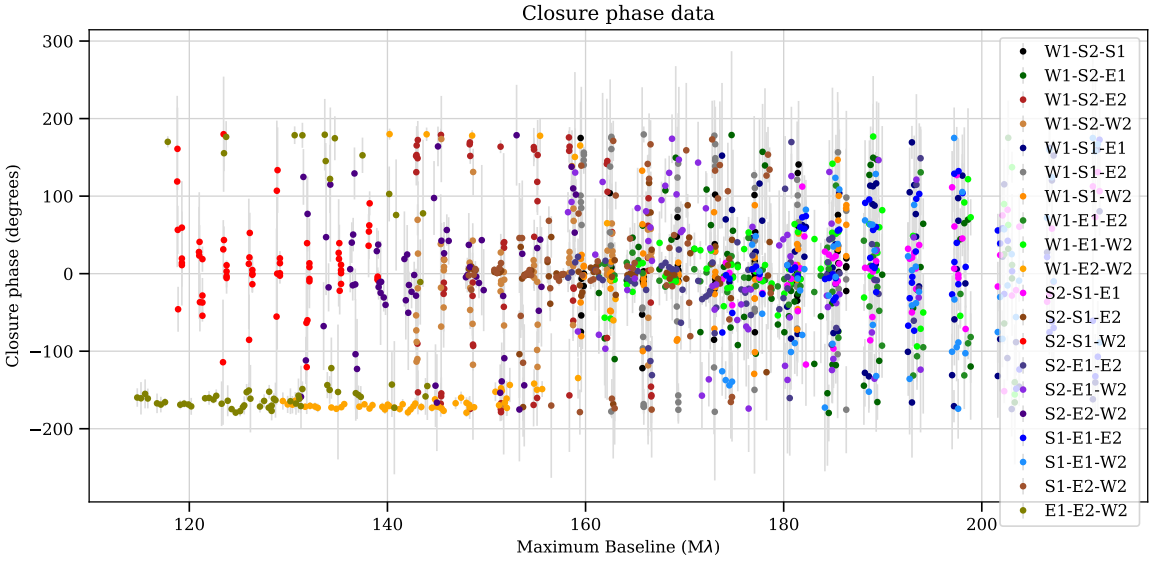

Figure A81: Closure phases of V366 And in 2016

Q V424 Lac

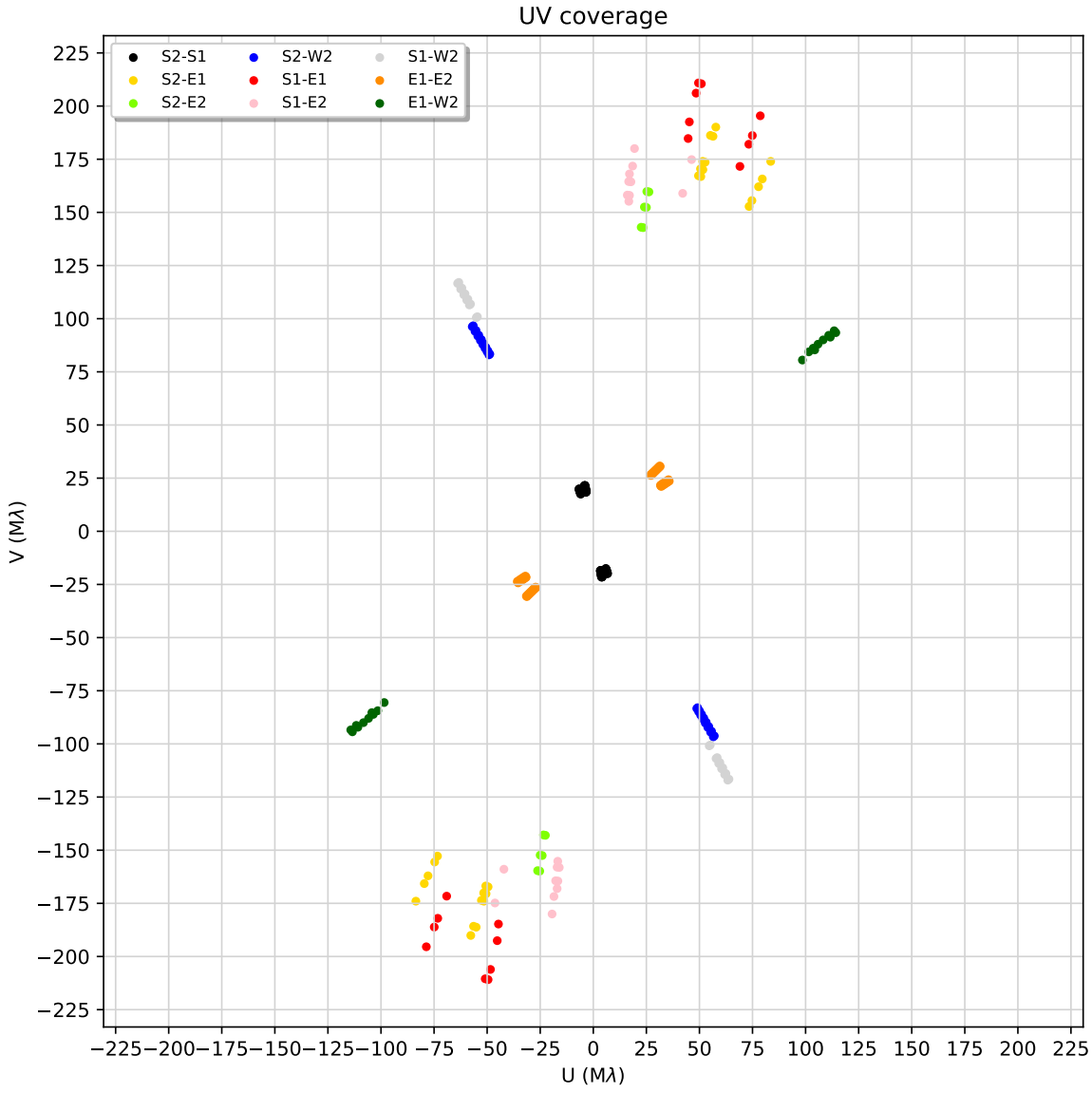

Figure A82: (u, v) coverage for V424 Lac in 2016

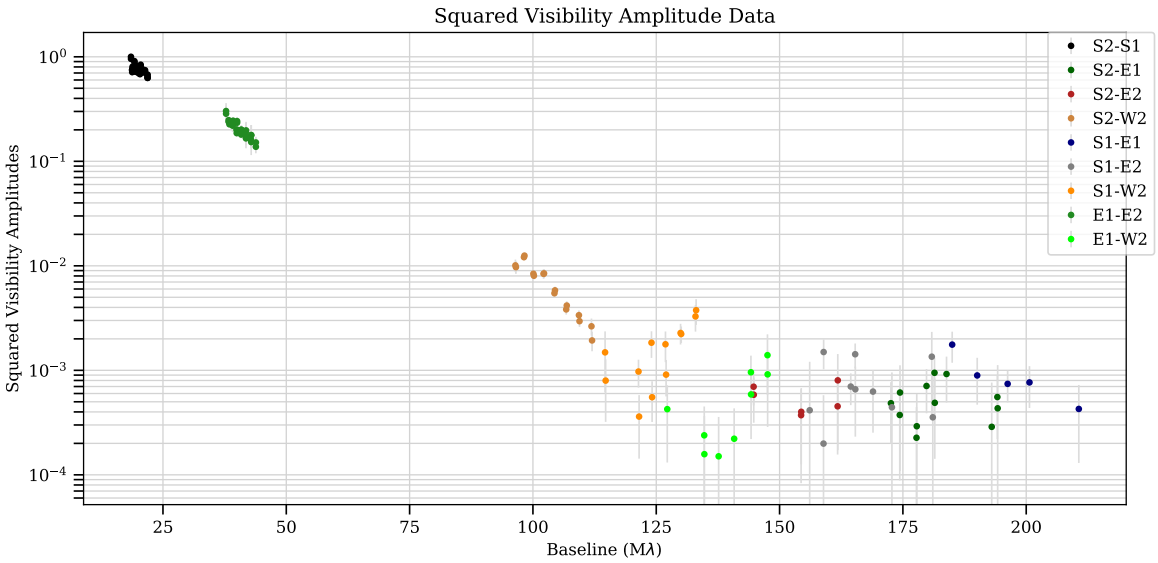

Figure A83: V^2 of V424 Lac in 2016

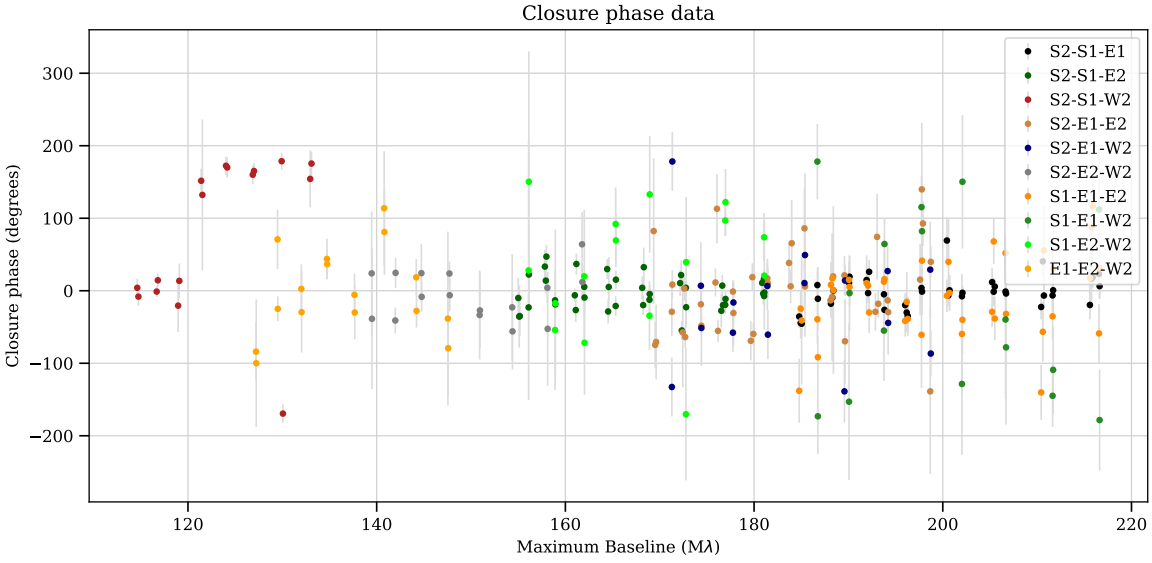

Figure A84: Closure phases of V424 Lac in 2016

R W Per

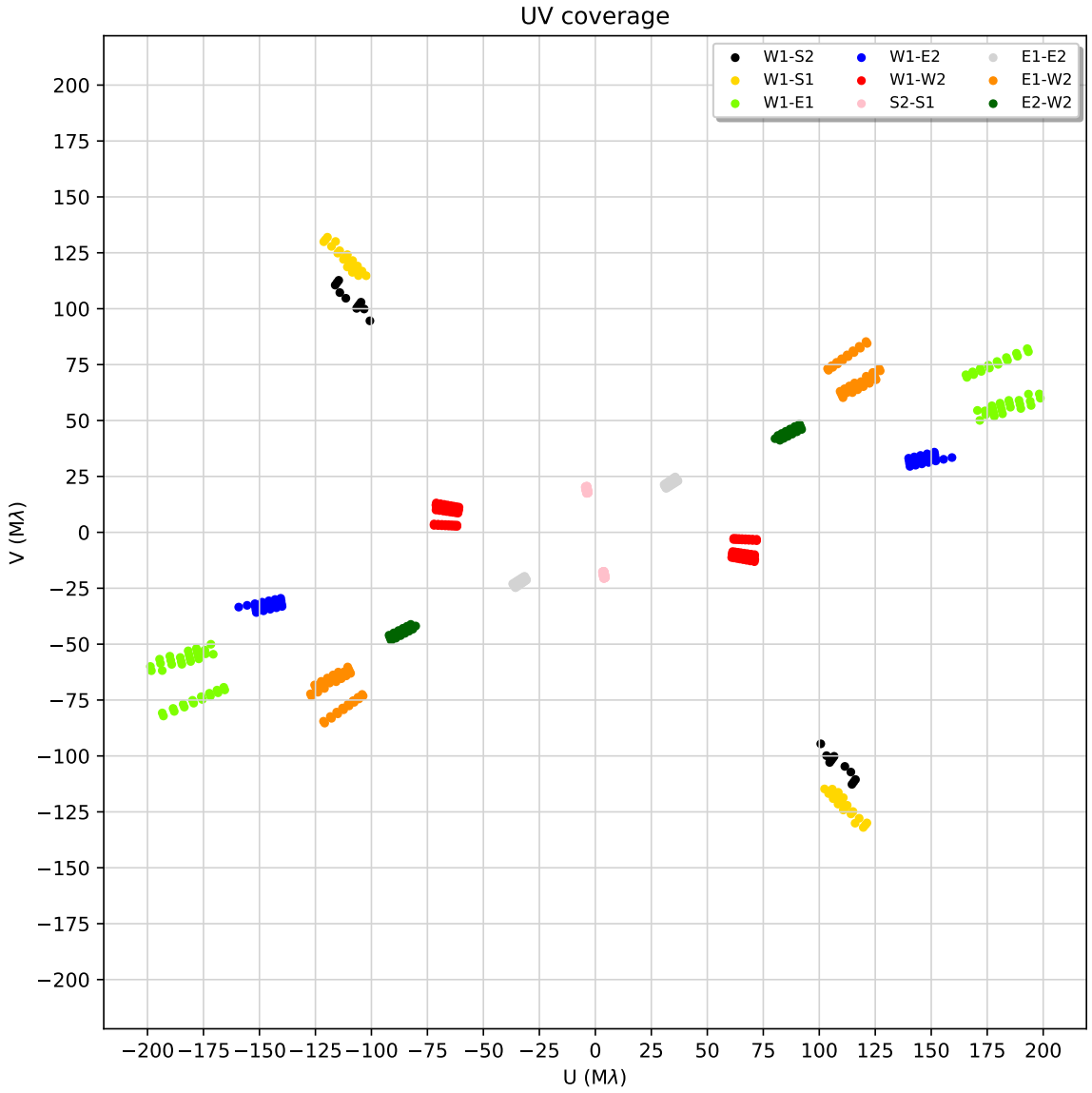

Figure A85: (u, v) coverage for W Per in 2016 August

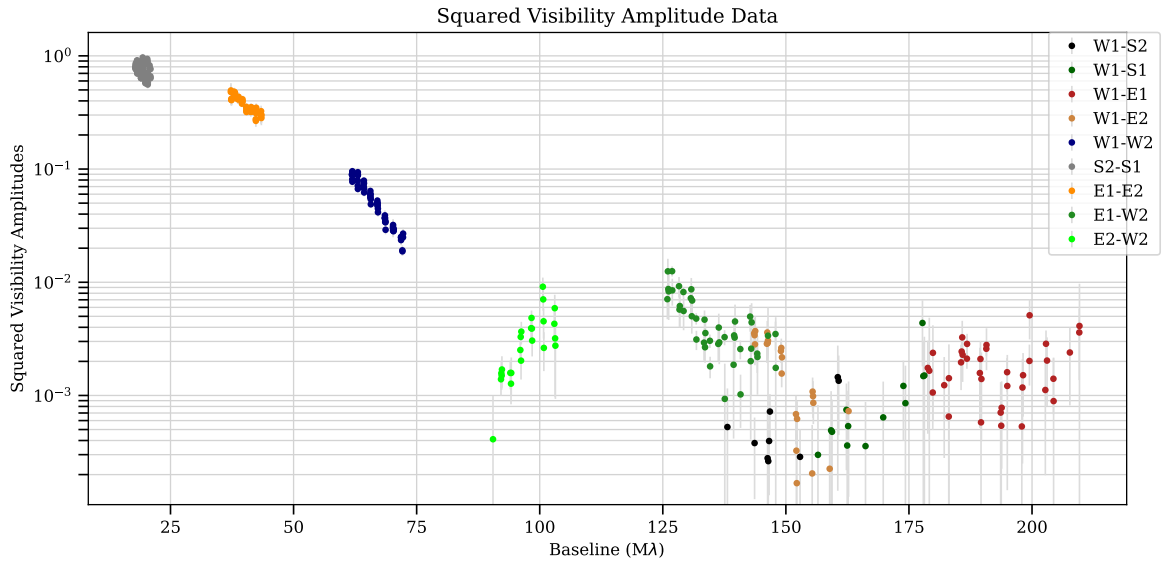

Figure A86: V^2 of W Per in 2016 August

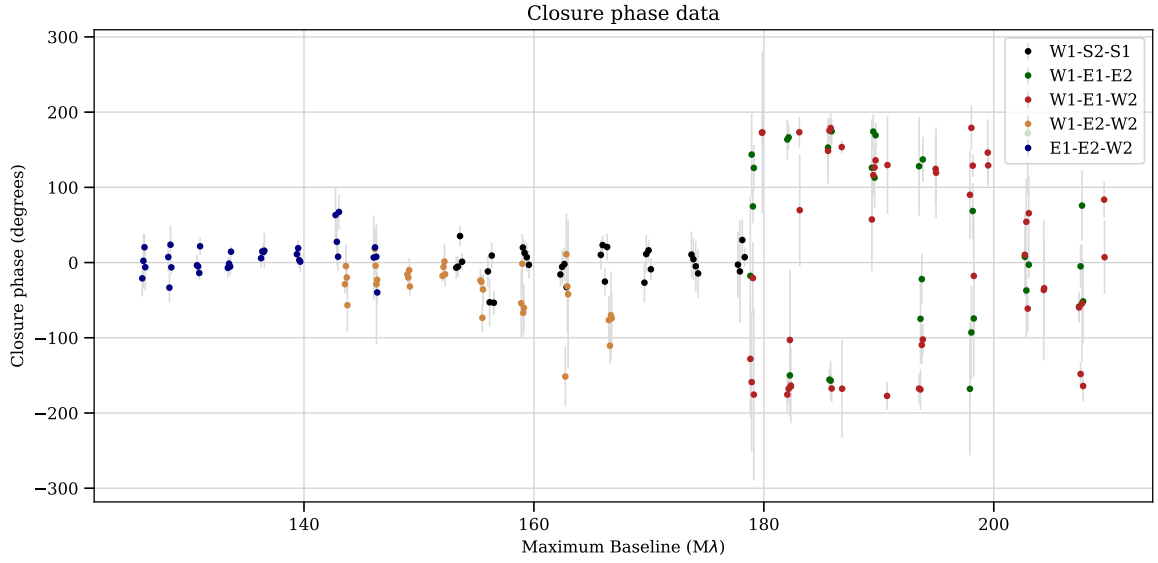

Figure A87: Closure phases of W Per in 2016 August

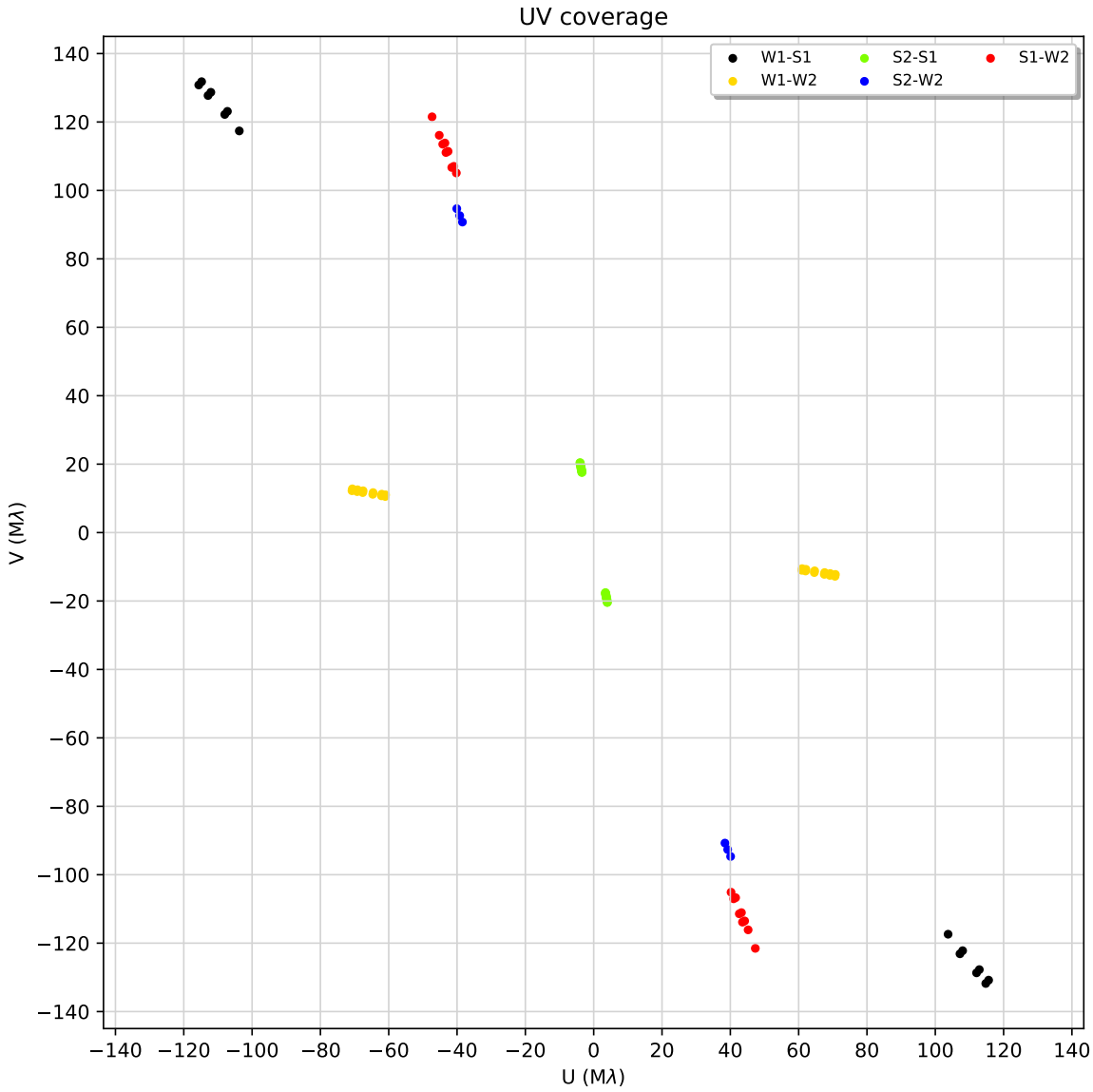

Figure A88: (u, v) coverage for W Per in 2016 October

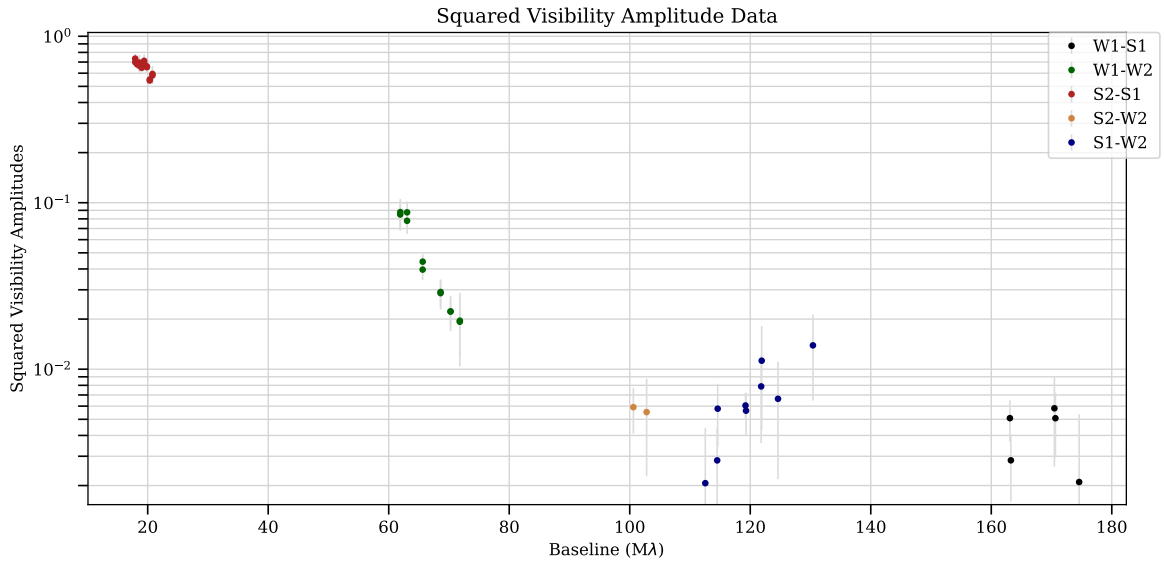

Figure A89: V^2 of W Per in 2016 October

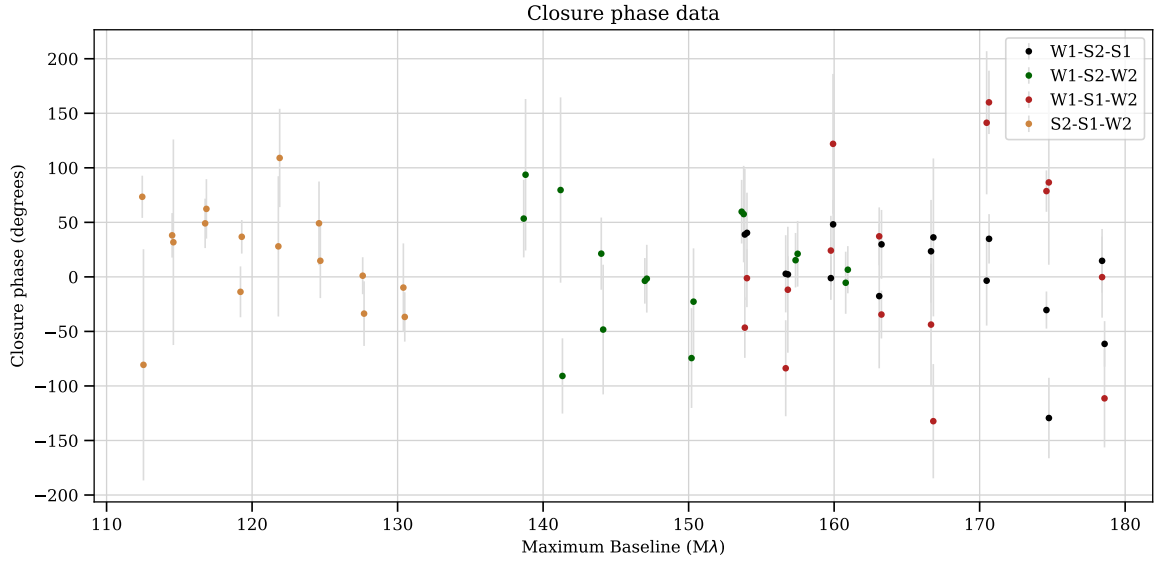

Figure A90: Closure phases of W Per in 2016 October

S WY Gem

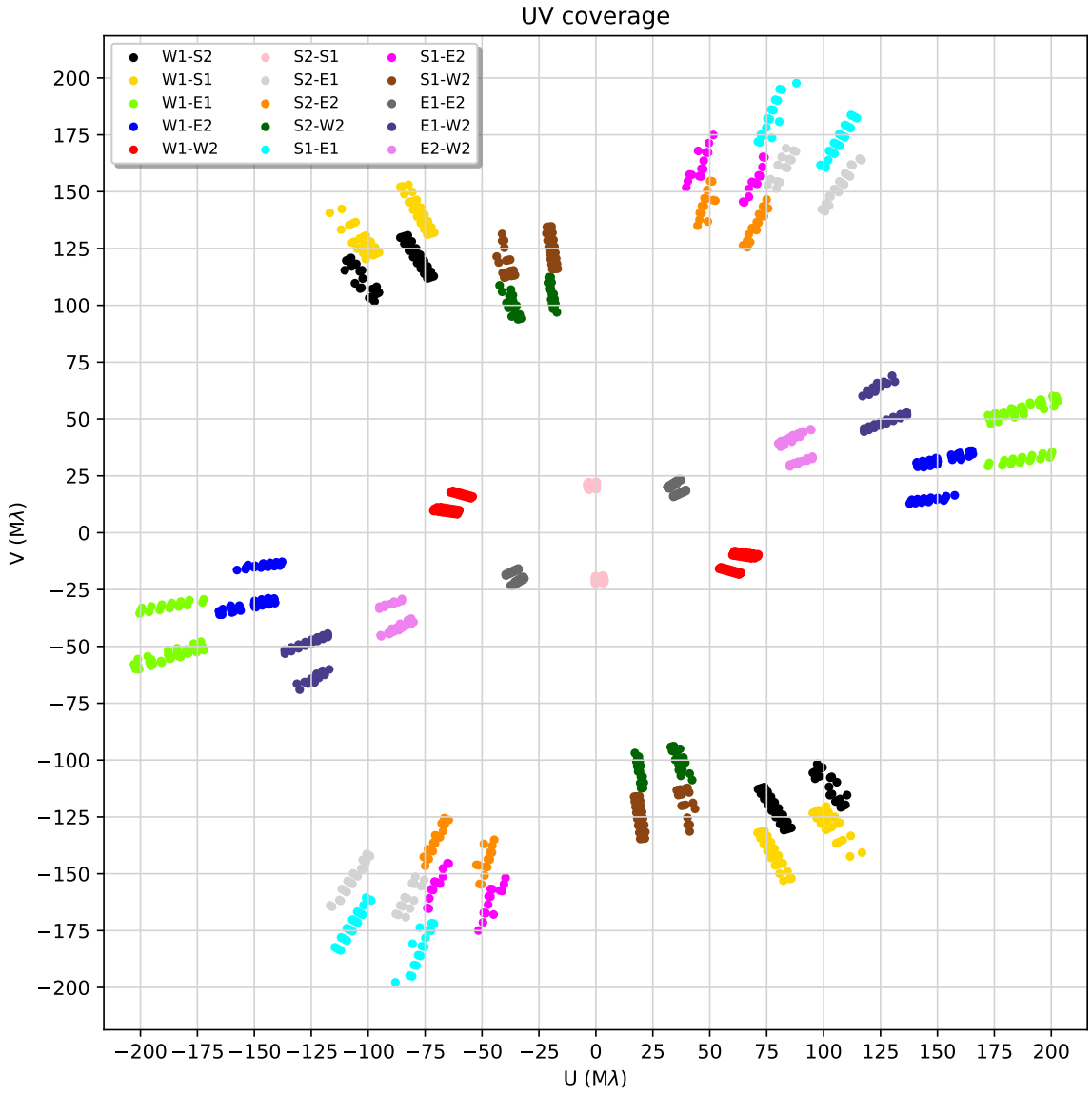

Figure A91: (u, v) coverage for WY Gem in 2016

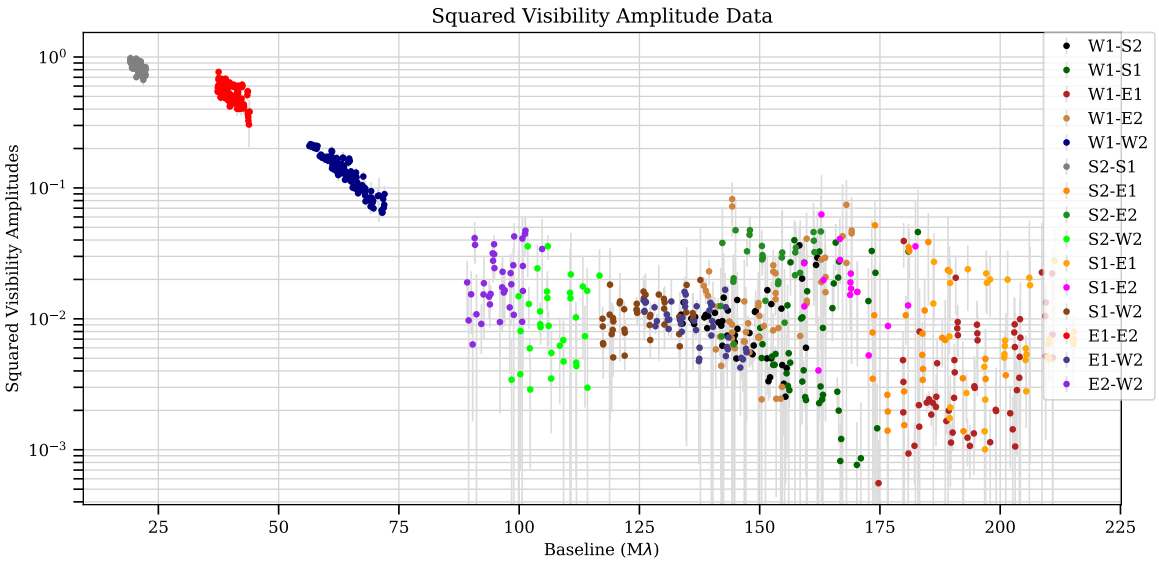

Figure A92: V^2 of WY Gem in 2016

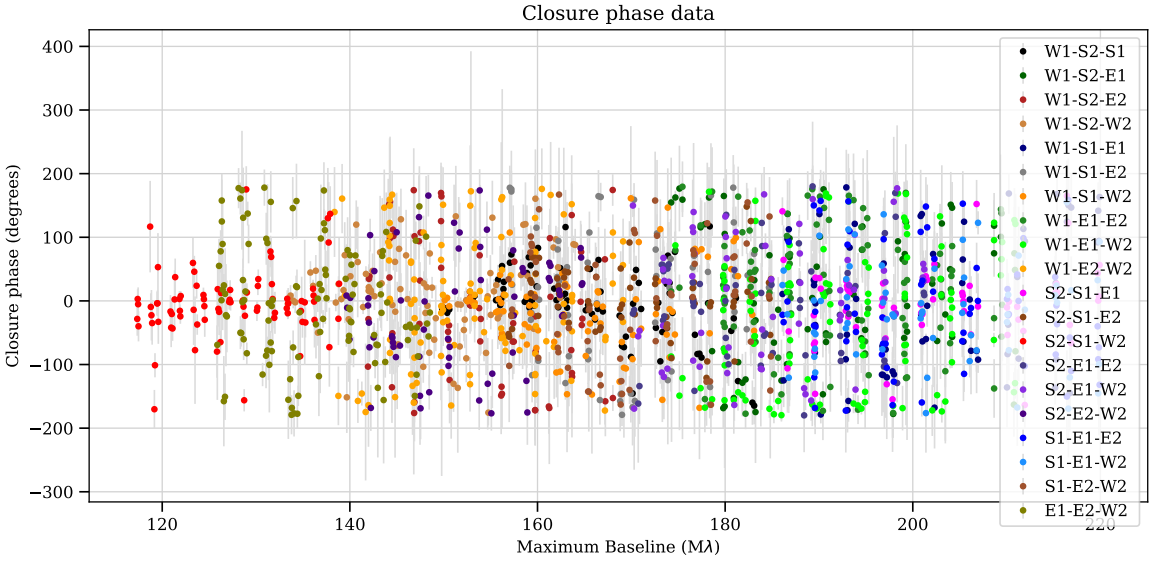

Figure A93: Closure phases of WY Gem in 2016

T XX Per

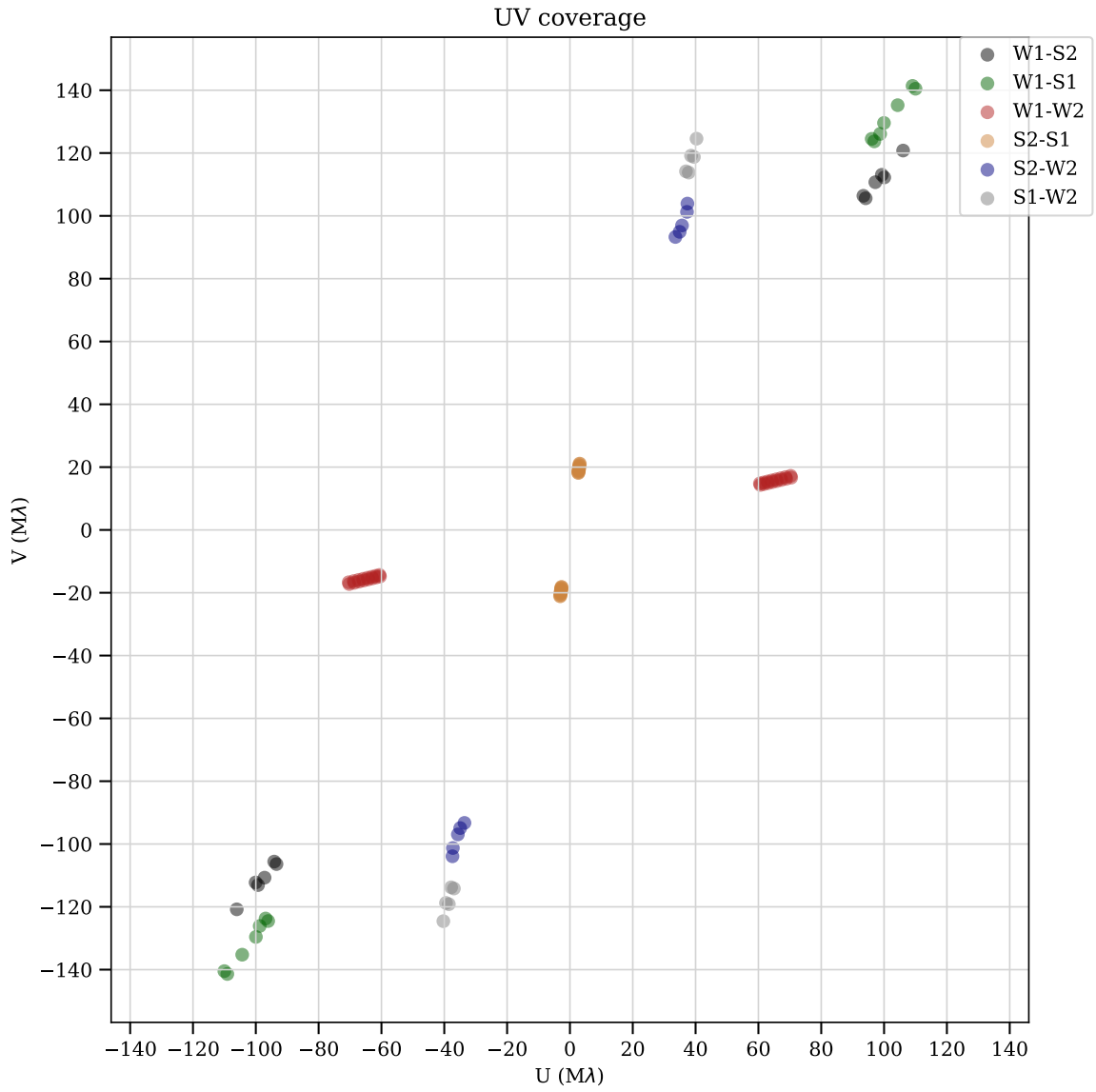

Figure A94: (u, v) coverage for XX Per in 2015

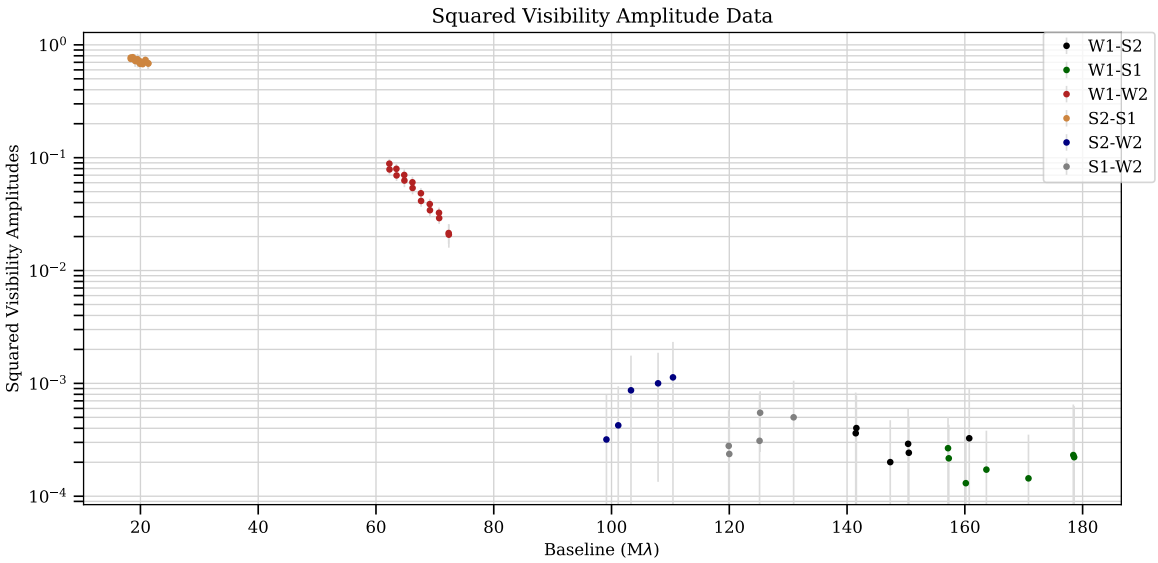

Figure A95: V^2 of XX Per in 2015

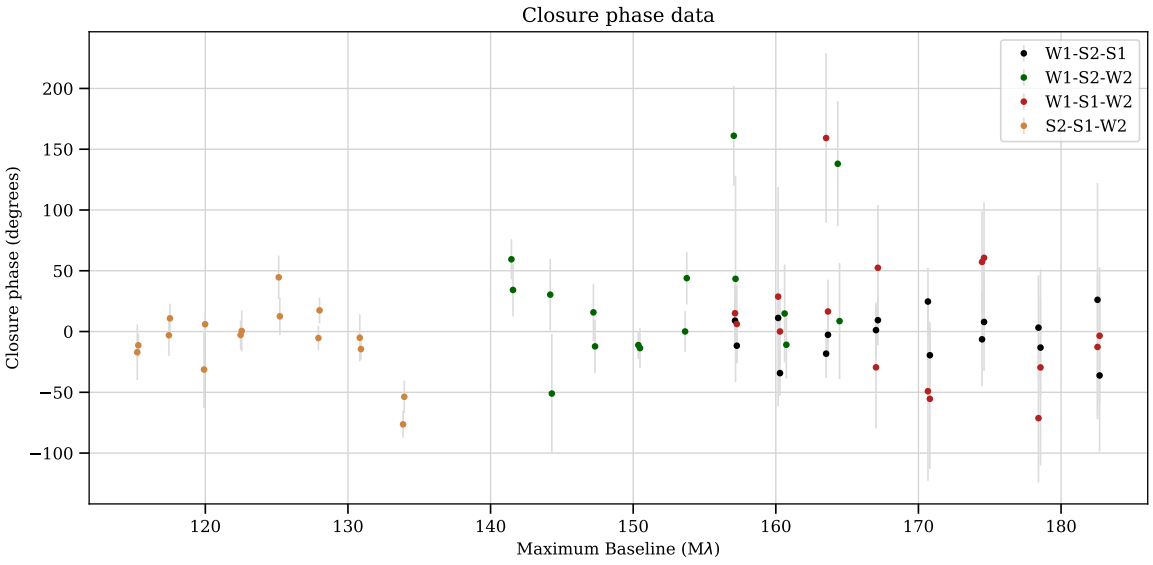

Figure A96: Closure phases of XX Per in 2015

B Comparisons of SQUEEZE Reconstructions to Observations

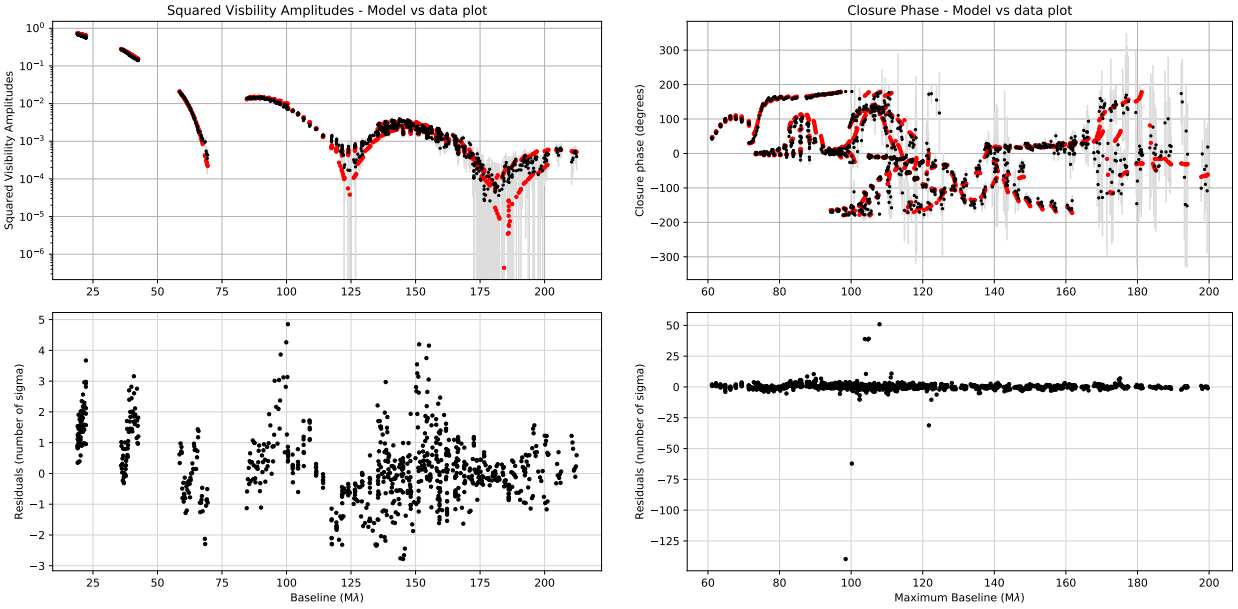

AZ Cyg 2011 Squared Visbilities

AZ Cyg 2011 Closure Phases

Figure B1: Comparision of AZ Cyg 2011 observations (black) to squared visibilities and closure phases calculated from the mean SQUEEZE image (red).

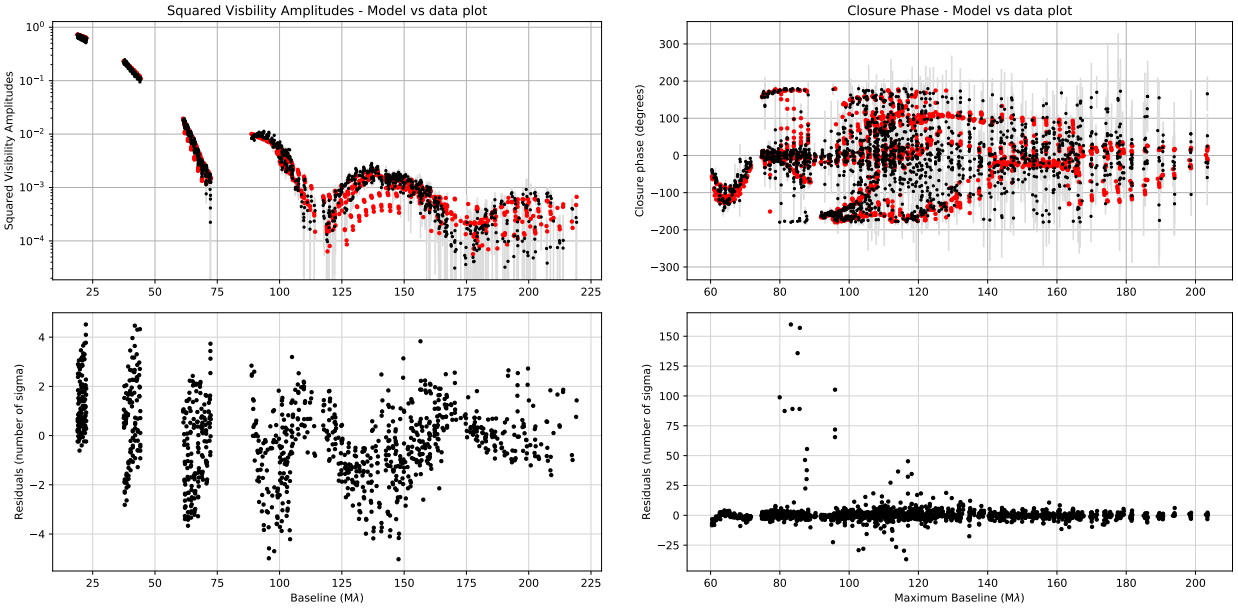

AZ Cyg 2012 Squared Visbilities

AZ Cyg 2012 Closure Phases

Figure B2: Comparision of AZ Cyg 2012 observations (black) to squared visibilities and closure phases calculated from the mean SQUEEZE image (red).

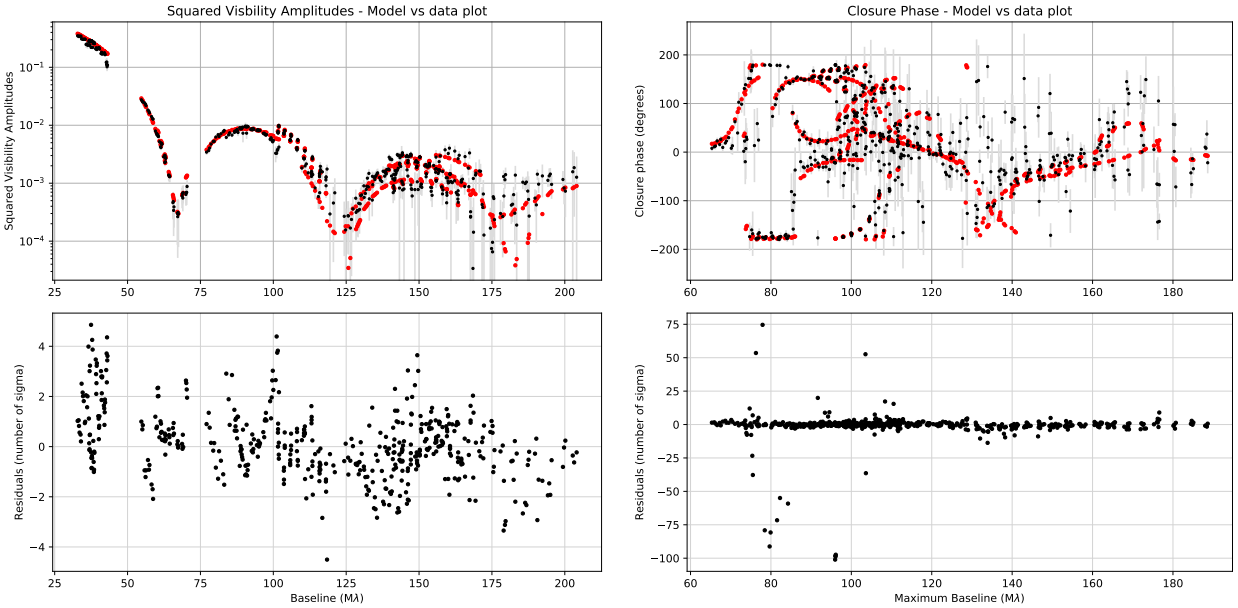

AZ Cyg 2014 Squared Visbilities

AZ Cyg 2014 Closure Phases

Figure B3: Comparision of AZ Cyg 2014 observations (black) to squared visibilities and closure phases calculated from the mean SQUEEZE image (red).

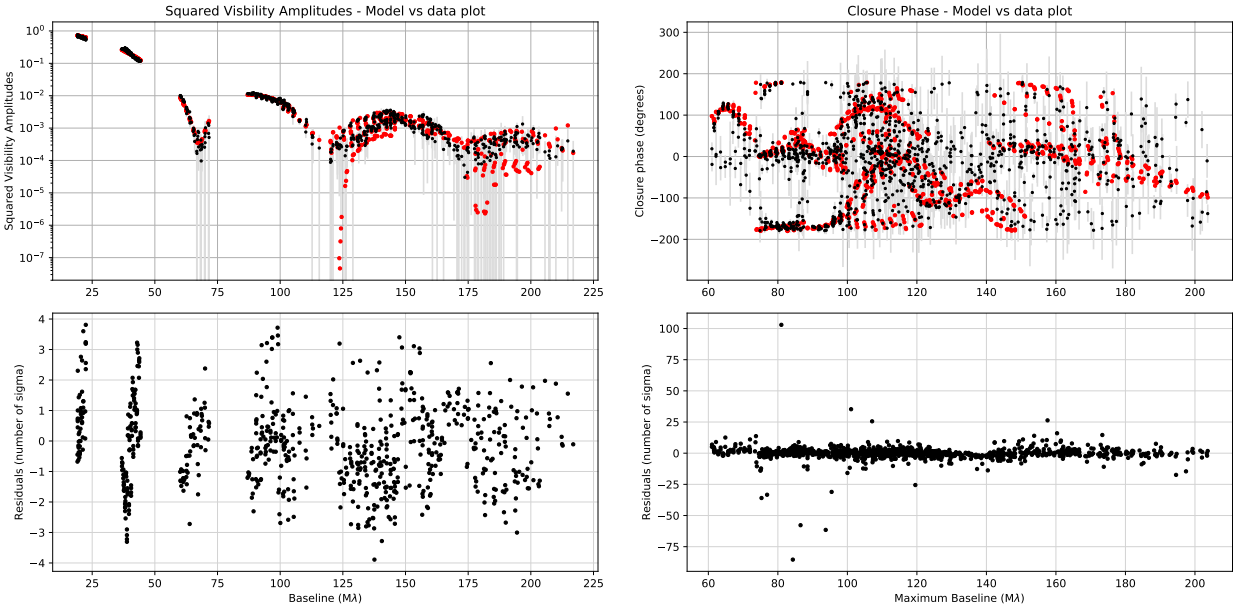

AZ Cyg 2015 Squared Visbilities

AZ Cyg 2016 Closure Phases

Figure B4: Comparision of AZ Cyg 2015 observations (black) to squared visibilities and closure phases calculated from the mean SQUEEZE image (red).

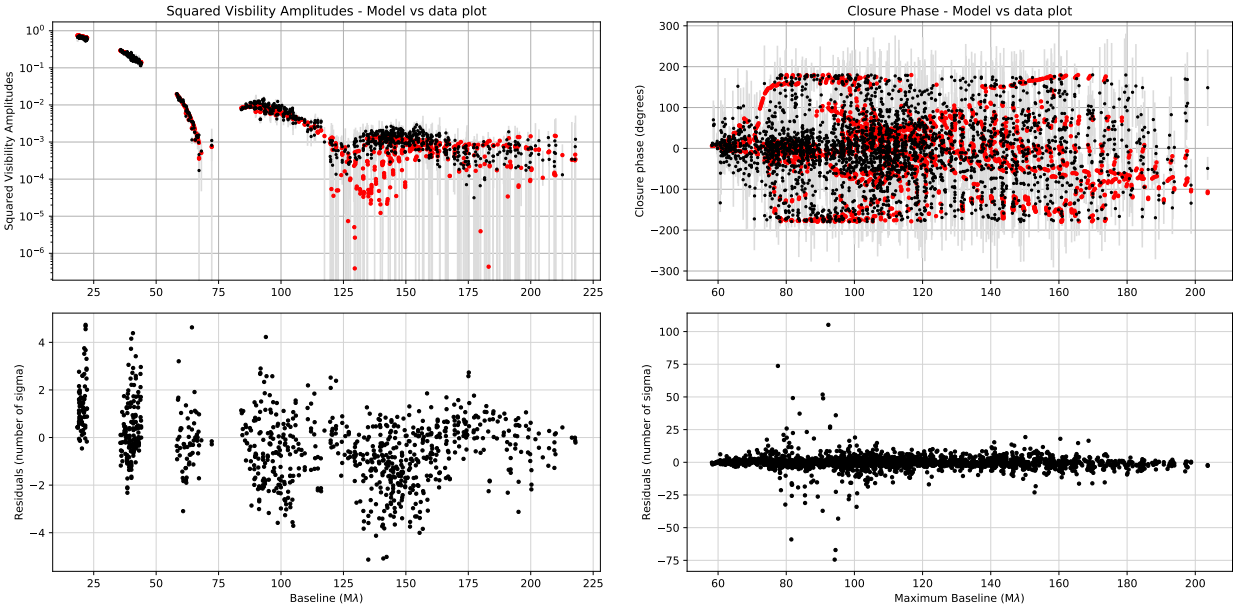

AZ Cyg 2016 Squared Visbilities

AZ Cyg 2016 Closure Phases

Figure B5: Comparision of AZ Cyg 2016 observations (black) to squared visibilities and closure phases calculated from the mean SQUEEZE image (red).

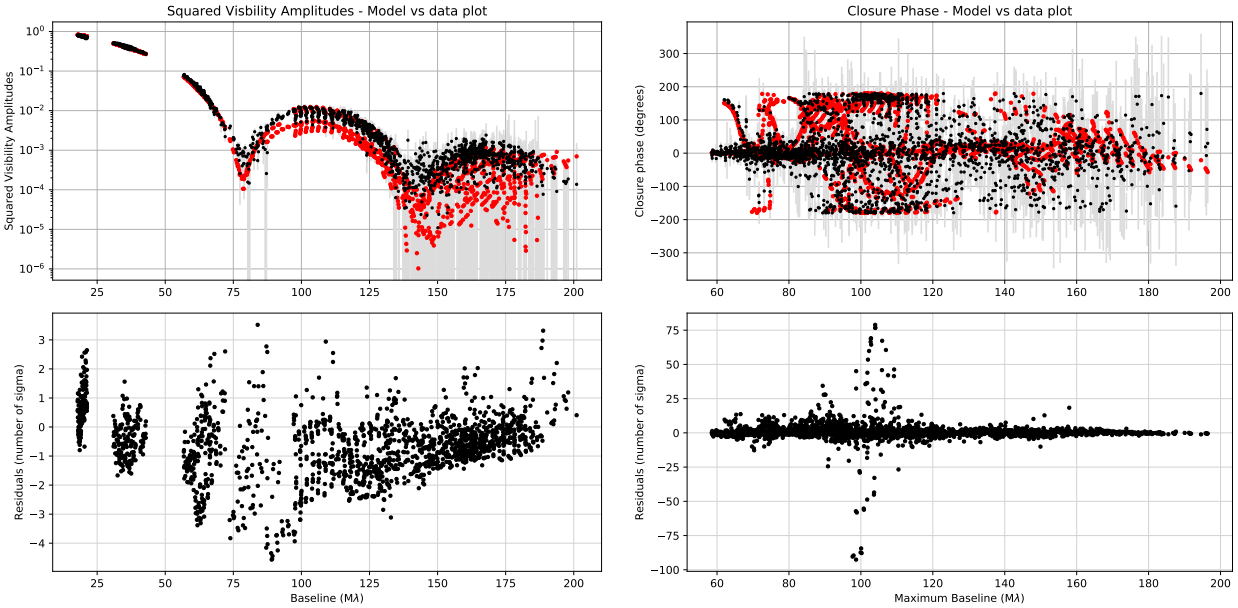

SU Per 2015 Squared Visibilities

SU Per 2015 Closure Phases

Figure B6: Comparision of SU Per 2015 observations (black) to squared visibilities and closure phases calculated from the mean SQUEEZE image (red).

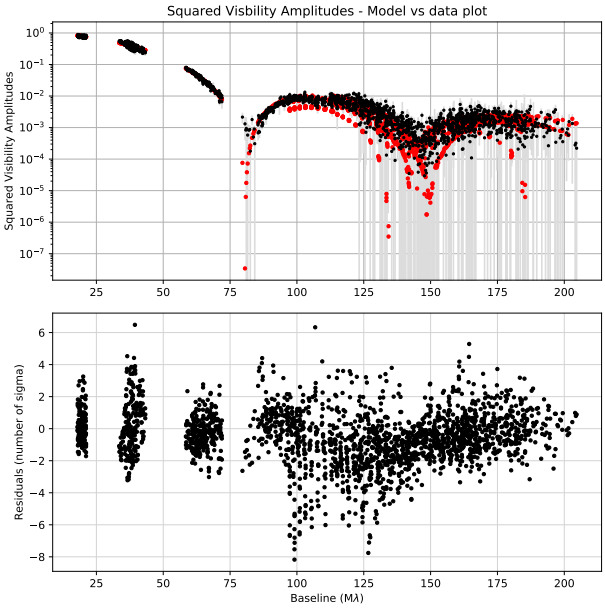

SU Per 2016 August Squared Visibilities

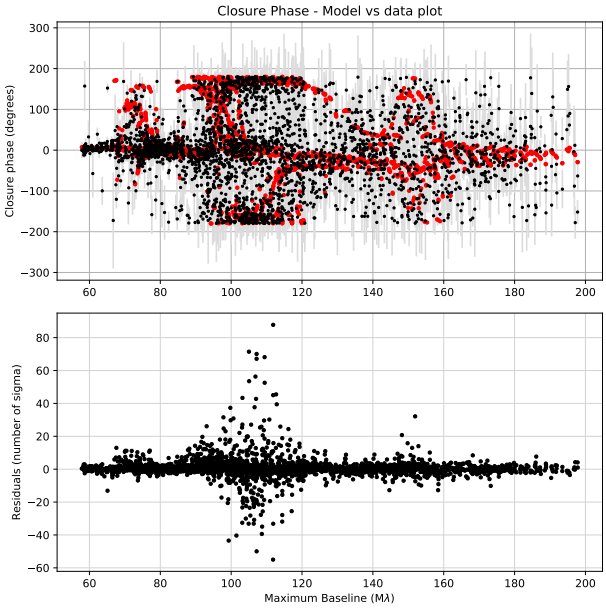

SU Per 2016 August Closure Phases

Figure B7: Comparision of SU Per 2016 August observations (black) to squared visibilities and closure phases calculated from the mean SQUEEZE image (red).

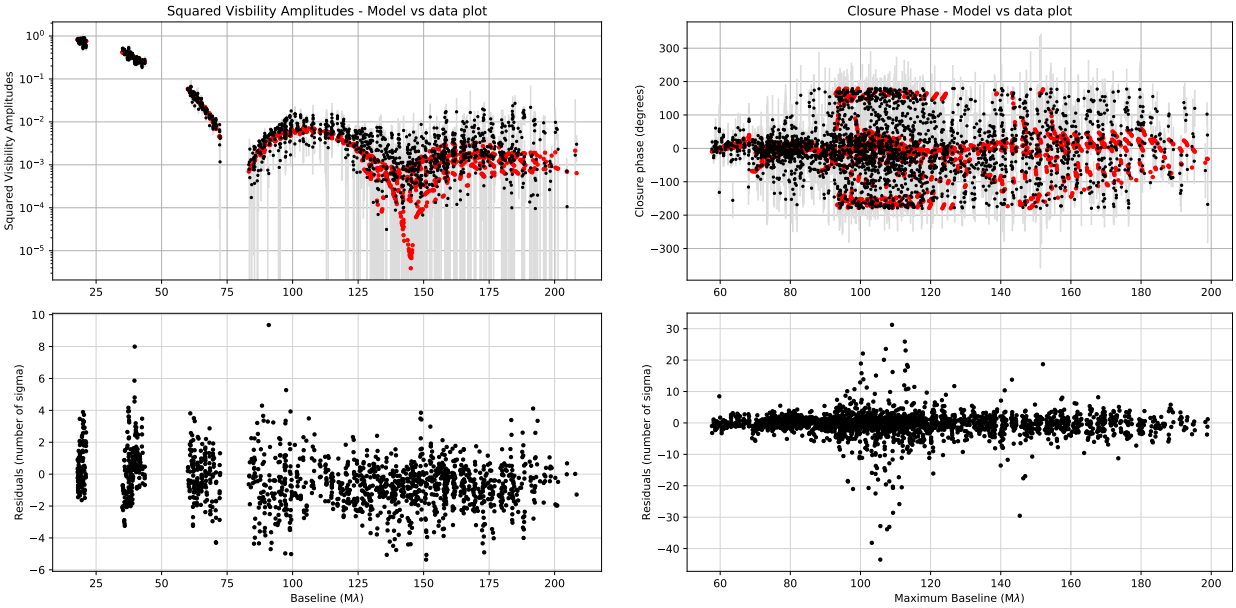

SU Per 2016 October Squared Visibilities

SU Per 2016 October Closure Phases

Figure B8: Comparision of SU Per 2016 October observations (black) to squared visibilities and closure phases calculated from the mean SQUEEZE image (red).

REFERENCES

Alighieri, D. 1966, La Commedia secondo l'antica vulgata, ed. G. Petrocchi (Mondadori)

Allende Prieto, C., & Lambert, D. L. 1999, A&A, 352, 555

Alvarez, R., & Plez, B. 1998, A&A, 330, 1109

Anugu, N. et al. 2018, in Society of Photo-Optical Instrumentation Engineers (SPIE) Conference Series, Vol. 10701, Optical and Infrared Interferometry and Imaging VI, 1070124

Arroyo-Torres, B. et al. 2015, A&A, 575, A50

Asaki, Y., Deguchi, S., Imai, H., Hachisuka, K., Miyoshi, M., & Honma, M. 2010, ApJ, 721, 267

Bailer-Jones, C. A. L., Rybizki, J., Fouesneau, M., Mantelet, G., & Andrae, R. 2018, AJ, 156, 58

Baron, F. 2016, in Astronomy at High Angular Resolution, ed. H. M. J. Boffin, G. Hussain, J.-P. Berger, & L. Schmidtobreick, Vol. 439, 75

Baron, F. et al. 2014, ApJ, 785, 46

Baron, F., Monnier, J. D., & Kloppenborg, B. 2010, in Proc. SPIE, Vol. 7734, Optical and Infrared Interferometry II, 77342I

——. 2012, ApJ, 752, 20

Böhm-Vitense, E. 1958, Zeitschrift für Astrophysik, 46, 108

Bourgés, L., Lafrasse, S., Mella, G., Chesneau, O., Bouquin, J. L., Duvert, G., Chelli, A., & Delfosse, X. 2014, in Astronomical Society of the Pacific Conference Series, Vol. 485,

Astronomical Data Analysis Software and Systems XXIII, ed. N. Manset & P. Forshay, 223

Bowers, R. L., & Deeming, T. 1984, Astrophysics. Volume 1 - Stars (Boston, MA, Jones and Bartlett Publishers, Inc)

Burns, D. et al. 1997, MNRAS, 290, L11

Buscher, D. F., Haniff, C. A., Baldwin, J. E., & Warner, P. J. 1990, MNRAS, 245, 7P

Cardelli, J. A., Clayton, G. C., & Mathis, J. S. 1989, ApJ, 345, 245

Cecchini, R., & Pelosi, G. 1990, IEEE Antennas and Propagation Magazine, 32, 27

Chatys, F. W., Bedding, T. R., Murphy, S. J., Kiss, L. L., Dobie, D., & Grindlay, J. E. 2019, arXiv e-prints, arXiv:1906.03879

Che, X., Monnier, J. D., & Webster, S. 2010, in NA, Vol. 7734, 77342V

Chelli, A., Duvert, G., Bourgès, L., Mella, G., Lafrasse, S., Bonneau, D., & Chesneau, O. 2016, A&A, 589, A112

Cheng, A. Y. S., Hege, E. K., Hubbard, E. N., Goldberg, L., Strittmatter, P. A., & Cocke, W. J. 1986, ApJ, 309, 737

Chiavassa, A., Haubois, X., Young, J. S., Plez, B., Josselin, E., Perrin, G., & Freytag, B. 2010a, A&A, 515, A12

Chiavassa, A. et al. 2010b, A&A, 511, A51

Chiavassa, A., Plez, B., Josselin, E., & Freytag, B. 2009, A&A, 506, 1351

Currie, T. et al. 2010, ApJS, 186, 191

Cushing, M. C., Vacca, W. D., & Rayner, J. T. 2004, PASP, 116, 362

Danchi, W. C., Bester, M., Degiacomi, C. G., Greenhill, L. J., & Townes, C. H. 1994, AJ, 107, 1469

Davies, B., & Beasor, E. R. 2018, MNRAS, 474, 2116

Davies, B., Kudritzki, R.-P., Gazak, Z., Plez, B., Bergemann, M., Evans, C., & Patrick, L. 2015, ApJ, 806, 21

Davies, B. et al. 2013, ApJ, 767, 3

Davies, B. et al. 2013, The Astrophysical Journal, 767, 3

de Jager, C., Nieuwenhuijzen, H., & van der Hucht, K. A. 1988, A&AS, 72, 259

Drout, M. R., Massey, P., & Meynet, G. 2012, ApJ, 750, 97

Ducati, J. R. 2002, VizieR Online Data Catalog

Duchene, G., Berger, J.-P., Duvert, G., Zins, G., & Mella, G. 2004, in Proc. SPIE, Vol. 5491, New Frontiers in Stellar Interferometry, ed. W. A. Traub, 611

Dyck, H. M., Benson, J. A., van Belle, G. T., & Ridgway, S. T. 1996a, AJ, 111, 1705

Dyck, H. M., van Belle, G. T., & Benson, J. A. 1996b, AJ, 112, 294

Elias, J. H., Frogel, J. A., & Humphreys, R. M. 1985, ApJS, 57, 91

ESA, ed. 1997, The HIPPARCOS and TYCHO catalogues. Astrometric and photometric star catalogues derived from the ESA HIPPARCOS Space Astrometry Mission, Vol. 1200

Finnila, A. B., Gomez, M. A., Sebenik, C., Stenson, C., & Doll, J. D. 1994, Chemical Physics Letters, 219, 343

Freytag, B., Holweger, H., Steffen, M., & Ludwig, H.-G. 1997, in Science with the VLT Interferometer, ed. F. Paresce, 316

Freytag, B., Steffen, M., & Dorch, B. 2002, Astronomische Nachrichten, 323, 213

Freytag, B., Steffen, M., Ludwig, H. G., Wedemeyer-Böhm, S., Schaffenberger, W., & Steiner, O. 2012, Journal of Computational Physics, 231, 919

Gaia Collaboration. 2018, VizieR Online Data Catalog, I/345

Gaia Collaboration et al. 2018, A&A, 616, A1

——. 2016, A&A, 595, A1

Gaposchkin, C. H. P., & Shapley, H. 1938, Annals of Harvard College Observatory, 89, 192

Gazak, J. Z., Davies, B., Kudritzki, R., Bergemann, M., & Plez, B. 2014, The Astrophysical Journal, 788, 58

Gazak, J. Z. et al. 2015, ApJ, 805, 182

Gilliland, R. L., & Dupree, A. K. 1996, ApJ, 463, L29

Goldberg, L., Hege, E. K., Hubbard, E. N., Strittmatter, P. A., & Cocke, W. J. 1982, SAO Special Report, 392, 131

Gomes, N., Garcia, P. J. V., & Thiébaut, É. 2017, MNRAS, 465, 3823

Gray, D. F. 2000, ApJ, 532, 487

——. 2008a, AJ, 135, 1450

——. 2008b, AJ, 135, 1450

Gray, D. F., & Pugh, T. 2012, AJ, 143, 92

Guizar-Sicairos, M., Thurman, S. T., & Fienup, J. R. 2008, Opt. Lett., 33, 156

Gustafsson, B., Edvardsson, B., Eriksson, K., Jørgensen, U. G., Nordlund, ., & Plez, B. 2008, Astronomy and Astrophysics, 486, 951

Haubois, X. et al. 2009, A&A, 508, 923

Hebden, J. C., Christou, J. C., Cheng, A. Y. S., Hege, E. K., Strittmatter, P. A., Beckers, J. M., & Murphy, H. P. 1986, ApJ, 309, 745

Hestroffer, D. 1997, A&A, 327, 199

Humphreys, R. M., & Davidson, K. 1979, ApJ, 232, 409

Ireland, M. J., Monnier, J. D., & Thureau, N. 2006, in Proc. SPIE, Vol. 6268, Society of Photo-Optical Instrumentation Engineers (SPIE) Conference Series, 62681T

Jackson, J. D. 1998, Classical Electrodynamics, 3rd Edition (ISBN 0-471-30932-X. Wiley-VCH), 832

Jennison, R. C. 1958, MNRAS, 118, 276

Josselin, E., & Plez, B. 2007, A&A, 469, 671

Jura, M., & Kleinmann, S. G. 1990, ApJS, 73, 769

Kadowaki, T., & Nishimori, H. 1998, Phys. Rev. E, 58, 5355

Kholopov, P. N., Samus, N. N., Kazarovets, E. V., & Perova, N. B. 1985, Information Bulletin on Variable Stars, 2681

Kiss, L. L., Monnier, J. D., Bedding, T. R., Tuthill, P., Zhao, M., Ireland, M. J., & ten Brummelaar, T. A. 2010, in Astronomical Society of the Pacific Conference Series, Vol. 425, Hot and Cool: Bridging Gaps in Massive Star Evolution, ed. C. Leitherer, P. D. Bennett, P. W. Morris, & J. T. Van Loon, 140

Kiss, L. L., Szabó, G. M., & Bedding, T. R. 2006, MNRAS, 372, 1721

Kravchenko, K. 2018, in Imaging of Stellar Surfaces, 20

Kravchenko, K., Van Eck, S., Chiavassa, A., Jorissen, A., Freytag, B., & Plez, B. 2018, A&A, 610, A29

Kurucz, R. L. 1993, SYNTHE spectrum synthesis programs and line data (Smithsonian Astrophysical Observatory)

Labeyrie, A. 1970, A&A, 6, 85

Labeyrie, A., Lipson, S. G., & Nisenson, P. 2006, An Introduction to Optical Stellar Interferometry (NA), 360

Lacour, S. et al. 2008, A&A, 485, 561

Lançon, A., Hauschildt, P. H., Ladjal, D., & Mouhcine, M. 2007, A&A, 468, 205

Lancon, A., & Rocca-Volmerange, B. 1992, A&AS, 96, 593

Lawson, P. R., ed. 2000, Principles of Long Baseline Stellar Interferometry

Lester, J. B., & Neilson, H. R. 2008, A&A, 491, 633

Levesque, E. M. 2017, Astrophysics of Red Supergiants (NA)

Levesque, E. M., Massey, P., Olsen, K. A. G., Plez, B., Josselin, E., Maeder, A., & Georges Meynet. 2005, The Astrophysical Journal, 628, 973

Levesque, E. M., Massey, P., Olsen, K. A. G., Plez, B., Josselin, E., Maeder, A., & Meynet, G. 2005, ApJ, 628, 973

Lindegren, L. et al. 2018, A&A, 616, A2

López Ariste, A. et al. 2018, A&A, 620, A199

Lundqvist, M., & Wahlgren, G. M. 2005, Nuclear Physics A, 758, 304

Luri, X. et al. 2018, A&A, 616, A9

Lynds, C. R., Worden, S. P., & Harvey, J. W. 1976, ApJ, 207, 174

Massey, P., Plez, B., Levesque, E. M., Olsen, K. A. G., Clayton, G. C., & Josselin, E. 2005, ApJ, 634, 1286

Mauron, N., & Josselin, E. 2011, A&A, 526, A156

McDonald, I., Zijlstra, A. A., & Boyer, M. L. 2012, MNRAS, 427, 343

McDonnell, M. J., & Bates, R. H. T. 1976, ApJ, 208, 443

Meynet, G. et al. 2015, A&A, 575, A60

Michelson, A. A. 1891a, PASP, 3, 274

——. 1891b, PASP, 3, 217

——. 1920, ApJ, 51, 257

Michelson, A. A., & Pease, F. G. 1921, ApJ, 53

Monnier, J. D. 2007, New A Rev., 51, 604

Monnier, J. D., Berger, J.-P., Millan-Gabet, R., & ten Brummelaar, T. A. 2004, in NA, Vol. 5491, 1370

Monnier, J. D. et al. 2012, The Astrophysical Journal Letters, 761, L3

Monnier, J. D. et al. 2006, in Michigan Infrared Combiner (MIRC): commissioning results at the CHARA Array, Vol. 6268, 62681P

——. 2007, Science, 317, 342

Montargès, M., Norris, R., Chiavassa, A., Tessore, B., Lèbre, A., & Baron, F. 2018, A&A, 614, A12

Mourard, D. et al. 2015, A&A, 577, A51

Norris, R., Baron, F. R., Chiavassa, A., Montargès, M., Paladini, C., & Young, J. S. 2019, in American Astronomical Society Meeting Abstracts, Vol. 233, American Astronomical Society Meeting Abstracts #233, 336.05

Norris, R. P., Wahlgren, G. M., & Blackwell-Whitehead, R. 2010, in Bulletin of the American Astronomical Society, Vol. 42, American Astronomical Society Meeting Abstracts #215, 339

Ochsenbein, F., Bauer, P., & Marcout, J. 2000, A&AS, 143, 23

O'Gorman, E., Kervella, P., Harper, G. M., Richards, A. M. S., Decin, L., Montargès, M., & McDonald, I. 2017, A&A, 602, L10

Ohnaka, K., Weigelt, G., & Hofmann, K.-H. 2017, Nature, 548, 310

Paladini, C. et al. 2018, Nature, 553, 310

Patrick, L. R., Evans, C. J., Davies, B., Kudritzki, R.-P., Gazak, J. Z., Bergemann, M., Plez, B., & Ferguson, A. M. N. 2015, ApJ, 803, 14

Percy, J. R., & Khatu, V. C. 2014, Journal of the American Association of Variable Star Observers (JAAVSO), 42, 1

Percy, J. R., & Sato, H. 2009, JRASC, 103, 11

Pickles, A., & Depagne, É. 2010, PASP, 122, 1437

Pignatari, M., Gallino, R., Heil, M., Wiescher, M., Käppeler, F., Herwig, F., & Bisterzo, S. 2010, ApJ, 710, 1557

Plez, B. 2012, Turbospectrum: Code for spectral synthesis, Astrophysics Source Code Library

Prša, A. et al. 2016, AJ, 152, 41

Pugh, T., & Gray, D. F. 2013, ApJ, 777, 10

Rayner, J. T., Cushing, M. C., & Vacca, W. D. 2009, ApJS, 185, 289

Rayner, J. T., Toomey, D. W., Onaka, P. M., Denault, A. J., Stahlberger, W. E., Vacca, W. D., Cushing, M. C., & Wang, S. 2003, PASP, 115, 362

Renard, S., Thiébaut, E., & Malbet, F. 2011, A&A, 533, A64

Schwarzschild, M. 1975, ApJ, 195, 137

Shapiro, A. E. 1989, Notes and Records of the Royal Society of London, 43, 223

Slesnick, C. L., Hillenbrand, L. A., & Massey, P. 2002, ApJ, 576, 880

Stein, R. F., & Nordlund, Å. 1998, ApJ, 499, 914

Stothers, R., & Leung, K. C. 1971, A&A, 10, 290

Stothers, R. B. 2010, ApJ, 725, 1170

Sukhbold, T., & Adams, S. 2019, arXiv e-prints, arXiv:1905.00474

Thiébaut, E. 2008, in Society of Photo-Optical Instrumentation Engineers (SPIE) Conference Series, Vol. 7013, Optical and Infrared Interferometry, 70131I

Trampedach, R., Asplund, M., Collet, R., Nordlund, Å., & Stein, R. F. 2013, ApJ, 769, 18

Tremblay, P. E., Ludwig, H. G., Freytag, B., Steffen, M., & Caffau, E. 2013, A&A, 557, A7

Tuthill, P. G., Haniff, C. A., & Baldwin, J. E. 1997, MNRAS, 285, 529

Vacca, W. D., Cushing, M. C., & Rayner, J. T. 2003, PASP, 115, 389

van Belle, G. T., Creech-Eakman, M. J., & Hart, A. 2009, Monthly Notices of the Royal Astronomical Society, 394, 1925

van Loon, J. T., Cioni, M.-R. L., Zijlstra, A. A., & Loup, C. 2005, A&A, 438, 273

Venegas-Andraca, S. E., Cruz-Santos, W., McGeoch, C., & Lanzagorta, M. 2018, Contemporary Physics, 59, 174

Wahlgren, G. M., Carpenter, K. G., & Norris, R. P. 2009, in American Institute of Physics Conference Series, Vol. 1094, 15th Cambridge Workshop on Cool Stars, Stellar Systems, and the Sun, ed. E. Stempels, 892–895

Welter, G. L., & Worden, S. P. 1980, ApJ, 242, 673

Wenger, M. et al. 2000, A&AS, 143, 9

Wilkerson, M. S., & Worden, S. P. 1977, AJ, 82, 642

Wilson, R. W., Baldwin, J. E., Buscher, D. F., & Warner, P. J. 1992, MNRAS, 257, 369

Wilson, R. W., Dhillon, V. S., & Haniff, C. A. 1997, MNRAS, 291, 819

Wittkowski, M. et al. 2017, A&A, 606, L1

Wittkowski, M., Aufdenberg, J. P., & Kervella, P. 2004, A&A, 413, 711

Worden, S. P., Lynds, C. R., & Harvey, J. W. 1976, Journal of the Optical Society of America (1917-1983), 66, 1243

Young, J. S. et al. 2000, MNRAS, 315, 635

Zernike, F. 1938, Physica, 5, 785

Zhao, M. et al. 2008, ApJ, 684, L95

Zhao, M. et al. 2011, Publications of the Astronomical Society of the Pacific, 123, 964

Ziggelaar, A. 1980, Annals of Science, 37, 179